

Locating transient disturbance sources and modelling their interaction with transmission lines: use of electromagnetic time reversal and asymptotic theory

THÈSE N° 7043 (2016)

PRÉSENTÉE LE 23 SEPTEMBRE 2016

À LA FACULTÉ DES SCIENCES ET TECHNIQUES DE L'INGÉNIEUR

GROUPE SCI STI FR

PROGRAMME DOCTORAL EN GÉNIE ÉLECTRIQUE

ÉCOLE POLYTECHNIQUE FÉDÉRALE DE LAUSANNE

POUR L'OBTENTION DU GRADE DE DOCTEUR ÈS SCIENCES

PAR

Gaspard LUGRIN

acceptée sur proposition du jury:

Prof. M. Paolone, président du jury

Prof. F. Rachidi-Haeri, Dr S.-R. Cherkaoui, directeurs de thèse

Prof. M. Rubinstein, rapporteur

Prof. F. Paladian, rapporteur

Prof. A. Skrivervik, rapporteur



ÉCOLE POLYTECHNIQUE
FÉDÉRALE DE LAUSANNE

Suisse
2016

Til Kjersti

Résumé

Cette thèse porte sur l'application du retournement temporel en électromagnétisme à la localisation de sources de perturbations transitoires et l'utilisation de la théorie asymptotique à la modélisation de leur interaction avec des lignes de transmission.

Tout d'abord, quelques aspects de la phénoménologie et de la modélisation de la décharge de foudre sont présentés, de même que le calcul des champs électromagnétiques associés. En effet, la méthode de localisation de sources transitoire proposée dans cette thèse va être appliquée au cas des décharges orageuses. Les systèmes actuels de détection et de localisation de la foudre (SLF) sont passés en revue. Les erreurs moyennes des SLF sont inférieures à quelques centaines de mètres; cependant, dans certains cas, l'erreur peut être bien supérieure. Le retournement temporel (RT) a de nombreuses applications dans le domaine du traitement du signal et des ondes, et peut servir à la localisation de sources de rayonnement. Le RT a été récemment appliqué à la localisation de la foudre, dans le cas d'un sol parfaitement conducteur.

Nous démontrons que la méthode des temps d'arrivée, qui est une des méthodes les plus couramment utilisées pour localiser la foudre, peut être vue comme un cas particulier de la théorie du RT. Le problème d'un sol comportant des pertes qui affectent la propagation des transitoires électromagnétiques générés par un coup de foudre est discuté en proposant trois modèles de rétro-propagation et en comparant leurs performances en termes de précision de localisation. Les approches proposées sont évaluées par deux types de simulations.

Le premier type de simulation utilise des champs générés numériquement et l'algorithme proposé donne de très bons résultats même pour un sol comportant des pertes. En particulier, nous montrons qu'un modèle pour lequel les pertes sont inversées durant la rétro-propagation fournit des résultats de localisation quasiment exacts. Si la forme complète de l'onde n'est pas disponible, les erreurs de localisation peuvent être plus importantes, même si les erreurs obtenues sont du même ordre ou inférieures à celles des SLF actuels.

Un deuxième groupe de simulations utilise des données du système autrichien de localisation de la foudre (ALDIS). Les localisations obtenues au moyen de la méthode du RT utilisant uniquement les données disponibles (amplitude, temps d'arrivée et temps de montée) diffèrent des estimations fournies par le SLF de quelques kilomètres. Nous discutons des causes possibles de cette divergence dans cette thèse.

La seconde partie de ce document concerne le calcul du courant induit dans une ligne sous l'effet d'un champ électromagnétique. Différentes approches peuvent être utilisées pour résoudre ce problème: la méthode quasi-statique, les méthodes numériques basées sur la théorie des antennes, la théorie des lignes de transmission et les théories des lignes de transmission dites améliorées, parmi lesquelles figurent la théorie asymptotique. Du fait des limitations fréquentielles du modèle quasi-statique et de la théorie des lignes de transmissions et des besoins importants en ressources de calcul des modèles numériques, les modèles de lignes de transmission améliorés nous semblent être des modèles intermédiaires intéressants.

Parmi ces modèles, la méthode asymptotique est particulièrement prometteuse, puisqu'elle fournit une expression analytique pour le courant et donc donne une perception de la physique du problème. Elle fournit des résultats précis au-delà de la fréquence limite de la théorie des lignes de transmission classique et peut aussi être appliquée à des terminaisons arbitraires. Comme elle permet d'éviter l'application de méthodes numériques ou de les appliquer sur de plus petits systèmes, elle est particulièrement efficace pour des lignes électriquement longues. Cependant, avant le début de ce travail, cette méthode était limitée à des lignes à un seul conducteur.

Nous dérivons des expressions valables en haute fréquence pour le courant induit par une onde plane le long d'une ligne à plusieurs conducteurs. Plusieurs approches sont proposées pour calculer les matrices de dispersion et de réflexion qui modélisent les effets de terminaisons. Des expressions mathématiques de ces matrices sont dérivées dans le cas particulier de lignes ouvertes en utilisant une méthode itérative. Pour le cas général de terminaisons arbitraires, une approche utilisant des lignes auxiliaires courtes résolues numériquement est proposée. En basse fréquence, la formulation proposée peut être adaptée à des lignes avec pertes et des expressions analytiques pour les coefficients peuvent être calculées, ce qui correspond à une formulation nouvelle et élégante de la théorie des lignes de transmission classique. La théorie proposée est validée par des simulations numériques et des expériences et est nettement plus efficace que les approches numériques traditionnelles en termes de ressources de mémoire et de calcul.

La méthode asymptotique est aussi appliquée à des sources localisées avec une méthode analogue à celle utilisée pour le couplage d'une onde plane. Une méthode pour la détermination des matrices de coefficients est aussi présentée.

Mots clefs

Retournement temporel (RT) en électromagnétisme, modèles de ligne de transmission améliorés, champ électromagnétique à haute fréquence, systèmes de localisation de la foudre (SLF), méthode des temps d'arrivée, théorie des lignes de transmission.

Abstract

This thesis deals with the application of electromagnetic time reversal to locating transient disturbance sources and the use of the asymptotic theory for the modelling of their interaction with transmission lines.

First, some aspects of the phenomenology and modelling of lightning discharge are discussed, together with the computation of the associated electromagnetic fields. Indeed, the proposed method for locating transient sources will be applied to the case of lightning discharges. The currently used classical lightning detection and location systems (LLSs) are reviewed. Mean location errors of LLSs are within a few hundreds of meters; however, in some cases, the error can be considerably larger. The electromagnetic time reversal (EMTR) theory has found numerous applications in the field of signal processing and waves and has been applied to locate electromagnetic radiation sources. EMTR has recently been considered as a mean to locate lightning discharges above a perfectly-conducting ground plane.

We demonstrate that the time-of-arrival, which is one of the most commonly used methods to locate lightning discharges, can be seen as a special case of time reversal. The problem of a lossy ground that affects the propagation of electromagnetic transient fields generated by a lightning strike is addressed by proposing three different back-propagation models and comparing their performances in terms of location accuracy. Two sets of simulations are carried out to evaluate the accuracy of the proposed approaches.

The first set of simulations is performed using numerically-generated fields and the proposed algorithm is shown to yield very good results even if the soil is not perfectly conducting. In particular, it is shown that considering a model in which losses are inverted in the back-propagation yields theoretically exact results for the source location. We also show that a lack of access to the complete recorded waveforms may lead to higher location errors, although the computed errors are found to be within the range of performance of the present LLSs.

A second set of simulations is performed using the sensor data reported by the Austrian Lightning Location System (ALDIS). The locations obtained by way of the EMTR method using only the available sensor data (amplitude, arrival time and time-to-peak), are observed to be within a few kilometres of the locations supplied by the LLS. The possible sources of this discrepancy are discussed in the thesis.

The second part of this document deals with the computation of the current induced in a line due to an external electromagnetic field. Different approaches can be used to solve this problem: the ‘quasi-static’ method, the ‘full-wave’ methods, the ‘transmission line’ theory, and the so-called ‘enhanced’ transmission line theories, and among them the ‘asymptotic’ theory. Due to the frequency limitation of the ‘quasi-static’ and transmission line theories and the large requirements in terms of computer resources of full-wave models, we focus on the ‘enhanced’ transmission line theories.

Among these theories, the asymptotic theory is particularly promising, because it offers an

analytical expression for the current and hence gives insight into the physics of the problem. It provides accurate results above the frequency limit of the classical transmission line theory and can also be applied to arbitrary terminals. As it allows to avoid the application of a full-wave method, or to apply a full-wave method on a smaller system only, it is particularly effective for electrically long lines.

We derive high-frequency expressions for the current induced along a multiconductor line by an external plane wave, in which the effects of the terminals of the line are modelled by matrices of scattering and reflection coefficients. Different approaches are proposed to compute the coefficients that feed the analytical expression for the current induced along the line. Using an iterative method, mathematical expressions are derived, for the particular case of open-circuit lines. For the general case of arbitrary line terminations, an approach using auxiliary short lines, solved with a numerical solver is proposed. At low frequencies, the proposed three-term formulation can be adapted to lossy lines and analytical expressions for the coefficients, providing a new and elegant formulation for the classical transmission line theory. The proposed theory is validated through numerical simulations and experiments and is found to be much more effective than the traditional full-wave approaches in terms of memory requirements and computational times.

The asymptotic theory is also applied to a lumped source excitation, according to a procedure analogous to the one for a plane wave excitation. A method for the determination of matrices of coefficients is also presented.

Keywords

Electromagnetic Time Reversal (EMTR), enhanced transmission line model (ETL), high frequency electromagnetic field excitation, lightning location systems (LLS), time-of-arrival (ToA), transmission line (TL) theory.

Acknowledgements

It is with immense gratitude that I acknowledge the support of everyone who has shared their knowledge and given of their time to make this project possible.

First of all, I would like to express my deepest gratitude to my thesis director, Prof. Farhad Rachidi, for his kindness, support during the thesis, respect and confidence in the work done and for creating a friendly atmosphere in the laboratory.

I warmly thank my thesis co-director, Dr. Rachid Cherkaoui, who helped me for the parts of my work dealing with power systems and always kept his sense of humour.

My gratitude is addressed to the president of the jury Prof. Mario Paolone for the valuable discussions concerning time reversal, and to Prof. Marcos Rubinstein for his ideas, enthusiasm and careful review of my manuscripts.

Furthermore, I would like to thank jury members Prof. Anja Skrivervik and Prof. Françoise Paladian for their presence at my thesis defense and for their interesting remarks and advice.

I owe thanks to Dr. Sergei Tkachenko for his kind help and for the time he spent explaining theoretical aspects of the asymptotic theory and of electromagnetism, and to Dr. Gerhard Diendorfer for the experimental data from the Austrian lightning detection and information system (ALDIS).

This project was made possible by the financial support of Swisselectric Research, European seventh framework programme (FP7) and armasuisse science and technology.

I thank the former *Atelier d'électro-mécanique de l'EPFL*, especially Jean-Paul Brugger, Pierre-André Pognant and Stéphane Haldner for their advice and the creation of parts for the experimentation.

Several other people with whom I have had the honour to collaborate deserve my special acknowledgement, in particular Pierre Bertholet, Dr. Markus Nyffeler, from armasuisse, for the lent equipment; to Dr. Armin Kälin, from EMProtec, for sharing his knowledge about surge protective devices; to Bertrand Daout and Werner Hirschi from Montena Technology, for their equipment and advice; to Sana Sliman, Mirjana Stojilovic and David Recordon for their collaboration.

I would like to express my gratitude to my present and former colleagues in the laboratory, Dr. Nicolas Mora for his collaboration and help with the experiments, Mohammad Azadifar, Dr. Aleksandr Smorgonskii, Prof. Felix Vega, Dr. Abbas Mosaddeghi, Dr. Carlos Romero for his help and valuable advice, Zhaoyang Wang, Dr. Pierre Zweacker for his help with the experiments; and to the visitors, Juan Miguel David Becerra Tobar, Damir Cavka, John Jairo Pantoja, and Akiyoshi Tatematsu.

Andrée Moinat and Sophie Flynn deserve my special thanks for solving practical issues and for their organisational skills, as well as Jean-Michel Buemi for his help with IT equipment and questions.

I also owe deep gratitude to every one of my other colleagues for the friendly atmosphere in the lab, Maryam Bahramipناه Marco Pignati, Dr. Reza Razzaghi, Lorenzo Reyes, Dr. Fabrizio Sosan, Dr. Mokhtar Bozorg, Asia Codino, Dr. Daniele Colangelo, Asja Derviskadic, Andreas Kettner,

Mostafa Nick, Thomas Pidancier, Sylvain Robert, Dr. Paolo Romano, Dr. Georgios Sarantakos, Dr. Stela Sarri, Enrica Scolari, Dr. Dimitri Torregrossa, Sadegh Azizi, Nadia Christakou, Dr. Omid Alizadeh, Emil Namor, Lorenzo Zanni, and Mathilde Brocard.

Last, but not least, I thank my family and Kjersti for their support and encouragement throughout this work.

Contents

Résumé	i
Abstract	iii
Acknowledgements	v
1 Introduction	1
1.1 Context	1
1.2 Locating transient sources	1
1.3 Electromagnetic coupling to transmission lines	2
1.4 Organisation of the thesis	2
I Location of transient disturbance sources with special reference to lightning	5
2 Lightning discharge and classical detection systems	7
2.1 Introduction	7
2.1.1 Content	7
2.2 Lightning discharge phenomenology	7
2.2.1 Downward Negative Lightning Flash	8
2.3 Electric field radiated by lightning	9
2.3.1 Classes of return-stroke models	9
2.3.2 Radiated field in the case of a lossless ground	10
2.3.3 Radiated field in the case of a lossy ground	10
2.4 Classical detection and location methods	11
2.4.1 Time of arrival	12
2.4.2 Interferometry	13
2.4.3 Magnetic direction finding	13
2.4.4 Combination of several methods	14
2.5 Need of further research	14
3 Application of EMTR to lightning location	15
3.1 Introduction	15
3.1.1 History and characteristics of electromagnetic time reversal	15
3.1.2 Applications of EMTR	16
3.1.3 On the concept of time reversal in electromagnetism	16
3.1.4 Chapter outline	17

3.2	Basics of EMTR	17
3.2.1	Time reversal operator	17
3.2.2	Time reversal invariance of Maxwell's equations	18
3.2.3	Properties of EMTR	18
3.2.4	Location of a source of radiation	19
3.2.5	Example	20
3.3	Application to lightning location	21
3.3.1	Theoretical justification	21
3.3.2	Physical limits	23
3.3.3	Practical implementation	23
3.3.4	Matrix Pencil method	24
3.4	Deriving ToA from EMTR	25
3.5	Time reversal with lossy medium	25
3.5.1	Model 1: Perfect ground back-propagation	26
3.5.2	Model 2: Lossy ground back-propagation	26
3.5.3	Model 3: Inverted losses back-propagation	26
3.5.4	Remarks on the considered models	27
3.6	Simulations	27
3.6.1	First set of simulations	28
3.6.2	Location with finite number of waveform parameters	29
3.7	Application to experimental data from LLS	31
3.8	Concluding remarks	34

II Electromagnetic coupling to transmission lines with special reference to high-frequency excitation 37

4	Available Analysis Methods 39
4.1	Transmission line approximation 39
4.1.1	Assumptions 39
4.1.2	Derivation of the coupling equations 41
4.1.3	Agrawal's model 43
4.1.4	Taylor's model 45
4.1.5	Rachidi's model 45
4.1.6	Boundary conditions 46
4.1.7	BLT equations 46
4.1.8	Modelling of the risers, in the framework of the TL theory 46
4.1.9	Basic model: approximate solution for the lumped sources 47
4.1.10	Exact-field model: exact solution for the lumped sources 48
4.1.11	Distributed-source model for the risers 48
4.2	Enhanced transmission line theories 50
4.2.1	Asymptotic theory 51
4.2.2	Transmission line super theory 52
4.2.3	Numerical methods 53
4.2.4	Other theories 53
4.3	Need of further research 53
4.3.1	Limitation of the transmission line model 53

4.3.2	Enhanced transmission line theories	55
5	Elaboration of an enhanced TL model for field-to-transmission line interaction	57
5.1	Introduction	57
5.2	Solution of the MPIE for an infinite line	57
5.3	Semi-infinite line	59
5.4	Finite-length line	61
5.5	Analytical expressions for the scattering and reflection coefficients: iterative method	62
5.5.1	Reformulating the MPIE equations in an appropriate form	62
5.5.2	Iterative expressions	64
5.5.3	Analytical expression for the reflection coefficient matrices $\hat{\mathbf{C}}_+$ and $\hat{\mathbf{C}}_-$. . .	64
5.5.4	Analytical expression for the reflection coefficient matrices $\hat{\mathbf{R}}_+$ and $\hat{\mathbf{R}}_-$. . .	67
5.6	Computation of the scattering and reflection coefficients	69
5.6.1	Simulation of $2N$ auxiliary lines excited by lumped sources	70
5.6.2	Extraction of $\mathbf{I}_{1,ls}$ and $\mathbf{I}_{2,ls}$	71
5.6.3	Matrices of reflection coefficients	71
5.6.4	Terminations	72
5.6.5	Simulation of an auxiliary line	73
5.6.6	Extraction of \mathbf{I}_0 , $\mathbf{I}_{1,pw}$ and $\mathbf{I}_{2,pw}$	73
5.6.7	Scattering coefficients	73
5.6.8	Terminations	73
5.6.9	Current in a line of arbitrary length	74
5.6.10	Synthesis	74
5.7	Non-linear load	74
5.8	Low-frequency approximation, with lossy ground plane and wires	75
5.8.1	TL Equations	75
5.8.2	Exciting field	76
5.8.3	Solution: current induced in an infinite line	76
5.8.4	Solution: current induced in a finite line	77
5.8.5	Lossless ground and wires	79
5.9	Radiation-resistance model	79
5.10	Validation by simulation	80
5.10.1	Example 1: Open-circuit line	80
5.10.2	Example 2: Arbitrary terminations	82
5.11	Experimental validation	84
5.11.1	Setup	84
5.11.2	Field measurement	85
5.11.3	Parameters of the line	86
5.11.4	Measurement of the induced voltage	87
5.11.5	Modelling	89
5.11.6	Results	89
5.12	Concluding remarks	91
6	Application of the asymptotic theory to a lumped source excitation	93
6.1	Introduction	93
6.2	Derivation of the method	93
6.2.1	Right semi-infinite line	93

6.2.2	Left semi-infinite line	94
6.2.3	Finite line	95
6.2.4	Determination of the matrices of coefficients	96
6.2.5	Left terminal	97
6.2.6	Right terminal	98
6.3	Extension for the risers	98
6.4	Low frequency approximation	99
6.5	Radiation resistance model	99
6.6	Validation by simulation	99
6.6.1	Parameters	99
6.6.2	Results	99
6.7	Experimental validation	101
6.7.1	Setup	101
6.7.2	Results	102
6.8	Concluding remarks	105
7	Conclusion and perspectives	107
7.1	Summary	107
7.2	Original contributions	108
7.3	Perspectives	108
A	Comparison between model predictions and experimental data	111
	Bibliography	125
	Curriculum vitae	139

Chapter 1

Introduction

1.1 Context

New technological trends involving complex systems operating at lower power levels, and the emergence of sources of disturbances with higher frequency content (such as high power microwave and ultra-wide band systems) make today's systems more susceptible to external electromagnetic interferences. Therefore, the electromagnetic compatibility (EMC) of modern electronic systems represents a challenging task. In particular, locating sources of disturbances and evaluating their effects on systems are among important topics of research in EMC.

The increase in the operating frequency of disturbance sources has led to a breakdown of the classical transmission line approximation's basic assumptions for a number of applications. In the last decade or so, the generalization of the TL theory to take into account high frequency effects has emerged as an important topic of study in electromagnetic compatibility (e.g., [1])

Within this context, the objective of this thesis is twofold. In the first part of the thesis, we will describe the application of electromagnetic time reversal to locating transient disturbance sources, with particular reference to lightning discharges. The second part of the thesis deals with the problem of the high-frequency modelling of the electromagnetic coupling with transmission lines, by means of the so-called asymptotic theory.

1.2 Locating transient sources

Time reversal, which corresponds to the idea of reversing the direction of time, was popularised during the 1990s by experimental applications in the area of waves [2] and aroused a large attention among the scientific community. In particular, electromagnetic time reversal, EMTR, gave rise to plenty of applications based on its captivating properties. One of these properties is the ability under certain circumstances for a transient field to propagate back to its source. This effect can be used notably for the location of transient disturbance sources.

Lightning is a major source of electromagnetic radiation. The interest of locating lightning in real time or afterwards is shared in numerous and various fields such as aviation, weather services, land management entities, forest services, public utilities, geophysical research and in forensic and insurance applications [3]. An estimation of the strike point can be provided by so-called lightning location systems (LLSs), which typically measure and process the electromagnetic fields radiated by lightning strikes.

What is the link between lightning and time reversal? It is in fact possible to apply EMTR to lightning location [4]. The idea is to measure the field transients generated by a lightning strike

and propagate them back, by simulation, to their source. A theoretical and simulation study in the case of an ideal, lossless model indicated that the method was promising [4]; EMTR could be an elegant way to take the propagation medium into account and eventually increase the location accuracy of lightning location systems. An associated challenge would be the adaptation of the method to the case of a lossy propagation medium, for which EMTR does not apply in theory.

1.3 Electromagnetic coupling to transmission lines

Sources of transients, such as intentional electromagnetic interferences [5], can contain frequency components much higher than lightning. Their potential effects on electrical or electronic systems have been a concern in the past decade (e.g. [6–8]). Since measurements are not always possible or desirable, the computation of the transfer function between an external electromagnetic field and the current or voltage induced at the inputs of a device is of importance.

Lines and interconnects act as antennas which catch the electromagnetic field and propagate them to the devices to which they are connected. Electromagnetic coupling to transmission lines (TL) is in fact an important problem in electromagnetic compatibility and is approached classically by three kinds of methods [1, 9, 10]. The quasi-static method or circuit theory is the most simple one, but can be applied only when the line is electrically short. For lines that are electrically long, but have an electrically small cross-section, one can use the so-called transmission line theory. When the cross-section of the line is larger than the wavelength of the field, numerical ‘full-wave’ methodologies directly based on Maxwell’s equations can be adopted. When electrically long lines are involved, however, these numerical approaches require long computational times and large computer resources, which become prohibitive when multiple computations are required, in the case of parametric analysis for example.

Additionally, in the last decades or so, ‘enhanced’ transmission lines theories were developed, which aim at keeping the relative simplicity of the classical transmission line theory, while modelling high-frequency effects such as radiation and providing more accurate solution at high frequencies than the classical TL theory. Among these methods, the asymptotic theory is based on the fact that non-TEM (transverse electromagnetic) modes tend to vanish after a long propagation along a uniform transmission line under certain conditions. The asymptotic theory is a promising method, but was derived only for the case of single conductor lines. In this study, we propose a generalization of the asymptotic theory to multiconductor lines.

1.4 Organisation of the thesis

This report is divided into two main parts. The **first part** (Chapters 2 and 3) deals with the location of transient disturbance sources using the theory of time reversal with special reference to lightning location. The **second part** (Chapters 4, 5 and 6) concerns the electromagnetic coupling to transmission lines with special reference to high-frequency excitation for which the classical transmission line is not applicable.

In **Chapter 2**, some characteristics of lightning discharges and location systems are reviewed. After a brief presentation of the lightning discharge phenomenology, some aspects of the modelling of lightning discharge and the computation of the associated electromagnetic fields are discussed. Further, the currently used classical detection and location systems are reviewed. The chapter ends with concluding remarks and the need for further research.

In **Chapter 3**, electromagnetic time reversal is applied to lightning location. First, the basics

of EMTR are reviewed. An algorithm for lightning location is presented and justified theoretically. The problem of a lossy ground that affects the propagation of electromagnetic transient fields generated by a lightning strike is addressed by comparing different back-propagation models. The proposed algorithm is validated using numerical simulations and experimental data from the Austrian lightning location system.

Chapter 4 presents the available analysis methods for the classical problem of the computation of the current induced in a line due to an external electromagnetic wave. After a brief introduction concerning the ‘quasi-static’ and ‘full-wave’ methods, we review two other types of approaches, i.e. the transmission line theory, and the so-called enhanced transmission line theories, and among them the ‘asymptotic’ theory.

Chapter 5 is devoted to the elaboration of an enhanced TL model for field-to-transmission line interaction. We derive expressions for the current induced along a multiconductor line by an external plane wave, in which the effects of the terminals of the line are modelled by matrices of scattering and reflection coefficients. These coefficients are then computed analytically in the particular case of open boundaries or at low frequencies, and with numerical methods in the general case. The proposed theory is validated using full-wave simulations and experimental data.

In **Chapter 6**, the asymptotic theory is applied to a lumped source excitation. The theory is developed in a procedure analogous to the one in the previous chapter. A method for the determination of the matrices of reflection and coupling coefficients is then presented. In the case of a single-conductor line, an expression for the current in the vertical risers is derived. At low frequencies, analytical expressions are derived for the scattering coefficients. The use of a radiation resistance allows to account for the radiation occurring near the line terminals. The developed models are validated using full-wave simulations and experimental measurements.

Finally, general conclusions and perspectives for future work are presented in **Chapter 7**.

Part I

Location of transient disturbance sources with special reference to lightning

Chapter 2

Lightning discharge and classical detection systems

2.1 Introduction

Lightning is one of the largest causes of transients, faults, and outages in power grids and can have harmful effects on electronic systems. In order to locate lightning and help to identify damages caused by it, automatic lightning locating systems (LLSs) have been developed since the 1920s [3]. Modern LLSs are able to determine the location, intensity, and movement of thunderstorms in real time. Archived and real-time lightning data are used by weather services, aviation, land management entities, forest services, public utilities, geophysical research and in forensic and insurance applications [3].

2.1.1 Content

In this chapter, we will review some characteristics of lightning discharges and location systems that will be useful for the next chapter. After a brief presentation of the lightning discharge phenomenology, some aspects of the modelling of lightning discharge and computation of the associated electromagnetic fields are discussed. Further, the currently used classical detection and location systems are reviewed. The chapter ends with concluding remarks and the need for further research.

2.2 Lightning discharge phenomenology

Cumulonimbus are the main source of lightning phenomena, even though in general, stratiform clouds [11], covering territories hundreds of times larger than thunderclouds, can in some cases be highly charged [12, 13]. The cloud electrification is thought to be caused by either micro-scale phenomena involving collisions of hydrometeors in different phases [14], or charge by induction, melting, freezing and capturing / releasing of free ions on charged aerosol particles [15] or by large scale phenomena. Large scale phenomena are in general associated with air current convection transport of charge or involve cosmic-ray particles that were shown to contribute to the electric field enhancement process [16].

The net result of electrification is that an excess of charge develops and gets accumulated in different parts of the cloud, thus generating large electric fields gradients [13]. The cloud electrical distribution model is also still an object of research. In general, the classical tripolar electric model provides a charge distribution compatible with various measurement campaigns and experiments

[11]. In this model, positive charges are located in the upper part of the cumulonimbus cloud, negative charges in the middle, and small pockets of positive charges in the cloud bottom. In some cases, however, the electrical structure of the thunderstorm cloud may be more complex than a dipole or a tripole, with reduced regions of alternate polarity in the cloud base [17, 18].

Lightning discharges can be classified in four groups according to their discharge paths: i) intra-cloud lightning, ii) inter-cloud or cloud-to-cloud lightning (CC), iii) cloud-to-ground (CG) and ground-to-cloud (GC) lightning, iv) cloud-to-air lightning, and, finally, iv) middle and upper atmospheric discharges [13, 19]. Even if intra-cloud lightning (IC) is thought to account for the majority of the discharges [20], this work will focus on cloud-to-ground CG or GC lightning, due to its impact on humans activities and as a cause of possible damages on ground systems.

2.2.1 Downward Negative Lightning Flash

Cloud-to-ground lightning flashes can be classified into four categories depending on the direction of propagation of the ionised channel (either downward and upward) and the sign of charge transferred to ground (either positive or negative) [21]. The majority of cloud-to-ground flashes are of downward negative type. A preliminary discharge within the electrified thundercloud initiates the sequence of processes which concur in the development of a cloud-to-ground strike, described in Figure 2.1 [22, 23].

A gas discharge may be initiated when gas pressure and electric field exceed a threshold sufficient to start an electron avalanche and create a conductive channel or region. The most accepted theories for the breakdown are the emission of positive streamers from hydrometeors induced by high surrounding electric fields [24, 25] and the cosmic ray participation to runaway electron avalanches (the so-called runaway breakdown) [13, 24, 26, 27].

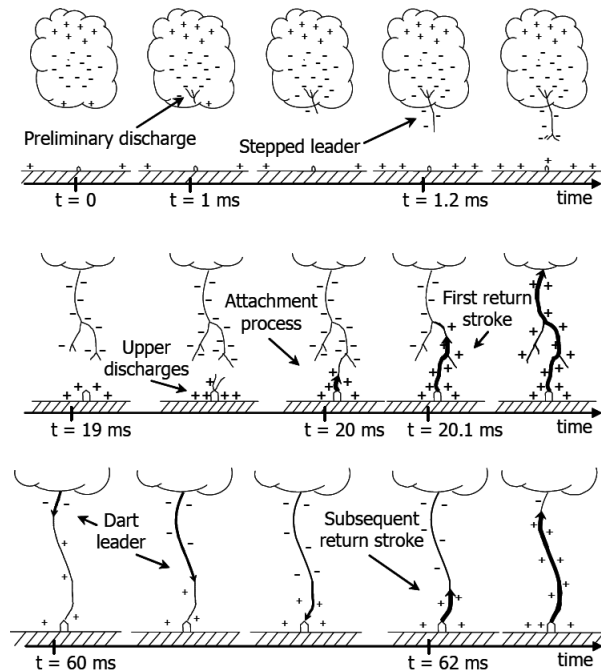


Figure 2.1: Illustration of some of the various processes comprising a negative cloud-to-ground lightning flash (adapted from [23]).

A stepped leader (see Figure 2.1) induced by the preliminary discharge propagates from the thundercloud to ground in a series of discrete steps. As the leader tip nears ground, the electric

field at sharp objects on the ground or at irregularities of the ground itself exceeds the breakdown value of air and one or more upward-moving discharges from the ground are initiated at those points, thus starting the attachment process [23].

When one of the upward-moving discharges from the ground contacts the downward moving stepped leader some tens of meters above ground, the leader tip is connected to ground potential. The leader channel is then discharged when the first return-stroke propagates continuously up the previously ionised and charged leader path [22].

After the return-stroke current has ceased to flow, the flash may end. Otherwise, if additional charge is available at the top of the channel, a continuous dart leader may propagate down the residual first-stroke channel. The dart leader then initiates the second or any subsequent (up to about 20) return-strokes. The current of the return-strokes ranges from a few kA up to about 300 kA, and generates an electromagnetic field with a spectrum ranging from DC to a few tens of MHz, even if emissions happen also at higher frequencies, for example in the visible light [11].

2.3 Electric field radiated by lightning

2.3.1 Classes of return-stroke models

Lightning return-stroke models can be categorised into four different classes, essentially distinguished by the type of governing equations [11, 22].

The first defined class of models, the so-called gas-dynamic or “physical” models, is primarily concerned with the radial evolution of a short segment of the lightning channel and its associated shock wave. The principal model outputs include temperature, pressure and mass density as a function of the radial coordinate and time (e.g. [28–30]).

The second class is represented by the electromagnetic models which are usually based on a lossy, thin-wire antenna approximation of the lightning channel. A numerical solution of Maxwell’s equations allows to find the current distribution along the channel from which remote electric and magnetic field can be computed (e.g. [31–33]).

The third class of models is the distributed-circuit models, also called RLC transmission line models. They can be viewed as an approximation to the electromagnetic models and they represent the lightning discharge as a transient process on a transmission line characterised by per-unit-length resistance, inductance and capacitance (e.g. [34, 35]).

The last class of models corresponds to the engineering models, in which a temporal and spatial distribution of the channel current or the channel line charge density is specified based on such characteristics as the current at the channel base, the speed of the upward-propagating front, and the channel luminosity profile (e.g. [36]). In these models, the emphasis is placed on achieving agreement between the model-predicted electromagnetic fields and those observed experimentally at distances from tens of meters to hundreds of kilometres.

Within this last class of so-called engineering models, the model that is used in this work is the transmission line (TL) model [37]. In this model, the return-stroke channel is represented as a lossless transmission line along which a current pulse travels upward undistorted at the return-stroke velocity. The advantage of this model is the fact that the electric field can be readily computed as a function of the channel base current. It is worth noting, however, that the developments made in Chapter 3 can be extended to any return-stroke model.

2.3.2 Radiated field in the case of a lossless ground

According to the transmission line model, the radiated (far field) vertical electrical far field can be expressed as [3, 38, 39].

$$E_z(\vec{r}, t) = -\frac{v}{2\pi\epsilon_0 c^2 \|\vec{r} - \vec{r}_s\|} i_s \left(t - \frac{\|\vec{r} - \vec{r}_s\|}{c} \right) = -\frac{\mu_0 v}{2\pi \|\vec{r} - \vec{r}_s\|} i_s \left(t - \frac{\|\vec{r} - \vec{r}_s\|}{c} \right) \quad (2.1)$$

where v is the return stroke speed, generally in the order of one-third to two-third the speed of light in vacuum, and $i_s(t)$ is the current at the base of the channel. ϵ_0 is the vacuum permittivity, μ_0 the vacuum permeability, c the speed of light in vacuum, \vec{r}_s the stroke location and $i_s(t)$ is the channel base current.

Formula (2.1) indicates that the radiated field has the same shape as the channel base current. This shape is time shifted, due to the propagation of the wave at the speed of light c . The amplitude decreases as a function of $1/r$ due to the fact that the wave spreads in space.

2.3.3 Radiated field in the case of a lossy ground

Electromagnetic fields generated by lightning change their character as they propagate over ground surface due to selective attenuation of high-frequency components by a finitely conducting ground [40]. These effects are often referred to as propagation effects. In the case of a lossy ground, the equations of the field involve Sommerfeld's integrals, the solution of which is complex and in general require a careful numerical integration [40].

Simplified methods have been proposed to compute the radiated electric field. In particular, a method to compute the radiated field with a finite-conductivity ground is presented in [20], p. 372-373. It was shown that this approximated expression provides accurate results better than 10% in the distance range of 10 m to 1 km, the accuracy increasing with increasing distance of propagation [41]. According to this model, the field is first propagated under the assumption of a perfectly conducting ground and then the effect of the finite ground conductivity is taken into account by a convolution product with an impulse response $s_f(D, t)$ accounting for the propagation effect along a lossy line.

$$E_{z,\sigma}(D, t) = \int_0^t E_z(D, t - \tau) s_f(D, \tau) d\tau \quad (2.2)$$

where D is the distance between the source and the observation point, $E_{z,\sigma}(D, t)$ is the radiated field over a lossy ground, $E_z(D, t)$ is the radiated field over a lossless ground. $s_f(D, t)$ is expressed as follows [20].

$$s_f(D, t) = \frac{d}{dt} \left\{ 1 - \exp \left(-\frac{t^2}{4\zeta^2} \right) + 2\beta(\epsilon_r + 1) \frac{J(x)}{t} \right\} \quad (2.3)$$

with:

$$\begin{aligned} J(x) &= x^2(1 - x^2) \exp(-x^2) & x &= \frac{t}{2\zeta} \\ \beta &= \frac{1}{\mu_0 \sigma c^2} & \zeta^2 &= \frac{D}{2\mu_0 \sigma c^3} \end{aligned} \quad (2.4)$$

It depends mainly on the distance of propagation and the ground electric parameters.

For a computer implementation, the division by t poses a problem at $t = 0$. On the other hand, the time derivative can be computed analytically in order not to have to implement a numerical derivative, which is a source of inaccuracies. The explicit expression of the derivative in (2.3)

reads [42]:

$$s_f(D, t) = \frac{2t}{4\zeta^2} \exp\left(-\frac{t^2}{4\zeta^2}\right) + 2\beta(\varepsilon_r + 1) \frac{d}{dt} \frac{J(x)}{t} \quad (2.5)$$

where the derivative of the second term can be computed explicitly.

$$\begin{aligned} \frac{d}{dt} \frac{J(x)}{t} &= \frac{\partial}{\partial x} \left(\frac{J(x)}{x \cdot 2\zeta} \right) \cdot \frac{dx}{dt} = \left[\frac{1}{2\zeta} \cdot (1 - x^2) \cdot \exp(-x^2) + \right. \\ &\quad \left. + \frac{x}{2\zeta} \cdot (-2x) \cdot \exp(-x^2) + \frac{x}{2\zeta} \cdot (1 - x^2) \cdot (-2x) \exp(-x^2) \right] \frac{1}{2\zeta} \end{aligned} \quad (2.6)$$

In the frequency domain, the electric field measured by a sensor at a location \vec{r}_n can be written as follows:

$$E_n(\omega) = -\frac{v}{2\pi\varepsilon_0 c^2} \underbrace{\frac{1}{\|\vec{r}_n - \vec{r}_s\|}}_{\text{geometric attenuation}} \underbrace{e^{-j\omega \frac{\|\vec{r}_n - \vec{r}_s\|}{c}}}_{\text{propagation delay}} \underbrace{S_f(\|\vec{r}_n - \vec{r}_s\|, \omega)}_{\text{effect of losses}} \mathcal{F}\{i_s(t)\} \quad (2.7)$$

where \mathcal{F} denotes the Fourier transform of a time function. The presence of the ground attenuates mostly high frequencies; hence $S_f(\omega)$ is a low-pass filter attenuating the peak value of the lightning electromagnetic pulse as it propagates and it also introduces dispersion, which increases its rise time.

Note that the attenuation effect is nowadays modelled in operational LLSs using an exponential decay model. Cramer et al. [43] suggest that an exponential model

$$RNSS = SS \cdot \left(\frac{r}{100}\right)^b \cdot \exp\left(\frac{r - 100}{L}\right) \quad (2.8)$$

employing $b = 1$ and a space constant L (e.g. $L = 1000$ km) results in a better fit than a power-law model with $b = 1.13$ (e.g. [44]), especially for networks with long base lines or large networks, when sensors at large distances (> 600 km) contribute. In (2.8), RNSS stands for range-normalised signal strength and SS for signal strength.

In contrast to (2.8) which applies only to the amplitude of the signal, expression (2.3) applies to the whole waveform.

2.4 Classical detection and location methods

Lightning Location Systems (LLSs) provide information about the location, intensity and movement of thunderstorms in real time, and can be used to locate lightning-caused damages [3]. The most widely used lightning location techniques are the Time-of-Arrival method (ToA) and the Magnetic Direction Finding (MDF) method [11]. The mean location errors associated with these methods are within a few hundreds of meters [3].

Several sectors of human activity are concerned with data about lightning, for example: weather forecast, outdoor activities exposed to lightning, sensitive installations, air-traffic control, forest fire forecast, etc [45].

All emissions due to lightning can produce a location method. Hence the entire electromagnetic spectrum, from low to high frequencies, even visible light and also acoustic waves (thunder) can be used. Three methods which are often used in LLSs are described in the following sections, namely [11]:

- time of arrival;

- interferometry;
- magnetic direction finding.

Other methods exist as well, such as the use of the field amplitude, satellite observation, optical detection from the Earth, sound, radar, etc [11]. The obtained location accuracy highly depends on the used method.

2.4.1 Time of arrival

Time of arrival (ToA) is based on the fact that the propagation time is proportional to the travelling distance [3, 11].

There are three types of networks, classified as a function of the distance between the sensors.

- When the distance between the sensors is very short, in the order of few tens to hundreds of meters, the VHF radiation is used. Such a system can determine the azimuth and elevation angles of the stroke, but cannot localise it.
- When the distance between the sensors is short, in the order of few tens of kilometres, the HF radiation is used. This kind of system allows locating lightning in 3 dimensions.
- When the distances between sensors are large, in the order of hundreds of kilometres, the LF or VLF radiation is used. The first system of this type was realised in 1960. Location is considered as a mean location or as the stroke location at the ground. This third kind of network is the most widely used in present commercial LLSs [46] and it is considered in this work.

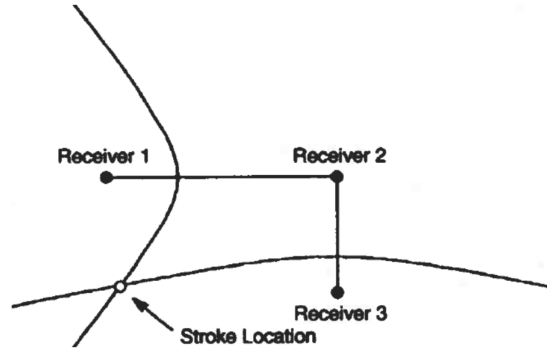


Figure 2.2: Determination of the lightning stroke location by three ToA receivers. Adapted from [11].

Let us assume that the receiver number 1, located at \vec{r}_1 , measures the time of arrival of the EM field radiated by the return stroke at time t_1 . Similarly, another receiver, numbered as 2, located at \vec{r}_2 , measures the time of arrival at t_2 . Assuming that a lightning strikes at point \vec{r}_s and at time t_0 , and that it radiates a field travelling at speed c , the times of arrival at the sensors are as follows.

$$\begin{aligned} t_1 &= t_0 + \frac{\|\vec{r}_1 - \vec{r}_s\|}{c} \\ t_2 &= t_0 + \frac{\|\vec{r}_2 - \vec{r}_s\|}{c} \end{aligned} \quad (2.9)$$

Δt_{12} is defined as the difference of time of arrival:

$$\Delta t_{12} := t_1 - t_2 = \frac{1}{c} (\|\vec{r}_1 - \vec{r}_s\| - \|\vec{r}_2 - \vec{r}_s\|) \quad (2.10)$$

This corresponds to the equation of a conic (hyperbola), which can be defined for each pair of sensors. The intersection between these curves is the estimation of the lightning location (see Figure 2.2). If three sensors are used, the obtained location is not necessarily unique – it can be double – because the instant of the stroke is not known in absolute terms. As soon as more than three sensors are available, the intersections between the hyperbolas may not appear at a single point, due to measurements errors for example, and a χ^2 minimisation method can be used.

2.4.2 Interferometry

Interferometry is based on the same principle than ToA, for very close sensors, and using the difference of phase instead of the difference of time of arrival [3, 11]. The first interferometer for the study of lightning was designed in 1979.

Lightning does not only radiate isolated pulses, but also produces noise-like bursts of radiation which are arduous to locate using ToA techniques, due to the difficulty in identifying individual pulses. However, the measurement of the phase difference allows to use these data.

With a single station, it is possible to determine the azimuth and elevation angles of the radiation source. With two stations or more, location is possible, with a method similar to direction finding (see next section).

If the sensors are limited in bandwidth, it is useful to use two inter-sensor distances: a long distance, in order to have a good accuracy; a short one, to suppress the ambiguity due to the 2π uncertainty of the phase. If the sensors have a large bandwidth, the electric distance – the geometrical distance divided by the wavelength – varies as a function of the frequency so a single inter-sensor distance is enough.

2.4.3 Magnetic direction finding

Magnetic Direction Finding (MDF) was used from the 1920s onwards [3, 11]. The sensors which measure the magnetic field are generally made of two orthogonal loops (north-south and east-west oriented). The ratio of the measured field is proportional to the tangent of the azimuth angle to the stroke point. There is nevertheless a 180° indeterminacy, so such sensors are often associated to an electric field sensor to determine the direction of the electric field and hence the propagation direction.

The uncertainty on the direction is in the order of one degree, but it can be much higher in certain sites [11]. Location is already possible with two sensors only. Starting from three sensors, the impact point can be determined with an optimisation method. For example, by minimising the χ^2 function below [11]:

$$\chi^2 = \sum_{n=1}^N \left(\frac{\vartheta_{mn} - \vartheta_n}{\sigma_{\vartheta n}} \right)^2 + \sum_{n=1}^N \left(\frac{E_{mn} - E_n}{\sigma_{E n}} \right)^2 \quad (2.11)$$

where ϑ_n and E_n are the unknown azimuths and amplitudes of the electric fields, ϑ_{mn} and E_{mn} are the azimuths and amplitudes of the measured electric fields and σ are the measurement error estimates.

This optimisation method has the double advantage of providing the most probable location and also an estimation of the uncertainty of this location. Note that as presented in (2.11), the method does not use only the MDF, but also the electric field amplitude.

2.4.4 Combination of several methods

In practice, in order to improve the accuracy, several of these methods can be used simultaneously. For example, the ToA method can be combined with magnetic direction finding in IMPACT (*IMProved Accuracy from Combined Technology*) sensors used in the ALDIS (Austrian Lightning Detection and Information System) LLS networks [47].

2.5 Need of further research

Mean location errors of LLSs are within a few hundreds of meters [3]. However, in some cases, the error can be much larger [48, 49]. In order to go beyond the accuracy limit of the classical detection systems, we would like to develop a method with the ability to intrinsically consider the propagation effects and inhomogeneity of the propagation path. For this reason, in Chapter 3, a lightning location algorithm based on the electromagnetic time reversal is described, assessed and tested.

Chapter 3

Application of EMTR to lightning location

3.1 Introduction

Electromagnetic time reversal (EMTR) is based on the fact that Maxwell's equations remain valid after a change of the direction of time. The idea of applying EMTR to create an algorithm for lightning location was proposed by Mora et al. [4]. This chapter presents further developments of EMTR to lightning location and is based on [42, 50–53].

3.1.1 History and characteristics of electromagnetic time reversal

The first experiment using time reversal in electromagnetism was reported by Bogert in 1957 [54]. He experimented a method of correcting delay distortion by time reversal on a slow-speed picture transmission system. It was followed in 1965 by experiments of signal transmission under the ocean based on time reversal [55].

The time reversal process has been popularised later among the scientific community by Fink and his colleagues in the 1990s in articles which described the application of time reversal in acoustics [2, 56–58]. Results obtained in acoustics are of interest for EM application because they can often be translated into electromagnetism, due to the similarity of the equations in the two fields. In particular, time reversal in acoustics or using elastic waves is used in varied applications such as under-ocean communication [59, 60], medical applications, such as destruction of tumours and kidney stones [61], or landmine detection [62, 63].

However, there are also important differences between acoustics and electromagnetism. Acoustics deals with scalar fields, whereas electromagnetism deals with vector fields. Electromagnetic antennas do not have the same properties as electro-acoustic transducers. The frequencies associated to the acquisition, time reversal and re-generation of the signals are much lower when using ultrasound than microwaves. Hence, the adaptation of techniques from acoustics to electromagnetism has been discussed by several authors (e.g. [64]).

Lerosey et al. [65] reported the first experimental demonstration of time reversal focusing with electromagnetic microwaves. The wave is found to converge to its initial source and is compressed in time. The quality of focusing is determined by the frequency bandwidth and the spectral correlation of the field within the cavity.

Chaiken et al. [66] showed the poor time reversal behaviour in regimes of chaotic particle motion. This effect was confirmed by Snieder [67] who showed that in classical particle chaos,

perturbations in the system grow exponentially in time, while for the corresponding wave system, perturbations grow as the square root of time. This is a reason why time reversal works much better experimentally for electromagnetic or acoustic waves, as it does in mechanics, even though laws of mechanics are also theoretically invariant under time reversal.

Time reversal experiments usually use a large number of transducers. Draeger et al. [68, 69] showed that it is possible to perform a time reversal using a single element in a reflecting cavity with negligible absorption. Bal et al. [70] showed that the focusing of a wave is affected by the fact that the propagation medium is different in time reversal from the medium in normal time. In a cluttered environment and under certain conditions, the resolution of the refocused signal can be better than the diffraction limit that would be obtained in a homogeneous medium; this is called super-resolution [71]. Not only the propagation environment, but also the window duration and the bandwidth of the time-reversed signals, affect the time reversal process [72].

3.1.2 Applications of EMTR

Time reversal in electromagnetism (EMTR) has been used in a large number of applications. As EMTR is a powerful technique for the compensation of phase distortions [73], it was used in wireless communications [74–78] and power line communication (PLC) [79, 80].

EMTR can be used as an iterative process in order to focus a field to the strongest scatterer in a multi-target medium [81] and for target focusing in a cluttered background [82]. It can be also used for source localisation [83] and identification [84].

Reflectometry-based methods can be used to detect soft faults in wire networks based on the DORT (décomposition de l'opérateur de retournement temporel) method [85, 86]. EMTR has also been applied successfully to locating faults in power networks [87–92].

Baba et al. [93] presented a way to shape an EM field using time reversal by simulation. In [94], time reversal is used to generate high power microwave pulses from a low power arbitrary wave generator. Similarly, Cozza et al. [95] proposed a technique, named time reversal electromagnetic chamber (TREC), which operates a reverberation chamber as a generator of deterministic pulsed wavefronts. Non-linear EMTR [96, 97] can also lead to interesting applications.

3.1.3 On the concept of time reversal in electromagnetism

Dyab et al. [98–100] raised a controversy about the definition of time reversal. They stated that the term ‘time reversal’ cannot be considered as a back-propagation process and should instead be considered as a signal processing method. Their argumentation is based on the fact that a single antenna, considered as a voltage-to-field transducer, is non-reciprocal. However, a two-antenna system is reciprocal.

In our opinion, the problem raised is mainly semantic. If one applies TR in an experiment, one has to use two antennas (or sensors), then the measurable quantities are at the ports of the antennas, which form a reciprocal system. If one applies the process by simulation, no antennas are needed, and the non-reciprocity of a single antenna is no more an issue. The link between reciprocity and time reversal was analysed in detail in [101]. In particular, in a lossless system, reciprocity was shown to be equivalent to time reversal invariance.

Dyab et al. claimed that focusing is not an ‘intrinsic’ property of TR. In fact, the implementation of time reversal is generally based on one or several transducers or sources, a propagation medium and an algorithm. This complete system as a whole has some features which can be assessed and from which, it is possible to derive properties such as focusing. Moreover, a number of very different

algorithms inspired by time reversal theory has been proposed. They may not refer to a single and strict definition, but that is not a problem in our opinion. The term ‘back-propagation’ refers generally and in particular in our work to the propagation of a re-emitted, time-reversed version of a measured signal. In realistic configurations, it does not correspond exactly to the initial field that would be played in reverse.

Moreover, Roux et al. [102] showed that the experimental implementation of a time reversal mirror (TRM) does not require a probe source collocated with the receiver array. They also showed that nonreciprocity-based time reversal procedure can yield better results than the classical time reversal method.

3.1.4 Chapter outline

This chapter is organised as follows. First, the basics of electromagnetic time reversal are reviewed. An algorithm for lightning location is presented and justified theoretically. The problem of a lossy ground that affects the propagation of electromagnetic transient fields generated by a lightning stroke is addressed by comparing different back-propagation models. The proposed algorithm is validated using numerical simulations and experimental data from the Austrian lightning location system. Finally concluding remarks are given.

3.2 Basics of EMTR

In this section, we present the basic theory and properties of EMTR.

3.2.1 Time reversal operator

The TR method is based on the “reversal” of the direction of time (see e.g. [103]):

$$t \mapsto -t \quad (3.1)$$

The definition (3.1) can be applied directly to the electric field $\vec{E}(\vec{r}, t)$ and to the charge density $\rho(\vec{r}, t)$ (equation (3.2a)). The electric field and charge density are said to be even functions under time reversal. Additionally, when time-reversing an EM field, the propagation direction, given by the cross-product of the electric and magnetic fields, must also be reversed. For that reason, the time reversal of the magnetic field $\vec{H}(\vec{r}, t)$ requires, in addition to (3.1), an inversion of the vector direction (equation (3.2b)). Similarly, time-reversing the current $\vec{J}(\vec{r}, t)$ also yields a vector in the opposite direction (equation (3.2b)). The magnetic field and current are said to be odd functions under time reversal. The time reversal operator in electromagnetism can be written as follows:

$$\vec{E}(\vec{r}, t) \mapsto \vec{E}(\vec{r}, -t) \quad \rho(\vec{r}, t) \mapsto \rho(\vec{r}, -t) \quad (3.2a)$$

$$\vec{H}(\vec{r}, t) \mapsto -\vec{H}(\vec{r}, -t) \quad \vec{J}(\vec{r}, t) \mapsto -\vec{J}(\vec{r}, -t) \quad (3.2b)$$

A necessary condition for the application of time reversal is the invariance of the physical equations. An equation is said to be time reversal invariant if the time-reversed versions of its solutions are also valid solutions of the physical equations.

3.2.2 Time reversal invariance of Maxwell's equations

In a linear medium of permittivity $\varepsilon(\vec{r})$ and permeability $\mu(\vec{r})$, Maxwell's equations can be written as:

$$\begin{aligned}\nabla \cdot (\varepsilon(\vec{r})\vec{E}(\vec{r}, t)) &= \rho(\vec{r}, t) \\ \nabla \cdot (\mu(\vec{r})\vec{H}(\vec{r}, t)) &= 0 \\ \nabla \times \vec{E}(\vec{r}, t) &= -\mu(\vec{r})\frac{\partial \vec{H}(\vec{r}, t)}{\partial t} \\ \nabla \times \vec{H}(\vec{r}, t) &= \varepsilon(\vec{r})\frac{\partial \vec{E}(\vec{r}, t)}{\partial t} + \vec{J}(\vec{r}, t)\end{aligned}\tag{3.3}$$

Applying the TR operator to the fields, currents and charges as defined in (3.1) and (3.2), and using the linearity of the derivative, one obtains:

$$\begin{aligned}\nabla \cdot (\varepsilon(\vec{r})\vec{E}(\vec{r}, -t)) &= \rho(\vec{r}, -t) \\ -\nabla \cdot (\mu(\vec{r})\vec{H}(\vec{r}, -t)) &= 0 \\ \nabla \times \vec{E}(\vec{r}, -t) &= -\mu(\vec{r})\frac{-\partial \vec{H}(\vec{r}, -t)}{\partial t} \\ -\nabla \times \vec{H}(\vec{r}, -t) &= \varepsilon(\vec{r})\frac{\partial \vec{E}(\vec{r}, -t)}{\partial t} - \vec{J}(\vec{r}, -t)\end{aligned}\tag{3.4}$$

Equations (3.4) can be shown through straightforward mathematical manipulations (including a change of variable $t' = -t$, going along with $\partial t' = -\partial t$) to be identical to equations (3.3). The detailed proof of the TR invariance of Maxwell's equations can be found, for instance, in [103].

A small controversy was raised by a statement [104] that Maxwell's equation would not be time reversal invariant due to the necessity of changing the sign of the magnetic field (see (3.2b)). In fact, Earman [105], Malament [106], Arntzenius and Greaves [107] showed that the magnetic field must in fact be reversed by application of the time reversal operator, using symmetry considerations, four-vector formalism or quantum field theory.

3.2.3 Properties of EMTR

Frequency domain

Although EMTR is defined in the time domain, it can also be applied in the frequency domain. The Fourier transform of the function $\vec{E}(\vec{r}, t)$ is defined as follows:

$$\mathfrak{F}\{\vec{E}(\vec{r}, t)\} = \int_{-\infty}^{+\infty} \vec{E}(\vec{r}, t)e^{-j\omega t} dt\tag{3.5}$$

The Fourier transform of the time-reversed version of the function is hence:

$$\mathfrak{F}\{\vec{E}(\vec{r}, -t)\} = \int_{-\infty}^{+\infty} \vec{E}(\vec{r}, -t)e^{-j\omega t} dt\tag{3.6}$$

The application of the change of variable $t' = -t$ leads to $dt' = -dt$ and the integration boundaries are inverted:

$$\mathfrak{F}\{\vec{E}(\vec{r}, -t)\} = \int_{+\infty}^{-\infty} \vec{E}(\vec{r}, t')e^{+j\omega t'}(-dt')\tag{3.7}$$

This expression can be rewritten as follows:

$$\mathfrak{F} \left\{ \vec{E}(\vec{r}, -t) \right\} = \int_{-\infty}^{+\infty} \vec{E}(\vec{r}, t') \left(e^{-j\omega t'} \right)^* dt' \quad (3.8)$$

where $*$ denotes the complex conjugate. If $\vec{E}(\vec{r}, t)$ is a real function, its imaginary part is equal to zero and one has $\vec{E}(\vec{r}, t) = \vec{E}^*(\vec{r}, t)$. Finally:

$$\mathfrak{F} \left\{ \vec{E}(\vec{r}, -t) \right\} = \left(\int_{-\infty}^{+\infty} \vec{E}(\vec{r}, t') e^{-j\omega t'} dt' \right)^* \quad (3.9)$$

In conclusion, time-reversing a real function corresponds to taking the complex conjugate in the frequency domain [101].

$$\mathfrak{F} \left\{ \vec{E}(\vec{r}, -t) \right\} = \left(\mathfrak{F} \left\{ \vec{E}(\vec{r}, t) \right\} \right)^* \quad (3.10)$$

Losses

Lossy media are not TR invariant. This can be shown by considering for example Ohm's law, $\vec{J}(\vec{r}, t) = \sigma(\vec{r})\vec{E}(\vec{r}, t)$. Applying the TR operator one obtains:

$$-\vec{J}(\vec{r}, -t) \neq \sigma(\vec{r})\vec{E}(\vec{r}, -t) \quad (3.11)$$

where $\sigma(\vec{r})$ is the conductivity of the medium. A reason why a lossy medium is not time reversal invariant is the fact that losses are associated with the increase of entropy. Reversing time would lead to a decrease of entropy, which is impossible according to the second law of thermodynamics.

For Ohm's law to be TR invariant, the sign of the conductivity would need to be changed by the time reversal transformation ($\sigma(\vec{r}) \mapsto -\sigma(\vec{r})$). A more complete analysis of the question of losses is addressed with back-propagation models in Section 3.5

Time delay

In practical implementations, a signal is necessarily measured only during a finite time period from an initial time selected here as the origin $t = 0$ to a final time $t = T$, where T is the duration of the signal. That is to say, we will consider only $0 < t < T$. To avoid effects of windowing [108], we will assume here that the time origin and the duration T are chosen in such a way that the signal is not truncated. To make the argument of the time-reversed variables positive for the duration of the signal, we will add, in addition to time reversal, a time delay T :

$$t \mapsto T - t \quad (3.12)$$

3.2.4 Location of a source of radiation

This section presents an illustration of how EMTR can be used for localising a radiation source. The used algorithm requires two main steps. In the first step, a source generates an EM field which propagates and is measured by one or several sensors. This step will be referred to as the 'normal' time. During the second step, the stored waveforms at the previous step are time-reversed. The sensors, which become emitters, re-emit this time-reversed version of the waveform they measured. All the contribution of the sensors-emitters somehow mimic the initial wave in normal time, but time-reversed. For this reason, the produced waveform resembles a concentric waveform which focuses on the original source (e.g. [65]).

3.2.5 Example

In Figure 3.1, the source point (red triangle) generates a field which is reflected by the two walls represented by grid patterns. According to image theory, the walls could be replaced by three additional mirrored sources. Hence, the sensor (blue triangle) receives four successive waves.

Click to start the animation

Figure 3.1: Positive time.

In Figure 3.2, the sensor re-emits the time-reversed version of the field which it measured in Figure 3.1. Note that due to the presence of the reflecting walls, the sensor (and each of its three mirrored versions) re-emit four successive waves, which are in turn reflected, creating 16 waves. Indeed, in this case, this single sensor is enough to generate a field that concentrates into the source point. If the area had not be limited by reflecting walls, a minimum of three sensors would have been needed to have a focusing effect.

Click to start the animation

Figure 3.2: Time reversal.

3.3 Application to lightning location

The use of the so-called electromagnetic time reversal (EMTR) technique as a means of locating lightning was investigated by Mora et al. [4, 39], who derived equations for the focusing of electromagnetic fields back to the source by time reversal, and demonstrated that the wavefronts generated by back-propagating the time-reversed fields will add up in phase at the lightning stroke location. Based on this observation, they proposed an algorithm to locate lightning discharges that requires at least three field sensors, and they showed it to yield excellent results under the ideal conditions of propagation along a perfectly conducting ground.

In this section, we further discuss the use of EMTR to locate lightning, by addressing the effect of propagation along a lossy ground.

3.3.1 Theoretical justification

Consider a lightning stroke at point \vec{r}_s , and N sensors located at \vec{r}_n , where $n = 1, 2, \dots, N$, that measure and record the electric fields $E_n(t)$ from the lightning discharge, as shown in figure 3.3.

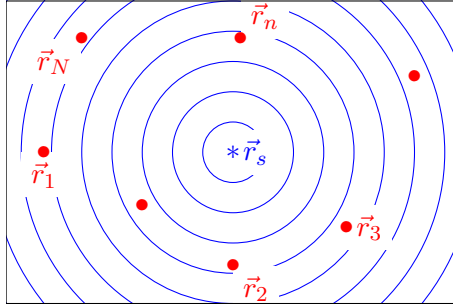


Figure 3.3: Schematic diagram of N sensors \bullet that record the far-field from the lightning discharge $*$. Adapted from [4].

In the EMTR method, the fields recorded at each sensor are flipped over in time, retransmitted using the sensors as emitters and propagated back by simulation. We will first illustrate the application of the EMTR method to lightning location for the case of a perfectly conducting ground as shown in [4, 39]. In this case, the far electric field $\vec{E}(\vec{r}, t)$ radiated by a lightning return stroke can be written as:

$$\vec{E}(\vec{r}, t) = \frac{\vec{\phi}\left(t - \frac{\|\vec{r} - \vec{r}_s\|}{c}\right)}{\|\vec{r} - \vec{r}_s\|} \quad (3.13)$$

where $\vec{\phi}(t)$ is a function whose form depends on the temporal-spatial behaviour of the return stroke current along the lightning channel. For example, if the *Transmission Line* (TL) model is assumed [37], $\vec{\phi}(t)$ is the radiation component of the vertical electric field normalised to a distance of 1 m equal to $\phi(t) = -\frac{v}{2\pi\epsilon_0 c^2} i_s(t)$, with $i_s(t)$ the channel-base lightning current. c is the speed of light, v is the return stroke speed and ϵ_0 is the dielectric permittivity of vacuum. The relation between the channel-base current and the radiated fields for other engineering models can be found in [37].

Using the aforementioned model, the electric field $\vec{E}_n(t)$, measured by the sensor at location \vec{r}_n is equal to:

$$\vec{E}_n(t) = \vec{E}(\vec{r}_n, t) = \frac{\vec{\phi}\left(t - \frac{\|\vec{r}_n - \vec{r}_s\|}{c}\right)}{\|\vec{r}_n - \vec{r}_s\|} \quad (3.14)$$

This field can be time reversed using expression (3.12):

$$\vec{E}_n(T-t) = \frac{\vec{\phi}\left(T-t + \frac{\|\vec{r}_n - \vec{r}_s\|}{c}\right)}{\|\vec{r}_n - \vec{r}_s\|} \quad (3.15)$$

The sensors are now used as emitters that re-radiate the time-reversed version of the received electric field as illustrated schematically in figure 3.4.

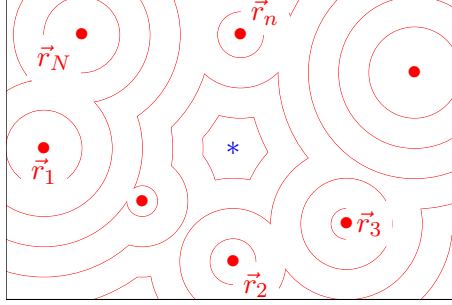


Figure 3.4: Schematic diagram of N sensors \bullet that emit time-reversed versions of the recorded fields. The lightning discharge is shown as $*$. To be compared with Figure 3.3.

Note that, according to the EMTR technique, after having recorded the field waveform, each sensor injects the time-reversed field back into the same medium. Therefore, the back-propagation will be characterised by the same geometric ($1/r$) dependence as in the direct propagation. As a result, the contribution from each sensor might become prohibitively small beyond some critical distances, leading to numerical errors. To prevent this effect and also to remove the singularities arising at the positions of the sensors (during back-propagation), it is convenient to keep the field amplitude constant while field back propagates, as explained in [4, 39, 109]. As a result, the back-propagation and the propagation models are not exactly the same. Hence, the contribution of each sensor n to the time-reversed (TR) field in this 1st model is:

$$\vec{E}_{TRn1}(\vec{r}, t) = \vec{E}_n\left(T-t - \frac{\|\vec{r} - \vec{r}_n\|}{c}\right) \quad (3.16)$$

The total back-propagated field is, therefore, equal to:

$$\vec{E}_{TR1}(\vec{r}, t) = \sum_{n=1}^N \vec{E}_{TRn1}(\vec{r}, t) = \sum_{n=1}^N \frac{\vec{\phi}\left(T-t + \frac{\|\vec{r}_n - \vec{r}_s\|}{c} - \frac{\|\vec{r} - \vec{r}_n\|}{c}\right)}{\|\vec{r}_n - \vec{r}_s\|} \quad (3.17)$$

At the stroke point, equation (3.17) reduces to the following expression:

$$\vec{E}_{TR1}(\vec{r}_s, t) = \vec{\phi}(T-t) \sum_{n=1}^N \frac{1}{\|\vec{r}_s - \vec{r}_n\|} \quad (3.18)$$

At the source point, the contributions of the different sensors are in phase. It follows that, at this location, the back-propagated fields will combine constructively to reach a maximum. This is the condition that will be used to locate the source.

It should be noted that in the analysis, we considered only the radiation component of the field and disregarded the static and induction terms. These components may have an influence at close distances. However, as far as the early-time response of the field is concerned, the effect of the static and induction components can be disregarded down to distances of a few kilometres or so

(e.g. [110]).

In the case of an elevated source such as a cloud-to-cloud lightning discharge, the same general methodology could be used.

3.3.2 Physical limits

Apart from the limitations of the technique such as the electromagnetic noise and measurements errors, the uncertainty of the soil parameters, the GPS synchronisation error, etc., the physical limitation for the accuracy, that is the spatial resolution is determined by the upper frequency used. However, using time-reversal, the size of the focal spot, which is related to the spatial resolution, could be reduced in a cluttered environment where important diffraction effects appear. This phenomenon is called super-resolution (eg. [71]) However, it is not possible to count on it in the case of a lightning discharge, where the propagation happens mainly in an open environment.

3.3.3 Practical implementation

Method 1: Maximum of the electric field amplitude

The method requires the measurement of the electric (or magnetic) field waveform generated by a lightning discharge by at least three sensors. By simulation, each waveform is then time-reversed using equation (3.12), re-emitted by the respective sensor and back-propagated. The peak amplitude at location \vec{r} is computed as the time maximum of the back-propagated field at this location:

$$E_{TR1}(\vec{r}) = \max_t \left\| \vec{E}_{TR1}(\vec{r}, t) \right\| \quad (3.19)$$

From this information, the estimation $\vec{r}_{s,estimated}$ of the stroke point location is the point in which the field reaches its maximum peak:

$$\vec{r}_{s,estimated} = \arg \max_{\vec{r}} (E_{TR1}(\vec{r})) \quad (3.20)$$

Note that, if only two sensors are used, the solution is not unique, leading to an ambiguity in the location. Three sensors can also have in certain cases an ambiguity on the location. Four sensors or more provide, in general, a single location.

The application of this method when the complete waveform is not available is challenging. This problem will be addressed in Section 3.6.2.

Method 2: Maximum of the electric field energy

A variant of the previous algorithm is to consider the energy of the signal associated to the electric field.

$$\xi(\vec{r}) = \int_{t_2}^{t_1} \vec{E}_{TR1}^2(\vec{r}, t) dt \quad (3.21)$$

One could multiply this equation by a factor expressed in $\text{m}^2\Omega^{-1}$ in order to have a quantity homogeneous to an energy. Integration limits t_1 and t_2 must be chosen adequately; they are typically depending on the measured waveforms. The stroke point location is then evaluated as the point which minimises the energy.

$$\vec{r}_{s,estimated} = \arg \max_{\vec{r}} (\xi(\vec{r})) \quad (3.22)$$

This method is expected to be less sensitive to noise than the previous one.

Method 3: Correlation matrix

For sake of completeness, we describe now another method proposed by Jemaïel in [52]. The correlation matrix is a mathematical description of the interdependency between several variables. If N sensors are involved, the correlation matrix is a square matrix of size $N \times N$ which elements are as follow:

$$R_{mn} = \frac{\text{cov}(X_m, X_n)}{\sqrt{\text{cov}(X_m, X_m)\text{cov}(X_n, X_n)}} \quad (3.23)$$

where cov is the covariance operator. The coefficients R_{mn} are contained between -1 and 1. Two variables are positively correlated if this coefficient is positive, negatively if the coefficient is negative; two variables are said independent if this coefficient is equal to zero. If all the variables are independent, the correlation matrix is equal to the unit matrix.

The application of this method to the back-propagated fields $\vec{E}_{TR_i}(\vec{r}, t)$ shows that at the stroke location, the back-propagated field are in phase, and hence the correlation matrix elements have larger values than at other locations [52]. In order to locate the stroke point, one searches for the point \vec{r} which maximises the sum of the elements of the correlation matrix applied to the back-propagated fields associated to the different sensors.

$$\vec{r}_{s,estimated} = \arg \max_{\vec{r}} \left(\sum_{m=1}^N \sum_{n=1}^N R_{mn} \right) \quad (3.24)$$

3.3.4 Matrix Pencil method

As discussed in [53], the implementation of an EMTR-based lightning location system requires that a certain number of practical difficulties be overcome, including the fact that most of the deployed lightning location networks (e.g. ALDIS [47]) do not record the complete electric or magnetic field waveforms but only certain information such as the trigger time, the peak time and the peak amplitude. The main reason is limited available memory to store more data. A way of tackling this problem could be through the use of the matrix pencil method (MPM) [111], which allows to minimise the amount of information needed to reconstruct lightning waveforms in an accurate way. This method consists in approximating a function $y(t)$ by a sum of M exponential functions:

$$y(t) \cong \sum_{i=0}^{M-1} R_i e^{s_i t} \quad (3.25)$$

where s_i et R_i are respectively the poles and the residues of the system.

When considering the discrete version of $y(t)$ into N samples, with T_s being the sampling time, one obtains:

$$y(kT_s) \cong \sum_{i=0}^{M-1} R_i z_i^k \quad (3.26)$$

with $k = 0, 1, \dots, N-1$ and $z_i^k = e^{s_i T_s}$. A detailed computation of the parameters M , s_i and R_i can be found in [111].

The performance of the MPM was evaluated in [53] using measured waveforms of electric and magnetic fields from distant natural lightning and it is shown that using only 46 poles and residues, it is possible to reproduce the measured waveforms very accurately.

3.4 Deriving ToA from EMTR

Starting from equation (3.17), we will now demonstrate mathematically that the Time-of-Arrival (ToA) method to locate lightning [11] is actually a particular case of EMTR.

Let us consider only the vertical component of the electric field. The vector quantities $\vec{\phi}(t)$ and $\vec{E}_{TR1}(\vec{r}, t)$ have only one component and can therefore be considered scalar. Since $\|\vec{r}_n - \vec{r}_s\|$ is fixed, the maximum amplitude of $E_{TR1}(\vec{r}, t)$ is obtained when the functions $\phi(t)$ all have the same phase shift (and therefore interfere constructively), and it coincides in time with the peak of $\phi(t)$. For the back-propagated signals to interfere constructively, the phase term in (3.17) should be equal for all the sensors:

$$T + \frac{\|\vec{r}_n - \vec{r}_s\|}{c} - \frac{\|\vec{r} - \vec{r}_n\|}{c} = K \quad \forall \vec{r}_n \quad (3.27)$$

where K is an undetermined constant.

The left-hand side of this equation becomes independent of \vec{r} for $\vec{r} = \vec{r}_s$ leading to $K = T$. Under this condition, the function $E_{TR1}(\vec{r}, t)$ reaches its maximum.

Let us now re-arrange equation (3.27) and write it for two different sensors at location \vec{r}_i and \vec{r}_j :

$$\|\vec{r}_i - \vec{r}_s\| - \|\vec{r} - \vec{r}_i\| = c(K - T) \quad (3.28a)$$

$$\|\vec{r}_j - \vec{r}_s\| - \|\vec{r} - \vec{r}_j\| = c(K - T) \quad (3.28b)$$

Subtracting these two equations, simplifying and dividing by c , we obtain:

$$\frac{\|\vec{r}_i - \vec{r}_s\|}{c} - \frac{\|\vec{r}_j - \vec{r}_s\|}{c} = \frac{\|\vec{r} - \vec{r}_i\|}{c} - \frac{\|\vec{r} - \vec{r}_j\|}{c} \quad (3.29)$$

The left hand side is recognised as the difference in time of arrival from the stroke point to the sensors i and j , which can be determined from the waveforms recorded at those two sensors. The right hand side represents the difference in time of arrival from a general point \vec{r} to the same two sensors. The equation defines a hyperbola and it is the basic equation used to locate lightning using the ToA technique (e.g. [11]).

3.5 Time reversal with lossy medium

We have used the approach based on (2.3) to account for losses, according to which not only the amplitude, but the whole waveform, is affected by the ground conductivity.

We showed in Section 3.2.3 that a propagation along a lossy ground is not time reversal invariant unless the sign of the ground conductivity is reversed. Three different propagation models are proposed in the next three sections to cope with this problem.

It should be noted that, in a practical implementation, the measured electromagnetic field waveforms are affected by propagation effects along a lossy ground whose electrical parameters are often not well known. On the other hand, as the back-propagation is carried out by simulation, a back-propagation model is needed. Hence, in the following paragraphs, we will describe three models for the back-propagation which will be analysed in Section 3.6. In the following development, we will assume that the (direct) propagation takes place along a homogeneous, lossy ground for which the field can be evaluated using (2.7).

3.5.1 Model 1: Perfect ground back-propagation

In this model, the losses in the back-propagation are simply disregarded. Under this condition, the contribution of sensor n to the time-reversed field is given by

$$E_{TRn1}(\vec{r}, \omega) = E_n^*(\omega) e^{-j\omega \frac{\|\vec{r} - \vec{r}_n\|}{c}} \quad (3.30)$$

Recall that $E_n^*(\omega)$ is the time-reversed version of the field captured by the sensor at location \vec{r}_n . This first model neglects attenuation and dispersion effects, but it accounts for the time delay $(\|\vec{r} - \vec{r}_n\|)/c$ due to the back-propagation. Note that the dispersion and attenuation effects due to propagation from the lightning channel to the sensors are still present.

Introducing Equation (2.7) into (3.30), we obtain, at the stroke location:

$$E_{TRn1}(\vec{r}_s, \omega) = S_f^*(\|\vec{r}_s - \vec{r}_n\|, \omega) \cdot \frac{1}{\|\vec{r}_s - \vec{r}_n\|} \phi^*(\omega) \quad (3.31)$$

Since, as seen from (3.31), propagation effects influence the fields computed at the stroke location, the computed contributions from the different sensors will, in general, be out of phase with each other. This is in contrast with the results for a lossless ground (equation (3.18)).

3.5.2 Model 2: Lossy ground back-propagation

This model takes into account the losses while calculating the back-propagating field:

$$E_{TRn2}(\vec{r}, \omega) = E_n^*(\omega) e^{-j\omega \frac{\|\vec{r} - \vec{r}_n\|}{c}} S_f(\|\vec{r} - \vec{r}_n\|, \omega) \quad (3.32)$$

Inserting (2.7) into (3.32), we obtain, at the stroke location:

$$E_{TRn2}(\vec{r}_s, \omega) = |S_f(\|\vec{r}_s - \vec{r}_n\|, \omega)|^2 \cdot \frac{1}{\|\vec{r}_s - \vec{r}_n\|} \phi^*(\omega) \quad (3.33)$$

During propagation from the lightning to the sensors, phase distortion is introduced by the effect of the finite ground conductivity. This phase distortion is compensated in model 2, since losses are taken into account in the back propagation of the time-reversed fields.

3.5.3 Model 3: Inverted losses back-propagation

In this model, an inverted filter S_f is used in the back propagation to equalise the propagation effects. The equalisation filter can be viewed as having the effect of propagation over a fictitious ‘inverted-loss’ ground:

$$E_{TRn3}(\vec{r}, \omega) = E_n^*(\omega) e^{-j\omega \frac{\|\vec{r} - \vec{r}_n\|}{c}} \frac{1}{S_f^*(\|\vec{r} - \vec{r}_n\|, \omega)} \quad (3.34)$$

Again, inserting (2.7) into (3.34), we obtain at the stroke location

$$E_{TRn3}(\vec{r}_s, \omega) = \frac{1}{\|\vec{r}_s - \vec{r}_n\|} \phi^*(\omega) \quad (3.35)$$

It can be seen that the effect of losses is absent in (3.35), since the effects of the propagation filter and of the inverted filter cancel out. This assumes, of course, that the back-propagation model corresponds exactly to the propagation model.

This model presents two drawbacks. The first one is the fact that $\frac{1}{S_f(\|\vec{r}-\vec{r}_n\|,\omega)}$ tends to infinity when ω goes to infinity. This can be addressed by introducing a properly specified low-pass filter $H(\omega)$ so that the expression $\frac{H(\omega)}{S_f(\|\vec{r}-\vec{r}_n\|,\omega)}$ decreases as ω increases to infinity. To avoid changes in the phase, a zero-phase filter could be used.

The second drawback is the fact that, under this model, the signal amplitude increases with propagation distance. Due to this effect, the maximum of the field is no longer usable as a means to detect the stroke location.

It is nevertheless possible to avert this difficulty by dividing the signal by a factor A_n to keep the amplitude constant regardless of the propagation distance. In the time domain, A_n can be chosen to be:

$$A_n = \frac{\max_t(E_{n,\text{filtered}}(t))}{\max_t(E_n(t))} \quad (3.36)$$

where $\max_t(\cdot)$ is the maximum over time of its argument and $E_{n,\text{filtered}}(t)$ is the field $E_n(t)$ after filtering by $\frac{H(\omega)}{S_f(\|\vec{r}-\vec{r}_n\|,\omega)}$.

Finally, the characteristic equation of this third model reads

$$E_{TRn3}(\vec{r}, \omega) = E_n^*(\omega) e^{-j\omega \frac{\|\vec{r}-\vec{r}_n\|}{c}} \left(\frac{H(\omega)}{S_f(\|\vec{r}-\vec{r}_n\|, \omega)} \right)^* \frac{1}{A_n} \quad (3.37)$$

with $H(\omega)$ and A_n chosen as described above.

Inserting (2.7) into (3.37), it can be readily seen that the effect of the losses will disappear in the bandwidth of $H(\omega)$.

3.5.4 Remarks on the considered models

Note that, from a theoretical point of view, the back-propagation model 3 corresponds to a soil of negative electric conductivity for which, as discussed in Section 3.2.3, Ohm's law is TR invariant. As a result, model 3 can be considered as the most rigorous among the three considered models. However, since in the real world the propagation is affected by uncertainties (ground electrical parameters, terrain profile, etc.), and since some commercial simulation programs does not allow negative values for the conductivity, models 1 and 2 could be useful to implement.

Note that, as expected, if the losses are neglected ($S_f(\omega) \equiv 1$, $H(\omega) \equiv 1$), all the three models become identical.

3.6 Simulations

In this section, we use simulations to test the three proposed models.

The studied area is a surface of $100 \text{ km} \times 100 \text{ km}$. A lightning discharge is assumed to occur at \vec{r}_s . Three sensors are considered and their locations (\vec{r}_1 , \vec{r}_2 , \vec{r}_3) are shown in figure 3.5.

The ground, described by its electric permittivity ε and conductivity σ , is assumed to be flat and homogeneous. We have found, after several simulations, that the propagation effect from equation (2.3) is essentially determined by the ground electric conductivity, and the ground permittivity does not significantly affect the generated electromagnetic fields. Consequently, the relative permittivity was set equal to 10 in all of our simulations. We used three values for the conductivity: (i) 1 S/m , corresponding to an almost ideally conducting ground for the considered distances, (ii) $0,01 \text{ S/m}$, and (iii) $0,002 \text{ S/m}$.

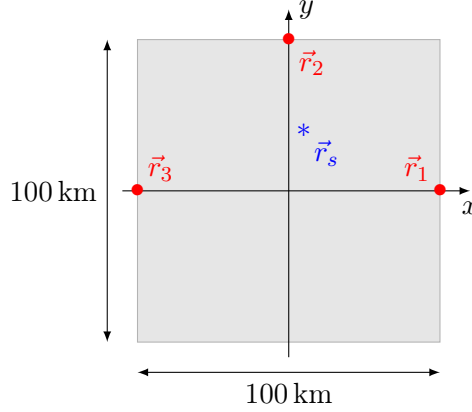


Figure 3.5: Simulation domain. The sensor locations are marked by dots \bullet . The stroke location is shown as an asterisk $*$. Back-propagation is made on the grey-coloured surface, which measures $100 \text{ km} \times 100 \text{ km}$.

Two sets of simulations were performed, the first one using the complete waveforms measured by the sensors and the second using only a small number of parameters extracted from the waveforms.

3.6.1 First set of simulations

The diagram illustrating the different steps involved in the first set of simulations is shown in Figure 3.6. The first step involves the definition of the waveshape of the return stroke current and the specification of the position of the stroke point. The sampling interval is set to 20 ns for all the simulations.

Once the source has been specified, the electric fields at the locations of all the sensors are computed using the propagation model described by (2.7).

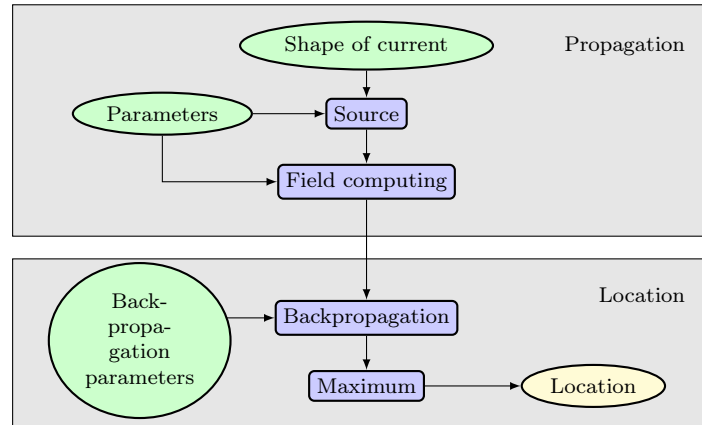


Figure 3.6: Structure of algorithm for the first set of simulations.

The fields at the sensor locations are then time-reversed and back-propagated using each one of the three models described in section 3.5 and a space sampling of $10 \text{ m} \times 10 \text{ m}$.

The sum of the contributions from each sensor gives the total field, from which the peak value is extracted. The spatial maximum gives an estimate of the stroke location.

The results of the simulations are shown in Table 3.1. In this Table, the specified values for the soil conductivity were used for the direct propagation model. For back-propagation (reversed time), the same value of the soil conductivity was used for models 2 and 3. For model 1, the back-propagation was carried out assuming the soil as a perfect conductor. The third proposed

model, i.e. the one that inverts the losses, provides correct results for all three conductivities. Note that the error is not exactly zero due to the non-zero size of the discrete elements of the space grid used in the simulations.

Table 3.1: Location error in m, as a function of soil conductivity and backpropagation model used.

	Soil conductivity σ (S/m)		
	1	0.01	0.002
Backpropagation model	Location error (m)		
Model #1	5.4	138.7	260.5
Model #2	3.6	64.1	115.1
Model #3	3.6	3.6	3.6
Model #3, *	10.6	13.2	25.9

* σ underestimated by a factor of 2 in the back-propagation.

The size of the discrete elements is 10 m \times 10 m.

When the finite conductivity of the ground is neglected in the back-propagation (model #1), the errors observed are of the order of hundreds of meters. On the other hand, if losses are inverted (model #3), the error due to the method itself is zero and the only remaining errors are due to the finite size of the discrete spatial grid. To test the sensitivity of model #3 to errors in the conductivity, a test was performed using, for the back-propagation, a conductivity underestimated by a factor of 2. The results, presented in the last line of Table 3.1, show that, at least in the cases tested in our simulations, the errors are as low as a few tens of meters.

Note also that the use of three sensors may lead to a location ambiguity (more than one fix for a return stroke). This is also an issue in the ToA method. A solution, both for TR and for ToA, is the use of additional sensors.

3.6.2 Location with finite number of waveform parameters

Many LLS, such as EUCLID [47] and NLDN [44], do not record the complete electric or magnetic fields. Instead, they extract and store only a number of signal parameters such as typically the triggering time, the rise-time and the peak value [47]. This is not the case for other networks such as GLD360 [46] or LINET [112], where the waveforms are stored for each flash.

Figure 3.7 presents a diagram of the steps followed in the second set of simulations, in which only some parameters of the signals will be used. A comparison between the algorithms presented in figures 3.6 and 3.7 reveals that the only difference lies in the blocks “*sampling*” and “*fitting*” that have been added to the latter.

We now describe the sampling process with reference to Figure 3.8 which illustrates the idealised, noiseless initial part of the radiation return stroke electric field. From the electric field computed at the location of the sensors, called “*captured field*” in Figure 3.8, we can extract the signal’s onset time t_{on} , the peak value E_p , and the time t_p at which this value is reached. These parameters are labelled “*memorised data*” in Figure 3.8 and they are similar to the ones provided by a real LLS.

To implement the time reversal method, we use the onset time, peak amplitude and time to peak to derive a complete wave labelled “*extrapolated curve*” in Figure 3.8. This process is named the *fitting* process. The shape of the extrapolated curve is deliberately chosen to be different from the original waveform in order to evaluate the impact of the sampling-fitting process and study

Table 3.2: Location error, as a function of soil conductivity and used back-propagation model

	Soil conductivity σ (S/m)		
	1	0.01	0.002
Backpropagation model	Location error (m)		
Model #1, *	15.8	120.2	304.4
Model #2, *	7.1	57.0	190.4
Model #3, *	7.1	95.1	139.5

* with sampling-fitting (see figure 3.8).

The size of the discrete elements is $10 \text{ m} \times 10 \text{ m}$.

time, the time to peak and the amplitude. A comparison with the results in Table 3.1 reveals that the accuracy reduces considerably if only a finite number of waveform parameters are used. However, the resulting location errors remain, for all the considered cases, within acceptable limits (below 300 m or so).

3.7 Application to experimental data from LLS

In this section, we present simulations based on data from the Austrian lightning location system ALDIS [47]. The ALDIS system is made up of the 8 sensors installed across Austria as shown in figure 3.9. Based on ground-truth data from lightning to an instrumented tower in Austria the CG (cloud to ground) flash detection efficiency of ALDIS (EUCLID) was determined to be higher than 98%. A stroke detection efficiency of 85% and 99% was determined for all strokes and strokes with peak currents above 10 kA, respectively. The median location accuracy of ALDIS detected strokes to the Gaisberg Tower in 2000 - 2005 was about 370 m [114].

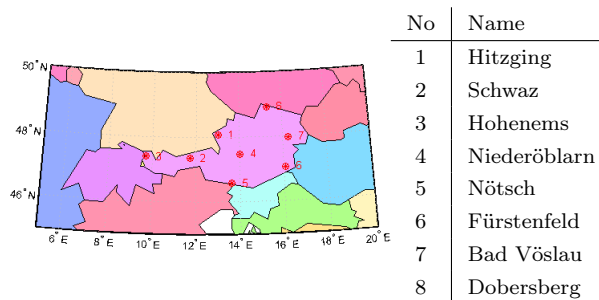


Figure 3.9: Position of ALDIS sensors in Austria.

We have used data for 8 different strokes for which three or more ALDIS sensors were involved in the determination of the location, as summarised in Table 3.3. These strokes were selected to have occurred in the central area of Austria in order to have relatively short distances (maximum 300 to 400 km) to the sensors located in Austria, and the strokes are located by a minimum of three Austrian sensors. This is the reason why these otherwise randomly selected strokes have relatively high peak currents (see Table 3.3). This selection justifies to some extent the application of a simple propagation model over a homogeneous soil. Nevertheless, the propagation to some of the sensors included parts along mountainous regions. For each stroke, the sensors from the ALDIS involved in its detection are listed (their respective locations are shown in Fig. 7), along with the

stored parameters, namely:

1. the amplitude of the electric field in LLP units (1158 LLP units corresponds to 52 V/m),
2. the triggering time, which corresponds to the onset time t_{on} in Fig. 3.8, and
3. the risetime, which corresponds to the zero-to-peak time ($t_p - t_{on}$ in Fig. 3.8).

Table 3.3: Data on sensors involved in locating the 8 considered strokes, along with their associated data. 1158 LLP units corresponds to 52 V/m.

stroke no	Type	Peak Current Estimate (kA)	Semi-major axis (m)	Sensor no	Amplitude (LLP)	Trigger time (ns)	Rise time (μ s)
1	first stroke	143.2	300	7	938.2	441952778	23.1
				6	326.6	442276550	22
				4	388.8	442359997	28.8
				1	267.1	442490054	28
				2	115.5	442884994	25.8
				3	97	443361355	26.1
2	first stroke	87.7	200	6	252.5	344669653	10.5
				4	220.3	344750834	10.8
				1	207.3	344881607	10
				5	122.2	345059348	12.4
				2	73.2	345275474	9.8
				3	66.7	345752431	9.1
3	first stroke	-43.7	200	8	-380.3	59205843	20.6
				7	-310.3	59259010	14.4
				6	-122.9	59586597	9.5
				4	-126.5	59646679	16.1
				1	-89.2	59760762	9
				5	-68.5	59962583	14.8
				2	-35.5	60161067	11.8
				3	-30.3	60632182	8.5
4	first stroke	30.8	200	8	275.8	918331576	6.5
				4	75.2	918721748	9.5
				1	58.7	918849898	6
				5	43	919031931	10
				2	23.6	919245077	8.4
				3	19.6	919721080	7.5
5	first stroke	51.8	300	7	402.8	894199325	17.3
				8	435.6	894217444	16.1
				6	148.5	894526792	17
				4	143.1	894609762	13.8
				1	123.2	894739581	13.1
				5	79.7	894919468	13.8
				2	44.6	895136667	10
				3	39.3	895613147	9.5
6	first stroke	-20.9	300	6	-63	766733123	20.1
				4	-65.7	766803099	21.8
				5	-33.6	767117692	17.6
				2	-17.5	767333580	11.8
7	first stroke	91.6	200	4	192.8	652246786	17.6
				1	167	652381969	13.4
				5	117.2	652549101	18.6
				2	63.2	652775598	15.8
				3	56.7	653253270	12.4
8	sub-sequent stroke*	-9.5	400	7	-82.4	788471056	2.2
				8	-66.7	788496805	18
				6	-22.8	788805200	2.3

* Same flash as the stroke #7.

A coordinate transformation, namely a cylindrical projection, from geographic to a Cartesian coordinate system, allows the use of the same algorithm as presented before. For the simulations, the soil conductivity was assumed to be $\sigma = 0.002 \text{ S/m}$. A sensitivity analysis was performed and showed that the location is not strongly dependent on the value of the soil conductivity.

For each stroke, the difference between the TR location and that given by the LLS is shown in figure 3.10. The smallest difference is observed for the second model, which implements physical losses.

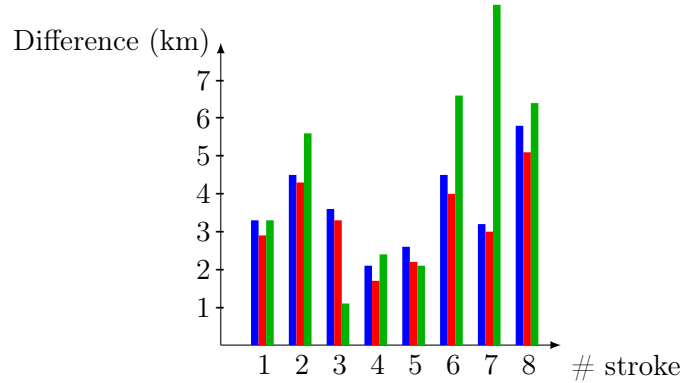


Figure 3.10: Location difference, as a function of stroke number and back-propagation model. For each stroke, three bars represent from left to right the model 1 (perfect ground back-propagation), model 2 (lossy ground back-propagation) and model 3 (inverted losses back-propagation).

Figure 3.11 shows, as an example, the peak amplitude of the back-propagated field for the fifth considered stroke, using the second model. The location provided by the EMTR, corresponding to the maximum amplitude, is shown by a green star. In the same figure, the location provided by the LLS is also shown (blue asterisk).

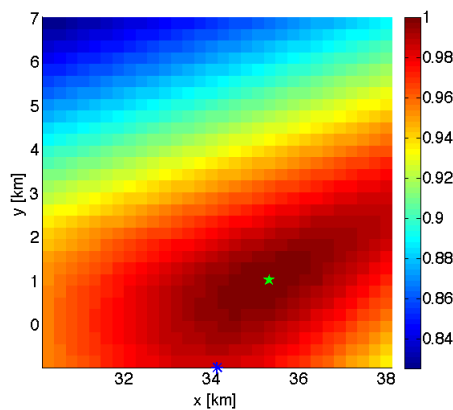


Figure 3.11: Peak amplitude of the back-propagated field for stroke number 5, computed using Model 2 (lossy ground back-propagation). The amplitude is scaled by its spatial maximum and colour coded. The location provided by the EMTR method (corresponding to the maximum) is shown by a green star (*). The location provided by the LLS is also shown by a blue asterisk (*). The (0,0) coordinate does not correspond to any specific geographical location.

Using the LLS estimated locations as ground-truth, the errors observed from the three methods can be as large as a few km. The errors come from a number of sources, including

- a) The lack of access to the complete curves

- b) The transformation from geographic to Cartesian coordinates
- c) The use of a simple propagation model considering the soil as homogeneous
- d) The fact that the LLS stroke locations, which are used as ground-truth reference were taken from the EUCLID network data stream and therefore include the contribution of numerous sensors (time and angle) located around Austria. For the simulation, only time information from the 8 sensors located in Austria is used.

In addition to the possible causes of errors of the EMTR method, it is important to note that lightning location systems are also characterised by location errors. Even though these errors are generally in the order of a few hundreds of meters on average, higher errors in the order of a few kilometres or so can be observed for individual strokes. In addition, the ALDIS system optimises the location using a combination of ToA and DF. Moreover, sensors located outside Austria are also used for calculating the optimised stroke point. As a result, the presented comparison should not be considered as a quantitative test of the proposed method.

3.8 Concluding remarks

We discussed the use of the Electromagnetic Time Reversal (EMTR) method to locate lightning strokes. After a brief description of EMTR and its application to lightning location, we demonstrated that the Time-of-Arrival method can be seen as a special case of EMTR. We proposed three different models of back-propagation to address the issue of EMTR not being invariant for lossy media. Two sets of simulations were carried out to evaluate the accuracy of the proposed methods.

The first set of simulations was performed using numerically-generated fields, and the proposed algorithm was shown to give very good results even if the soil is not perfectly conducting. In particular, it was shown that considering a model in which losses are inverted in the back propagation yields theoretically exact results for the source location. We also showed that a lack of access to the complete recorded waveforms may lead to higher location errors, although the computed errors were found to be within the range of performance of the present LLS.

A second set of simulations was performed using the sensor data reported by the Austrian Lightning Location System. The locations obtained by way of the EMTR method using only the available sensor data (amplitude, arrival time and time-to-peak) was observed to be within a few kilometres of the locations supplied by the LLS. The possible sources of error were discussed, including the fact that the exact stroke location is not known exactly. Work is in progress to use lightning strokes to instrumented towers for which the exact stroke location is known as ground-truth data .

Perspectives

Should LLS provide more accurate information in the future, the proposed method which takes advantage of the whole waveform of the measured fields (including amplitude and time of arrival), may be very promising in terms of achievable location accuracy and detection efficiency.

It is also possible that progress in the back-propagation models may lead to improvements in the accuracy over those obtained by current Lightning Location Systems. In particular, a 3D model, for example using FDTD (finite difference time domain), could be implemented in order to take the topography (mountains,...) and inhomogeneity of the soil into account during the back-propagation. In order to run the algorithm in real time, special attention should be paid to

optimisation of the computation. A possible approach would be the use of another method (for example ToA) as a first estimation and the application of the EMTR method on a reduced area around this point.

Another challenge would be the adaptation of the algorithm when two sources of radiation are radiating simultaneously or almost simultaneously.

Moreover, in order to test and develop the present proposed algorithms, a more complete experimental data set would be required. These data would include the exact location of strokes and complete field waveforms measured at different locations and synchronised by GPS.

Part II

Electromagnetic coupling to transmission lines with special reference to high-frequency excitation

Chapter 4

Available Analysis Methods

The coupling between an electromagnetic field and a transmission line, the propagation of transients along a line or the cross-coupling between parallel conductors can be solved by numerous approaches [1]. One such approach makes use of the quasi-static approximation in which propagation is neglected and coupling is described by lumped elements [10]. This approach can be adopted only when the overall dimensions of the circuit are much smaller than the minimum significant wavelength of the electromagnetic field. Unfortunately, this condition is not satisfied for many practical cases.

When the dimensions of the line is longer than the wavelength of the field, ‘antenna-theory’ or ‘full-wave’ methodologies directly based on Maxwell’s equations can be adopted [10]. When electrically long lines are involved, however, these numerical approaches require long computational times and large computer resources, which become prohibitive when multiple computations are required, in the case of parametric analysis for example.

In this chapter, we review two other approaches, the transmission line theory in Section 4.1, and the so-called enhanced transmission line theories in Section 4.2.

4.1 Transmission line approximation

One of the most used models for the computation of the coupling and propagation along a line is the classical transmission line (TL) theory [10, 115, 116]. It is relatively ‘simple’ compared to models based on antenna theory, and it has limited requirements in terms of computer resources. Another advantage is the fact that in some cases, it provides analytical expressions, which give insight into the physics of the problem. Its validity domain is, however, limited in frequency.

4.1.1 Assumptions

The assumptions associated with the transmission line approximation are thoroughly discussed in numerous books on electromagnetism (see e.g. [10, 115, 116]). Here, we will give a brief overview of these assumptions.

The propagation is assumed to occur along the line axis. This happens when the cross section of the line is electrically small; furthermore, the line is assumed to be made of parallel, straight and uniform wires, exhibiting a translational symmetry along the length of the line. The radius of the wires is assumed to be small compared to the wavelength and the other dimensions of the line. This assumption allows the following simplifications: (i) The current flows along an infinitely thin filament in the central axis of the wire. (ii) All currents are axial. (iii) The boundary conditions

can be expressed on any arbitrary contour along the wire. The fact that the currents are axial along straight, infinitely thin conductors implies a transverse magnetic (TM) propagation mode.

Another assumption of the classical TL theory is that the sum of the currents flowing in all the wires (including the reference wire) on a cross-section is zero. This fact is guaranteed by the presence of a perfect electric conductor (PEC) ground plane, because according to image theory, the currents flowing in the mirrored wires are equal in amplitude and opposite in direction to the ones in the real wires [117]. In this case, the electric field generated by the line is perpendicular to it (transverse electric (TE) mode), except if it is illuminated by an external field, leading to a scattered field having a component parallel to the line. On the other hand, when the ground plane is not perfectly conducting or when the wires are in free space, it is possible to have antenna-mode currents [118].

These assumptions are generally valid when the cross-section of the line is electrically small, typically less than about one tenth of the wavelength. According to these assumptions, the propagation along the line is quasi transverse electromagnetic (TEM). It is worth noting that the presence of discontinuities along the line, such as bends, terminals or lumped impedance, can generate radiation modes and evanescent modes, which are not considered by the TL theory [1].

Definition of the assessed system

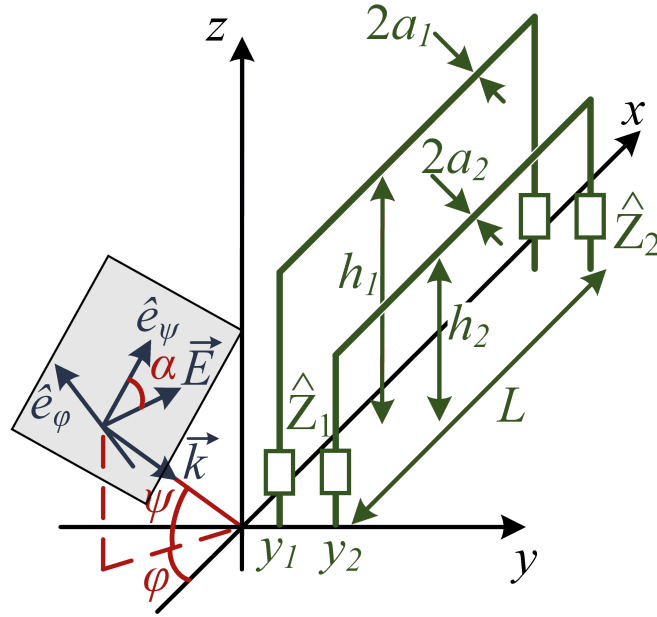


Figure 4.1: Two-wire line illuminated by a plane wave.

An example of the system assessed in this chapter is illustrated in Figure 4.1. N PEC and straight wires of circular cross-section with diameter $2a_n$ and length L are located at a height h_n above a perfect ground plane, at a horizontal position y_n , with $n = 1, \dots, N$. The wires are terminated to ground by impedances given by the matrices $\hat{\mathbf{Z}}_1$ and $\hat{\mathbf{Z}}_2$. The line is illuminated with a plane wave, characterised by its amplitude E_0 and three angles: the elevation angle ψ , the azimuth angle ϕ , and the polarisation angle α of the electric field [10].

The exciting field is computed in absence of the line and corresponds to the sum of the incident field and the reflected field due to the ground. In the case of a plane wave over a perfectly conducting

ground, the x and z component of the exciting electric field can be written as follows [10]:

$$\begin{aligned} E_x^e(x, y, z) &= E_0 A e^{-jk_x x} e^{jk_y y} (e^{jk_z z} - e^{-jk_z z}) \\ E_z^e(x, y, z) &= E_0 B e^{-jk_x x} e^{jk_y y} (e^{jk_z z} + e^{-jk_z z}) \end{aligned} \quad (4.1)$$

where

$$\begin{aligned} A &= \cos \alpha \sin \psi \cos \phi + \sin \alpha \sin \phi \\ B &= \cos \alpha \cos \psi \\ k_x &= k \cos \psi \cos \phi \\ k_y &= k \cos \psi \sin \phi \\ k_z &= k \sin \psi \end{aligned} \quad (4.2)$$

and where $k = \omega/c$ is the propagation constant in free space.

4.1.2 Derivation of the coupling equations

Because using the fields often requires working in the spectral domain (as done, for instance, in [119]), the mixed-potential integral equations (MPIE) are used here, with reference to [120]. In this section, the case of an infinite line is analysed and the boundary conditions associated with terminals will be introduced in another section.

The total tangential field, i.e. the sum of the exciting field and the scattered field (the field generated by the induced currents and charges in the line), is zero at the surface of the PEC wires:

$$E_{x,n}^e(x) + E_{x,n}^s(x) = 0 \quad n = 1, \dots, N \quad (4.3)$$

where $E_{x,n}^e(x)$ and $E_{x,n}^s(x)$ are the x -component, respectively, of the scattered and the excitation electric field at the position of the wire number n . The induced currents and per-unit-length charges in each wire $I_n(z)$, $Q_n(z)$, $n = 1, \dots, N$, in turn create a scattered field. The scattered electric field can be expressed using the scalar and vector potentials:

$$\vec{E}^s(x, y, z) = -\nabla \varphi(x, y, z) - j\omega \vec{A}(x, y, z) \quad (4.4)$$

In particular, the x -component reads:

$$E_x^s(x, y, z) = -\frac{\partial \varphi(x, y, z)}{\partial x} - j\omega A_x(x, y, z) \quad (4.5)$$

We will now express the x -component of the vector potential at the surface of the n^{th} wire in the Lorenz gauge. The thin-wire approximation allows us to replace the integral over the surface of all wires by a sum of line integrals along each wire.

$$A_{x,n}(x) = \frac{\mu_0}{4\pi} \int_{-\infty}^{\infty} \sum_{n=1}^N g(\vec{r}, \vec{r}_n') I_n(x') dx' \quad (4.6)$$

where $I_n(x)$ is the current in the n^{th} wire, $\vec{r}_n' := (x', y_n, h_n)$ is the position along the n^{th} wire and

$g(\vec{r}, \vec{r}')$ is a Green's function that can be expressed as:

$$g(\vec{r}, \vec{r}') = \underbrace{\frac{e^{-jk|\vec{r}-\vec{r}'|}}{|\vec{r}-\vec{r}'|}}_{\text{real wire}} - \underbrace{\frac{e^{-jk|\vec{r}-\tilde{\vec{r}}'|}}{|\vec{r}-\tilde{\vec{r}}'|}}_{\text{mirrored wire}} \quad (4.7)$$

where the second term corresponds to the mirrored wires located at $\vec{r}_n' := (x', y_n, -h_n)$ that simulate the effect of the ground according to image theory.

The scalar potential applied to the geometry of interest reads:

$$\varphi(x, y, z) = \frac{1}{4\pi\epsilon_0} \int_{-\infty}^{\infty} \sum_{n=1}^N g(\vec{r}, \vec{r}_n') Q_n'(x') dx' \quad (4.8)$$

where $Q_n'(x)$ is the per-unit-length charge in the n^{th} wire.

In order to reduce the number of variables, we will express the charge density as a function of the current through the continuity equation

$$\nabla \cdot \vec{I} + j\omega Q = 0 \quad (4.9)$$

where \vec{I} is the current density and Q is the volume charge density. Due to the thin-wire approximation, the current flows only along the x -axis, so the continuity equation can be written:

$$\frac{\partial I_n(x)}{\partial x} + j\omega Q_n'(x) = 0 \quad (4.10)$$

Expressing the per-unit-length charge as a function of the current yields

$$Q_n'(x) = -\frac{1}{j\omega} \frac{\partial I_n(x)}{\partial x} \quad (4.11)$$

Introducing (4.11) into (4.8) leads to:

$$\varphi(x, y, z) = -\frac{1}{j\omega 4\pi\epsilon_0} \int_{-\infty}^{\infty} \sum_{n=1}^N g(\vec{r}, \vec{r}_n') \frac{\partial I_n(x')}{\partial x'} dx' \quad (4.12)$$

$\varphi_n(x)$ is defined as the scalar potential at the location of the n^{th} wire:

$$\varphi_n(x) := \varphi(x, y_n, h_n) \quad (4.13)$$

Equations (4.3), (4.5) and (4.6) lead to:

$$\frac{\partial \varphi_n(x)}{\partial x} + j\omega \frac{\mu_0}{4\pi} \int_{-\infty}^{\infty} \sum_{m=1}^N g(\vec{r}_n, \vec{r}_m') I_m(x') dx' = E_x^e(x) \quad (4.14)$$

in which the summation index n was replaced by m to avoid a confusion.

Equations (4.8) and (4.13) lead to:

$$\varphi_n(x) + \frac{1}{j\omega 4\pi\epsilon_0} \int_{-\infty}^{\infty} \sum_{m=1}^N g(\vec{r}_n, \vec{r}_m') \frac{\partial I_m(x')}{\partial x'} dx' = 0 \quad (4.15)$$

To simplify the notations that include summations, (4.14) and (4.15) are written now using a matrix notation. For example, the currents, the potentials and electric fields are grouped into vectors:

$$\mathbf{I}(x) = \begin{bmatrix} I_1(x) \\ \vdots \\ I_N(x) \end{bmatrix} \quad \boldsymbol{\varphi}(x) = \begin{bmatrix} \varphi_1(x) \\ \vdots \\ \varphi_N(x) \end{bmatrix} \quad \mathbf{E}_x(x) = \begin{bmatrix} E_x^e(x, y_1, h_1) \\ \vdots \\ E_x^e(x, y_N, h_N) \end{bmatrix} \quad (4.16)$$

where the square brackets are used to concatenate numbers or matrices into a matrix. As a convention of notation, bold roman font is used for matrices (topped by a circumflex) and vectors. Note that they should not be confused with three component, physical vectors, like the electric field, which are topped by an arrow. Here, every component of a vector is related to a wire, hence the size of the vectors is generally $N \times 1$ and the matrices $N \times N$.

$$\begin{aligned} \frac{\partial}{\partial x} \boldsymbol{\varphi}(x) + j\omega \frac{\mu_0}{4\pi} \int_{-\infty}^{\infty} \hat{\mathbf{g}}(x - x') \mathbf{I}(x') dx' &= \mathbf{E}_x^e(x) \\ \boldsymbol{\varphi}(x) + \frac{1}{j\omega 4\pi\epsilon_0} \int_{-\infty}^{\infty} \hat{\mathbf{g}}(x - x') \frac{\partial}{\partial x'} \mathbf{I}(x') dx' &= \mathbf{0} \end{aligned} \quad (4.17)$$

where the elements of $\hat{\mathbf{g}}(x - x')$ are given by:

$$g_{mn}(x - x') = \frac{e^{-jk\sqrt{(x-x')^2 + (d_{mn})^2}}}{\sqrt{(x-x')^2 + (d_{mn})^2}} - \frac{e^{-jk\sqrt{(x-x')^2 + (\tilde{d}_{mn})^2}}}{\sqrt{(x-x')^2 + (\tilde{d}_{mn})^2}} \quad (4.18)$$

with the following geometrical distances:

$$\begin{aligned} d_{mn} &= \begin{cases} \sqrt{(y_n - y_m)^2 + (h_n - h_m)^2} & n \neq m \\ a_n & n = m \end{cases} \\ \tilde{d}_{mn} &= \begin{cases} \sqrt{(y_n - y_m)^2 + (h_n + h_m)^2} & n \neq m \\ 2h_n & n = m \end{cases} \end{aligned} \quad (4.19)$$

In (4.18) and (4.19), derived from (4.7), the radius of the wires is disregarded for $n \neq m$. However, when $n = m$, the radius of the wire has to be taken into account.

4.1.3 Agrawal's model

During the development made up to now, only the thin-wire assumption was used. Let us now use the low-frequency assumption in three steps.

1st step On the one hand, according to the transmission-line assumptions, the wavelength associated with the exciting field is much larger than the cross-section of the line. On the other hand,

at low frequencies, the Green's function becomes negligible when its argument is larger than about a few times the cross-section. Hence, the current can be considered as almost constant over the effective length of integration in (4.17) and can be taken out of the integral (see [1], p.128).

$$\begin{aligned} \int_{-\infty}^{\infty} \widehat{\mathbf{g}}(x-x') \mathbf{I}(x') dx' &\cong \int_{-\infty}^{\infty} \widehat{\mathbf{g}}(x-x') dx' \mathbf{I}(x) \\ \int_{-\infty}^{\infty} \widehat{\mathbf{g}}(x-x') \frac{\partial}{\partial x'} \mathbf{I}(x') dx' &\cong \int_{-\infty}^{\infty} \widehat{\mathbf{g}}(x-x') dx' \frac{d}{dx} \mathbf{I}(x) \end{aligned} \quad (4.20)$$

2nd step In the Green's functions (4.18), taking the low-frequency limit $k \rightarrow 0$ allows to get rid of the exponential terms ($e^{-jkx} \cong 1$). The integral in (4.20) can be computed after a change of variable $\xi := x' - x$.

$$\begin{aligned} \int_{-\infty}^{\infty} g_{mn}(x-x') dx' &\cong \int_{-\infty}^{\infty} \frac{1}{\sqrt{\xi^2 + (d_{mn})^2}} - \frac{1}{\sqrt{\xi^2 + (\tilde{d}_{mn})^2}} d\xi = \\ &= \ln \left(\sqrt{\xi^2 + (d_{mn})^2} + \xi \right) \Big|_{-\infty}^{\infty} - \ln \left(\sqrt{\xi^2 + (\tilde{d}_{mn})^2} + \xi \right) \Big|_{-\infty}^{\infty} = \\ &= 2 \ln \left(\frac{\tilde{d}_{mn}}{d_{mn}} \right) =: G_{mn}^{TL} \end{aligned} \quad (4.21)$$

In fact, the integral is independent on the position and the frequency.

3rd step The 'scattered voltage' is defined as the low-frequency limit of the scattered scalar potential.

$$\mathbf{U}^s(x) := \lim_{f \rightarrow 0} \boldsymbol{\varphi}(x) \quad (4.22)$$

Interestingly, a development using the Coulomb gauge, which would provide a different definition of the potential, would lead to exactly the same result at low frequencies [121].

The per-unit-length matrices of inductance and capacitance are defined as follows [115]:

$$\begin{aligned} \widehat{\mathbf{L}}'_0 &:= \frac{\mu_0}{4\pi} \widehat{\mathbf{G}}^{TL} \\ \widehat{\mathbf{C}}'_0 &:= 4\pi\epsilon_0 \widehat{\mathbf{G}}^{TL-1} \end{aligned} \quad (4.23)$$

The application of definitions (4.22) and (4.23) into (4.17) leads to the telegrapher's equations in the formulation proposed by Agrawal, Price and Gurbaxani [122].

$$\begin{aligned} \frac{d}{dx} \mathbf{U}^s(x) + j\omega \widehat{\mathbf{L}}'_0 \mathbf{I}(x) &= \mathbf{E}_x^e(x) \\ \frac{d}{dx} \mathbf{I}(x) + j\omega \widehat{\mathbf{C}}'_0 \mathbf{U}^s(x) &= \mathbf{0} \end{aligned} \quad (4.24)$$

This model expresses the coupling in terms of electric field only.

For the sake of completeness, two different but completely equivalent formulations, known as Taylor's and Rachidi's models, are presented in the next two sections.

4.1.4 Taylor's model

The total voltage is linked with the scattered voltage through:

$$\mathbf{U}(x) = \mathbf{U}^s(x) + \mathbf{U}^e(x) = \mathbf{U}^s(x) - \left[\int_0^{h_n} E_z^e(x, y_n, z) dz \right] \quad (4.25)$$

where the brackets correspond to a vector; the term inside the brackets corresponds to the n^{th} component of this vector.

Besides, the exciting field must satisfy the Maxwell-Faraday equation.

$$\nabla \times \vec{E}^e(x, y, z) = -j\omega \vec{B}^e(x, y, z) \quad (4.26)$$

In particular the y -component of this equation, at the position $y = y_n$, reads:

$$\frac{d}{dx} E_z^e(x, y_n, z) - \frac{d}{dz} E_x^e(x, y_n, z) = -j\omega B_y^e(x, y_n, z) \quad (4.27)$$

This equation can be integrated along z , while considering that the exciting field tangent to the ground is zero.

$$\frac{d}{dx} \int_0^{h_n} E_z^e(x, y_n, z) dz - E_x^e(x, y_n, h_n) = \int_0^{h_n} -j\omega B_y^e(x, y_n, z) dz \quad (4.28)$$

Applying (4.25) and (4.28) into (4.24) leads to the coupling model of Taylor, Satterwhite and Harrison [123].

$$\begin{aligned} \frac{d}{dx} \mathbf{U}(x) + j\omega \hat{\mathbf{L}}'_0 \mathbf{I}(x) &= -j\omega \left[\int_0^{h_n} B_y^e(x, y_n, z) dz \right] \\ \frac{d}{dx} \mathbf{I}(x) + j\omega \hat{\mathbf{C}}'_0 \mathbf{U}(x) &= -j\omega \hat{\mathbf{C}}'_0 \left[\int_0^{h_n} E_z^e(x, y_n, z) dz \right] \end{aligned} \quad (4.29)$$

This model expresses the coupling using directly the total voltage without needing the scattered voltage.

4.1.5 Rachidi's model

A 'scattered current' can be defined in a similar way as the scattered voltage [38].

$$\mathbf{I}(x) = \mathbf{I}^s(x) + \mathbf{I}^e(x) = \mathbf{I}^s(x) - \hat{\mathbf{L}}_0'^{-1} \left[\int_0^{h_n} B_y^e(x, y_n, z) dz \right] \quad (4.30)$$

Besides, the exciting field must satisfy the Ampere-Maxwell law in absence of current:

$$\nabla \times B^e(x, y, z) = j\omega \mu_0 \varepsilon_0 E^e(x, y, z) \quad (4.31)$$

Applying (4.30), (4.31) and the equivalence between the per-unit-length inductance and capacitance (4.23) into Taylor's equations (4.29) leads after simplification to Rachidi's model [38].

$$\begin{aligned} \frac{d}{dx} \mathbf{U}(x) + j\omega \hat{\mathbf{L}}'_0 \mathbf{I}^s(x) &= 0 \\ \frac{d}{dx} \mathbf{I}^s(x) + j\omega \hat{\mathbf{C}}'_0 \mathbf{U}(x) &= \hat{\mathbf{L}}_0'^{-1} \left[\int_0^{h_n} \frac{\partial}{\partial y} B_x^e(x, y_n, z) dz \right] \end{aligned} \quad (4.32)$$

This model characterises the coupling in terms of magnetic field only.

4.1.6 Boundary conditions

The line terminations are modelled by impedance matrices: $\hat{\mathbf{Z}}_1$ at $x = 0$ and $\hat{\mathbf{Z}}_2$ at $x = L$.

$$\begin{aligned}\mathbf{U}(0) &= -\hat{\mathbf{Z}}_1 \mathbf{I}(0) \\ \mathbf{U}(L) &= \hat{\mathbf{Z}}_2 \mathbf{I}(L)\end{aligned}\tag{4.33}$$

In the classical transmission line theory, the terminals are considered as electrically short, allowing the use of Ohm's law for a lumped source. However, a more accurate modelling of the risers in the framework of the TL theory will be presented in Section 4.1.11.

4.1.7 BLT equations

The line response at its terminal loads can be expressed in a compact way by using the Baum, Liu, Tesche (BLT) equations [10].

$$\begin{bmatrix} \mathbf{I}(0) \\ \mathbf{I}(L) \end{bmatrix} = \begin{bmatrix} \hat{\mathbf{Z}}_C^{-1} & \hat{\mathbf{0}} \\ \hat{\mathbf{0}} & \hat{\mathbf{Z}}_C^{-1} \end{bmatrix} \begin{bmatrix} \hat{\mathbf{1}} - \hat{\boldsymbol{\rho}}_1 & \hat{\mathbf{0}} \\ \hat{\mathbf{0}} & \hat{\mathbf{1}} - \hat{\boldsymbol{\rho}}_2 \end{bmatrix} \begin{bmatrix} -\hat{\boldsymbol{\rho}}_1 & \hat{\mathbf{1}}e^{jkL} \\ \hat{\mathbf{1}}e^{jkL} & -\hat{\boldsymbol{\rho}}_2 \end{bmatrix}^{-1} \begin{bmatrix} \mathbf{S}_1 \\ \mathbf{S}_2 \end{bmatrix}\tag{4.34}$$

where $\hat{\mathbf{1}}$ is a unit matrix, $\hat{\mathbf{Z}}_C$ is the characteristic impedance

$$\hat{\mathbf{Z}}_C := c\hat{\mathbf{L}}'_0 = \frac{1}{c}\hat{\mathbf{C}}_0'^{-1}\tag{4.35}$$

$\hat{\boldsymbol{\rho}}_1$ and $\hat{\boldsymbol{\rho}}_2$ are the reflection coefficients at the left and right terminal respectively.

$$\begin{aligned}\hat{\boldsymbol{\rho}}_1 &= (\hat{\mathbf{Z}}_1 + \hat{\mathbf{Z}}_C)^{-1}(\hat{\mathbf{Z}}_1 - \hat{\mathbf{Z}}_C) \\ \hat{\boldsymbol{\rho}}_2 &= (\hat{\mathbf{Z}}_2 + \hat{\mathbf{Z}}_C)^{-1}(\hat{\mathbf{Z}}_2 - \hat{\mathbf{Z}}_C)\end{aligned}\tag{4.36}$$

\mathbf{S}_1 and \mathbf{S}_2 are source terms which are defined in the following way for a lumped voltage source \mathbf{U}_0 located in x_s .

$$\begin{aligned}\mathbf{S}_1 &= \frac{1}{2}\mathbf{U}_0 e^{jkx_s} \\ \mathbf{S}_2 &= -\frac{1}{2}\mathbf{U}_0 e^{jk(L-x_s)}\end{aligned}\tag{4.37}$$

If $\mathbf{U}'_0(x_s)$ is a distributed source between $x = a$ and $x = b$, the source terms are defined in the following way.

$$\begin{aligned}\mathbf{S}_1 &= \frac{1}{2} \int_a^b \mathbf{U}'_0(x_s) e^{jkx_s} dx_s \\ \mathbf{S}_2 &= -\frac{1}{2} \int_a^b \mathbf{U}'_0(x_s) e^{jk(L-x_s)} dx_s\end{aligned}\tag{4.38}$$

The source terms for a plane wave excitation will be defined in the following sections.

4.1.8 Modelling of the risers, in the framework of the TL theory

Three different ways of modelling the vertical risers are reviewed, all in the general framework of the transmission line theory. These three models will be referred to as:

- ‘Basic case’, adapted from [10];
- ‘Exact-field’ model, adapted from [1];
- ‘Distributed-source excitation’ model, adapted from [124].

All these models can be integrated into the BLT formulation.

4.1.9 Basic model: approximate solution for the lumped sources

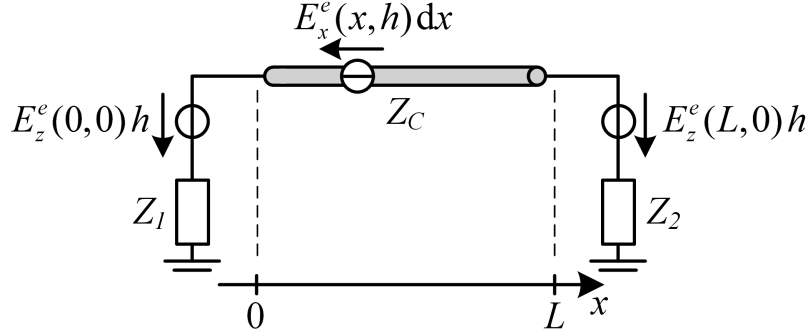


Figure 4.2: Scheme of the ‘basic case’ coupling model.

The application of (4.25) into (4.33) reads

$$\begin{aligned} \mathbf{U}^s(0) &= -\hat{\mathbf{Z}}_1 \mathbf{I}(0) + \left[\int_0^{h_n} E_z^e(0, y_n, z) dz \right] \\ \mathbf{U}^s(L) &= \hat{\mathbf{Z}}_2 \mathbf{I}(L) + \left[\int_0^{h_n} E_z^e(L, y_n, z) dz \right] \end{aligned} \quad (4.39)$$

In [10], it is assumed that the vertical variation of the field along the risers can be neglected. Hence, the integral used in the computation of the ‘exciting’ voltage can be reduced to a product between the field at the ground level and the height of the riser:

$$U_n^e(x) = - \int_0^{h_n} E_z^e(x, y_n, z) dz \cong -E_z^e(x, y_n, 0)h \quad (4.40)$$

This modelling corresponds to the scheme in Figure 4.2. Based on (4.37), the source terms can be expressed as:

$$\begin{aligned} \mathbf{S}_1 &= E_0 e^{jk_y y} \left(e^{j(k-k_x)L} - 1 \right) jk_z h \left(\frac{A}{j(k-k_x)} - \frac{B}{jk_z} \right) \\ \mathbf{S}_2 &= -E_0 e^{jk_y y} e^{jkL} \left(e^{-j(k+k_x)L} - 1 \right) jk_z h \left(\frac{A}{-j(k+k_x)} - \frac{B}{jk_z} \right) \end{aligned} \quad (4.41)$$

with

$$\begin{aligned} A &= \cos \alpha \sin \psi \cos \varphi + \sin \alpha \sin \varphi \\ B &= \cos \psi \cos \alpha \end{aligned} \quad (4.42)$$

where then exponential of a vector is a taken elementwise and where the angles ϕ , ψ and α are defined in Figure 4.1.

This model is expected to be accurate at low frequencies, when the length of the riser is electrically short, that is under the classical transmission line assumptions.

4.1.10 Exact-field model: exact solution for the lumped sources

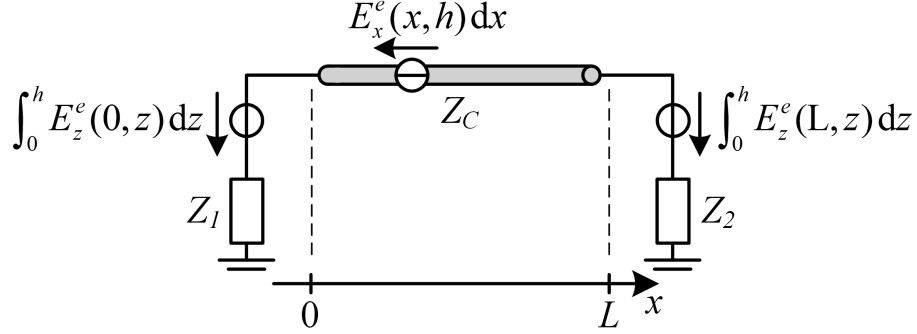


Figure 4.3: Scheme of the ‘exact-field’ coupling model.

If the actual field is used to compute the source associated with the vertical risers, the sources are given by the following expressions:

$$\begin{aligned} \mathbf{S}_1 &= \frac{E_0}{2} e^{jk_y y} \left(e^{j(k-k_x)L} - 1 \right) \left(e^{jk_z h} - e^{-jk_z h} \right) \left(\frac{A}{j(k-k_x)} - \frac{B}{jk_z} \right) \\ \mathbf{S}_2 &= -\frac{E_0}{2} e^{jk_y y} e^{jkL} \left(e^{-j(k+k_x)L} - 1 \right) \left(e^{jk_z h} - e^{-jk_z h} \right) \left(\frac{A}{-j(k+k_x)} - \frac{B}{jk_z} \right) \end{aligned} \quad (4.43)$$

This model corresponds to the Figure 4.3. It is expected to provide results similar to the *basic model* at low frequencies and when ψ is small, and more accurate results than the basic case in other situations. As this model is not computationally much heavier than the basic case, we recommend to use this one instead.

4.1.11 Distributed-source model for the risers

Vance [124] modelled the risers as conical transmission lines (see Figure 4.4).

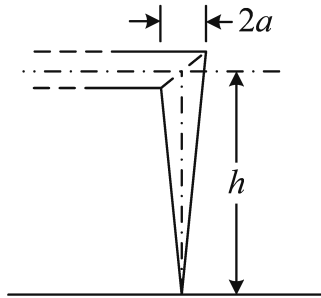


Figure 4.4: Vertical element at the end of a transmission line, adapted from [124].

According to Schelkunoff ([125], Equation 4-(28) p.105 or [126], p.287) the characteristic impedance of a transmission line formed by a conical tower of half-angle Ψ above a perfect ground reads:

$$Z_C^{cone} = \frac{1}{2\pi} \sqrt{\frac{\mu_0}{\epsilon_0}} \ln \cot \left(\frac{\Psi}{2} \right) \quad (4.44)$$

In the case of a vertical riser, $\tan \Psi = \frac{a}{h} \ll 1$, and (4.44) reduces to [125, 126]:

$$Z_C^{cone} \cong \frac{1}{2\pi} \sqrt{\frac{\mu_0}{\varepsilon_0}} \ln \left(\frac{2h}{a} \right) \quad (4.45)$$

Equation (4.45) corresponds to the expression of the horizontal line characteristic impedance. Hence, an effect of the risers is the lengthening of the line by the length of the risers, modelled in [124] by modified reflection coefficients:

$$\rho'_i = \rho_i e^{-2\gamma h} \quad i = 1; 2 \quad (4.46)$$

The field coupling to the risers is modelled as distributed sources along the risers. An expression for the current at the extremities of the horizontal line, that is at $z = h$ and not at the ground level, is given in [124].

Degauque and Zeddami [127] considered the lengthening of the line due to the risers in a particular example when the electric field is horizontal and parallel to the horizontal line, i.e. no direct coupling occurs to the risers. Later, Degauque et al. [128] applied (4.46) in the classical expression of the current given in [129], providing a theory for general incidence of the field. However, they used lumped sources for the coupling to the vertical risers and did not provide readily usable expressions.

The lengthening effect of the risers was also noticed in [130].

Pignari and Bellan [131] modelled the risers as cylindrical. According to Schelkunoff (for a symmetrical antenna, [125] Equation 13-(89) p.426), the characteristic impedance of a vertical cylindrical antenna reads:

$$Z_C^{cylinder} = \frac{1}{2\pi} \sqrt{\frac{\mu_0}{\varepsilon_0}} \left(\ln \left(\frac{2h}{a} \right) - 1 \right) \quad (4.47)$$

In this case, even if $h \gg a$, the characteristic impedance is not the same as the impedance of the horizontal part of the line. Hence, in [131] the system was modelled as three lines connected in cascade and excited by distributed sources.

Modelling of the risers as transmission lines excited by distributed sources

In this section, the line is modelled as three cascaded transmission lines, corresponding respectively to the left riser, the horizontal part and the right riser. As shown in Figure 4.5, the lines corresponding to the risers are excited by distributed sources whose amplitude corresponds to the vertical component of the electric field, whereas the horizontal line is excited by the horizontal component of the electric field.

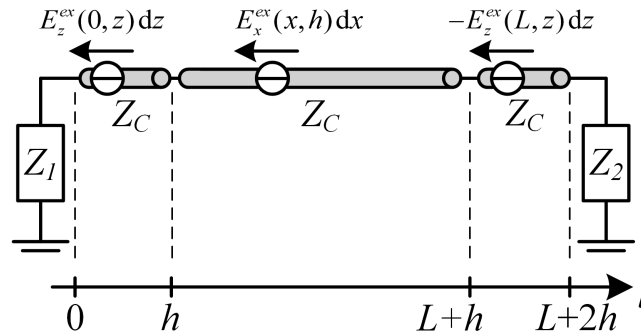


Figure 4.5: Modelling of a TL.

As the three lines in Figure 4.5 are supposed to have the same characteristic impedance, they can be merged into a single line of length $L + 2h$. This simplifies the computations and allows the use of the standard BLT equation (4.34) where L is replaced by $L + 2h$.

The change of coordinates from the TL 1D coordinate along the wire (including the riser) to the 3D usual coordinates for the field is done differently depending on the part of the line which is considered.

$$\begin{cases} 0 \leq l < h & x = 0 & z = l \\ h \leq l \leq L + h & x = l - h & z = h \\ L + h < l \leq L + 2h & x = L & z = L + 2h - l \end{cases} \quad (4.48)$$

After the change of coordinate presented in (4.48) and integration of the distributed sources along the lines, the source terms are derived.

$$\begin{aligned} S_1 &= \frac{E_0}{2} e^{jk_y y} \left[B \left(\frac{e^{j(k+k_z)h} - 1}{j(k+k_z)} + \frac{e^{j(k-k_z)h} - 1}{j(k-k_z)} \right) \right. \\ &\quad + A(e^{jk_z h} - e^{-jk_z h})e^{jkh} \left(\frac{e^{j(k-k_x)L} - 1}{j(k-k_x)} \right) \\ &\quad \left. - Be^{-jk_x L} e^{jk(L+h)} \left(e^{jk_z h} \frac{e^{j(k-k_z)h} - 1}{j(k-k_z)} + e^{-jk_z h} \frac{e^{j(k+k_z)h} - 1}{j(k+k_z)} \right) \right] \\ S_2 &= -\frac{E_0}{2} e^{jk_y y} e^{jk(L+2h)} \left[B \left(\frac{e^{-j(k-k_z)h} - 1}{-j(k-k_z)} + \frac{e^{-j(k+k_z)h} - 1}{-j(k+k_z)} \right) \right. \\ &\quad + A(e^{jk_z h} - e^{-jk_z h})e^{-jkh} \left(\frac{e^{-j(k+k_x)L} - 1}{-j(k+k_x)} \right) \\ &\quad \left. - Be^{-jk_x L} e^{-jk(L+h)} \left(e^{jk_z h} \frac{e^{-j(k+k_z)h} - 1}{-j(k+k_z)} + e^{-jk_z h} \frac{e^{-j(k-k_z)h} - 1}{-j(k-k_z)} \right) \right] \end{aligned} \quad (4.49)$$

Note that, equations (4.49) are presented, for the case of a single-conductor line. In fact, the used coordinate is associated to one wire and the extension of this model to a multiconductor line is not straightforward, as it would require the adaptation of the coordinate to the other wires, which would be particularly difficult with vertical risers with different heights.

Then one can apply these source terms to the BLT equation (4.34), where the length of the line L is replaced by $L + 2h$.

Note that this model is similar to Pignari and Bellan's [131] with the exception that the characteristic impedance of the risers is supposed here to be the same as the one of the horizontal line. This model is expected to provide more accurate solutions than the *basic* and *exact-field* models, but may overestimate the amplitude of the induced current, since it does not consider the radiation effects.

4.2 Enhanced transmission line theories

Significant efforts have been put into the elaboration of generalisations of the TL theory, to incorporate effects that are not considered by the classical TL theory, while keeping as much as possible the relative simplicity of the TL equations. In these models, one or several of the assumptions of the classical TL approximation are relaxed. The models reviewed in this section consider for example lines made of thick wires, non-uniform wires, or they take into account radiation effects

occurring at high frequency, or non TEM modes, such as radiation, leaky or antenna modes.

Leviatan and Adams showed that not only a TEM mode, but also higher-order modes can occur into a two-wire infinite line excited either by a plane wave or by a lumped source [132]. In the case of a lumped source, the higher-order modes propagate with less attenuation at higher frequencies; they are still attenuated, while the amplitude of the TEM mode remains constant.

Nitsch et Tkachenko showed that the parameters of a thin, infinite and lossless line in fact depend on the excitation and on the gauge [121]. However, for a grazing incidence ($\psi \rightarrow 0$) the propagation becomes TEM; moreover, at low frequencies, the characteristic impedance becomes gauge independent and equal to the classical parameters.

Haase et al. [133] presented the modelling of discontinuities and non-uniformities in transmission lines with the aid of extended telegrapher equations. They proposed simple static models for risers, bend, wires through holes, and a wire crossing a slit.

4.2.1 Asymptotic theory

Tkachenko et al. [134] derived a TL-like pair of equations for evaluating currents and potentials induced by external electromagnetic fields on a single wire above a perfect conducting ground. Based on perturbation theory, an iterative procedure was proposed to solve the derived coupling equations. Later in 2001, Tkachenko et al. [135] extended their method to take into account the presence of line terminations and discontinuities. The results of the asymptotic method were also used in the application of the singularity expansion method in [136, 137].

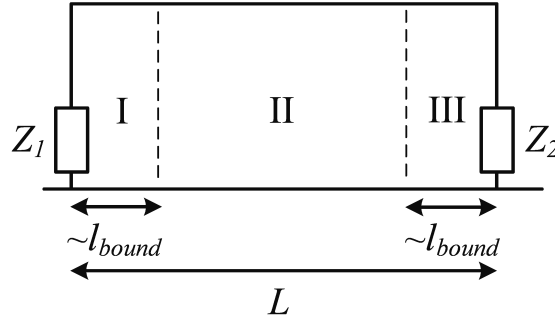


Figure 4.6: Line decomposition into zones. Adapted from [135].

As shown in Figure 4.6, the line can be conceptually split up into three regions [135]:

- Region I and III correspond to the regions near the terminals, where the transverse electromagnetic (TEM) mode, leaky modes and radiating modes can be found. The computation of the solution in these regions requires, in general, a numerical full-wave method.
- Region II corresponds to the region far enough from the terminal that the leaky modes and radiation modes have asymptotically vanished and only the TEM mode remains.

l_{bound} is the length of the terminal zones; its value is directly related to the cross-section of the line and frequency; it corresponds to the distance where the leaky and radiation modes due to the line terminals may be neglected in comparison with the TEM fields associated with the currents along the wires.

In region II, the current is the sum of three terms.

$$I(x) = I_0 e^{-jk_x x} + I_1 e^{jk_x x} + I_2 e^{-jk_x x} \quad (4.50)$$

$I_0 e^{-jk_x x}$ corresponds to the current that would flow in an infinite line with the same cross section. $I_1 e^{jk_x x}$ and $I_2 e^{-jk_x x}$ are TEM respectively backward and forward propagating waves due to the presence of the terminals.

Analytical expressions exist for the current I_0 in an infinite line [119]. On the other hand, for certain simple types of load, e.g. for an open circuit, analytical solution exist for I_1 and I_2 [137]. However, in general, the use of a full-wave numerical method is needed to compute I_1 and I_2 .

This method present similarities with the theories developed for microwave networks. In microwave engineering, a multiport network is typically modelled by a scattering matrix seen from a reference plane which is placed at a distance from the geometric termination of the waveguide where the higher-order modes have died out [138, 139]. The differences between microwave theories and the asymptotic theory are the following. Waveguides have typically a bounded cross-section, which suits well to the application of a port limited in space, whereas the transmission lines studied by the asymptotic method have a more open structure. Moreover, the asymptotic theory gives insights into the terminal parts of the structure. Furthermore, the asymptotic theory considers in a direct manner the effect of an external electromagnetic field coupling to the line.

4.2.2 Transmission line super theory

Researchers from the University of Magdeburg [133, 140–152] developed enhanced versions of the transmission line theory and proposed in particular a so-called transmission line super theory (TLST). Maxwell's equations for a lossless nonuniform multiconductor transmission line above a perfectly conducting ground can be transformed into generalised telegrapher equations. This formulation extends to general modes, very high frequencies and include radiation effects.

Among other formulations, the generalised telegrapher's equations can be written in a supermatrix notation. The formulation presented here uses current and per-unit-length charge as variables, expressed as a function of the length parameter ζ [152].

$$\frac{\partial}{\partial \zeta} \begin{bmatrix} \mathbf{q}(\zeta) \\ \mathbf{I}(\zeta) \end{bmatrix} + j\omega \bar{\mathbf{P}}_q(\zeta) \begin{bmatrix} \mathbf{q}(\zeta) \\ \mathbf{I}(\zeta) \end{bmatrix} = \begin{bmatrix} \mathbf{q}'_s(\zeta) \\ \mathbf{0} \end{bmatrix} \quad (4.51)$$

$\bar{\mathbf{P}}_q(\zeta)$ is a super-matrix associated with the geometry of the line, and the vector $\mathbf{q}'_s(\zeta)$ is linked with the excitation. Equation (4.51) has the same structure as the classical telegrapher equations but entails the full information of Maxwell's equations. Only geometric restrictions regarding the form of the charge and current distribution along the transmission line have been made. In particular, all information on field modes and radiation effects are kept [152]. Other formulations of (4.51) exists, using the scalar potential instead of the per-unit-length charge, as in e.g. [133].

Several solution methods can be used, like iterative methods or numerical integration techniques. In particular, analytical expressions for the reflection and scattering parameters associated to risers short-circuited to the ground were computed in [153].

Nitsch and Tkachenko [154] applied the full-wave analysis to a vertical half-circular loop above conducting ground excited by a lumped source. Their approach is based on the symmetry of the analysed system. They gave analytical expressions for the current and potential lowest modes appearing in the half loop and obtained in particular that the propagation is characterised by a phase velocity larger than the speed of light and by an attenuation due to radiation.

Gronwald et al. made a comparison between the generalised transmission line theories and the singularity expansion and eigenmode expansion methods (SEM/EEM) [155]. Both approaches are based on a common physical basis and basic procedure. Differences exist in the spatial integration

procedures which allow to reduce the relevant field problem to a network problem. In general, both approaches may lead to complex-valued network elements; it is also possible to take into account radiation effects by redefining the excitation sources rather than by redefining the transmission line parameters.

4.2.3 Numerical methods

Cui and Chew developed a full-wave numerical model for thick wires with an arbitrary shape [156]. Poljak et al. developed a generalised form of the telegrapher's equations for finite-length transmission lines above a lossy ground [157]. The resulting equations were handled numerically via the Galerkin-Bubnov indirect boundary element method. Obtained results showed that the TL approximation can result in a significant underestimation of the induced currents. Later, they derived a time-domain variant of this theory [158].

Researchers from the universities of Napoli and Cassino [159–162] proposed a full-wave model for the analysis of lossless lines, able to describe the high-frequency mixed-mode propagation. Their model consists of a mixed system of differential and integral equations. The solution was computed by using a numerical method based on the collocation method.

In [163], a regularisation technique is applied to solve the the generalised model proposed in [134].

4.2.4 Other theories

Vukicevic et al. derived an integral equation describing the antenna-mode currents along a two-wire transmission line [118]. At low frequencies, the integral equation reduces to a pair of TL-like equations with equivalent p.u.l. inductance and capacitance. The derived equations make it possible to compute the antenna-mode currents using any classical TL coupling code with appropriate parameters.

Nitsch et al. [164] showed that the current propagation along a thin wire of arbitrary geometric form near a ground-plane can be reduced to a Schrödinger-like differential equation. Using the formalism of transfer matrices, they found an analytical expression for the transmission coefficient of the finite number of periodically located non-uniformities which also contains the scattering data of one non-uniformity.

Chabane et al. [165–167] recompute the transmission line parameters and obtain a frequency-dependent complex characteristic impedance. Moreover, they propose to add a distributed resistance along the line. Their theory has the advantage to be straightforwardly applicable, but the physical soundness of this theory is unclear.

4.3 Need of further research

4.3.1 Limitation of the transmission line model

In this section the applicability of classical TL theory for the analysis of the field-to-wire coupling problem is assessed by comparing the solutions provided by a full wave method, and the three models for the vertical risers defined in Sections 4.1.9–4.1.11.

In principle, the validity of the solutions provided by TL theory is constrained to transmission lines having electrically small cross sections. We have tried to assess the deviations from the full wave solutions occurring at high frequencies when the wavelength becomes much smaller than the studied lines' cross sections.

We analyse the canonical case of a plane wave coupling to a lossless single wire above a ground plane in the frequency domain. The line is terminated on its characteristic impedance at its first terminal and short-circuited at its left terminal. A summary of the parameters of the line used for the comparison is shown in Table 4.1.

Table 4.1: Parameters of the transmission line.

Parameter	Value
Length L	3 m
Radius a	0.7 mm
Height h	10 cm
Impedance Z_1	339Ω
Impedance Z_2	0Ω
Elevation angle ψ	45°
Azimuth angle ϕ	0°
Polarisation angle α	0°

The transfer function between the incident plane wave and the current induced in the first terminal at the level of the ground is shown in Figure 4.7. Results obtained using the considered TL models for the risers are compared with full-wave results using CST Microwave Studio[®] (using the finite integration technique (FIT) in the time domain), used here as a reference.

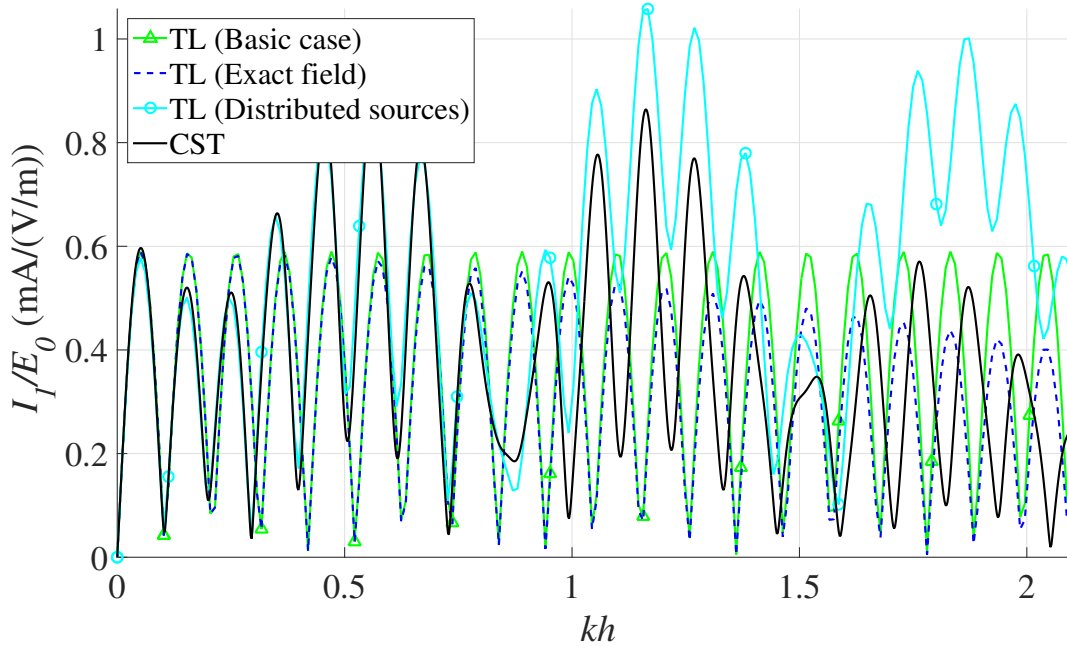


Figure 4.7: I_1/E_0 transfer functions calculated with three models based on the classical TL theory (basic case, exact field, distributed sources) and with a full-wave code (CST).

It can be seen from Figure 4.7 that all the considered models provide basically the same results at low frequencies up to about $kh \cong 0.13$ (60 MHz), while the TL theory is supposed to be valid up to about $kh \cong 0.31$ (150 MHz). The basic model and the exact-field model provide solutions which are not exact even below the frequency limit of the TL theory. The distributed source model for the risers provides very accurate results up to about $kh \cong 0.84$ (400 MHz), but deviates significantly

at higher frequencies with respect to full-wave results.

This result indicates, as many examples in the literature e.g. [165,168], that the transmission line theory could provide inaccurate results when the cross-section cannot be considered as electrically small. However, as the recourse to a full-wave numerical solution can be prohibitive in terms of computational resources for electrically very long lines, we will propose improvements of the modelling of the vertical risers, in order to push back the frequency limitation and increase the accuracy at high frequencies in Chapter 5.

4.3.2 Enhanced transmission line theories

Among other ‘enhanced’ transmission line theories, the asymptotic theory is particularly promising, because it proposes an analytical expression for the current and hence gives a physical insight of the problem. It provides accurate results above the frequency limit of the classical transmission line theory and can be also applied to arbitrary terminals. As it allow to avoid the application of a full-wave method, or to apply a full-wave method on a smaller system only, it is particularly effective for electrically long lines. However, as it is described in the literature [135], it is limited to monoconductor lines. In real cases, lines are often made of several conductors. For this reason, the application of the asymptotic theory will also be extended to multi-conductor lines in Chapter 5 and to lumped source excitation in Chapter 6.

Chapter 5

Elaboration of an enhanced TL model for field-to-transmission line interaction

5.1 Introduction

In this chapter, the asymptotic theory is extended to multiconductor lines [169]. We derive expressions for the current induced along a multiconductor line by an external plane wave, in which the effects of the terminals of the line are modelled by matrices of scattering and reflection coefficients. These coefficients are then computed analytically in the particular case of open boundaries or at low frequencies, and with numerical methods in the general case. The proposed theory is validated by simulations and experiments.

5.2 Solution of the MPIE for an infinite line

The mixed potential integral equations (MPIE) (equation (4.17)) presented in Chapter 4 are recalled here.

$$\frac{\partial}{\partial x}\varphi(x) + j\omega\frac{\mu_0}{4\pi}\int_{-\infty}^{\infty}\widehat{\mathbf{g}}(x-x')\mathbf{I}(x')dx' = \mathbf{E}_x^e(x) \quad (5.1)$$

$$\varphi(x) + \frac{1}{j\omega 4\pi\epsilon_0}\int_{-\infty}^{\infty}\widehat{\mathbf{g}}(x-x')\frac{\partial}{\partial x'}\mathbf{I}(x')dx' = \mathbf{0} \quad (5.2)$$

If the exciting field is a plane wave, the excitation is in the form $\mathbf{E}_x^e(x) = \mathbf{E}_x^e e^{-jk_x x}$ with $E_{x,n}^e = E_0 A e^{jk_y y_n} (e^{jk_z h_n} - e^{-jk_z h_n})$ as defined in Chapter 4. In order to solve (5.1) and (5.2), the solutions are assumed to be in the same form as the excitation [119]:

$$\begin{aligned} \mathbf{I}(x) &= \mathbf{I}_0 e^{-jk_x x} \\ \varphi(x) &= \varphi_0 e^{-jk_x x} \end{aligned} \quad (5.3)$$

Replacing the solution for the current in the integral of (5.1) leads to the following expression:

$$\int_{-\infty}^{\infty}\widehat{\mathbf{g}}(x-x')\mathbf{I}(x')dx' = \int_{-\infty}^{\infty}\widehat{\mathbf{g}}(\xi)e^{-jk_x \xi}d\xi \mathbf{I}_0 e^{-jk_x x} = \widehat{\mathbf{G}} \mathbf{I}_0 e^{-jk_x x} \quad (5.4)$$

where we used a change of variable $\xi = x' - x$ and the symmetry $\widehat{\mathbf{g}}(-\xi) = \widehat{\mathbf{g}}(\xi)$. The elements of the $\widehat{\mathbf{G}}$ matrix are defined in the following way:

$$G_{mn} := \int_{-\infty}^{\infty} g_{mn}(\xi) e^{-jk_x \xi} d\xi = \int_{-\infty}^{\infty} \frac{e^{-jk_x \xi} e^{-jk \sqrt{\xi^2 + d_{mn}^2}}}{\sqrt{\xi^2 + d_{mn}^2}} - \frac{e^{-jk_x \xi} e^{-jk \sqrt{\xi^2 + \tilde{d}_{mn}^2}}}{\sqrt{\xi^2 + \tilde{d}_{mn}^2}} d\xi \quad (5.5)$$

Let us express the first part of this integral by replacing complex exponential functions by sums of sine and cosine, according to Euler's formula.

$$\int_{-\infty}^{\infty} \frac{(\cos(k_x \xi) - j \sin(k_x \xi)) (\cos(k \sqrt{\xi^2 + d_{mn}^2}) - j \sin(k \sqrt{\xi^2 + d_{mn}^2}))}{\sqrt{\xi^2 + d_{mn}^2}} d\xi$$

Then, expanding the product, we obtain four terms.

$$\begin{aligned} \int_{-\infty}^{\infty} & \frac{\cos(k_x \xi) \cos(k \sqrt{\xi^2 + d_{mn}^2})}{\sqrt{\xi^2 + d_{mn}^2}} - \frac{j \cos(k_x \xi) \sin(k \sqrt{\xi^2 + d_{mn}^2})}{\sqrt{\xi^2 + d_{mn}^2}} \\ & - \frac{j \sin(k_x \xi) \cos(k \sqrt{\xi^2 + d_{mn}^2})}{\sqrt{\xi^2 + d_{mn}^2}} - \frac{\sin(k_x \xi) \sin(k \sqrt{\xi^2 + d_{mn}^2})}{\sqrt{\xi^2 + d_{mn}^2}} d\xi \end{aligned}$$

Since the integral of an odd function over a symmetric interval vanishes, the third and fourth terms in the previous integral are equal to zero. The remaining integrals are even and are evaluated between 0 and ∞ in [170], 2.5.25, expressions 15 and 9. Using these expressions leads to:

$$-\pi Y_0 \left(d_{mn} \sqrt{k^2 - k_x^2} \right) - j\pi J_0 \left(d_{mn} \sqrt{k^2 - k_x^2} \right)$$

This sum of Bessel functions can be expressed as a Hankel function (see [171], equation 9.1.4).

$$-j\pi \left\{ J_0 \left(d_{mn} \sqrt{k^2 - k_x^2} \right) - jY_0 \left(d_{mn} \sqrt{k^2 - k_x^2} \right) \right\} = -j\pi H_0^{(2)} \left(d_{mn} \sqrt{k^2 - k_x^2} \right) \quad (5.6)$$

The second part of the integral in (5.5) is computed by replacing d_{mn} by \tilde{d}_{mn} in (5.6). Hence, the explicit expression of the elements of $\widehat{\mathbf{G}}$ can be written as a difference of two Hankel functions (as for a monoconductor wire in [124], equation (3.22)).

$$G_{mn} = -j\pi \left\{ H_0^{(2)} \left(d_{mn} \sqrt{k^2 - k_x^2} \right) - H_0^{(2)} \left(\tilde{d}_{mn} \sqrt{k^2 - k_x^2} \right) \right\} \quad (5.7)$$

Injecting (5.3) and (5.4) into (5.1) and (5.2) leads after simplification to the following equations.

$$\begin{aligned} -jk_x \boldsymbol{\varphi}_0 + j\omega \frac{\mu_0}{4\pi} \widehat{\mathbf{G}} \mathbf{I}_0 &= \mathbf{E}_x^e \\ -jk_x \mathbf{I}_0 + j\omega 4\pi \varepsilon_0 \widehat{\mathbf{G}}^{-1} \boldsymbol{\varphi}_0 &= \mathbf{0} \end{aligned} \quad (5.8)$$

In order to make the link with the standard transmission line theory, it is possible to define generalised per-unit-length inductance and capacitance.

$$\begin{aligned} \widehat{\mathbf{L}}' &:= \frac{\mu_0}{4\pi} \widehat{\mathbf{G}} \\ \widehat{\mathbf{C}}' &:= 4\pi \varepsilon_0 \widehat{\mathbf{G}}^{-1} \end{aligned} \quad (5.9)$$

These generalised p.u.l. inductance and capacitance are complex valued and frequency dependent [151].

Expressions for \mathbf{I}_0 and $\boldsymbol{\varphi}_0$ are finally obtained by solving the linear system of equations (5.8).

$$\begin{aligned}\boldsymbol{\varphi}_0 &= \frac{k_x}{j(k^2 - k_x^2)} \mathbf{E}_x^e = \frac{\cos \psi \cos \phi}{jk(1 - \cos^2 \psi \cos^2 \phi)} \mathbf{E}_x^e \\ \mathbf{I}_0 &= \frac{\omega 4\pi \varepsilon_0}{j(k^2 - k_x^2)} \hat{\mathbf{G}}^{-1} \mathbf{E}_x^e = \frac{4\pi}{j\omega \mu_0 (1 - \cos^2 \psi \cos^2 \phi)} \hat{\mathbf{G}}^{-1} \mathbf{E}_x^e\end{aligned}\quad (5.10)$$

Interestingly, the expression for the potential on a wire depends only on its position, but not on its diameter or on the position of the other wires. Note also that the expression for the potential is gauge-dependent [151].

Grazing incidence or low-frequency

When $\phi, \psi \rightarrow 0$ with the field propagating in the same direction as the direction of the line ($k_x \rightarrow k$) or at low frequencies ($k \rightarrow 0$), one can apply in (5.7) the small-argument development of the Hankel function: $H_0^{(2)}(x \ll 1) \cong 1 - j\frac{2}{\pi} (\ln(\frac{x}{2}) + \gamma)$, where $\gamma = 0.5772\dots$ is the Euler's constant.

$$\begin{aligned}G_{mn} &\cong j\pi \left\{ +j\frac{2}{\pi} \left(\ln \left(\frac{d_{mn} \sqrt{k^2 - k_x^2}}{2} \right) + \gamma \right) - j\frac{2}{\pi} \left(\ln \left(\frac{\tilde{d}_{mn} \sqrt{k^2 - k_x^2}}{2} \right) + \gamma \right) \right\} = \\ &= 2 \ln \left(\frac{\tilde{d}_{mn}}{d_{mn}} \right)\end{aligned}\quad (5.11)$$

This result corresponds to equation (4.21). Introducing (5.11) into (5.9) provides the classical values for the p.u.l. parameters.

5.3 Semi-infinite line

To assess the effect of the line terminations, we will consider the same line configuration subjected to the same excitation field, but terminated at its left end in arbitrary impedances, while extending to $+\infty$ at the other end (see Figure 5.1). This line will be referred to as the right semi-infinite line. The line can be conceptually split up into two regions, as defined in [135] and reminded in Chapter 4: Region I corresponds to the region near the terminal, Region II corresponds to the region far from the terminal, and l_{bound} is the position of the separation between the two zones.

The current induced in the right semi-infinite line ($0 \leq x < \infty$) due to an external electromagnetic field can be written in the following manner:

$$\mathbf{I}_+^e(x) = \hat{\boldsymbol{\Psi}}_+^e(x) \mathbf{I}_0 \quad (5.12)$$

where \mathbf{I}_0 is defined in (5.10) and $\hat{\boldsymbol{\Psi}}_+^e(x)$ is an auxiliary function that can have a complex form in region I ($0 \leq z \leq l_{bound}$, see Figure 5.1) and can be replaced by its asymptotic development in region II.

$$\hat{\boldsymbol{\Psi}}_+^e(x) = \begin{cases} \text{exact solution,} & 0 \leq x \leq l_{bound} \quad (\text{region I}) \\ \hat{\mathbf{1}} e^{-jk_x x} + \hat{\mathbf{C}}_+ e^{-jk_x x}, & x \gg l_{bound} \quad (\text{region II}) \end{cases} \quad (5.13)$$

where $\hat{\mathbf{1}}$ is the unit matrix and $\hat{\mathbf{C}}_+$ is a matrix of scattering coefficients that depends on the termination of the line and the exciting field. This matrix characterises the effect of the line

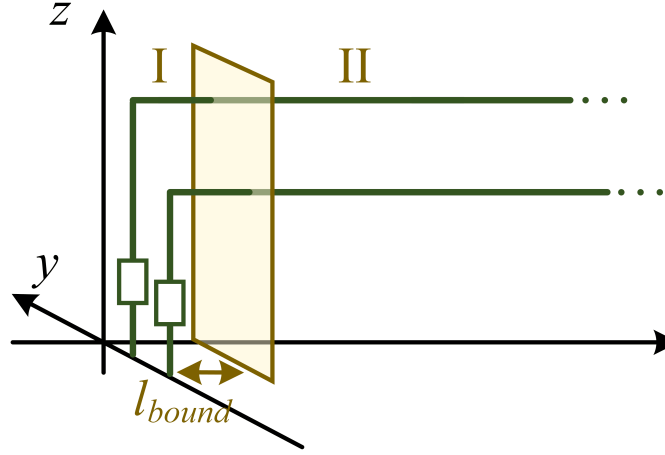


Figure 5.1: Right semi-infinite line and the two regions I and II.

terminals on the current directly induced in the horizontal part of the wire by the plane wave. The response due to a hypothetical current $\tilde{\mathbf{I}}_1 e^{jkx}$ is in the same form as the response due to a plane wave excitation:

$$\mathbf{I}_+^0(x) = \hat{\Psi}_+^0(x) \tilde{\mathbf{I}}_1 \quad (5.14)$$

where

$$\hat{\Psi}_+^0(x) = \begin{cases} \text{exact solution,} & 0 \leq x \leq l_{\text{bound}} \quad (\text{region I}) \\ \hat{\mathbf{1}} e^{jkx} + \hat{\mathbf{R}}_+ e^{-jkx}, & x \gg l_{\text{bound}} \quad (\text{region II}) \end{cases} \quad (5.15)$$

where $\hat{\mathbf{R}}_+$ is a matrix of reflection coefficients. At low frequencies, it corresponds to the matrix of reflection coefficients for the currents defined in the classical multiconductor transmission line theory. Hence, in case of an MTL connected to loads linking each conductor to the ground (i.e. without any differential loads), this matrix will in fact be diagonal, at low frequencies. The complete response is the sum of the forced and the free responses:

$$\mathbf{I}_+(z) = \hat{\Psi}_+^e(x) \mathbf{I}_0 + \hat{\Psi}_+^0(x) \tilde{\mathbf{I}}_1 \quad (5.16)$$

Replacing (5.13) and (5.15) in (5.16) in region II leads to the following expression:

$$\mathbf{I}_+(x) = \left(\hat{\mathbf{1}} e^{-jk_x x} + \hat{\mathbf{C}}_+ e^{-jkx} \right) \mathbf{I}_0 + \left(\hat{\mathbf{1}} e^{jkx} + \hat{\mathbf{R}}_+ e^{-jkx} \right) \tilde{\mathbf{I}}_1 \quad (5.17)$$

Similar developments can be done considering a left semi-infinite line (terminated on its right end and extending to $-\infty$, Figure 5.2), replacing the subscripts '+' by '-' and k by $-k$. The response for a left-semi-infinite line ($-\infty < x \leq L$) excited by the same plane wave and simultaneously by a current $\tilde{\mathbf{I}}_2$ is thus given by (5.18). Note that a shift by L was introduced, corresponding to the fact that, in this case, the line extremity is not at $x = 0$ but at $x = L$. The reason for this choice will become apparent in the next section.

$$\mathbf{I}_-(x) = \hat{\Psi}_-^e(x - L) \mathbf{I}_0 e^{-jk_x L} + \hat{\Psi}_-^0(x - L) \tilde{\mathbf{I}}_2 \quad (5.18)$$

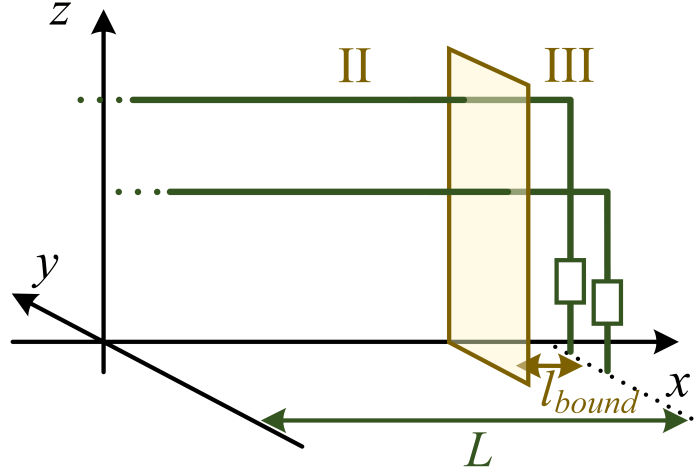


Figure 5.2: Left semi-infinite line and the two regions II and III.

With the associated $\hat{\Psi}$ functions in region II:

$$\begin{aligned}\hat{\Psi}_-^e(x) &= \hat{\mathbf{1}}e^{-jk_x x} + \hat{\mathbf{C}}_-e^{jk_x x}, \quad x \ll -l_{\text{bound}} \\ \hat{\Psi}_-^0(x) &= \hat{\mathbf{1}}e^{-jk_x x} + \hat{\mathbf{R}}_-e^{jk_x x}, \quad x \ll -l_{\text{bound}}\end{aligned}\quad (5.19)$$

where $\hat{\mathbf{C}}_-$ and $\hat{\mathbf{R}}_-$ are, respectively, the scattering and reflection matrices associated with the right terminal. Replacing (5.19) into (5.18) in the region II leads to the following expression:

$$\mathbf{I}_-(x) = \left(\hat{\mathbf{1}}e^{-jk_x(x-L)} + \hat{\mathbf{C}}_-e^{jk(x-L)} \right) \mathbf{I}_0e^{-jk_x L} + \left(\hat{\mathbf{1}}e^{-jk(x-L)} + \hat{\mathbf{R}}_-e^{jk(x-L)} \right) \tilde{\mathbf{I}}_2 \quad (5.20)$$

5.4 Finite-length line

In this section, a finite line (see Figure 5.3) is built up as the association of the right and the left semi-infinite lines presented in the previous section.

Let us focus on Region II, far from the two terminals. First, the expressions for the currents (5.17) and (5.20) in the two semi-infinite lines are re-arranged in order to display the propagating modes.

$$\mathbf{I}_+(x) = \mathbf{I}_0e^{-jk_x x} + \tilde{\mathbf{I}}_1e^{jk_x x} + \left(\hat{\mathbf{C}}_+\mathbf{I}_0 + \hat{\mathbf{R}}_+\tilde{\mathbf{I}}_1 \right) e^{-jk_x x} \quad (5.21)$$

$$\mathbf{I}_-(x) = \mathbf{I}_0e^{jk_x x} + \left(\hat{\mathbf{C}}_-\mathbf{I}_0e^{-j(k+k_x)L} + \hat{\mathbf{R}}_-\tilde{\mathbf{I}}_2e^{-jkL} \right) e^{jk_x x} + \tilde{\mathbf{I}}_2e^{jkL}e^{-jk_x x} \quad (5.22)$$

Imposing that the solution in the asymptotic region be the same in the two semi-infinite lines, that is (5.21) = (5.22) in region II leads to:

$$\mathbf{I}(x) = \mathbf{I}_+(x) = \mathbf{I}_-(x) = \mathbf{I}_0e^{-jk_x x} + \mathbf{I}_1e^{jk_x x} + \mathbf{I}_2e^{-jk_x x} \quad (5.23)$$

with

$$\begin{aligned}\mathbf{I}_1 &= \tilde{\mathbf{I}}_1 = \hat{\mathbf{C}}_-\mathbf{I}_0e^{-j(k+k_x)L} + \hat{\mathbf{R}}_-\tilde{\mathbf{I}}_2e^{-jkL} \\ \mathbf{I}_2 &= \tilde{\mathbf{I}}_2e^{jkL} = \hat{\mathbf{C}}_+\mathbf{I}_0 + \hat{\mathbf{R}}_+\tilde{\mathbf{I}}_1\end{aligned}\quad (5.24)$$

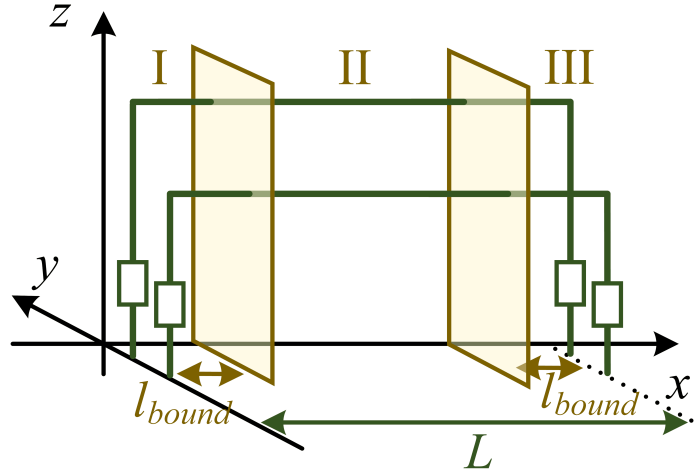


Figure 5.3: Finite-length, loaded multiconductor line excited by a high frequency plane wave. Decomposition into zones.

When putting the two semi-infinite lines together, the usefulness of $\tilde{\mathbf{I}}_1$ and $\tilde{\mathbf{I}}_2$ becomes clear; these terms are associated with the currents produced by the opposite terminal. In (5.23), $\mathbf{I}_0 e^{-jk_x x}$ corresponds to the current that would flow in an infinite line with the same cross section; an expression for \mathbf{I}_0 is given by (5.10). $\mathbf{I}_1 e^{jk_x x}$ and $\mathbf{I}_2 e^{-jk_x x}$ are TEM respectively backward and forward propagating waves due to the presence of the terminals. Their expression is given by solving the linear system of equations (5.24).

$$\begin{aligned} \mathbf{I}_1 &= \left(\hat{\mathbf{1}} - \hat{\mathbf{R}}_- \hat{\mathbf{R}}_+ e^{-2jkL} \right)^{-1} \left(\hat{\mathbf{C}}_- e^{-j(k+k_x)L} + \hat{\mathbf{R}}_- \hat{\mathbf{C}}_+ e^{-2jkL} \right) \mathbf{I}_0 \\ \mathbf{I}_2 &= \left(\hat{\mathbf{1}} - \hat{\mathbf{R}}_+ \hat{\mathbf{R}}_- e^{-2jkL} \right)^{-1} \left(\hat{\mathbf{C}}_+ + \hat{\mathbf{R}}_+ \hat{\mathbf{C}}_- e^{-j(k+k_x)L} \right) \mathbf{I}_0 \end{aligned} \quad (5.25)$$

The goal of the next sections is to provide values for the matrices of scattering and reflection coefficients.

5.5 Analytical expressions for the scattering and reflection coefficients: iterative method

The goal of this section is to obtain analytical expressions for the reflection coefficient matrices $\hat{\mathbf{C}}_+$, $\hat{\mathbf{C}}_-$, $\hat{\mathbf{R}}_+$ and $\hat{\mathbf{R}}_-$, in the case of a multiconductor transmission line that is open-circuited at its two terminals. To this purpose, we use an iterative method based on perturbation theory, with reference to [135].

5.5.1 Reformulating the MPIE equations in an appropriate form

First of all, the MPIE equations (5.1) and (5.2) are written in the same form as the standard TL equations, but with additional “correction” terms. In order to do so, the property of the derivative of a product of functions $f(x)$ and $g(x)$, i.e. $f(x) \frac{d}{dx} h(x) = \frac{d}{dx} (f(x)h(x)) - h(x) \frac{d}{dx} f(x)$, is applied

to (5.2):

$$\int_0^L \frac{\partial}{\partial x'} (\hat{\mathbf{g}}(x - x') \cdot \mathbf{I}(x')) dx' - \int_0^L \frac{\partial \hat{\mathbf{g}}(x - x')}{\partial x'} \cdot \mathbf{I}(x') dx' + j\omega 4\pi\epsilon_0 \phi(x) = \mathbf{0} \quad (5.26)$$

The first term of (5.26) can be integrated in a trivial way. For the second term, we use the fact that $\frac{\partial}{\partial x'}(x - x') = -\frac{\partial}{\partial x}(x - x') = -1$, which can be applied in particular to the argument of the Green's function.

$$\frac{\partial}{\partial x'} \hat{\mathbf{g}}(x - x') = -\frac{\partial}{\partial x} \hat{\mathbf{g}}(x - x') \quad (5.27)$$

Hence (5.26) becomes

$$\hat{\mathbf{g}}(x - L) \cdot \mathbf{I}(L) - \hat{\mathbf{g}}(x - 0) \cdot \mathbf{I}(0) + \int_0^L \frac{\partial}{\partial x} \hat{\mathbf{g}}(x - x') \cdot \mathbf{I}(x') dx' + j\omega 4\pi\epsilon_0 \phi(x) = \mathbf{0} \quad (5.28)$$

As the line is open-circuited at both extremities, the boundary conditions reads:

$$\mathbf{I}(0) = \mathbf{0} \quad (5.29)$$

$$\mathbf{I}(L) = \mathbf{0} \quad (5.30)$$

so we finally find:

$$\frac{\partial}{\partial x} \phi(x) + j\omega \frac{\mu_0}{4\pi} \int_0^L \hat{\mathbf{g}}(x - x') \cdot \mathbf{I}(x') dx' = \mathbf{E}_x^e \quad (5.31)$$

$$\frac{\partial}{\partial x} \int_0^L \hat{\mathbf{g}}(x - x') \cdot \mathbf{I}(x') dx' + j\omega 4\pi\epsilon_0 \phi(x) = \mathbf{0} \quad (5.32)$$

where (5.31) was rewritten and is the same as (5.1). Note that this procedure is also valid if the line is infinite or semi-infinite ($L \rightarrow \infty$), because $\lim_{\xi \rightarrow \infty} \hat{\mathbf{g}}(x - \xi) = \hat{\mathbf{0}}$ for an arbitrary but finite x . This also applies asymptotically to a long but finite line with arbitrary terminals, when considering a position very far from a terminal or a discontinuity of the line.

Let us re-write equations (5.31) and (5.32) adding the same terms at both sides of the equations:

$$\begin{aligned} \frac{\partial}{\partial x} \phi(x) + j\omega \hat{\mathbf{L}}'_0 \mathbf{I}(x) &= \mathbf{E}_x^e + j\omega \hat{\mathbf{L}}'_0 \mathbf{I}(x) - j\omega \frac{\mu_0}{4\pi} \int_0^L \hat{\mathbf{g}}(x - x') \cdot \mathbf{I}(x') dx' \\ \frac{\partial}{\partial x} \mathbf{I}(x) + j\omega \hat{\mathbf{C}}'_0 \phi(x) &= \frac{\partial}{\partial x} \mathbf{I}(x) - \hat{\mathbf{G}}^{TL-1} \frac{\partial}{\partial x} \int_0^L \hat{\mathbf{g}}(x - x') \cdot \mathbf{I}(x') dx' \end{aligned} \quad (5.33)$$

using the p.u.l. inductance and capacitance given by the classical transmission line theory (equation (4.23)). (5.33) can be written in a more compact way.

$$\begin{aligned} \frac{\partial}{\partial x} \phi(x) + j\omega \hat{\mathbf{L}}'_0 \mathbf{I}(x) &= \mathbf{E}_x^e + j\omega \hat{\mathbf{L}}'_0 \mathbf{F}\{\mathbf{I}(x)\} \\ \frac{\partial}{\partial x} \mathbf{I}(x) + j\omega \hat{\mathbf{C}}'_0 \phi(x) &= \frac{\partial}{\partial x} \mathbf{F}\{\mathbf{I}(x)\} \end{aligned} \quad (5.34)$$

where the operator \mathbf{F} applies on a current and is defined as follows:

$$\mathbf{F}\{\mathbf{I}(x)\} = \mathbf{I}(x) - \hat{\mathbf{G}}^{TL-1} \int_0^L \hat{\mathbf{g}}(x - x') \cdot \mathbf{I}(x') dx' \quad (5.35)$$

Equations (5.34) have the same form as the standard TL equations, but with additional correction terms. At low frequencies, these additional terms vanish and (5.34) reduces to the classical TL equations.

The system of equations (5.34) could also be written as follows.

$$\begin{aligned} \frac{\partial}{\partial x} \phi(x) + j\omega \hat{\mathbf{L}}_0' (\mathbf{I}(x) - \mathbf{F}\{\mathbf{I}(x)\}) &= \mathbf{E}_x^e \\ \frac{\partial}{\partial x} (\mathbf{I}(x) - \mathbf{F}\{\mathbf{I}(x)\}) + j\omega \hat{\mathbf{C}}_0' \phi(x) &= 0 \end{aligned} \quad (5.36)$$

With this notation, it is clarified that $\mathbf{I}(x) - \mathbf{F}\{\mathbf{I}(x)\}$ is equal to the TL approximation solution. Hence $\mathbf{F}\{\mathbf{I}(x)\}$ can be considered as a correction term to add to the TL current in order to find the ‘exact’ current. The correction term does not apply on $\phi(x)$ which is hence equal to the scattered voltage given by the transmission line theory.

5.5.2 Iterative expressions

Using the iterative method based on using the perturbation theory, as presented for a monoconductor wire in [1, 134, 135], we would like to obtain a solution in the form:

$$\begin{aligned} \mathbf{I}(x) &= \mathbf{I}_{(0)}(x) + \mathbf{I}_{(1)}(x) + \mathbf{I}_{(2)}(x) + \dots \\ \varphi(x) &= \varphi_{(0)}(x) + \varphi_{(1)}(x) + \varphi_{(2)}(x) + \dots \end{aligned} \quad (5.37)$$

Here, only the first order result, that is the two first terms, will be considered in order to obtain a good approximation of the reflection coefficients.

The zeroth iteration term is given by the solution of the equation when the perturbation term vanishes, that is to say when $\mathbf{F}\{\mathbf{I}(x)\} = \mathbf{0}$ in (5.34). It is hence the solution provided by the classical TL theory. The following iterations are based on (5.35) and (5.2) and are given by the perturbation theory.

$$\begin{aligned} \frac{\partial}{\partial x} \phi_{(n)}(x) + j\omega \hat{\mathbf{L}}_0' \mathbf{I}_{(n)}(x) &= j\omega \hat{\mathbf{L}}_0' \mathbf{F}\{\mathbf{I}_{(n-1)}(x)\} \\ \frac{\partial}{\partial x} \mathbf{I}_{(n)}(x) + j\omega \hat{\mathbf{C}}_0' \phi_{(n)}(x) &= \frac{\partial}{\partial x} \mathbf{F}\{\mathbf{I}_{(n-1)}(x)\} \end{aligned} \quad (5.38)$$

Decoupling the current from the potential in (5.38) leads to a Helmholtz equation:

$$\left(\frac{d^2}{dx^2} + k^2 \right) (\mathbf{I}_n(x) - \mathbf{F}\{\mathbf{I}_{(n-1)}(x)\}) = 0 \quad (5.39)$$

Imaginary exponential functions are known to be solutions of this kind of equations (e.g. [172]):

$$\mathbf{I}_{(n)}(x) - \mathbf{F}\{\mathbf{I}_{(n-1)}(x)\} = \mathbf{D}_1 e^{-jkx} + \mathbf{D}_2 e^{+jkx} \quad (5.40)$$

where the coefficients \mathbf{D}_1 and \mathbf{D}_2 can be computed by the application of the appropriate boundary conditions.

5.5.3 Analytical expression for the reflection coefficient matrices $\hat{\mathbf{C}}_+$ and $\hat{\mathbf{C}}_-$

In order to obtain the expressions for the reflection coefficients, we will consider a right semi-infinite line. Expressions obtained previously are still valid when pushing the right terminal to infinity, i.e.

$L \rightarrow \infty$. The current inside the line, far from the left terminal, can be written as follows:

$$\mathbf{I}_+^e(x) = \left(\hat{\mathbf{I}}e^{-jk_x x} + \hat{\mathbf{C}}_+e^{-jkx} \right) \cdot \mathbf{I}_0 = \mathbf{I}_0e^{-jk_x x} + \hat{\mathbf{C}}_+\mathbf{I}_0e^{-jkx} \quad (5.41)$$

Zeroth iteration: TL approximation

The equation for the zeroth iteration is equal to (5.39) without the correction term \mathbf{F} .

$$\left(\frac{d^2}{dx^2} + k^2 \right) \mathbf{I}_{+(0)}^e(x) = -j\omega \hat{\mathbf{C}}_0' \mathbf{E}_x^e(x) \quad (5.42)$$

First, we search for a response that has the same structure as the excitation.

$$\mathbf{I}_f^e(x) = \mathbf{I}_0^{TL} e^{-jk_x x} \quad (5.43)$$

The application of this solution into equation (5.42) leads after simplification to

$$\mathbf{I}_0^{TL} = \frac{4\pi}{j\omega\mu_0(1 - \cos^2\psi \cos^2\phi)} \hat{\mathbf{G}}^{TL-1} \mathbf{E}_x^e \quad (5.44)$$

This solution is essentially the same as (5.10) when replacing $\hat{\mathbf{G}}$ by $\hat{\mathbf{G}}^{TL}$. To find the solution for a right semi-infinite line, we will also consider a solution of equation (5.42) with no excitation:

$$\mathbf{I}_l^e(x) = \mathbf{D}_1 e^{+jkx} + \mathbf{D}_2 e^{-jkx} \quad (5.45)$$

As there is no lumped source on the line, there is no backward propagating wave, i.e. $\mathbf{D}_1 = \mathbf{0}$. The total solution is the sum of the two solutions:

$$\mathbf{I}_{+(0)}^e(x) = \mathbf{I}_f^e(x) + \mathbf{I}_l^e(x) = \mathbf{I}_0^{TL} e^{-jk_x x} + \mathbf{D}_2 e^{-jkx} \quad (5.46)$$

The expression for \mathbf{D}_2 is obtained by the application of the boundary condition $\mathbf{I}_{+(0)}^e(0) = \mathbf{0}$.

$$\mathbf{D}_2 = -\mathbf{I}_0^{TL} \quad (5.47)$$

The zeroth iteration term is finally:

$$\mathbf{I}_{+(0)}^e(x) = \left(e^{-jk_x x} - e^{-jkx} \right) \mathbf{I}_0^{TL} \quad (5.48)$$

and the associated scattering coefficient is $\hat{\mathbf{C}}_{+(0)} = -\hat{\mathbf{I}}$.

First iteration

We have to consider equation (5.39) and its solution (5.40) in the case of a right semi-infinite line, that is to say only with boundary condition (5.29). To obtain a third equation, we consider that the line is lossy, with the losses tending to zero. Hence \mathbf{D}_2 must vanish, to avoid a divergence ($e^{(\delta+jk)x} \rightarrow \infty$ when $x \rightarrow \infty$). In this case, the constants are:

$$\begin{aligned} \mathbf{D}_1 &= -\mathbf{F}\{\mathbf{I}_{(n-1)}(x)\}|_{x=0} \\ \mathbf{D}_2 &= \mathbf{0} \end{aligned} \quad (5.49)$$

and the current can be written as follows:

$$\mathbf{I}_{+(n)}^e(x) = \mathbf{F}\{\mathbf{I}_{+(n-1)}^e(x)\} - \mathbf{F}\{\mathbf{I}_{+(n-1)}^e(x)\}|_{x=0} e^{-jkx} \quad (5.50)$$

When $n = 1$, and with $L \rightarrow \infty$, because the line is considered to be semi-infinite, expression (5.35) is as follows:

$$\mathbf{F}\{\mathbf{I}_{+(0)}^e(x)\} = \mathbf{I}_0^{TL}(e^{-jk_x x} - e^{-jkx}) - \hat{\mathbf{G}}^{TL-1} \int_0^\infty \hat{\mathbf{g}}(x-x')(e^{-jk_x x'} - e^{-jkx'}) dx' \cdot \mathbf{I}_0^{TL} \quad (5.51)$$

In particular, the value of this function for $x = 0$ is the following:

$$\mathbf{F}\{\mathbf{I}_{(0)}^e(x)\}|_{x=0} = -\hat{\mathbf{D}}_1 \cdot \mathbf{I}_0^{TL} \quad (5.52)$$

where $\hat{\mathbf{D}}_1$ is defined as following:

$$\hat{\mathbf{D}}_1 := \hat{\mathbf{G}}^{TL-1} \int_0^\infty \hat{\mathbf{g}}(x')(e^{-jk_x x'} - e^{-jkx'}) dx' \quad (5.53)$$

Let us now compute the value of the function $\mathbf{F}\{\mathbf{I}_{+(0)}^e(x)\}$ for a very large x .

$$\begin{aligned} \mathbf{F}\{\mathbf{I}_{+(0)}^e(x)\}|_{x \rightarrow \infty} &= \lim_{x \rightarrow \infty} \left\{ (e^{-jk_x x} - e^{-jkx}) \mathbf{I}_0^{TL} \right. \\ &\quad \left. - \hat{\mathbf{G}}^{TL-1} \int_0^\infty \hat{\mathbf{g}}(x-x')(e^{-jk_x x'} - e^{-jkx'}) \mathbf{I}_0^{TL} dx' \right\} \\ &= \lim_{x \rightarrow \infty} \left\{ \hat{\mathbf{I}}(e^{-jk_x x} - e^{-jkx}) - \hat{\mathbf{G}}^{TL-1} \left(\hat{\mathbf{G}} e^{-jk_x x} - \hat{\mathbf{G}}^{TL} e^{-jkx} \right) \right\} \mathbf{I}_0^{TL} \\ &= \hat{\mathbf{D}}_2 \cdot \mathbf{I}_0^{TL} e^{-jk_x x}, \quad x \rightarrow \infty \end{aligned} \quad (5.54)$$

where $\hat{\mathbf{D}}_2$ was defined as follows.

$$\hat{\mathbf{D}}_2 := \hat{\mathbf{I}} - \hat{\mathbf{G}}^{TL-1} \hat{\mathbf{G}} \quad (5.55)$$

Replacing (5.52) and (5.54) into (5.50)

$$\begin{aligned} \mathbf{I}_{+(1)}^e(x \rightarrow \infty) &= \mathbf{F}\{\mathbf{I}_{+(0)}^e(x)\}|_{x \rightarrow \infty} - \mathbf{F}\{\mathbf{I}_{+(0)}^e(x)\}|_{x=0} e^{-jkx} = \\ &= \hat{\mathbf{D}}_2 \cdot \mathbf{I}_0^{TL} e^{-jk_x x} + \hat{\mathbf{D}}_1 \cdot \mathbf{I}_0^{TL} e^{-jkx} \end{aligned} \quad (5.56)$$

Considering the sum of the zeroth and the first iteration as an approximation of the current:

$$\begin{aligned} \mathbf{I}_+^e(x) &\cong \mathbf{I}_{+(0)}^e(x) + \mathbf{I}_{+(1)}^e(x) = \\ &= (e^{-jk_x x} - e^{-jkx}) \mathbf{I}_0^{TL} + \hat{\mathbf{D}}_2 \cdot \mathbf{I}_0^{TL} e^{-jk_x x} + \hat{\mathbf{D}}_1 \cdot \mathbf{I}_0^{TL} e^{-jkx} = \\ &= \left[(\hat{\mathbf{I}} + \hat{\mathbf{D}}_2) e^{-jk_x x} + (-\hat{\mathbf{I}} + \hat{\mathbf{D}}_1) e^{-jkx} \right] \cdot \mathbf{I}_0^{TL} = \\ &= \left[\hat{\mathbf{I}} e^{-jk_x x} + (-\hat{\mathbf{I}} + \hat{\mathbf{D}}_1) (\hat{\mathbf{I}} + \hat{\mathbf{D}}_2)^{-1} e^{-jkx} \right] \cdot (\hat{\mathbf{I}} + \hat{\mathbf{D}}_2) \cdot \mathbf{I}_0^{TL} \end{aligned} \quad (5.57)$$

If we use the two first terms of the Taylor series $(1+x)^{-1} = 1-x+\dots$, and neglect the upper order terms ($\hat{\mathbf{D}}_1, \hat{\mathbf{D}}_2 \ll 1 \Rightarrow \hat{\mathbf{D}}_1 \cdot \hat{\mathbf{D}}_2 \lll 1$), we obtain the following result.

$$(-\hat{\mathbf{I}} + \hat{\mathbf{D}}_1) (\hat{\mathbf{I}} + \hat{\mathbf{D}}_2)^{-1} \cong (-\hat{\mathbf{I}} + \hat{\mathbf{D}}_1) (\hat{\mathbf{I}} - \hat{\mathbf{D}}_2) \cong -\hat{\mathbf{I}} + \hat{\mathbf{D}}_1 + \hat{\mathbf{D}}_2 - \dots \quad (5.58)$$

hence

$$\mathbf{I}_+^e \cong \left[\widehat{\mathbf{I}} e^{-jk_x x} + \left(-\widehat{\mathbf{I}} + \widehat{\mathbf{D}}_1 + \widehat{\mathbf{D}}_2 \right) e^{-jk_x x} \right] \cdot \left(\widehat{\mathbf{I}} + \widehat{\mathbf{D}}_2 \right) \cdot \mathbf{I}_0^{TL} \quad (5.59)$$

Besides, comparing (5.10) with (5.44) allows to make the following connection:

$$\mathbf{I}_0^{TL} = \widehat{\mathbf{G}}^{TL-1} \widehat{\mathbf{G}} \mathbf{I}_0 \quad (5.60)$$

Introducing (5.55) into (5.60) leads to the following expression:

$$\mathbf{I}_0^{TL} = \left(\widehat{\mathbf{I}} - \widehat{\mathbf{D}}_2 \right) \mathbf{I}_0 \quad (5.61)$$

Using the fact that $\widehat{\mathbf{D}}_2 \ll 1$ and considering the first terms of the Taylor series $(1-x)^{-1} = 1+x+\dots$ allows to express \mathbf{I}_0 as a function of \mathbf{I}_0^{TL} .

$$\mathbf{I}_0 \cong \left(\widehat{\mathbf{I}} - \widehat{\mathbf{D}}_2 \right)^{-1} \mathbf{I}_0^{TL} \cong \left(\widehat{\mathbf{I}} + \widehat{\mathbf{D}}_2 \right) \mathbf{I}_0^{TL} \quad (5.62)$$

Introducing (5.62) into (5.59) leads to

$$\mathbf{I}_+^e(x) \cong \left[\widehat{\mathbf{I}} e^{-jk_x x} + \left(-\widehat{\mathbf{I}} + \widehat{\mathbf{D}}_1 + \widehat{\mathbf{D}}_2 \right) e^{-jk_x x} \right] \cdot \mathbf{I}_0 \quad (5.63)$$

The coefficient $\widehat{\mathbf{C}}_+$ is obtained by identification of equations (5.41) and (5.63):

$$\widehat{\mathbf{C}}_+ \cong -\widehat{\mathbf{I}} + \widehat{\mathbf{D}}_1 + \widehat{\mathbf{D}}_2 \quad (5.64)$$

$\widehat{\mathbf{C}}_-$ can be computed in a similar way, using a left semi-infinite line, or simply replacing k_x by $-k_x$.

5.5.4 Analytical expression for the reflection coefficient matrices $\widehat{\mathbf{R}}_+$ and $\widehat{\mathbf{R}}_-$

In this section, the expressions for the coefficient matrices $\widehat{\mathbf{R}}_+$ and $\widehat{\mathbf{R}}_-$, are computed according to the development made for a single-conductor line in [1], Section 4.2.4.

In order to compute $\widehat{\mathbf{R}}_+$, we consider a line which extends to infinity into the right direction and which is terminated into an open circuit at $x = 0$. An arbitrary current $\tilde{\mathbf{I}} e^{jk_x x}$ is incoming from the right. Due to this incident current, the left terminal of the line generates a reflected wave. For an observer located far from the boundary, i.e. mathematically for $x \rightarrow \infty$ and physically for $x \gg l_{bound}$, the reflected current can be written as the product of a reflection coefficient matrix and the incident current with reverse direction of propagation: $\widehat{\mathbf{R}}_+ \cdot \tilde{\mathbf{I}} e^{-jk_x x}$. Consequently, the total current is the sum of these two terms.

$$\mathbf{I}_+^0(x) = \left(\widehat{\mathbf{I}} e^{jk_x x} + \widehat{\mathbf{R}}_+ e^{-jk_x x} \right) \cdot \tilde{\mathbf{I}} \quad x \gg l_{bound} \quad (5.65)$$

As for the scattering coefficient, the reflection coefficient is written as a sum of terms based on the perturbation theory:

$$\widehat{\mathbf{R}}_+ = \widehat{\mathbf{R}}_{+(0)} + \widehat{\mathbf{R}}_{+(1)} + \dots \quad (5.66)$$

Again, we will only consider the two first terms, assuming that they provide sufficient accuracy. The zeroth iteration term is given by the TL theory. In this case, the matrix of reflection coefficients for the voltage, with a load impedance tending toward infinity, is the unit matrix [115].

$$\widehat{\mathbf{I}}_L = (\widehat{\mathbf{Z}}_L - \widehat{\mathbf{Z}}_C)(\widehat{\mathbf{Z}}_L + \widehat{\mathbf{Z}}_C)^{-1} \underset{\widehat{\mathbf{Z}}_L \rightarrow \infty}{=} \widehat{\mathbf{I}} \quad (5.67)$$

The reflection matrix for the current is minus the one for the voltage.

$$\widehat{\mathbf{R}}_{+(0)} = -\widehat{\mathbf{I}}_L = -\widehat{\mathbf{I}} \quad (5.68)$$

Hence inserting (5.68) into (5.65), the zero-iteration term reads:

$$\mathbf{I}_{+(0)}^0(x) = \left(e^{jkx} - e^{-jkx} \right) \tilde{\mathbf{I}} \quad (5.69)$$

In the same manner as for the scattering coefficient in (5.50), the first iteration term is given by the following expression.

$$\mathbf{I}_{+(1)}^0(x \rightarrow \infty) = \mathbf{F} \{ \mathbf{I}_{+(0)}^0(x) \} |_{x \rightarrow \infty} - \mathbf{F} \{ \mathbf{I}_{+(0)}^0(x) \} |_{x=0} e^{-jkx} \quad (5.70)$$

$\mathbf{F}_{(0)} \{ \mathbf{I}_{+}^0(x) \}$ vanishes for large arguments.

$$\lim_{x \rightarrow \infty} \mathbf{F}_{(0)} \{ \mathbf{I}_{+}^0(x) \} = \lim_{x \rightarrow \infty} \left(\mathbf{I}_{+(0)}^0(x) - \widehat{\mathbf{G}}^{TL-1} \cdot \widehat{\mathbf{G}}^{TL} \cdot \mathbf{I}_{+(0)}^0(x) \right) = 0 \quad (5.71)$$

Hence

$$\mathbf{I}_{+(1)}(x \rightarrow \infty) = -\mathbf{F} \left\{ \mathbf{I}_{+(0)}^0(x) \right\} \Big|_{x=0} e^{-jkx} = \widehat{\mathbf{R}}_{+(1)} \cdot \tilde{\mathbf{I}} e^{-jkx} \quad (5.72)$$

where the second equality is obtained by the subtraction of (5.65) – (5.69).

An approximation of the reflection coefficient is given by the first two iteration terms:

$$\widehat{\mathbf{R}}_{+} \cong \widehat{\mathbf{R}}_{+(0)} + \widehat{\mathbf{R}}_{+(1)} \quad (5.73)$$

Using equations (5.68), (5.69), (5.72) and (5.35) leads to the following expression:

$$\begin{aligned} \widehat{\mathbf{R}}_{+} &\cong -\widehat{\mathbf{I}} - \mathbf{I}_{+(0)}^0(0) + \widehat{\mathbf{G}}^{TL-1} \int_0^\infty \widehat{\mathbf{g}}(x') \cdot \mathbf{I}_{+(0)}^0(x') dx' \cdot \tilde{\mathbf{I}}^{-1} = \\ &= -\widehat{\mathbf{I}} + \widehat{\mathbf{G}}^{TL-1} \int_0^\infty \widehat{\mathbf{g}}(x') \cdot \left(e^{jkx'} - e^{-jkx'} \right) dx' \end{aligned} \quad (5.74)$$

To perform the integration, the matrix of Green's functions is considered term by term:

$$\begin{aligned} \left(\widehat{\mathbf{G}}^{TL} \cdot \left(\widehat{\mathbf{R}}_{+} + \widehat{\mathbf{I}} \right) \right)_{m,n} &\cong \int_0^\infty g_{m,n}(x') \left(e^{jkx'} - e^{-jkx'} \right) dx' = \\ &= \int_0^\infty \frac{e^{-jk(-x' + \sqrt{x'^2 + d_{mn}^2})}}{\sqrt{x'^2 + d_{mn}^2}} - \frac{e^{-jk(-x' + \sqrt{x'^2 + \tilde{d}_{mn}^2})}}{\sqrt{x'^2 + \tilde{d}_{mn}^2}} \\ &\quad - \frac{e^{-jk(x' + \sqrt{x'^2 + d_{mn}^2})}}{\sqrt{x'^2 + d_{mn}^2}} + \frac{e^{-jk(x' + \sqrt{x'^2 + \tilde{d}_{mn}^2})}}{\sqrt{x'^2 + \tilde{d}_{mn}^2}} dx' = \\ &= 2 \int_{kd_{mn}}^{k\tilde{d}_{mn}} \frac{1 - e^{-j\xi}}{\xi} d\xi = \\ &= 2 \left(\ln(k\tilde{d}_{mn}) + E_1(jk\tilde{d}_{mn}) - \ln(kd_{mn}) - E_1(jkd_{mn}) \right) \end{aligned} \quad (5.75)$$

where different changes of variable in the form of $\xi = k(\pm x' + \sqrt{x'^2 + d_{mn}^2})$ were applied and where $E_1(z)$ is the exponential integral.

A similar development with a left semi-infinite line would lead to the reflection coefficient $\widehat{\mathbf{R}}_{-}$. However, as the two boundaries are assumed to be the same, the associated reflection coefficients

at the left and at the right are simply the same, that is to say $\widehat{\mathbf{R}}_- = \widehat{\mathbf{R}}_+$.

Single-conductor line

In the case of a single conductor line, \tilde{d}_{mn} is equal to twice the height of the conductor above the ground and d_{mn} is equal to its radius. Hence the reflection coefficient (5.75) can be expressed as the following scalar number:

$$R_+ \cong -1 + \frac{1}{2 \ln(2h/a)} 2(\ln(2kh) + E_1(j2kh) - \ln(ka) - E_1(jka)) \quad (5.76)$$

Considering that $a \ll 2h$, it is possible to replace the second exponential integral in (5.76) by the first terms of its series representation:

$$E_1(jx) \cong -\gamma - \ln(x) - j\frac{\pi}{2} + \dots \quad (5.77)$$

where $\gamma = 0.5772\dots$ is the Euler's constant. This procedure is equivalent to taking the limit $a \rightarrow 0$, and it is valid here if $a \ll 2h$. Hence the reflection coefficient becomes:

$$R_+ \cong -1 + \frac{1}{\ln(2h/a)} \left(\ln(2kh) + E_1(j2kh) + \gamma + j\frac{\pi}{2} \right) \quad (5.78)$$

The exponential integral is linked with the exponential sine and cosine according to the following relation:

$$E_1(jx) = j \left(-\frac{\pi}{2} + \text{Si}(x) \right) - \text{Ci}(x) \quad (5.79)$$

Introducing this equivalence leads finally to the reflection coefficient found in [1], equation (69) p. 137.

$$R_+ \cong -1 + \frac{1}{\ln(2h/a)} (\ln(2kh) + j\text{Si}(2kh) - \text{Ci}(2kh) + \gamma) \quad (5.80)$$

5.6 Computation of the scattering and reflection coefficients

For certain simple types of load, e.g. for an open circuit as presented in the last section, it is possible to obtain an analytical solution for the scattering coefficients. However, in general, the use of a full-wave numerical method is needed.

The proposed method requires the simulations of $2N + 1$ auxiliary lines excited either by a lumped source or a plane wave. At first sight, it could seem that the simulation of several lines instead of one increases the complexity of the problem. However, the auxiliary lines are chosen much shorter than the original line, hence significantly reducing the simulation time and computer resources. Note also that the scattering and reflection coefficients in fact depend on the loads at the terminals of the line and should hence be recomputed if the loads are changed. Reflection and scattering coefficients being independent of the line length, shorter auxiliary lines will be used. The length of the auxiliary lines is denoted L_1 , with $L_1 \geq 3l_{\text{bound}}$. First, N short lines of length L_1 excited by lumped sources placed at the right terminal are simulated. This is illustrated in Figure 5.4 for a two-conductor line.

In each case, a lumped source is placed on one of the N wires to excite different modes of the line. The internal impedance of this source will not affect the procedure and can be chosen as desired. The line cross-section and the termination opposite to the lumped source (in this case, left-end termination) should be identical to the original line. For convenience, the terminations

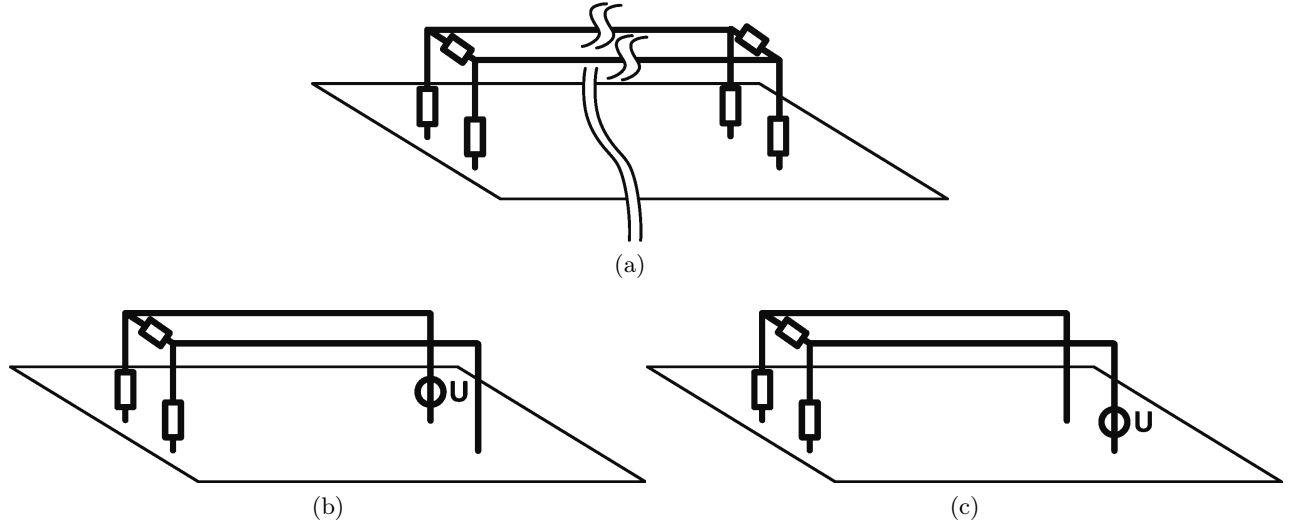


Figure 5.4: Illustration of the method using auxiliary lines to compute reflection coefficients associated with the line's left-end terminal (here in the case of a two-conductor line, $N = 2$). (a) Considered line. (b) Auxiliary line 1 where a lumped source is placed on the first wire. (c) Auxiliary line 2 where a lumped source is placed on the second wire.

at the excitation side are replaced by vertical risers, one of which is loaded with a lumped source (see Figure 5.4(b) and (c)). Similarly, N short lines excited by lumped sources placed at the left terminal are simulated as well (Figure 5.5).

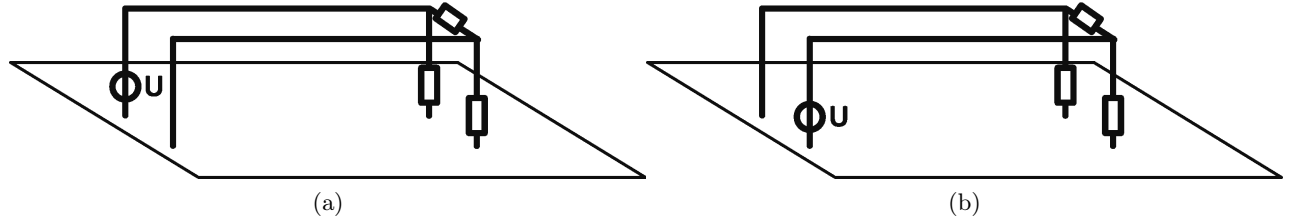


Figure 5.5: Illustration of the method using auxiliary lines to compute reflection coefficients associated with the line's right-end terminal (here in the case of a two-conductor line, $N = 2$). (a) Auxiliary line 1 where a lumped source is placed on the first wire. (b) Auxiliary line 2 where a lumped source is placed on the second wire.

Afterwards, a line with the same configuration than the original line but with a reduced length L_1 and excited by the plane wave is simulated. The currents obtained by simulation are then processed to extract the parameters required to evaluate the reflection and scattering coefficients that are independent of the length of the line. From these coefficients, the current along a line of arbitrary length is computed.

5.6.1 Simulation of $2N$ auxiliary lines excited by lumped sources

First, N short lines of length L_1 excited by lumped sources placed at the right terminal are simulated (see Figure 5.4). For each simulation $n = 1, \dots, N$, one obtains a current that is named $\mathbf{I}_+^n(x)$.

Then, N short lines excited by lumped sources placed at the left terminal are simulated as well (Figure 5.5). As a result of each n^{th} simulation, one obtains the current $\mathbf{I}_-^n(x)$.

5.6.2 Extraction of $\mathbf{I}_{1,ls}$ and $\mathbf{I}_{2,ls}$

In the presence of only a lumped source, the current flowing in the central part of the line, in the asymptotic zone, is the sum of backward and forward propagating waves:

$$\mathbf{I}_{ls}(x) = \mathbf{I}_{1,ls}e^{jkx} + \mathbf{I}_{2,ls}e^{-jkx} \quad (5.81)$$

Note that the index ‘ls’ is used to point out that the excitation is a lumped source. Two methods are proposed to extract the expressions for $I_{1,ls}$ and $I_{2,ls}$ based on the knowledge of $I_{ls}(x)$.

Method 1: by Derivation This method is inspired by [153]. After the computation of the derivative of (5.81), expressions for I_1 and I_2 are obtained as follows:

$$\begin{aligned} \mathbf{I}_{1,ls} &= \frac{e^{-jkx}}{2jk} \left(jk\mathbf{I}_{ls}(x) + \frac{d}{dx}\mathbf{I}_{ls}(x) \right) \\ \mathbf{I}_{2,ls} &= \frac{e^{jkx}}{2jk} \left(jk\mathbf{I}_{ls}(x) - \frac{d}{dx}\mathbf{I}_{ls}(x) \right) \end{aligned} \quad (5.82)$$

Note that according to this method, $\mathbf{I}_{1,ls}$ and $\mathbf{I}_{2,ls}$ in fact depend on the position x , especially near the terminals of the lines. However, in the asymptotic zone, they should be constant [153]. Hence, for the following steps, the value at the centre of the line can be chosen for convenience.

For the numerical implementation, the following expression ([171], Table 25.2) was found to provide the most accurate results to compute the derivative of the current:

$$\frac{d}{dx}\mathbf{I}_{ls}(x) \cong \frac{1}{12\Delta x} \left(-\mathbf{I}_{ls}(x+2\Delta x) + 8\mathbf{I}_{ls}(x+\Delta x) - 8\mathbf{I}_{ls}(x-\Delta x) + \mathbf{I}_{ls}(x-2\Delta x) \right) \quad (5.83)$$

Method 2: Least Squares Let us assume that we know the values of the current at location x_1, x_2, \dots, x_i . Equation (5.81) is valid in particular for these values:

$$\begin{cases} \mathbf{I}_{ls}(x_1) &= \mathbf{I}_{1,ls}e^{jkx_1} + \mathbf{I}_{2,ls}e^{-jkx_1} \\ \mathbf{I}_{ls}(x_2) &= \mathbf{I}_{1,ls}e^{jkx_2} + \mathbf{I}_{2,ls}e^{-jkx_2} \\ &\vdots \\ \mathbf{I}_{ls}(x_i) &= \mathbf{I}_{1,ls}e^{jkx_i} + \mathbf{I}_{2,ls}e^{-jkx_i} \end{cases} \quad (5.84)$$

Expressions for $\mathbf{I}_{1,ls}$ and $\mathbf{I}_{2,ls}$ can be found by solving this system of equations using the method of least squares.

The first method using the derivative is fast, since it only needs the direct computation of an expression based on five values of the current. On the other hand, the second method based on the least squares is expected to be numerically more stable, as it uses a significant number of points. However, it requires more numerical resources.

5.6.3 Matrices of reflection coefficients

For $n = 1, \dots, N$, \mathbf{I}_{1+}^n and \mathbf{I}_{2+}^n are extracted from the current $\mathbf{I}_+^n(x)$ obtain in Section 5.6.1, through one of the two methods described in Section 5.6.2. The obtained parameters are grouped into two

matrices:

$$\begin{aligned}\widehat{\mathbf{I}}_{1+} &:= \begin{bmatrix} \mathbf{I}_{1+}^1 & \mathbf{I}_{1+}^2 & \cdots & \mathbf{I}_{1+}^N \end{bmatrix} \\ \widehat{\mathbf{I}}_{2+} &:= \begin{bmatrix} \mathbf{I}_{2+}^1 & \mathbf{I}_{2+}^2 & \cdots & \mathbf{I}_{2+}^N \end{bmatrix}\end{aligned}\quad (5.85)$$

On the other hand, the link with the matrix of reflection coefficients at the left terminal is reminded here:

$$\widehat{\mathbf{R}}_+ \mathbf{I}_1 = \mathbf{I}_2 \quad (5.86)$$

As this expression is valid in particular for each current \mathbf{I}_{1+}^n and \mathbf{I}_{2+}^n , the expression for the matrix of reflection coefficients at the left terminal is as follows.

$$\widehat{\mathbf{R}}_+ = \widehat{\mathbf{I}}_{2+} \left(\widehat{\mathbf{I}}_{1+} \right)^{-1} \quad (5.87)$$

Note that in (5.87), the matrices defined in (5.85) were used, because the direct inversion of a vector does not exist.

An analogue procedure is followed for the right terminal. For $n = 1, \dots, N$, \mathbf{I}_{1-}^n and \mathbf{I}_{2-}^n are extracted from the current $\mathbf{I}_-^n(x)$. The obtained parameters are grouped into two matrices:

$$\begin{aligned}\widehat{\mathbf{I}}_{1-} &:= \begin{bmatrix} \mathbf{I}_{1-}^1 & \mathbf{I}_{1-}^2 & \cdots & \mathbf{I}_{1-}^N \end{bmatrix} \\ \widehat{\mathbf{I}}_{2-} &:= \begin{bmatrix} \mathbf{I}_{2-}^1 & \mathbf{I}_{2-}^2 & \cdots & \mathbf{I}_{2-}^N \end{bmatrix}\end{aligned}\quad (5.88)$$

The link with the matrix of reflection coefficients at the right terminal is reminded here:

$$\widehat{\mathbf{R}}_- \mathbf{I}_2 = \mathbf{I}_1 e^{2jkL} \quad (5.89)$$

Hence the expression for the matrix of reflection coefficients at the right terminal is as follows.

$$\widehat{\mathbf{R}}_- = \widehat{\mathbf{I}}_{1-} \left(\widehat{\mathbf{I}}_{2-} \right)^{-1} e^{2jkL} \quad (5.90)$$

5.6.4 Terminations

Near the right terminal, in zone I, the current is expressed as

$$\mathbf{I}_+(x) = \widehat{\Psi}_+^0(x) \mathbf{I}_{1+} \quad (5.91)$$

The currents are first grouped into a matrix:

$$\widehat{\mathbf{I}}_+(x) := \begin{bmatrix} \mathbf{I}_+^1(x) & \mathbf{I}_+^2(x) & \cdots & \mathbf{I}_+^N(x) \end{bmatrix} \quad (5.92)$$

Then

$$\widehat{\Psi}_+^0(x) = \widehat{\mathbf{I}}_+(x) (\mathbf{I}_{1+})^{-1} \quad (5.93)$$

Near the left terminal, in zone III, the current is expressed as

$$\mathbf{I}_-(x) = \widehat{\Psi}_-^0(x - L) \mathbf{I}_{2-} e^{-jkL} \quad (5.94)$$

The currents are first grouped into a matrix:

$$\widehat{\mathbf{I}}_-(x) := \begin{bmatrix} \mathbf{I}_-^1(x) & \mathbf{I}_-^2(x) & \cdots & \mathbf{I}_-^N(x) \end{bmatrix} \quad (5.95)$$

Then

$$\widehat{\Psi}_-^0(x) = \widehat{\mathbf{I}}_-(x + L_1) (\mathbf{I}_{2-})^{-1} e^{jkL_1} \quad (5.96)$$

5.6.5 Simulation of an auxiliary line

A line with the same configuration as the original line but with a reduced length L_1 and excited by the plane wave is simulated. As a result of this simulation, the current $I_{pw}(x)$ is obtained. Note that the subscript ‘pw’ is used to point out that the source is now a plane wave.

5.6.6 Extraction of \mathbf{I}_0 , $\mathbf{I}_{1,pw}$ and $\mathbf{I}_{2,pw}$

The current flowing in the centre of the line, in the asymptotic zone, is given by (5.23). The values of $\mathbf{I}_{1,pw}$ and $\mathbf{I}_{2,pw}$ can be derived similarly to the way it was done for the lines excited by lumped sources in Section 5.6.2, that is to say with two different methods.

Method 1: by Derivation $\mathbf{I}_{1,pw}$ and $\mathbf{I}_{2,pw}$ are obtained after derivation of (38) and algebraic manipulations.

$$\begin{aligned} \mathbf{I}_{1,pw} &= \frac{e^{-jkx}}{2jk} \left(jk\mathbf{I}_{pw}(x) + \frac{d}{dx}\mathbf{I}_{pw}(x) - j(k - k_x)\mathbf{I}_0 e^{-jk_x x} \right) \\ \mathbf{I}_{2,pw} &= \frac{e^{jkx}}{2jk} \left(jk\mathbf{I}_{pw}(x) - \frac{d}{dx}\mathbf{I}_{pw}(x) - j(k + k_x)\mathbf{I}_0 e^{-jk_x x} \right) \end{aligned} \quad (5.97)$$

where \mathbf{I}_0 was computed with (5.10).

Method 2: Least Squares Let us assume that we know the values of the current at location x_1, x_2, \dots, x_i . Equation (5.23) is valid in particular for these values.

$$\begin{cases} \mathbf{I}_{pw}(x_1) &= \mathbf{I}_0 e^{-jk_x x_1} + \mathbf{I}_{1,pw} e^{jk x_1} + \mathbf{I}_{2,pw} e^{-jk x_1} \\ \mathbf{I}_{pw}(x_2) &= \mathbf{I}_0 e^{-jk_x x_2} + \mathbf{I}_{1,pw} e^{jk x_2} + \mathbf{I}_{2,pw} e^{-jk x_2} \\ &\vdots \\ \mathbf{I}_{pw}(x_i) &= \mathbf{I}_0 e^{-jk_x x_i} + \mathbf{I}_{1,pw} e^{jk x_i} + \mathbf{I}_{2,pw} e^{-jk x_i} \end{cases} \quad (5.98)$$

Expressions for \mathbf{I}_0 , $\mathbf{I}_{1,pw}$ and $\mathbf{I}_{2,pw}$ can then be found by solving this system of equations using the least squares method.

5.6.7 Scattering coefficients

The scattering coefficients are then computed with the following expressions, obtained by algebraic manipulation of (5.24).

$$\begin{aligned} \widehat{\mathbf{C}}_+ \mathbf{I}_0 &= \mathbf{I}_{2,pw} - \widehat{\mathbf{R}}_+ \mathbf{I}_{1,pw} \\ \widehat{\mathbf{C}}_- \mathbf{I}_0 &= \mathbf{I}_{1,pw} e^{j(k+k_x)L_1} - \widehat{\mathbf{R}}_- \mathbf{I}_{2,pw} e^{-j(k-k_x)L_1} \end{aligned} \quad (5.99)$$

5.6.8 Terminations

The expression of the current near the left terminal reads:

$$\mathbf{I}_{pw}(x) = \widehat{\Psi}_+^e(x) \mathbf{I}_0 + \widehat{\Psi}_+^0(x) \mathbf{I}_{1,pw} \quad (5.100)$$

Considering that $\widehat{\Psi}_+^e(x)$ is always multiplied by \mathbf{I}_0 , only their product has to be computed.

$$\widehat{\Psi}_+^e(x)\mathbf{I}_0 = \mathbf{I}_{pw}(x) - \widehat{\Psi}_+^0(x)\mathbf{I}_{1,pw} \quad (5.101)$$

The expression of the current near the right terminal reads:

$$\mathbf{I}_{pw}(x) = \widehat{\Psi}_-^e(x - L_1)\mathbf{I}_0 e^{-jk_x L_1} + \widehat{\Psi}_-^0(x - L_1)\mathbf{I}_{2,pw} e^{-jk L_1} \quad (5.102)$$

Similarly, as $\widehat{\Psi}_-^e(x)$ is always multiplied by \mathbf{I}_0 , only their product needs to be computed:

$$\widehat{\Psi}_-^e(x)\mathbf{I}_0 = \mathbf{I}_{pw}(x + L_1) e^{jk_x L_1} - \widehat{\Psi}_-^0(x)\mathbf{I}_{2,pw} e^{-j(k - k_x)L_1} \quad (5.103)$$

5.6.9 Current in a line of arbitrary length

After the computation of the reflection and scattering coefficients and the functions as proposed in the above sections, the current along the line is given by:

$$\mathbf{I}(x) = \begin{cases} \widehat{\Psi}_+^e(x)\mathbf{I}_0 + \widehat{\Psi}_+^0(x)\mathbf{I}_1 & 0 \leq x \leq l_{bound} \\ \mathbf{I}_0 e^{-jk_x x} + \mathbf{I}_1 e^{jk_x x} + \mathbf{I}_2 e^{-jk_x x} & l_{bound} \leq x \leq L - l_{bound} \\ \widehat{\Psi}_-^e(x - L)\mathbf{I}_0 e^{-jk_x L} + \widehat{\Psi}_-^0(x - L)\mathbf{I}_2 e^{-jk L} & L - l_{bound} \leq x \leq L \end{cases} \quad (5.104)$$

with \mathbf{I}_0 , \mathbf{I}_1 and \mathbf{I}_2 given by (5.10) and (5.24).

5.6.10 Synthesis

The procedure is synthesised here:

1. Simulate $2N$ auxiliary short lines excited by lumped sources.
2. Extract $\mathbf{I}_{1\pm}^n$ and $\mathbf{I}_{2\pm}^n$, for $n = 1, \dots, N$.
3. Compute $\widehat{\mathbf{R}}_{\pm}$ and $\widehat{\Psi}_{\pm}^0(x)$.
4. Simulate a short line with the desired plane wave excitation.
5. Extract $\mathbf{I}_{1,pw}$ and $\mathbf{I}_{2,pw}$. Extract or compute \mathbf{I}_0 .
6. Compute $\widehat{\mathbf{C}}_{\pm}\mathbf{I}_0$ and $\widehat{\Psi}_{\pm}^e(x)\mathbf{I}_0$.
7. Compute the current for a line of arbitrary length.

5.7 Non-linear load

In real cases, the line can be terminated by protection equipment such as surge protective devices (SPD), which have a non-linear current-voltage characteristic. Although the method proposed in the previous section is strongly based on the linearity of the electromagnetic equations, it could be applied if one of the terminals has a non-linear response. The procedure that permits the determination of a non-linear system response in an indirect manner was used among others for an antenna connected to a non-linear load [173] and applied to lines excited by a field in [10], Section 7.7.

The basis of the method is to reduce the linear portion of the line into a Thévenin or Norton equivalent source, at the location of the non-linear element. This equivalent source is then converted into its time-domain equivalent by an inverse Fourier transform. In addition, if the non-linear device is specified, a non-linear Volterra integral equation for the load response is obtained and can be solved by a time-marching procedure.

5.8 Low-frequency approximation, with lossy ground plane and wires

At low frequencies, the proposed theory converges to the classical TL theory, and the TEM mode is supposed to be dominant along the whole line. The formulation for the currents in the line remains the same, but zones I and III are no longer considered and the asymptotic formulation (region II) is considered to be valid along the whole line.

In this section, the validity of the model is extended by considering lossy ground plane and wires. The finite conductivity of the ground plane affects the reflected field. On the other hand, the losses that occur during propagation modifies the transmission line parameters and hence the modes propagating along it.

In this section, the index TL is used to underline the fact the parameters are now computed under the classical TL assumptions.

5.8.1 TL Equations

The multiconductor TL equations of a lossy line in Agrawal's formulation are given by:

$$\begin{aligned} \frac{d}{dx} \mathbf{U}^s(x) + \hat{\mathbf{Z}}' \mathbf{I}^{TL}(x) &= \mathbf{E}_x^e(x) \\ \frac{d}{dx} \mathbf{I}^{TL}(x) + \hat{\mathbf{Y}}' \mathbf{U}^s(x) &= \mathbf{0} \end{aligned} \quad (5.105)$$

where the superscript ' TL ' indicates that the solution is computed under the transmission line theory. Equation (5.105) corresponds to (4.24) where the p.u.l. impedance term $j\omega \hat{\mathbf{L}}'$ was replaced by a more general p.u.l. impedance $\hat{\mathbf{Z}}'$, and where the p.u.l. capacitance term $j\omega \hat{\mathbf{C}}'$ was replaced by a p.u.l. admittance $\hat{\mathbf{Y}}'$.

For example, in the case of a overhead line, these matrices of line parameters are given by the following expressions [20].

$$\begin{aligned} \hat{\mathbf{Z}}' &= j\omega \hat{\mathbf{L}}' + \hat{\mathbf{Z}}'_w + \hat{\mathbf{Z}}'_g \\ \hat{\mathbf{Y}}' &= j\omega \hat{\mathbf{C}}' + \hat{\mathbf{G}}' \end{aligned} \quad (5.106)$$

The p.u.l. internal impedance of the wire is defined as follows.

$$Z'_{w,nn} = \frac{\gamma_w I_0(\gamma_w a_n)}{2\pi a \sigma_w I_1(\gamma_w a_n)} \quad (5.107)$$

The p.u.l. transverse conductance matrix is defined as follows.

$$\hat{\mathbf{G}}' = \frac{\sigma_{\text{air}}}{\varepsilon_0} \hat{\mathbf{C}}' \quad (5.108)$$

The p.u.l. ground impedance is defined as follows.

$$Z'_{g,mn} = \begin{cases} \frac{j\omega\mu_0}{\pi} \int_0^\infty \frac{e^{-2h_n x}}{\sqrt{x^2 + \gamma_g^2} + x} dx \cong \frac{j\omega\mu_0}{2\pi} \ln \frac{1 + \gamma_g h_n}{\gamma_g h_n} & m = n \\ \frac{j\omega\mu_0}{\pi} \int_0^\infty \frac{e^{-(h_m+h_n)x}}{\sqrt{x^2 + \gamma_g^2} + x} \cos((y_m - y_n)x) dx = & m \neq n \\ \cong \frac{j\omega\mu_0}{4\pi} \ln \frac{(1 + \gamma_g(h_m + h_n)/2)^2 + \gamma_g((y_m - y_n)/2)^2}{(\gamma_g(h_m + h_n)/2)^2 + \gamma_g((y_m - y_n)/2)^2} & \end{cases} \quad (5.109)$$

where I_0 and I_1 are the modified Bessel functions of zeroth and first order, respectively. The propagation constant in the wire and in the ground are defined as follows.

$$\begin{aligned} \gamma_w &= \sqrt{j\omega\mu_0(\sigma_w + j\omega\varepsilon_0\varepsilon_{rw})} \\ \gamma_g &= \sqrt{j\omega\mu_0(\sigma_g + j\omega\varepsilon_0\varepsilon_{rg})} \end{aligned} \quad (5.110)$$

Uncoupling the current and the voltage in (5.105) leads to an expression in the form of Helmholtz' equations.

$$\begin{aligned} \left(\frac{d^2}{dx^2} - \hat{\mathbf{Y}}' \hat{\mathbf{Z}}' \right) \mathbf{I}^{TL}(x) &= -\hat{\mathbf{Y}}' \mathbf{E}_x^e(x) \\ \left(\frac{d^2}{dx^2} - \hat{\mathbf{Z}}' \hat{\mathbf{Y}}' \right) \mathbf{U}^s(x) &= \frac{d}{dx} \mathbf{E}_x^e(x) \end{aligned} \quad (5.111)$$

5.8.2 Exciting field

If the incident field is a plane wave, the x -component of the electric field, parallel to the line, can be written in the following form [10, 124]:

$$\mathbf{E}_x^e(x) = \mathbf{E}_x^e e^{-jk_x x} \quad (5.112)$$

with

$$\begin{aligned} E_{x,n}^e &= E_0 \left(\cos \alpha \sin \psi \cos \phi \left(e^{jk_z h_n} - R_v e^{-jk_z h_n} \right) \right. \\ &\quad \left. + \sin \alpha \sin \phi \left(e^{jk_z h_n} + R_h e^{-jk_z h_n} \right) \right) e^{jk_y y_n} \end{aligned} \quad (5.113)$$

and where R_v and R_h are Fresnel reflection coefficients.

$$\begin{aligned} R_v &= \frac{\varepsilon_r (1 + \sigma_g/(j\omega\varepsilon_r\varepsilon_0)) \sin \psi - [\varepsilon_r (1 + \sigma_g/(j\omega\varepsilon_r\varepsilon_0)) - \cos^2 \psi]^{1/2}}{\varepsilon_r (1 + \sigma_g/(j\omega\varepsilon_r\varepsilon_0)) \sin \psi + [\varepsilon_r (1 + \sigma_g/(j\omega\varepsilon_r\varepsilon_0)) - \cos^2 \psi]^{1/2}} \\ R_h &= \frac{\sin \psi - [\varepsilon_r (1 + \sigma_g/(j\omega\varepsilon_r\varepsilon_0)) - \cos^2 \psi]^{1/2}}{\sin \psi + [\varepsilon_r (1 + \sigma_g/(j\omega\varepsilon_r\varepsilon_0)) - \cos^2 \psi]^{1/2}} \end{aligned} \quad (5.114)$$

5.8.3 Solution: current induced in an infinite line

The response due to the exciting field, without boundary conditions, will have the same structure as the excitation [119]:

$$\begin{aligned} \mathbf{I}_0^{TL}(x) &= \mathbf{I}_0^{TL} e^{-jk_x x} \\ \mathbf{U}_0^s(x) &= \mathbf{U}_0^s e^{-jk_x x} \end{aligned} \quad (5.115)$$

Applying a solution in the form of (5.115) into (5.111) leads after computation to:

$$\mathbf{I}_0^{TL} = \left(\hat{\mathbf{1}}k_x^2 + \hat{\mathbf{Y}}'\hat{\mathbf{Z}}' \right)^{-1} \hat{\mathbf{Y}}' \mathbf{E}_x^e \quad (5.116)$$

$$\mathbf{U}_0^s = jk_x \left(\hat{\mathbf{1}}k_x^2 + \hat{\mathbf{Z}}'\hat{\mathbf{Y}}' \right)^{-1} \mathbf{E}_x^e \quad (5.117)$$

Hence, \mathbf{U}_0^s can be rewritten as:

$$\mathbf{U}_0^s = \hat{\mathbf{Z}}_{C0} \mathbf{I}_0^{TL} \quad (5.118)$$

where the characteristic impedance of the quasi-TEM mode is defined as follows:

$$\hat{\mathbf{Z}}_{C0} := jk_x \left(\hat{\mathbf{1}}k_x^2 + \hat{\mathbf{Z}}'\hat{\mathbf{Y}}' \right)^{-1} \hat{\mathbf{Y}}'^{-1} \left(\hat{\mathbf{1}}k_x^2 + \hat{\mathbf{Y}}'\hat{\mathbf{Z}}' \right) \quad (5.119)$$

5.8.4 Solution: current induced in a finite line

The following expressions are suggested as solutions of (5.111).

$$\begin{aligned} \mathbf{I}^{TL}(x) &= \mathbf{I}_0^{TL} e^{-jk_x x} + \hat{\mathbf{T}} e^{+\hat{\gamma}x} \mathbf{i}_1 + \hat{\mathbf{T}} e^{-\hat{\gamma}x} \mathbf{i}_2 \\ \mathbf{U}^s(x) &= \hat{\mathbf{Z}}_{C0} \mathbf{I}_0^{TL} e^{-jk_x x} + \hat{\mathbf{Z}}_C \left(-\hat{\mathbf{T}} e^{+\hat{\gamma}x} \mathbf{i}_1 + \hat{\mathbf{T}} e^{-\hat{\gamma}x} \mathbf{i}_2 \right) \end{aligned} \quad (5.120)$$

where the matrix $\hat{\mathbf{T}}$ contains the eigenvectors and $\hat{\gamma}^2$ the eigenvalues associated to the diagonalisation of $\hat{\mathbf{Y}}'\hat{\mathbf{Z}}'$.

$$\left(\hat{\mathbf{Y}}'\hat{\mathbf{Z}}' \right) \hat{\mathbf{T}} = \hat{\mathbf{T}} \hat{\gamma}^2 \quad (5.121)$$

Introducing the backward propagating waves (i.e. assuming $\mathbf{I}_0 = \mathbf{i}_2 = \mathbf{E}_z^e = 0$) into (5.111), with the help of matrix calculus, leads to (5.121) and to

$$\left(\hat{\mathbf{Z}}'\hat{\mathbf{Y}}' \right) \left(\hat{\mathbf{Z}}_C \hat{\mathbf{T}} \right) = \left(\hat{\mathbf{Z}}_C \hat{\mathbf{T}} \right) \hat{\gamma}^2 \quad (5.122)$$

Hence, the matrix $\hat{\mathbf{Z}}'\hat{\mathbf{Y}}'$ can be diagonalised with eigenvectors $\hat{\mathbf{Z}}_C \hat{\mathbf{T}}$ and eigenvalues $\hat{\gamma}^2$.

Introducing the backward propagating wave into equations (5.105), with the help of matrix calculus, leads to:

$$\begin{aligned} -\hat{\mathbf{Z}}_C \hat{\mathbf{T}} \hat{\gamma} e^{+\hat{\gamma}z} \mathbf{i}_1 + \hat{\mathbf{Z}}' \hat{\mathbf{T}} e^{+\hat{\gamma}z} \mathbf{i}_1 &= \mathbf{0} \\ \hat{\mathbf{T}} \hat{\gamma} e^{+\hat{\gamma}z} \mathbf{i}_1 - \hat{\mathbf{Y}}' \hat{\mathbf{Z}}_C \hat{\mathbf{T}} e^{+\hat{\gamma}z} \mathbf{i}_1 &= \mathbf{0} \end{aligned} \quad (5.123)$$

As these equations must be valid for every \mathbf{i}_1 , the characteristic impedance must be equal to the following expressions:

$$\hat{\mathbf{Z}}_C = \hat{\mathbf{Z}}' \hat{\mathbf{T}} \hat{\gamma}^{-1} \hat{\mathbf{T}}^{-1} = \hat{\mathbf{Y}}'^{-1} \hat{\mathbf{T}} \hat{\gamma} \hat{\mathbf{T}}^{-1} \quad (5.124)$$

Both expressions are equivalent, due to definition (5.121). Note also that proceeding the same way with the forward propagating wave would lead to the same result.

The terminals are modelled by the following boundary conditions:

$$\mathbf{U}^s(0) = -\hat{\mathbf{Z}}_1 \mathbf{I}^{TL}(0) + \mathbf{U}_1 \quad (5.125)$$

$$\mathbf{U}^s(L) = \hat{\mathbf{Z}}_2 \mathbf{I}^{TL}(L) + \mathbf{U}_2 \quad (5.126)$$

where the n^{th} elements of \mathbf{U}_1 and \mathbf{U}_2 are defined as follows:

$$U_{1,n} := \int_0^{x_n} E_x^e(x, y_n, z=0) dx \quad (5.127)$$

$$U_{2,n} := \int_0^{x_n} E_x^e(x, y_n, z=L) dx \quad (5.128)$$

A direct computation of (5.127) and (5.128) shows that:

$$\mathbf{U}_2 = \mathbf{U}_1 e^{-jk_x L} \quad (5.129)$$

Hence, (5.126) can be rewritten as:

$$\mathbf{U}^s(L) = \hat{\mathbf{Z}}_2 \mathbf{I}^{TL}(L) + \mathbf{U}_1 e^{-jk_x L} \quad (5.130)$$

Introducing solutions (5.120) into the boundary conditions (5.125) and (5.130) leads after computation to:

$$\begin{aligned} \mathbf{i}_2 &= \hat{\mathbf{r}}_1 \mathbf{i}_1 + \hat{\mathbf{c}}_1 \mathbf{I}_0 \\ e^{\hat{\gamma}L} \mathbf{i}_1 &= \hat{\mathbf{r}}_2 e^{-\hat{\gamma}L} \mathbf{i}_2 + \hat{\mathbf{c}}_2 \mathbf{I}_0^{TL} e^{-jk_x L} \end{aligned} \quad (5.131)$$

where the modal reflection and scattering coefficients were introduced:

$$\begin{aligned} \hat{\mathbf{r}}_1 &:= \hat{\mathbf{T}}^{-1} \hat{\mathbf{R}}_1 \hat{\mathbf{T}} \\ \hat{\mathbf{r}}_2 &:= \hat{\mathbf{T}}^{-1} \hat{\mathbf{R}}_2 \hat{\mathbf{T}} \\ \hat{\mathbf{c}}_1 \mathbf{I}_0 &:= \hat{\mathbf{T}}^{-1} \hat{\mathbf{C}}_1 \mathbf{I}_0^{TL} \\ \hat{\mathbf{c}}_2 \mathbf{I}_0 &:= \hat{\mathbf{T}}^{-1} \hat{\mathbf{C}}_2 \mathbf{I}_0^{TL} \end{aligned} \quad (5.132)$$

based on the reflection and scattering coefficients:

$$\begin{aligned} \hat{\mathbf{R}}_1 &:= (\hat{\mathbf{Z}}_C + \hat{\mathbf{Z}}_1)^{-1} (\hat{\mathbf{Z}}_C - \hat{\mathbf{Z}}_1) \\ \hat{\mathbf{R}}_2 &:= (\hat{\mathbf{Z}}_C + \hat{\mathbf{Z}}_2)^{-1} (\hat{\mathbf{Z}}_C - \hat{\mathbf{Z}}_2) \\ \hat{\mathbf{C}}_1 \mathbf{I}_0^{TL} &:= (\hat{\mathbf{Z}}_C + \hat{\mathbf{Z}}_1)^{-1} ((-\hat{\mathbf{Z}}_1 - \hat{\mathbf{Z}}_{C0}) \mathbf{I}_0^{TL} + \mathbf{U}_1) \\ \hat{\mathbf{C}}_2 \mathbf{I}_0^{TL} &:= (\hat{\mathbf{Z}}_C + \hat{\mathbf{Z}}_2)^{-1} ((-\hat{\mathbf{Z}}_2 + \hat{\mathbf{Z}}_{C0}) \mathbf{I}_0^{TL} - \mathbf{U}_1) \end{aligned} \quad (5.133)$$

The reflection coefficients $\hat{\mathbf{R}}_{1,2}$ are usual reflection coefficients for the current. They make the link between a propagated TEM current and the reflected current due to the termination. On the other hand, the scattering reflection coefficients $\hat{\mathbf{C}}_{1,2}$ are not defined in the classical formulation and only apply to the current \mathbf{I}_0^{TL} . They make the link between the incident field and the scattered current due to the termination.

Solving the linear system (5.131) finally leads to:

$$\begin{aligned} \mathbf{i}_1 &= (\hat{\mathbf{1}} - \hat{\mathbf{r}}_1 e^{-\hat{\gamma}L} \hat{\mathbf{r}}_2 e^{-\hat{\gamma}L})^{-1} (\hat{\mathbf{r}}_1 e^{-\hat{\gamma}L} \hat{\mathbf{c}}_2 \mathbf{I}_0^{TL} e^{-jk_x L} + \hat{\mathbf{c}}_1 \mathbf{I}_0^{TL}) \\ \mathbf{i}_2 &= (\hat{\mathbf{1}} - e^{-\hat{\gamma}L} \hat{\mathbf{r}}_2 e^{-\hat{\gamma}L} \hat{\mathbf{r}}_1)^{-1} (e^{-\hat{\gamma}L} \hat{\mathbf{r}}_2 e^{-\hat{\gamma}L} \hat{\mathbf{c}}_1 \mathbf{I}_0^{TL} + e^{-\hat{\gamma}L} \hat{\mathbf{c}}_2 \mathbf{I}_0^{TL} e^{-jk_x L}) \end{aligned} \quad (5.134)$$

5.8.5 Lossless ground and wires

In the case of a lossless system, $\hat{\mathbf{T}}$ transformation matrix is no longer needed and the solutions can be simplified.

$$\begin{aligned}\mathbf{I}(x) &= \mathbf{I}_0^{TL} e^{-jk_x x} + \mathbf{I}_1^{TL} e^{jkx} + \mathbf{I}_2^{TL} e^{-jkx} \\ \mathbf{U}^s(x) &= \hat{\mathbf{Z}}_C \left(\cos \vartheta \cos \phi \mathbf{I}_0^{TL} e^{-jk_x x} - \mathbf{I}_1^{TL} e^{jkx} + \mathbf{I}_2^{TL} e^{-jkx} \right)\end{aligned}\quad (5.135)$$

with

$$\begin{aligned}\mathbf{I}_1^{TL} &= \left(\hat{\mathbf{1}} - \hat{\mathbf{R}}_1 \hat{\mathbf{R}}_2 e^{-2jkL} \right)^{-1} \left(\hat{\mathbf{R}}_1 \hat{\mathbf{C}}_2 \mathbf{I}_0^{TL} e^{-j(k+k_x)L} + \hat{\mathbf{C}}_1 \mathbf{I}_0^{TL} \right) \\ \mathbf{I}_2^{TL} &= \left(\hat{\mathbf{1}} - \hat{\mathbf{R}}_2 \hat{\mathbf{R}}_1 e^{-2jkL} \right)^{-1} \left(\hat{\mathbf{R}}_2 \hat{\mathbf{C}}_1 \mathbf{I}_0^{TL} e^{-2jkL} + \hat{\mathbf{C}}_2 \mathbf{I}_0^{TL} e^{-j(k+k_x)L} \right)\end{aligned}\quad (5.136)$$

Note that the reflection coefficients for the current $\hat{\mathbf{R}}_{1,2}$ depend only on the line parameters and on the terminal loads. The coefficients $\hat{\mathbf{C}}_{1,2}$ depend not only on the load, but also on the incident field. However, none of these coefficients depend on the length of the line.

Note finally that the derived equations (5.135) are equivalent to the general solutions obtained by the TL theory (e.g., [9, 10, 116]). However, they represent an elegant explicit solution of a multiconductor transmission line excited by a plane wave.

The derived expressions are compact and given as a sum of three (matrix) exponential functions. Since the solution is expressed in terms of quasi-TEM mode, backward propagating TEM mode and forward propagating TEM mode, it gives physical insight into the mechanisms involved in field-to-transmission line coupling. Moreover, by adapting the reflection and scattering coefficients, the proposed formulation remains accurate at higher frequencies, where effects such as radiation appear and where the TL theory is no longer valid.

5.9 Radiation-resistance model

The source terms defined in the paragraph 3.1.10 do not consider the radiation of the risers, which become very effective when the wavelength of the current is in the same order of magnitude as the length of the riser. In order to include this effect, an additional resistance, corresponding to the radiation resistance of an infinitesimal monopole of length h [174], is added to the terminal:

$$R_{rad} = \frac{4\pi}{3} \sqrt{\frac{\mu_0}{\varepsilon_0}} \left(\frac{h}{\lambda} \right)^2 \quad (5.137)$$

where $\lambda = c/f$ is the wavelength. In other words, the impedance at the left (respectively right) terminal is considered to be constituted of the actual impedance at the left (respectively right) terminal plus the radiation resistance.

$$\rho_i = \frac{(Z_i + R_{rad}) - Z_C}{(Z_i + R_{rad}) + Z_C} \quad i = 1, 2 \quad (5.138)$$

Then the source terms (4.49) can be applied into the BLT equation (4.34), in which the length of the line L will have been replaced by $L + 2h$, and where the reflection coefficients ρ_1 and ρ_2 have been modified (5.138) to consider the radiation resistance (5.137). This model is expected to be more accurate than the available models presented in Section 4.1.8 and following, especially at frequencies above the limit of the TL theory.

5.10 Validation by simulation

5.10.1 Example 1: Open-circuit line

This first validation example is a two-wire line, open at its two terminals. Its cross-section and the parameters of the exciting plane wave are defined in Table 5.1.

Table 5.1: Parameters.

Parameter	Value
Radius of the wires	1 mm
Height above the ground	[0.5; 0.3] m
Horizontal position	[0; 0.3] m
Horizontal angle ϕ	45°
Elevation angle ψ	90°
Polarisation angle α	0°
E-field amplitude	1 V/m

A comparison of the coefficients provided by the asymptotic theory using NEC simulation (Section 5.6), the explicit mathematical expressions (Section 5.5) and the TL approximation (Section 5.8) are shown in Figures 5.6 and 5.7, as a function of the frequency. As discussed earlier, reflection and scattering coefficients are independent of the line length.

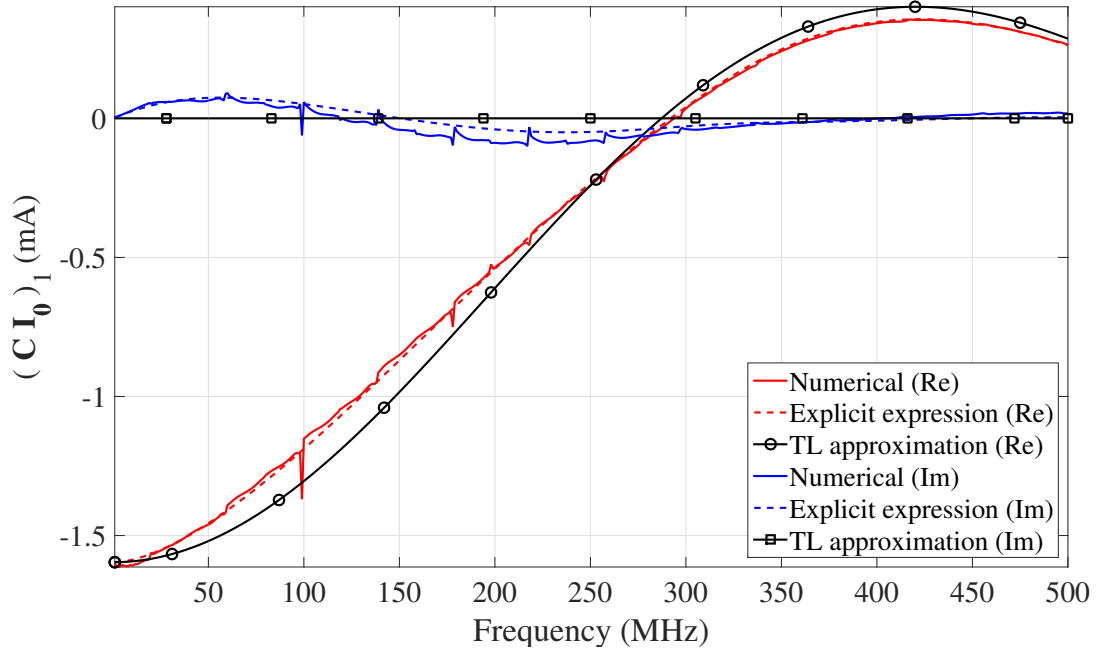


Figure 5.6: Real and imaginary parts of the first component of the left scattering coefficient multiplied by the current induced in an infinite line. Comparison between the asymptotic theory with numerical simulations, the explicit mathematical expression, and the TL approximation.

In Figure 5.6, the first component of $\hat{\mathbf{C}}\mathbf{I}_0$ is plotted. The explicit mathematical expression fits well with the numerical asymptotic theory, although at some frequencies (e.g. at 100 MHz), some numerical error is present. The TL approximation provides relatively accurate results even above its frequency limit (around 30 MHz in this case) due to the absence of vertical risers.

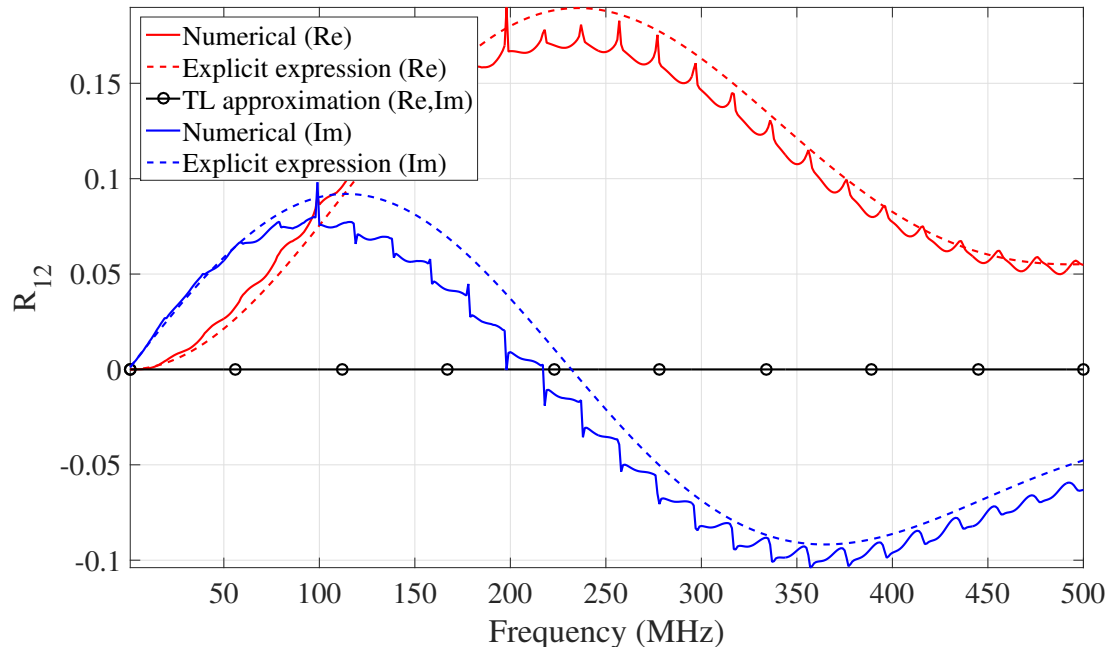


Figure 5.7: Real and imaginary parts of the R_{12} element of the matrix of reflection coefficient. Comparison between the asymptotic theory with numerical simulations, the explicit mathematical expression, and the TL approximation.

A non-diagonal term of the reflection coefficient matrix is presented in Figure 5.7. According to the TL theory, this coefficient is equal to zero. Indeed, its value is small in comparison with the diagonal terms, which are equal to -1 at low frequencies. The values obtained by the numerical asymptotic theory follow the same trend as the explicit mathematical expression. The spikes in the numerical values are certainly due to numerical errors.

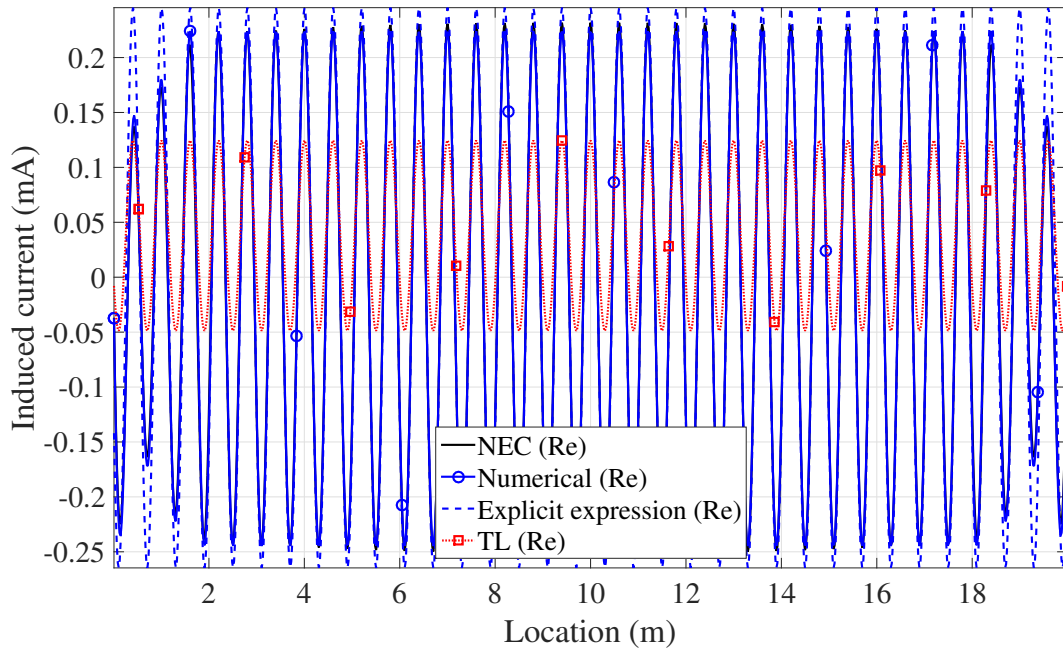


Figure 5.8: Induced current. Comparison between NEC, the asymptotic theory with numerical simulations, the explicit mathematical expression, and the TL approximation at 500 MHz.

The induced current in the second wire of a 20 m long line, at 500 MHz, is plotted in Figure 5.8.

The ‘exact’ current is computed with NEC-4 [175], based on the method of moments. The current is also computed using the reflection and scattering coefficients presented above. In Figure 5.8, the asymptotic theory with numerical simulations provides results that are in excellent agreement with NEC results. The explicit mathematical expressions provide results that are accurate in the centre of the line; however, they are not supposed to be valid near to the terminals where some additional modes are present. On the other hand, the amplitudes obtained with the transmission line theory significantly deviate from the exact results.

5.10.2 Example 2: Arbitrary terminations

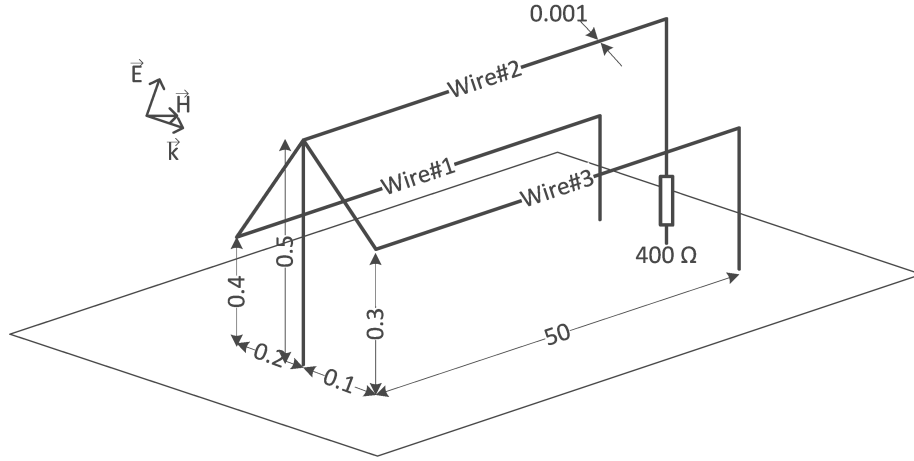


Figure 5.9: Three-conductor line system.

In this example, the line is made of three wires above a ground plane, with the geometry and terminal conditions shown in Fig. 5.9. The excitation field is a plane wave with an elevation angle of $\psi = 45^\circ$ (the azimuth and polarisation angles ϕ and α are set to zero). The reflection and scattering coefficients were determined by the proposed method with auxiliary lines of lengths $L_1 = 10$ m and by use of the least squares method for the extraction of the parameters (see Sections 5.6.2 and 5.6.6). The length of the segments for the sampling is 0.05 m.

The current induced along the third wire at 200 MHz is plotted in Figure 5.10. The proposed method offers results that are in excellent agreement with the ‘exact’ solutions obtained using NEC-4, whereas the classical TL theory does not provide accurate results for the considered frequency.

Figure 5.11 shows the current at the left termination of the line as a function of the frequency. The comparison shows that the proposed method provides results that are in excellent agreement with the full-wave ‘exact’ solutions. Beyond 30 MHz or so, the results obtained using the TL theory start to deviate significantly from the exact results.

As shown in Table 5.2, the proposed method is particularly effective in terms of memory requirements for long lines when compared with a full-wave method (MoM, method of moments).

It can also be noted that, while the simulation (on a virtual machine with four 2.4 GHz Intel Core i7 and 4 GB RAM) with the full-wave method took about 10 hours, the whole simulation time was about 1 hour with the proposed method. Finally, it is worth noting that once the coefficients of the equation are determined for a given line configuration, the proposed method makes it possible to obtain the solution for any line lengths by means of the analytical expression.

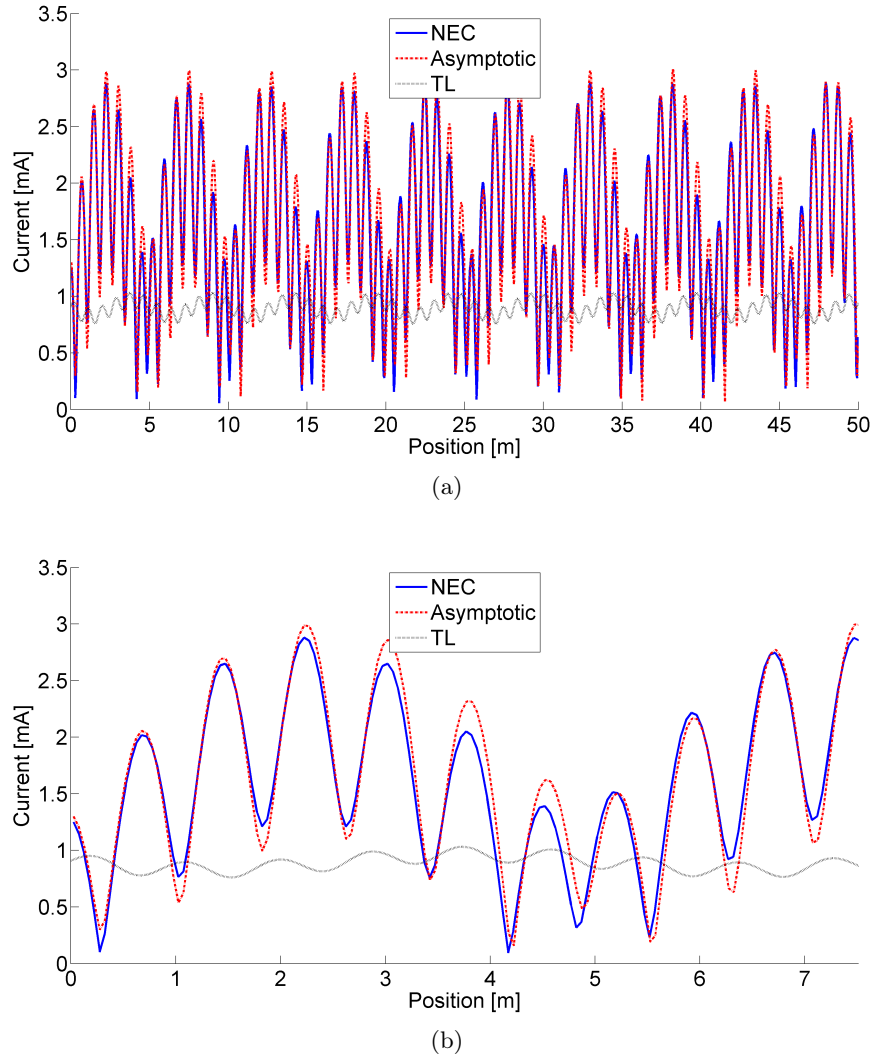


Figure 5.10: Amplitude of the current induced along the horizontal part of the line in the third conductor at 200 MHz. Comparison between the solutions provided by NEC, the proposed asymptotic method and the classical TL theory. (a) Whole line, (b), expanded view of the left part of the line.

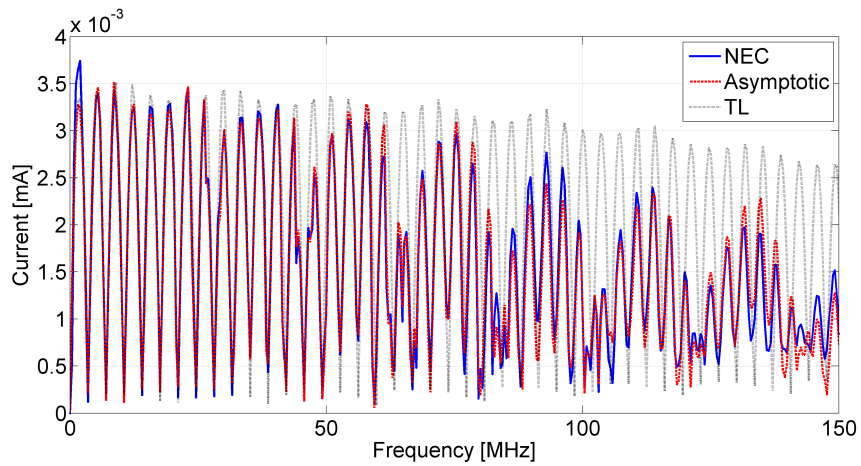


Figure 5.11: Amplitude of the induced current in the second (horizontal) conductor, at the first terminal of the line. Comparison between NEC, the proposed asymptotic method and the classical TL theory.

Table 5.2: Memory requirements as a function of the method and line length.

Line length L	Auxiliary line length L_1	Segment length	MoM	Proposed
50 m	10 m	5 cm	~144 MB	~40 MB
100 m	10 m	5 cm	~576 MB	~40 MB
1000 m	10 m	5 cm	~57 GB	~40 MB

5.11 Experimental validation

We report the measurement of the induced current at the terminal of a single line above a ground plane illuminated by an electromagnetic plane wave. The goal is to experimentally validate the models defined in the first part of the chapter.

5.11.1 Setup

The GTEM (gigahertz transverse electromagnetic) cell of Armasuisse in Bern was used to produce a wave resembling as much as possible a plane wave. Measurements were performed in the frequency domain, using a VNA (vector network analyser).

The measurements were performed in two steps:

1. measurement of the exciting field, in absence of the line;
2. measurement of the induced voltage at a terminal of a line.

A diagram of the setup for the measurement of the voltage in the frequency domain is shown in Figure 5.12. For the measurement of the field, the same setup was used with the exception that the line was replaced by a D-dot sensor.

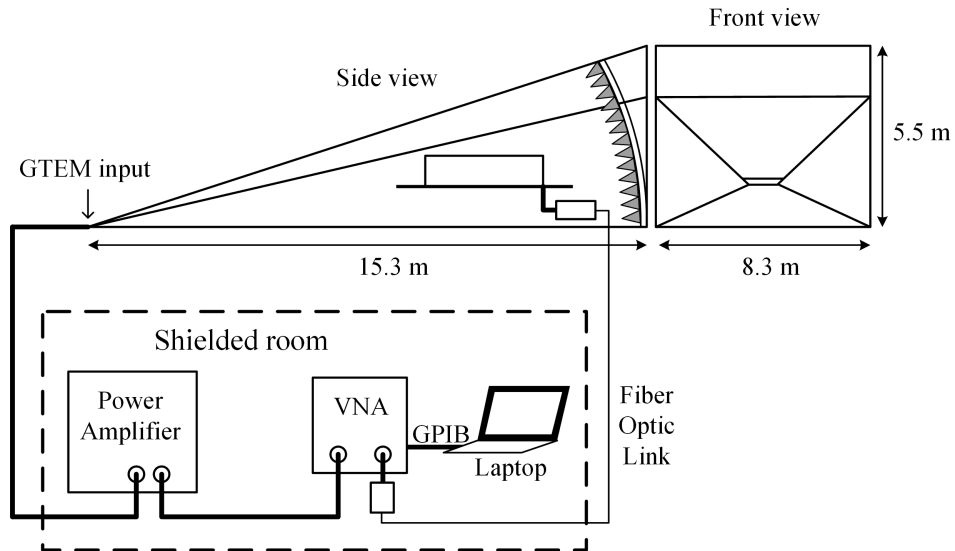


Figure 5.12: Experimental setup for the measurement of the induced voltage in the frequency domain.

Since the GTEM cell is supposed to create a homogeneous field up to about 1 GHz, and due to the low-frequency limitations of the used amplifier, the frequency range of the measurement was set to 1 MHz – 1 GHz.

The list of equipment used in the experiments is given in Table 5.3.

Table 5.3: Equipment list.

Denomination	Model and manufacturer	Characteristics
VNA	ZVRE, Rohde & Schwarz	9 kHz – 4 GHz
Calibration kit	85031 B, Hewlett Packard	7mm
Amplifier	50WD1000, Amplifier Research	0.5 – 1000 MHz
Optic link	MOL3000, Montena	200 Hz – 3.5 GHz
Electric-field probe	E1602, M��lop��e	

In addition to the list shown in Table 5.3, the following equipment was also used: laptop with GPIB link to retrieve the data from the VNA or oscilloscope, BNC attenuators, adapters (connectors), coaxial cables, etc.

5.11.2 Field measurement

A picture of the measurement of the vertical component of the electric field is shown in Figure 5.13. The measurement system is made of a D-dot sensor (derivative of the electric field), an attenuator, and a transmitter for the conversion of the electric signal to an optic signal.

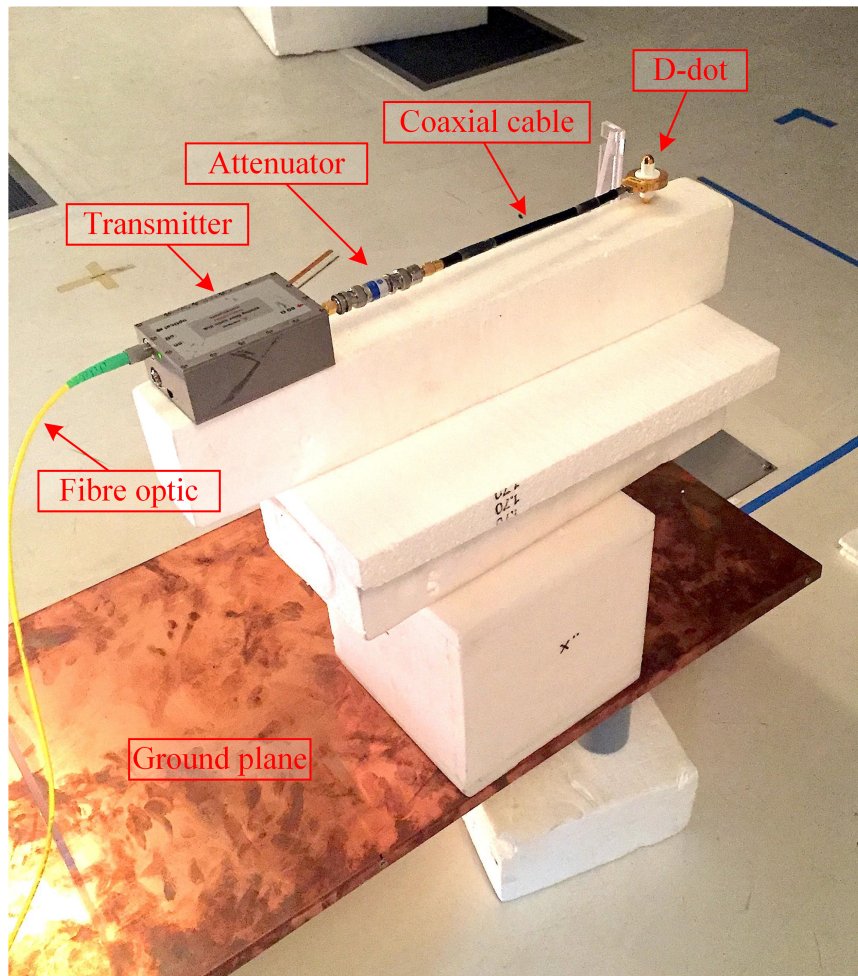


Figure 5.13: Picture of the field measurement, here in presence of the ground plane of the line.

In order to check the homogeneity of the field inside the cell, the E-field was measured at different locations listed in Table 5.4. For every location, the field was measured at four different heights (axis z) above the ground. The coordinate system used is presented in Figure 5.14.

Table 5.4: Field measurement locations.

x (cm)	y (cm)	z (cm)
0	-90	30 / 40 / 50 / 60
0	90	30 / 40 / 50 / 60
0	0	40
90	0	30 / 40 / 50 / 60
-90	0	30 / 40 / 50 / 60
-63.6	-63.6	30 / 40 / 50 / 60
-63.6	63.6	30 / 40 / 50 / 60

In Figure 5.14, the triplet made up of \vec{E} , \vec{H} and \vec{k} symbolises the wave propagating in the cell. The coordinates x , y , and z are used to describe the position of the field sensor. The angle ϕ will be used to describe the orientation of the line.

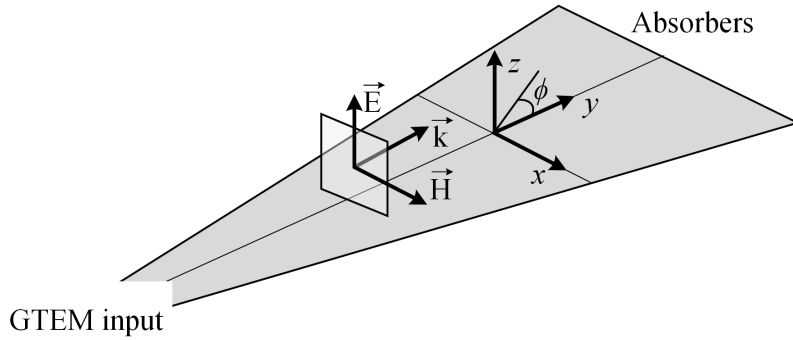


Figure 5.14: Coordinate system convention.

5.11.3 Parameters of the line

A single conductor above a ground plane with the parameters presented in Table 5.5 was used.

The length of the line was limited to 1.8 m, to be transportable and to be contained in a zone of the GTEM cell where the field is homogeneous. The height of the line was adjustable to 10, 20, 30 or 40 cm. The left terminal was connected to the measurement system, which corresponds to a $50\ \Omega$ load. The right terminal was terminated either on a short-circuit, or on a $50\ \Omega$ load.

The ground plane of the transmission line measures $0.4\text{ m} \times 2\text{ m}$ and was placed at 20 cm from the ground of the GTEM cell, in order to have enough place below it for the measurement equipment.

A picture of the line is shown in Figure 5.15. Four towers in polycarbonate maintain the wire horizontally. The wire is connected with a 4 mm plug to a BNC connector going through the ground plane.

Table 5.5: Line parameters.

Fixed parameters	Value
Length of the line	1.8 m
Diameter of the wire	2 mm
Left terminal	50 Ω
Variable parameters	Values
Height above the ground	0.1/0.2/0.3/0.4 m
Right terminal	short circuit/50 Ω
Orientation (ϕ)	0/-45°/-90°



Figure 5.15: Picture of the line.

5.11.4 Measurement of the induced voltage

A picture of the connection between the illuminated wire and the fibre optic link, for the voltage measurement, is shown in Figure 5.16.

An attenuator was placed before the transmitter in order to reduce the amplitude of the signal to the level (1 dBm) allowed by the transmitter. The connection between the attenuator and the transmitter was made as short as possible. In particular, the metallic enclosure of the transmitter was isolated from the ground, to avoid galvanic connection between the ground plane of the wire

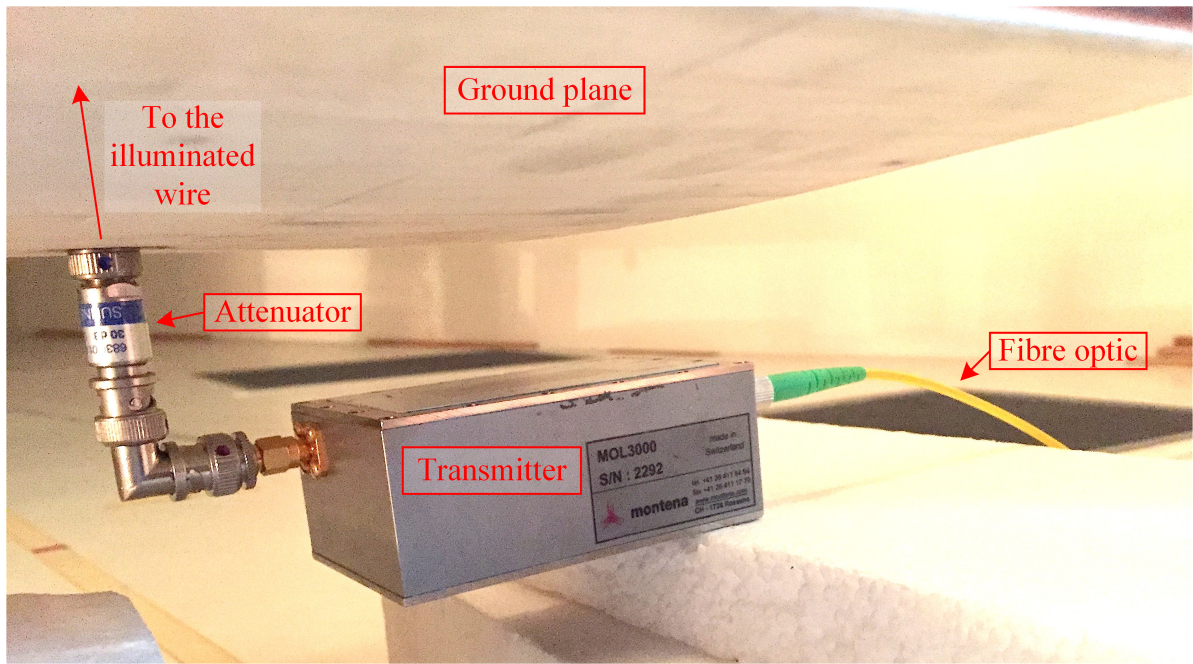


Figure 5.16: Picture of the voltage measurement.

and the ground plane of the GTEM cell, which could add artefacts to the measurement.

5.11.5 Modelling

The obtained measurement results are compared with the predictions of different models:

- the classical TL theory (Section 5.8);
- the TL theory with the proposed radiation resistance model for the vertical risers (Section 5.9);
- the proposed asymptotic theory (Section 5.6);
- numerical results obtained using NEC-4 (MoM) [175].

In all these models, both line and ground plane were considered perfect electric conductors. The incident field was considered to be a vertically polarised plane wave, whose amplitude was half the amplitude of the incident measured electric field, due to image theory.

5.11.6 Results

Field

As a first check, both vertical and horizontal components of the electric field were measured. As expected, the horizontal component was much smaller than the vertical one, allowing to neglect the horizontal component and measure only the vertical component.

For the sake of completeness, Figure 5.17 shows the vertical component of the electric field measured at all the 25 locations listed in Table 5.4 in the empty GTEM cell. Due to the $1/r$ attenuation of the field and the GTEM cell imperfections, the field is not exactly the same at all locations. However, according to Figure 5.17, the field is the most homogeneous between around 10 and 100 MHz.

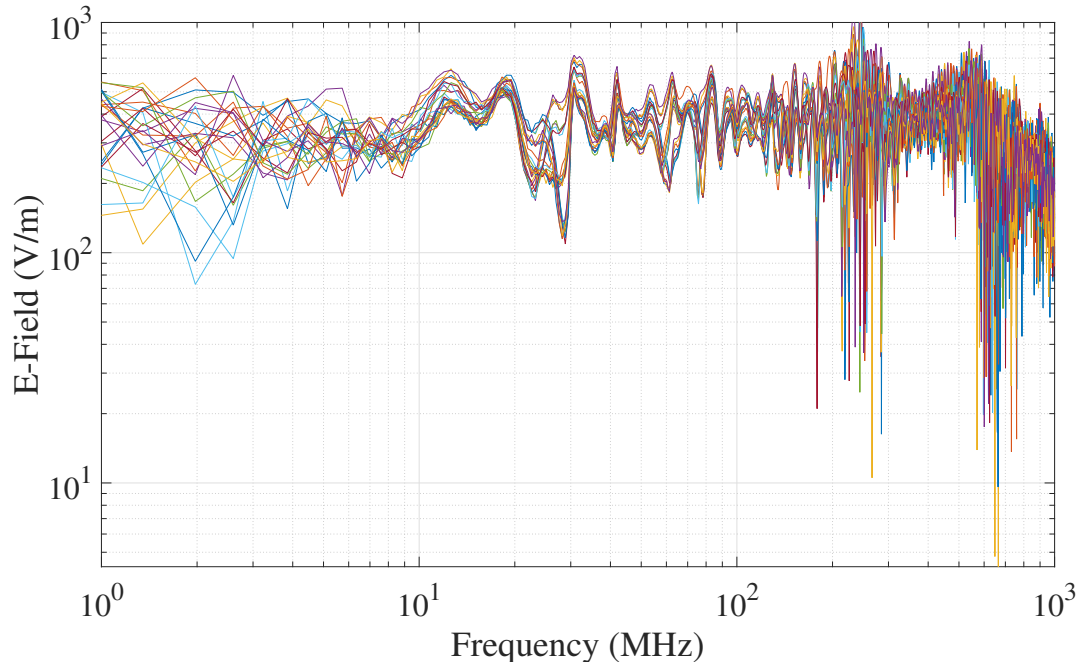


Figure 5.17: Vertical electric field amplitude at 25 locations in the cell, as a function of the frequency.

In the following, the field at location $(x = 0, y = 0, z = 40)$ was chosen as the reference exciting field.

Induced current

In the following measurements, a logarithmic distribution of the frequency points was used in order to have a good representation at low frequency.

The transfer function is computed as the ratio of the induced current and the incident electric field. Note that the incident electric field is half the measured exciting (incident + reflected) field, due to image theory.

Figure 5.18 shows the transfer function for the induced current in the right terminal for a height of 30 cm, an orientation of -90° and a terminal impedance at the left extremity of 50Ω .

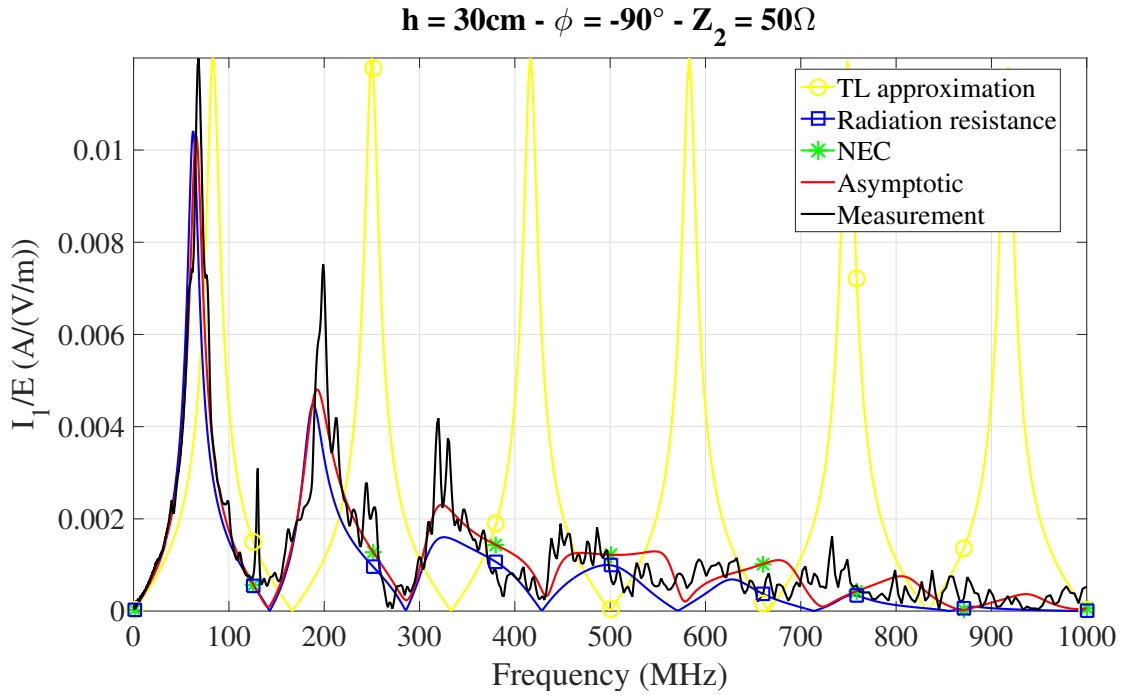


Figure 5.18: Transfer function current/field. Comparison between the classical TL theory (BLT), enhanced TL, NEC simulation, CST simulation and measurements. NEC and asymptotic results are essentially superimposed.

In this case, the TL theory has an upper frequency limit at about 50 MHz and shows a relatively good agreement within its domain of validity. At higher frequencies, the resonance frequencies and amplitudes are not well predicted. The proposed radiation resistance model provides more accurate resonance frequencies, and the amplitudes are also relatively well predicted at high frequency. The asymptotic theory and the full-wave simulation using NEC (Method of Moment) provide results that are essentially identical and in good agreement with measured values.

The results for other line parameters are presented in the appendix. Based on all these measurements, we can say that the classical transmission line provides accurate results at low frequencies, but the resonance frequencies and amplitude at high frequency are in general inaccurate. The radiation resistance model provides in general substantially better values for the resonance frequencies and amplitude, below and above the frequency limit of the transmission line theory. The asymptotic theory provides results in very good agreement with the results of the full-wave numerical method NEC, which could be taken as reference. The measurements, which may contain errors, are also close to the results obtained with NEC.

5.12 Concluding remarks

Based on the asymptotic theory of Tkachenko et al., we presented a theory and an efficient solution approach for the problem of electromagnetic field coupling to a long multi-conductor line with arbitrary terminations. The theory is applicable for a high-frequency plane wave electromagnetic field excitation, when the transmission line approximation is no longer valid.

Different approaches were proposed to compute the coefficients that feed the analytical expression for the current induced along the line. Using an iterative method, explicit mathematical expressions were derived, for the particular case of open-circuit lines. For the general case of arbitrary line terminations, an approach using auxiliary short lines and solved with a numerical code was proposed. At low frequencies, the proposed three-term formulation can be adapted to lossy lines and analytical expressions for the coefficients, providing another formulation for the classical transmission line theory.

The proposed method was shown to be very accurate taking as reference full-wave numerical solutions obtained using NEC-4. The use of the proposed approach to analyse high-frequency electromagnetic field coupling to long multi-conductor lines is considerably more effective than the traditional full-wave approach in terms of memory requirements and computational times.

In the framework of the classical transmission line theory, a distributed source model with radiation resistances was proposed for the vertical risers. The proposed model was shown to be more accurate than the classical theory, even at frequencies for which the cross-section cannot be considered electrically short.

Chapter 6

Application of the asymptotic theory to a lumped source excitation

6.1 Introduction

In Chapter 5, a high frequency model for the computation of the current induced by an external plane wave excitation was developed. In this chapter, the asymptotic theory is applied to a lumped source excitation.

First, the theory is developed in a procedure analogous to the one in the previous chapter. A method for the determination of the matrices of coupling and reflection coefficients is then presented. In the case of a single-conductor line, an expression for the current in the vertical risers is derived. At low frequencies, analytical expressions are derived for the scattering coefficients. The use of a radiation resistance allows to account for the radiation occurring near the line terminals. The developed models are validated using full-wave simulations and experimental measurements.

6.2 Derivation of the method

As for a plane wave excitation in Section 5.3, in order to analyse the response of a finite-length line, we will first examine semi-infinite lines.

6.2.1 Right semi-infinite line

The current in a right semi-infinite line such as the one depicted in Figure 6.1 and excited by lumped sources placed at its (left) terminal can be written as the sum of two terms:

$$\mathbf{I}_+(x) = \hat{\Psi}_+^0(x)\tilde{\mathbf{I}}_1 + \hat{\Psi}_+^s(x)\mathbf{I}_{s+} \quad (6.1)$$

where \mathbf{I}_{s+} is a vector of currents associated with the lumped sources placed at the terminal, and $\tilde{\mathbf{I}}_1$ is an additional vector of currents, the usefulness of which will become apparent afterwards. The ‘+’ subscript is used to indicate that we are assessing the effect of the left terminal. Equation (6.1) is valid along the whole line, and the functions $\hat{\Psi}_+(x)$ are *a priori* unknown, especially near the line terminal. However, in the asymptotic zone (II), $\hat{\Psi}_+(x)$ functions can be supposed to have the following functional forms:

$$\begin{aligned} \hat{\Psi}_+^0(x) &= \hat{\mathbf{I}}e^{jkx} + \hat{\mathbf{R}}_+e^{-jkx} \\ \hat{\Psi}_+^s(x) &= \hat{\mathbf{K}}_+e^{-jkx} \end{aligned} \quad (6.2)$$

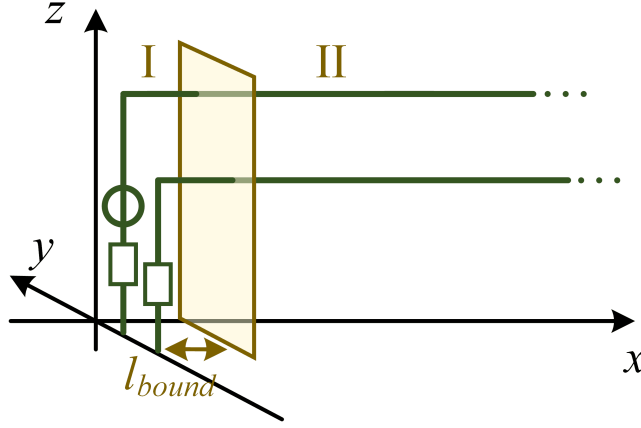


Figure 6.1: Schematic view of a right semi-infinite line excited by a lumped source.

where the matrix of reflection coefficients $\hat{\mathbf{R}}_+$ and the matrix of coupling coefficients $\hat{\mathbf{K}}_+$ were introduced and have to be determined. By introducing (6.2) into (6.1), one obtains:

$$\mathbf{I}_+(x) = \tilde{\mathbf{I}}_1 e^{jkx} + \left(\hat{\mathbf{R}}_+ \tilde{\mathbf{I}}_1 + \hat{\mathbf{K}}_+ \mathbf{I}_{s+} \right) e^{-jkx} \quad (6.3)$$

6.2.2 Left semi-infinite line

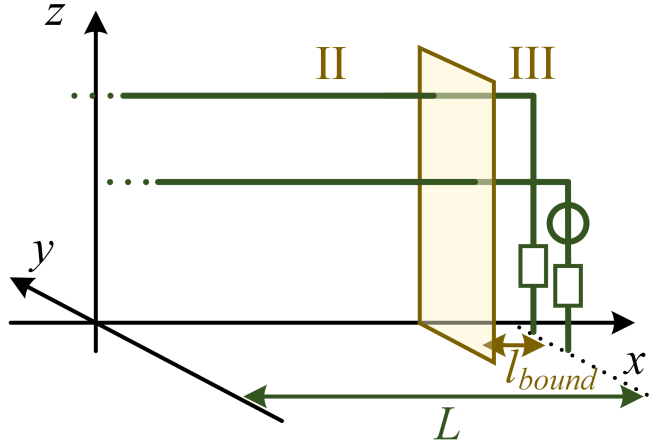


Figure 6.2: Schematic view of a left semi-infinite line excited by a lumped source.

A similar analysis is carried out for a left semi-infinite line (see Figure 6.2) whose terminal is at location $x = L$.

$$\mathbf{I}_-(x) = \hat{\Psi}_-^0(x-L) \tilde{\mathbf{I}}_2 + \hat{\Psi}_-^s(x-L) \mathbf{I}_{s-} \quad (6.4)$$

where \mathbf{I}_{s-} is a vector of currents associated to lumped sources placed at the terminal, and $\tilde{\mathbf{I}}_-$ is a vector of additional currents. In the asymptotic zone (II), $\hat{\Psi}_-(x)$ functions have the following form:

$$\begin{aligned} \hat{\Psi}_-^0(x) &= \hat{\mathbf{1}} e^{-jkx} + \hat{\mathbf{R}}_- e^{jkx} \\ \hat{\Psi}_-^s(x) &= \hat{\mathbf{K}}_- e^{jkx} \end{aligned} \quad (6.5)$$

where the matrices of coefficients $\hat{\mathbf{R}}_-$ and $\hat{\mathbf{K}}_-$ were introduced and have to be determined. By

introducing (6.5) into (6.4), one obtains:

$$\mathbf{I}_-(x) = \left(\hat{\mathbf{R}}_- \tilde{\mathbf{I}}_2 e^{-jkL} + \hat{\mathbf{K}}_- \mathbf{I}_{s-} e^{-jkL} \right) e^{jkx} + \tilde{\mathbf{I}}_2 e^{jkL} e^{-jkx} \quad (6.6)$$

6.2.3 Finite line

Let us connect the two semi-infinite lines together, in order to create a finite line, as shown in Figure 6.3.

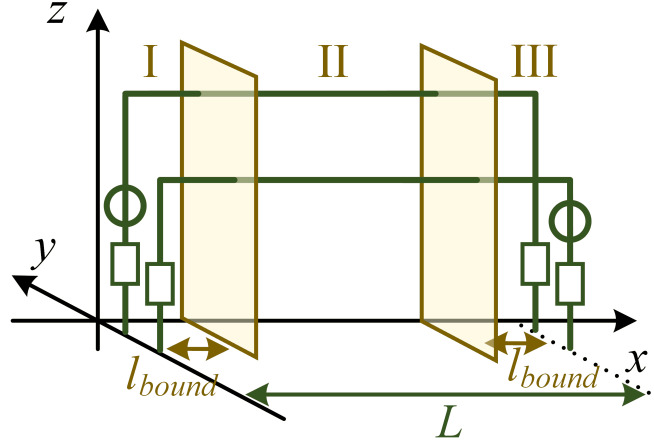


Figure 6.3: Schematic view of a multiconductor line excited by lumped sources.

Imposing that the current be the same in zone II for the two lines

$$\mathbf{I}(x) = \mathbf{I}_+(x) = \mathbf{I}_-(x) \quad (6.7)$$

leads to the following expression:

$$\mathbf{I}(x) = \mathbf{I}_1 e^{jkx} + \mathbf{I}_2 e^{-jkx} \quad (6.8)$$

with

$$\begin{aligned} \mathbf{I}_1 &= \tilde{\mathbf{I}}_1 = \hat{\mathbf{R}}_- \tilde{\mathbf{I}}_2 e^{-jkL} + \hat{\mathbf{K}}_- \mathbf{I}_{s-} e^{-jkL} \\ \mathbf{I}_2 &= \hat{\mathbf{R}}_+ \tilde{\mathbf{I}}_1 + \hat{\mathbf{K}}_+ \mathbf{I}_{s+} = \tilde{\mathbf{I}}_2 e^{jkL} \end{aligned} \quad (6.9)$$

For the sake of clarity, let us remove $\tilde{\mathbf{I}}_1$ and $\tilde{\mathbf{I}}_2$ from this system of equations:

$$\mathbf{I}_1 = \hat{\mathbf{R}}_- \mathbf{I}_2 e^{-2jkL} + \hat{\mathbf{K}}_- \mathbf{I}_{s-} e^{-jkL} \quad (6.10)$$

$$\mathbf{I}_2 = \hat{\mathbf{R}}_+ \mathbf{I}_1 + \hat{\mathbf{K}}_+ \mathbf{I}_{s+} \quad (6.11)$$

Solving this system of equations for \mathbf{I}_1 and \mathbf{I}_2 yields:

$$\begin{aligned} \mathbf{I}_1 &= \left(\hat{\mathbf{1}} - \hat{\mathbf{R}}_- \hat{\mathbf{R}}_+ e^{-2jkL} \right)^{-1} \left(\hat{\mathbf{R}}_- \hat{\mathbf{K}}_+ \mathbf{I}_{s+} e^{-2jkL} + \hat{\mathbf{K}}_- \mathbf{I}_{s-} e^{-jkL} \right) \\ \mathbf{I}_2 &= \left(\hat{\mathbf{1}} - \hat{\mathbf{R}}_+ \hat{\mathbf{R}}_- e^{-2jkL} \right)^{-1} \left(\hat{\mathbf{R}}_+ \hat{\mathbf{K}}_- \mathbf{I}_{s-} e^{-jkL} + \hat{\mathbf{K}}_+ \mathbf{I}_{s+} \right) \end{aligned} \quad (6.12)$$

Hence, if the four matrices of coefficients are known, the current along the line in zone II can be determined. To determine the current in zones I and III, $\hat{\Psi}(x)$ functions have also to be known in these zones.

6.2.4 Determination of the matrices of coefficients

Let us consider lines, with the same cross-section and terminal impedances, but with a much shorter length $L_1 < L$ and excited by a lumped source only at the left terminal, or at the right terminal, on different wires. This is illustrated in the case of a two-wire line in Figure 6.4.

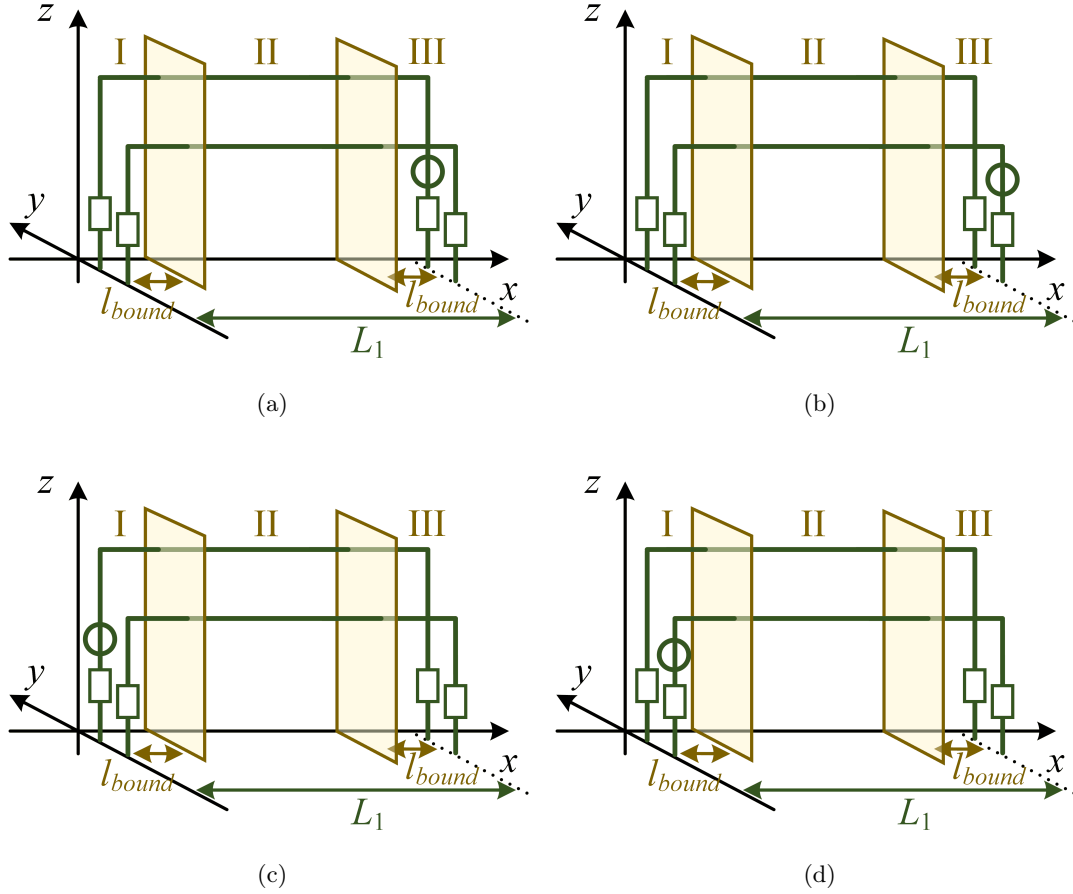


Figure 6.4: Example of shorter auxiliary lines: lumped source placed (a) at the right terminal, on the first wire (the current is $\mathbf{I}_-^1(x)$); (b) at the right terminal, on the second wire (the current is $\mathbf{I}_-^2(x)$); (c) at the left terminal, on the first wire (the current is $\mathbf{I}_+^1(x)$); (d) at the left terminal, on the second wire (the current is $\mathbf{I}_+^2(x)$).

Using for example a full-wave numerical code, the currents along the short auxiliary lines can be determined. These currents are named $\mathbf{I}_+^n(z)$ when the lumped source is placed in the left terminal on wire number n , and $\mathbf{I}_-^n(x)$ when the lumped source is placed in the right terminal on wire number n , with $n = 1, \dots, N$.

In zone II, $\mathbf{I}_+^n(x)$ and $\mathbf{I}_-^n(x)$ are written in the form of (6.8):

$$\begin{aligned} \mathbf{I}_+^n(x) &= \mathbf{I}_{1+}^n e^{jkx} + \mathbf{I}_{2+}^n e^{-jkx} \\ \mathbf{I}_-^n(x) &= \mathbf{I}_{1-}^n e^{jkx} + \mathbf{I}_{2-}^n e^{-jkx} \end{aligned} \quad (6.13)$$

where the coefficients $\mathbf{I}_{12,\pm}^n$ can be determined by the methods presented in Section 5.6.2, for

example by the method of least squares. Equation (6.10) applies in particular to these currents:

$$\begin{aligned}\mathbf{I}_{1+}^n &= \hat{\mathbf{R}}_- \mathbf{I}_{2+}^n e^{-2jkL_1} + \hat{\mathbf{K}}_- \mathbf{I}_{s-}^n e^{-jkL_1} \\ \mathbf{I}_{1-}^n &= \hat{\mathbf{R}}_- \mathbf{I}_{2-}^n e^{-2jkL_1}\end{aligned}\quad (6.14)$$

Similarly, according to (6.11)

$$\begin{aligned}\mathbf{I}_{2+}^n &= \hat{\mathbf{R}}_+ \mathbf{I}_{1+}^n \\ \mathbf{I}_{2-}^n &= \hat{\mathbf{R}}_+ \mathbf{I}_{1-}^n + \hat{\mathbf{K}}_+ \mathbf{I}_{s+}^n\end{aligned}\quad (6.15)$$

The non-existing source terms were removed in (6.14) and (6.15).

The current vectors can be grouped into matrices:

$$\hat{\mathbf{I}}_{a\pm} := \begin{bmatrix} \mathbf{I}_{a\pm}^1 & \mathbf{I}_{a\pm}^2 & \cdots & \mathbf{I}_{a\pm}^N \end{bmatrix} \quad (6.16)$$

with $a = 1, 2$ or s . Using these definitions in (6.14) and (6.15) leads to:

$$\begin{aligned}\hat{\mathbf{I}}_{1+} &= \hat{\mathbf{R}}_- \hat{\mathbf{I}}_{2+} e^{-2jkL_1} + \hat{\mathbf{K}}_- \hat{\mathbf{I}}_{s-} e^{-jkL_1} \\ \hat{\mathbf{I}}_{1-} &= \hat{\mathbf{R}}_- \hat{\mathbf{I}}_{2-} e^{-2jkL_1} \\ \hat{\mathbf{I}}_{2+} &= \hat{\mathbf{R}}_+ \hat{\mathbf{I}}_{1+} \\ \hat{\mathbf{I}}_{2-} &= \hat{\mathbf{R}}_+ \hat{\mathbf{I}}_{1-} + \hat{\mathbf{K}}_+ \hat{\mathbf{I}}_{s+}\end{aligned}\quad (6.17)$$

Hence, the matrices of coefficients can be formally written as:

$$\begin{aligned}\hat{\mathbf{R}}_+ &= \hat{\mathbf{I}}_{2+} \hat{\mathbf{I}}_{1+}^{-1} \\ \hat{\mathbf{R}}_- &= \hat{\mathbf{I}}_{1-} \hat{\mathbf{I}}_{2-}^{-1} e^{2jkL_1} \\ \hat{\mathbf{K}}_+ &= \left(\hat{\mathbf{I}}_{2-} - \hat{\mathbf{I}}_{2+} \hat{\mathbf{I}}_{1+}^{-1} \hat{\mathbf{I}}_{1-} \right) \hat{\mathbf{I}}_{s+}^{-1} \\ \hat{\mathbf{K}}_- &= \left(\hat{\mathbf{I}}_{1+} - \hat{\mathbf{I}}_{1-} \hat{\mathbf{I}}_{2-}^{-1} \hat{\mathbf{I}}_{2+} \right) \hat{\mathbf{I}}_{s-}^{-1} e^{jkL_1}\end{aligned}\quad (6.18)$$

6.2.5 Left terminal

The current near the left terminal, in zone I, is given by (6.1):

$$\begin{aligned}\mathbf{I}_+^n(x) &= \hat{\Psi}_+^0(x) \mathbf{I}_{1+}^n \\ \mathbf{I}_-^n(x) &= \hat{\Psi}_+^0(x) \mathbf{I}_{1-}^n + \hat{\Psi}_+^s(x) \mathbf{I}_{s+}^n\end{aligned}\quad (6.19)$$

Similarly to (6.16), let us group the currents into matrices:

$$\hat{\mathbf{I}}_{\pm}(x) := \begin{bmatrix} \mathbf{I}_{\pm}^1(x) & \mathbf{I}_{\pm}^2(x) & \cdots & \mathbf{I}_{\pm}^N(x) \end{bmatrix} \quad (6.20)$$

and introduce this definition into (6.19):

$$\begin{aligned}\hat{\mathbf{I}}_+(x) &= \hat{\Psi}_+^0(x) \hat{\mathbf{I}}_{1+} \\ \hat{\mathbf{I}}_-(x) &= \hat{\Psi}_+^0(x) \hat{\mathbf{I}}_{1-} + \hat{\Psi}_+^s(x) \hat{\mathbf{I}}_{s+}\end{aligned}\quad (6.21)$$

Hence the functions $\widehat{\Psi}(x)$ in zone I can be formally written as follows:

$$\begin{aligned}\widehat{\Psi}_+^0(x) &= \widehat{\mathbf{I}}_+(x) \widehat{\mathbf{I}}_{1+}^{-1} \\ \widehat{\Psi}_+^s(x) &= \left(\widehat{\mathbf{I}}_-(x) - \widehat{\mathbf{I}}_+(x) \widehat{\mathbf{I}}_{1+}^{-1} \widehat{\mathbf{I}}_{1-} \right) \widehat{\mathbf{I}}_{s+}^{-1}\end{aligned}\quad (6.22)$$

6.2.6 Right terminal

A similar development is done for the right terminal, starting from (6.4):

$$\begin{aligned}\mathbf{I}_+^n(x) &= \widehat{\Psi}_-^0(x - L_1) \mathbf{I}_{2+}^n e^{-jkL_1} + \widehat{\Psi}_-^s(x - L_1) \mathbf{I}_{s-}^n \\ \mathbf{I}_-^n(x) &= \widehat{\Psi}_-^0(x - L_1) \mathbf{I}_{2-}^n e^{-jkL_1}\end{aligned}\quad (6.23)$$

grouping the equations into matrices:

$$\begin{aligned}\widehat{\mathbf{I}}_+(x) &= \widehat{\Psi}_-^0(x - L_1) \widehat{\mathbf{I}}_{2+} e^{-jkL_1} + \widehat{\Psi}_-^s(x - L_1) \widehat{\mathbf{I}}_{s-} \\ \widehat{\mathbf{I}}_-(x) &= \widehat{\Psi}_-^0(x - L_1) \widehat{\mathbf{I}}_{2-} e^{-jkL_1}\end{aligned}\quad (6.24)$$

and finally obtaining the expression for the $\widehat{\Psi}(x)$ functions in zone III:

$$\begin{aligned}\widehat{\Psi}_-^0(x) &= \widehat{\mathbf{I}}_-(x + L_1) \widehat{\mathbf{I}}_{2-}^{-1} e^{jkL_1} \\ \widehat{\Psi}_-^s(x) &= \left(\widehat{\mathbf{I}}_+(x + L_1) - \widehat{\mathbf{I}}_-(x + L_1) \widehat{\mathbf{I}}_{2-}^{-1} \widehat{\mathbf{I}}_{2+} \right) \widehat{\mathbf{I}}_{s-}^{-1}\end{aligned}\quad (6.25)$$

6.3 Extension for the risers

The presented procedure allows to compute the current in the horizontal lines. However, it can be also interesting to know the current along the vertical risers, especially at the ground level. For this reason, we here present an extension of the method to compute the current in the vertical lines, in the case of a single-conductor line. The extension to multiconductor lines with risers having different heights is not straightforward.

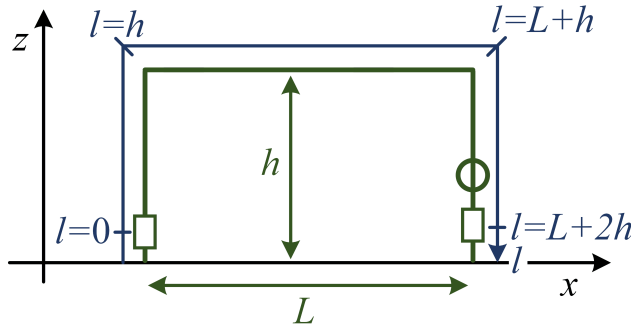


Figure 6.5: Definition of a coordinate system which follows the wire, risers included. Adapted from [120].

The overall procedure presented in Section 6.2 is kept the same. The main idea is to consider the vertical part as a part of the line (see e.g. [124, 176]). As shown in Figure 6.5, the coordinate along the line goes from 0 (left vertical terminal at the ground level) to $L + 2h$ (right vertical terminal at the ground level). Mathematically, the expression for the current along this new coordinate is computed by replacing L by $L + 2h$ and L_1 by $L_1 + 2h$ in (6.4), (6.12), (6.18) and (6.25).

6.4 Low frequency approximation

At low frequencies, expressions given for the zone II are supposed to be valid along the whole line. Applying the boundary conditions and according to this assumption, the expressions for the coefficients read:

$$\begin{aligned}\hat{\mathbf{R}}_{\pm} &= \left(\hat{\mathbf{Z}}_C + \hat{\mathbf{Z}}_{1_2}\right)^{-1} \left(\hat{\mathbf{Z}}_C - \hat{\mathbf{Z}}_{1_2}\right) \\ \hat{\mathbf{K}}_{\pm} &= \left(\hat{\mathbf{Z}}_C + \hat{\mathbf{Z}}_{1_2}\right)^{-1} \hat{\mathbf{Z}}_{1_2}\end{aligned}\tag{6.26}$$

6.5 Radiation resistance model

The radiation resistance model defined in Section 5.9 can easily be adapted to a lumped excitation. As the field excitation is removed, two modifications to the classical theory remain:

- The length of the line is considered to be $L + 2h$ instead of L (see Figure 6.5).
- The radiation effect from the line is modelled by an additional terminal impedance equal to the radiation resistance of a monopole of height h above the ground (see (5.137))

6.6 Validation by simulation

6.6.1 Parameters

A three-wire line above a ground plane is excited with a voltage source placed on the first wire at the left terminal. The parameters of the line are presented in Table 6.1.

Table 6.1: Line parameters.

Parameter	Value
Length of the line	10 m
Horizontal positions of wires	-0.2;0.0;0.1 m
Vertical positions of wires	0.4;0.5;0.3 m
Diameters of wires	1 mm
Left terminal	diag(50; 50; 50) Ω
Right terminal	diag(50; 50; 50) Ω

The simulation parameter used for the NEC simulations is 30 segments per wavelength. The l_{bound} length was chosen as twice the maximal height, that is 1 m. This rule of thumb applies for intermediate frequency when the wavelength is in the order of the cross-section, but l_{bound} is expected to be larger at higher frequencies. The length of the auxiliary line was chosen as 5 times l_{bound} , that is 5 m.

6.6.2 Results

The current in the third wire at the right terminal predicted by the proposed method is very similar to the prediction of NEC (see Figure 6.6).

In Figure 6.6, the classical TL model provides results that are accurate only well below its upper frequency limit of validity (around 30 MHz in this case). This poor behaviour is probably due to

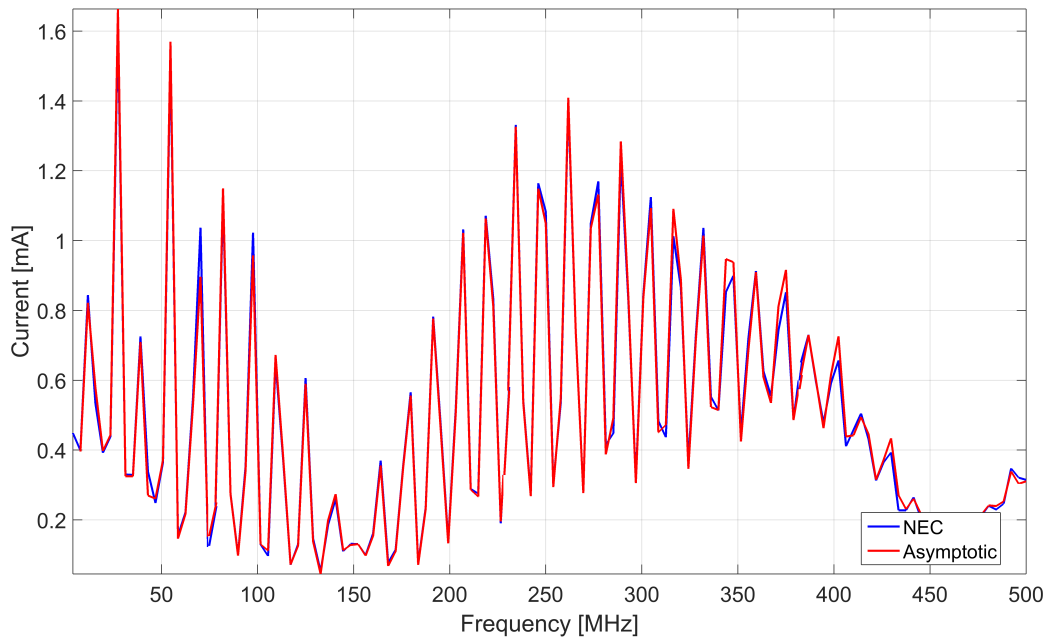


Figure 6.6: Induced current at the right terminal, in the second wire, as a function of the frequency. Predictions of NEC and asymptotic theory.

the coupling between the vertical risers, which is not considered by the TL theory, but significantly modifies the reflection coefficients.

As can be seen from Figure 6.7, the current in the second wire predicted by the proposed method at 500 MHz is very similar to the NEC predictions.

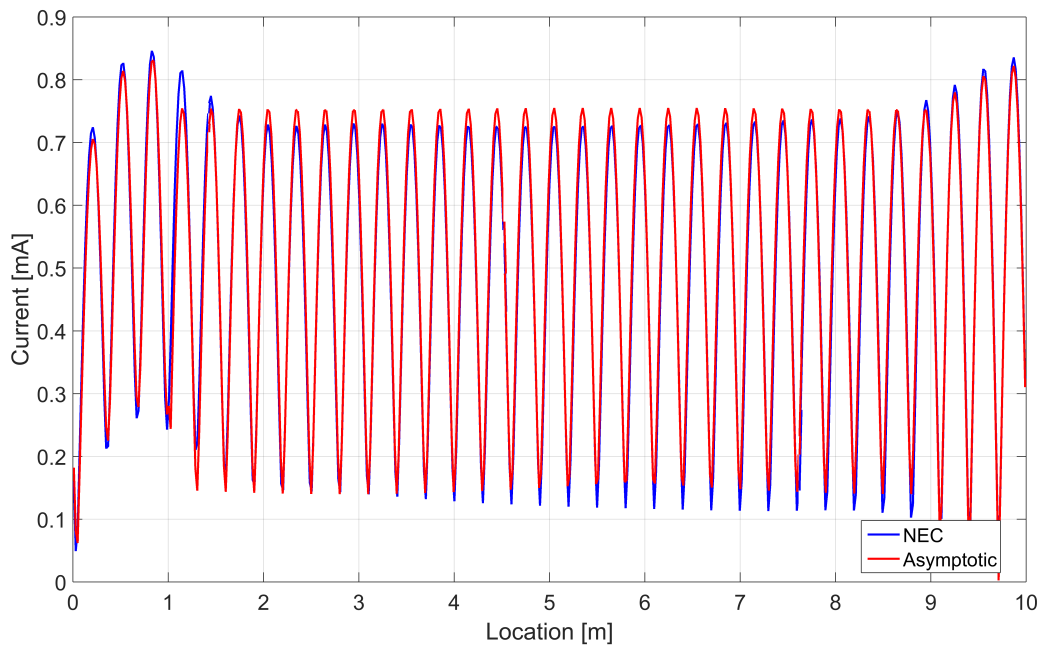


Figure 6.7: Induced current along the line in the second wire, at 500 MHz. Predictions of TL theory, NEC and asymptotic theory. Top: current along the whole line; bottom: zoom on the left extremity of the line.

A comparison between the ‘asymptotic’ reflection coefficient and the classical one is presented in Figure 6.8. The reflection coefficient provided by the asymptotic theory tends to be equal to the

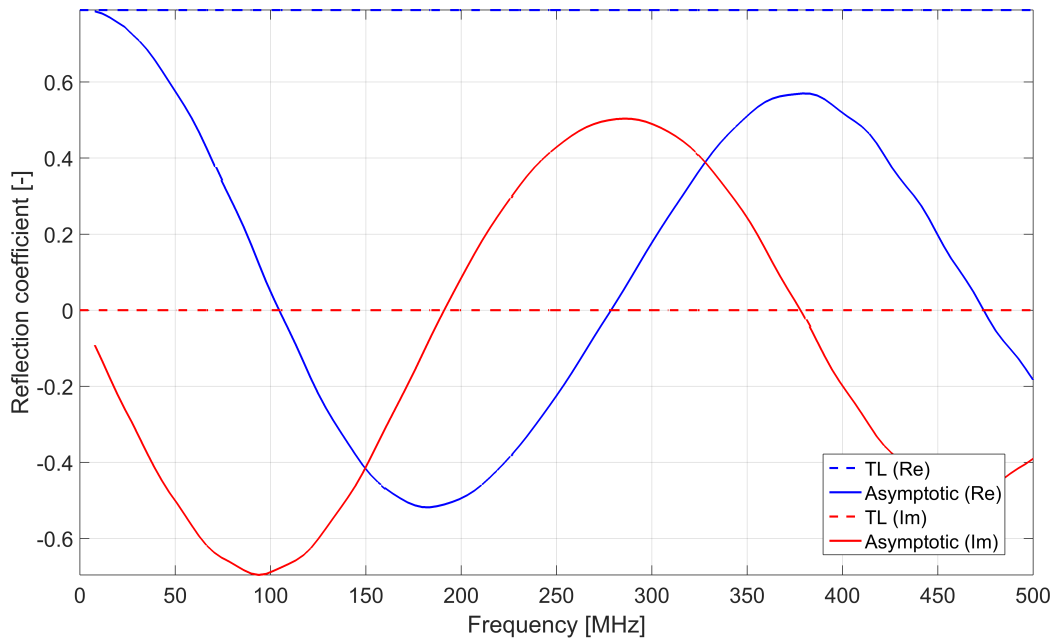


Figure 6.8: Real (Re) and imaginary (Im) part of the reflection coefficient at the left terminal. Comparison between TL and asymptotic theory.

one provided by the TL theory at low frequencies. At higher frequencies, the propagation along the risers leads to a phase shift which takes a cosine-like shape for the real part and a sine-like shape for the imaginary part.

6.7 Experimental validation

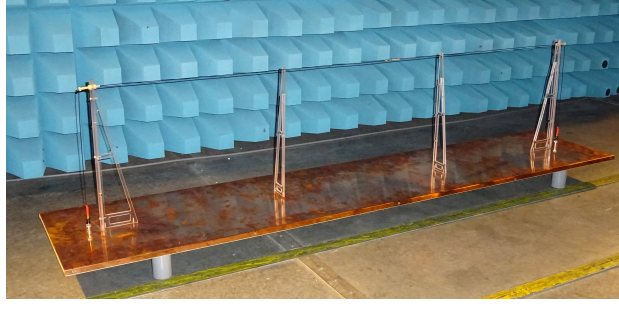
6.7.1 Setup

A single wire line above a ground plane with the parameters presented in Table 6.2 was used. The measurements were done considering four different heights of the wire above the ground, the other parameters remaining unchanged.

Table 6.2: Line parameters.

Parameter	Value
Length of the line	1.8 m
Height above the ground h	10; 20; 30; 40 cm
Diameters of wire	2 mm
Left terminal	50 Ω
Right terminal	50 Ω

A picture of the line is shown in Figure 6.9. The wire and ground plane are made of copper. Four towers in polycarbonate support the wire, possibly at different heights.

Figure 6.9: Picture of the line (with $h = 40$ cm)

As shown in Figure 6.10, a ZVRE Rhode & Schwarz vector network analyser (VNA) was connected with coaxial cables to the terminals of the line. The measured parameter is the S_{21} parameter, which corresponds to terminating the line by $50\ \Omega$ loads. A reference voltage is injected at the first terminal and the voltage at the second terminal is measured.

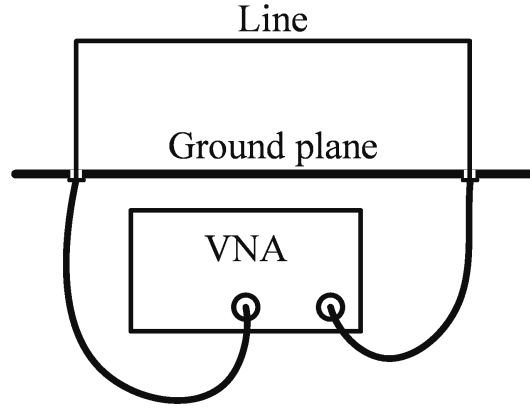


Figure 6.10: Scheme of the experimental setup.

The obtained experimental results are compared in the frequency domain with simulations obtained using NEC, asymptotic theory and classical TL.

6.7.2 Results

Comparison results in the frequency domain are shown in Figures 6.11–6.14. Figure 6.11 shows a comparison between the measurements, the classical TL model, NEC simulations and the proposed asymptotic method, with the parameters given in Table 6.2 and $h = 10$ cm. At low frequencies, (that is here below around 1 MHz) the line is almost “transparent” and the voltage is completely transmitted to the second terminal of the line. The voltage imposed by the source is divided by 2 because the terminal loads are the same. At higher frequencies, the mismatch between the $50\ \Omega$ source and the $318\ \Omega$ characteristic impedance of the line reduces the transmitted voltage down to around 0.15 V and resonances appear.

The transmission line theory is supposed to be valid up to around 150 MHz in this case, and all models provide results that agree well with the measurements up to this frequency. At higher frequencies, the additional length due to the vertical risers starts to shift the resonance frequencies, and the radiation of the line starts to affect the amplitude response of the line considerably. The phenomena are well predicted both by the asymptotic model and by NEC simulations, and also by the modified TL model which includes an additional length and a radiation resistance.

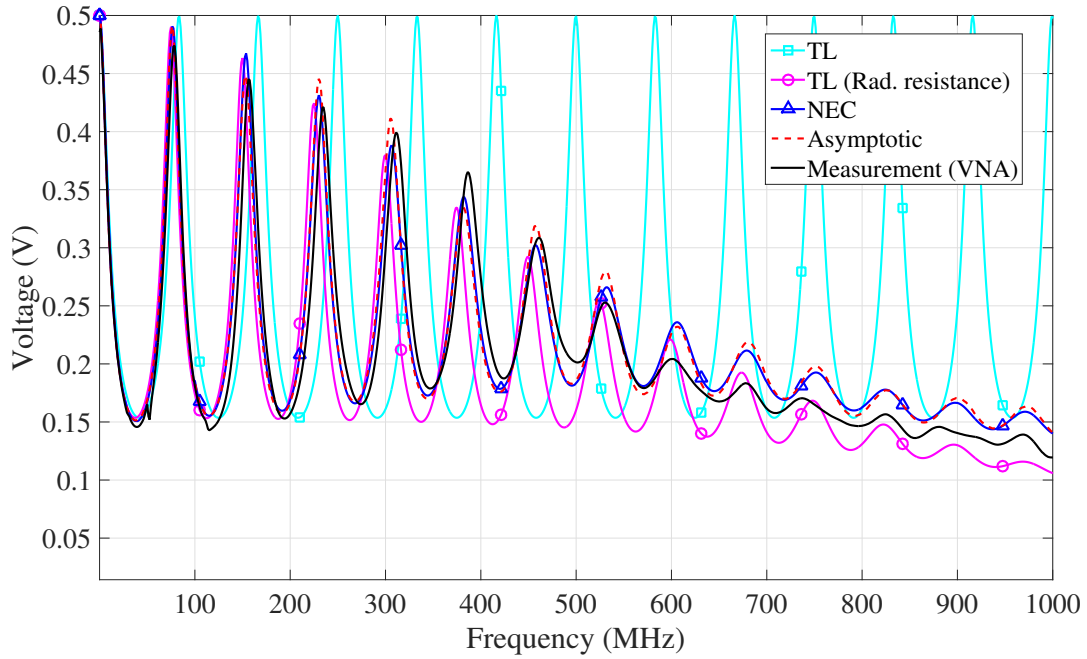


Figure 6.11: Comparison in the frequency domain between the classical TL theory, the TL-based radiation resistance model, the asymptotic theory, NEC simulations and measurements, in the case $h = 10$ cm.

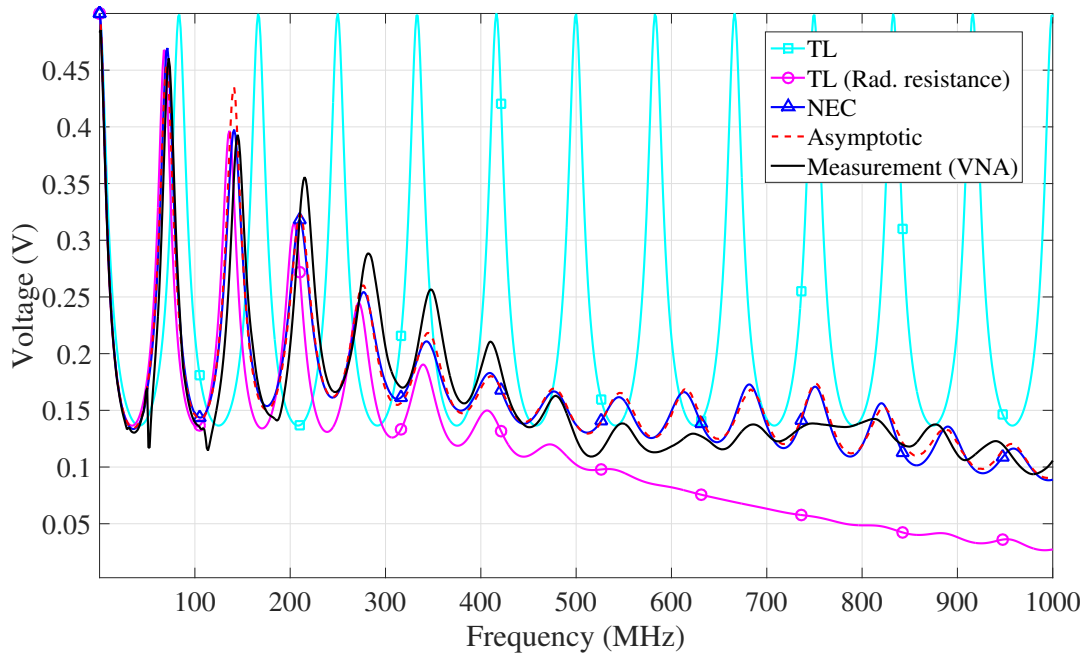


Figure 6.12: Comparison in the frequency domain between the classical TL theory, the TL-based radiation resistance model, the asymptotic theory, NEC simulations and measurements, in the case $h = 20$ cm

The same general conclusions can be drawn from Figures 6.12–6.14 as from Figures 6.11, while considering that the frequency limit is associated with the line height above the ground. However, the radiation resistance seems to attenuate the signal too much at high frequencies. A more complex model for this resistance could perhaps produce more accurate results. In any case, the modelling of the risers pushes the accuracy of the TL theory substantially higher than the classical upper limit.

Some errors affect the measurements, possibly due to the limited size of the ground, and the

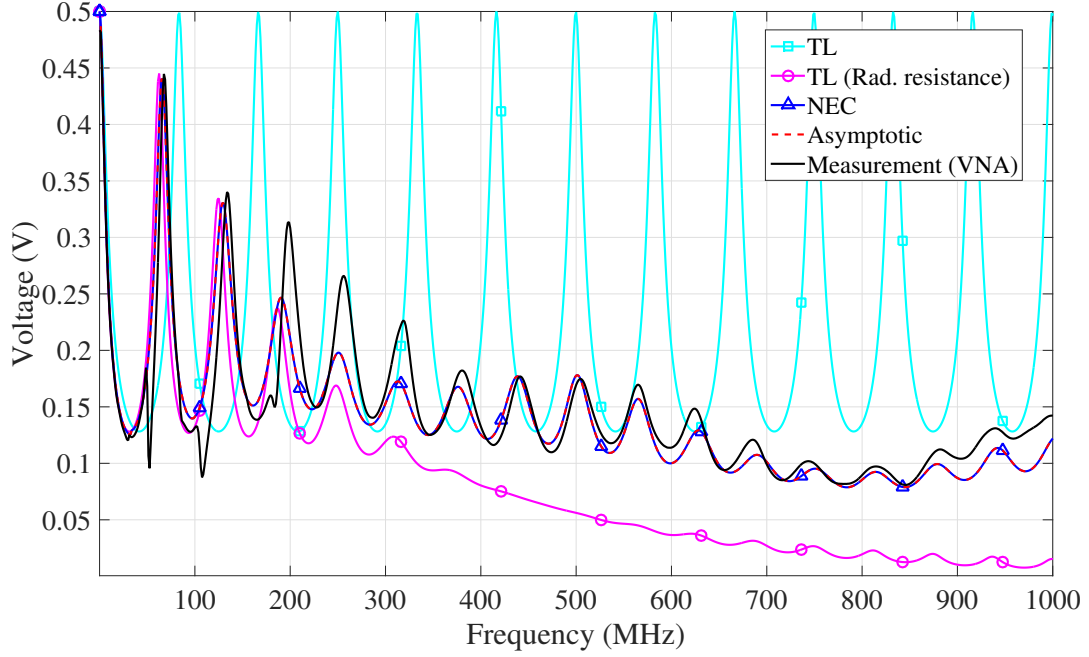


Figure 6.13: Comparison in the frequency domain between the classical TL theory, the TL-based radiation resistance model, the asymptotic theory, NEC simulations and measurements, in the case $h = 30$ cm.

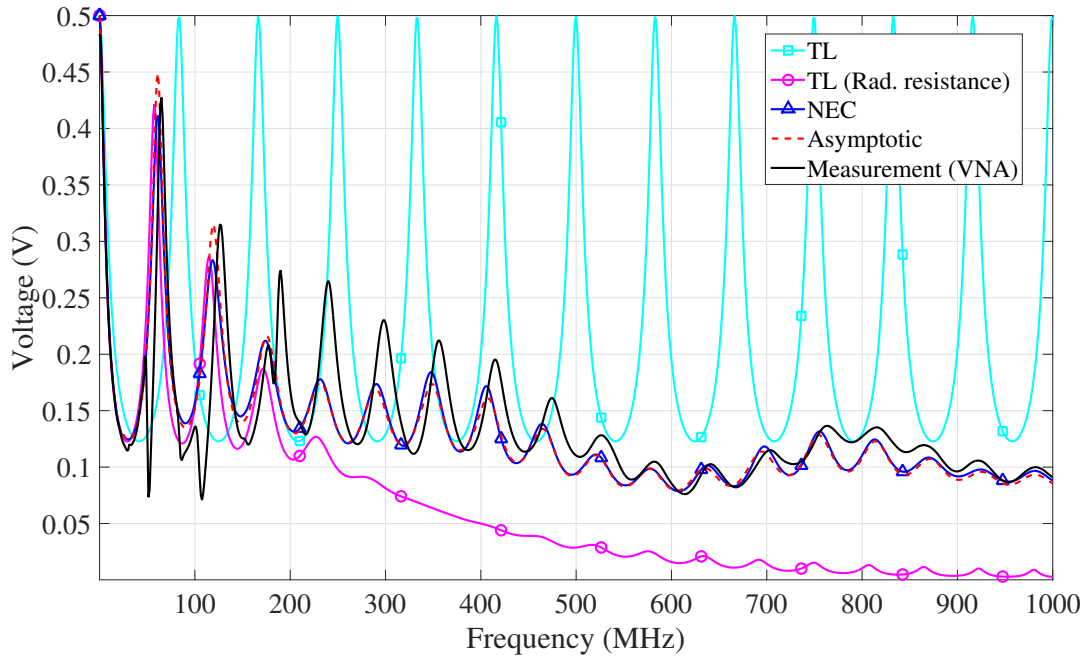


Figure 6.14: Comparison in the frequency domain between the classical TL theory, the TL-based radiation resistance model, the asymptotic theory, NEC simulations and measurements, in the case $h = 40$ cm.

error seems to increase as the height of the line increases.

The prediction of the TL theory is very good in its domain of validity (up to about 150 MHz in Figure 6.11 and 37 MHz in Figure 6.14), but the resonance frequencies and the amplitude are not accurate at higher frequencies. The asymptotic theory essentially yields the same results as NEC, and it corresponds well to the measurements.

A comparison between the ‘asymptotic’ reflection coefficient and the classical one is presented in Figure 6.15. The precision (stability) of the proposed method is reduced at low frequencies due

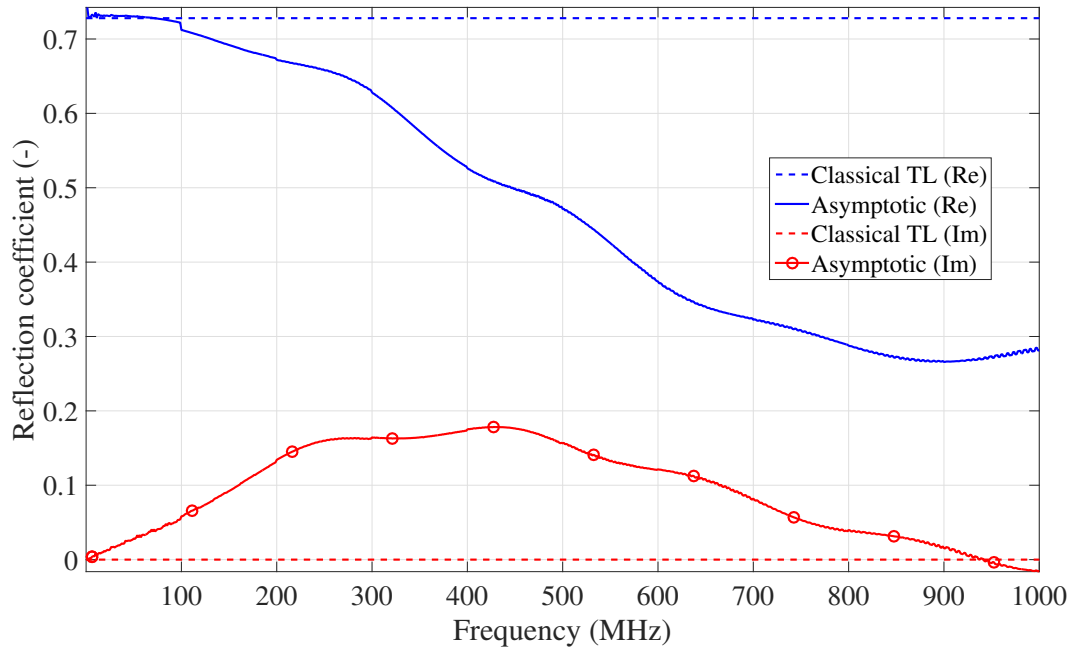


Figure 6.15: Real (Re) and imaginary (Im) part of the reflection coefficient at the left terminal, in the case $h = 10$ cm. Comparison between TL and asymptotic theory.

to the electric shortness of the line. However, the reflection coefficient provided by the asymptotic theory tends to be equal to the one provided by the TL theory at low frequencies. At higher frequencies, the amplitude of the reflection coefficient tends to decrease as the frequency increases, due to the radiation of the riser which acts as additional losses in the terminal.

6.8 Concluding remarks

The asymptotic theory was applied to a line excited by lumped sources. In absence of an external electromagnetic field, the current along the line can be expressed by a two-term equation (as opposed to the three-term formulation when an exciting field is present). Analytical expressions were obtained for the coefficient matrices at low frequencies, and a methodology was proposed for the computation at high frequencies. It was shown that the use of the radiation resistance is an efficient approach to extend the validity of the classical TL theory, taking into account radiation effects at the line terminals. The proposed models were validated by full-wave simulations and measurements.

Future work could include the improvement of the radiation resistance model, because the proposed model in some way overestimates the value of the resistance at very high frequencies. One possibility would be to use the approximation of the current in the vertical riser to compute the radiated power and hence refine the current in a one-iteration process. Another challenge would be to develop a multi-conductor version of the radiation resistance model. The main difficulties could be the different length of the vertical risers and the cross-coupling between them: the power radiated by one riser may couple to another riser.

Chapter 7

Conclusion and perspectives

7.1 Summary

In the first part, we discussed the use of the Electromagnetic Time Reversal (EMTR) method to locate lightning strikes. After a brief description of EMTR and its application to lightning location, we demonstrated mathematically that the Time-of-Arrival method can be seen as a special case of EMTR. We proposed three different models of back-propagation to address the issue of EMTR not being invariant for lossy media. Two sets of simulations were carried out to evaluate the accuracy of the proposed methods.

The first set of simulations was performed using numerically generated fields, and the proposed algorithm was shown to give very accurate results even when the soil is not perfectly conducting. In particular, it was shown that considering a model in which losses are inverted in the back-propagation yields theoretically exact results for the source location. We also showed that a lack of access to the complete recorded waveforms may lead to higher location errors, although the computed errors were found to be within the range of performance of the present LLSs.

A second set of simulations was performed using the sensor data reported by the Austrian Lightning Location System. The locations obtained by way of the EMTR method using only the available sensor data (amplitude, arrival time and time-to-peak), were observed to be within a few kilometres of the locations estimated by the LLS. Possible reasons for the discrepancy were discussed.

In the second part, based on the asymptotic theory of Tkachenko et al., we presented a theory and an efficient solution to the problem of electromagnetic field coupling to a long multiconductor line with arbitrary terminations. The theory is applicable for a high-frequency plane wave electromagnetic field excitation, when the transmission line approximation is no longer valid.

Different approaches were suggested to compute the coefficients that feed the analytical expression for the current induced along the line. Using an iterative method, mathematical expressions were derived for the particular case of open-circuit lines. For the general case of arbitrary line terminations, an approach using auxiliary short lines, solved with a numerical code was proposed. At low frequencies, the proposed three-term formulation can be adapted to lossy lines and analytical expressions for the coefficients, providing a new and elegant formulation for the classical transmission line theory.

The proposed method was shown to be very accurate, taking as reference full-wave numerical solutions obtained using NEC-4. The use of the suggested approach to analyse high-frequency electromagnetic field coupling to long multiconductor lines is considerably more effective than the traditional full-wave approach in terms of memory requirements and computational times.

In the framework of the classical transmission line theory, a distributed source model with radiation resistances was proposed for the vertical risers. The proposed model was shown to be more accurate than the classical theory, even at frequencies for which the cross-section cannot be considered electrically short.

The asymptotic theory was also extended to lumped excitation of multiconductor lines. In absence of an external electromagnetic field, the current along the line can be expressed by a two-term equation (as opposed to the three-term formulation when an exciting field is present). Analytical expressions were obtained for the coefficient matrices at low frequencies, and a methodology was proposed for their computation at high frequencies. It was shown that the use of the radiation resistance is an efficient approach to extend the validity of the classical TL theory, taking into account radiation effects at the line terminals. The proposed models were validated by full-wave simulations and measurements.

7.2 Original contributions

The main original contributions of this thesis are summarised in what follows.

- We showed that EMTR was applicable for the lightning location in the case of non-ideal propagation media. In particular, back-propagation models were proposed to discuss the application of EMTR to lossy grounds and were validated by simulations using numerically-generated fields and experimental data from lightning location systems. Time reversal can potentially increase the accuracy of current lightning location systems as it uses the complete waveform of the field to calculate the location of the strike point.
- The asymptotic theory was successfully applied to the problem of field coupling to a multiconductor line. We extended the available theory to multiconductor lines and proposed an algorithm for the computation of the current induced in a line with arbitrary terminations.
- Mathematical expressions for the matrix of scattering and reflection coefficients in the particular case of an open-circuit terminated line were proposed and validated. We showed that the expression obtained for the reflection coefficient can be reduced to available results in the literature in the case of a single-conductor line.
- A method for the computation of the current along the vertical risers in the case of a single-conductor line was proposed. This method requires only a small adaptation of the general asymptotic method and provides results that are in good agreement with full-wave methods.
- The asymptotic theory was extended to multiconductor lines excited by lumped sources. An algorithm for the computation of the current propagating in a line with arbitrary terminations was proposed.
- An approximate, TL-based analytical model in which the high-frequency radiation effects are taken into account through lumped radiation resistances was proposed. This approximate model can be straightforwardly implemented, and was shown to provide better results than does the classical transmission line theory.

7.3 Perspectives

Should LLS provide more accurate information in the future, the EMTR method which takes advantage of the whole waveform of the measured fields (including amplitude and time of arrival),

may be very promising in terms of achievable location accuracy and detection efficiency.

It is also possible that progress in the back-propagation models will lead to improvements in the accuracy over those obtained by current LLS. In particular, a 3D model, for example using FDTD (finite difference time domain), could be implemented in order to take the topography (mountains,...) and inhomogeneity of the soil into account during the back-propagation phase. In order to run the algorithm in real time, special attention should be paid to the computation optimisation.

Moreover, in order to test and develop the present proposed algorithms, a more complete experimental data set would be required. These data would include the exact location of strikes and complete field waveforms measured at different locations and synchronised by GPS.

The computation of the current along the vertical risers using asymptotic theory in the case of a multiconductor line remains a challenging task and should be considered in future work. Future work could also include the development a multiconductor version of the radiation resistance model developed for a single-wire line. The main challenge would be how to deal with the different lengths of the vertical risers and the cross-coupling between them: the power radiated by one riser can couple to another riser.

Appendix A

Comparison between model predictions and experimental data

This Appendix presents simulation results obtained using the various models described in Chapter 5 compared with experimental data (which were not shown in Section 5.11.6). The used models are classical transmission line (TL) theory, TL theory with radiation resistances, NEC-4 numerical simulations, and the asymptotic method. A list of the figures is presented in Table A.1. The parameters which are not mentioned in this table are given in Table 6.2 .

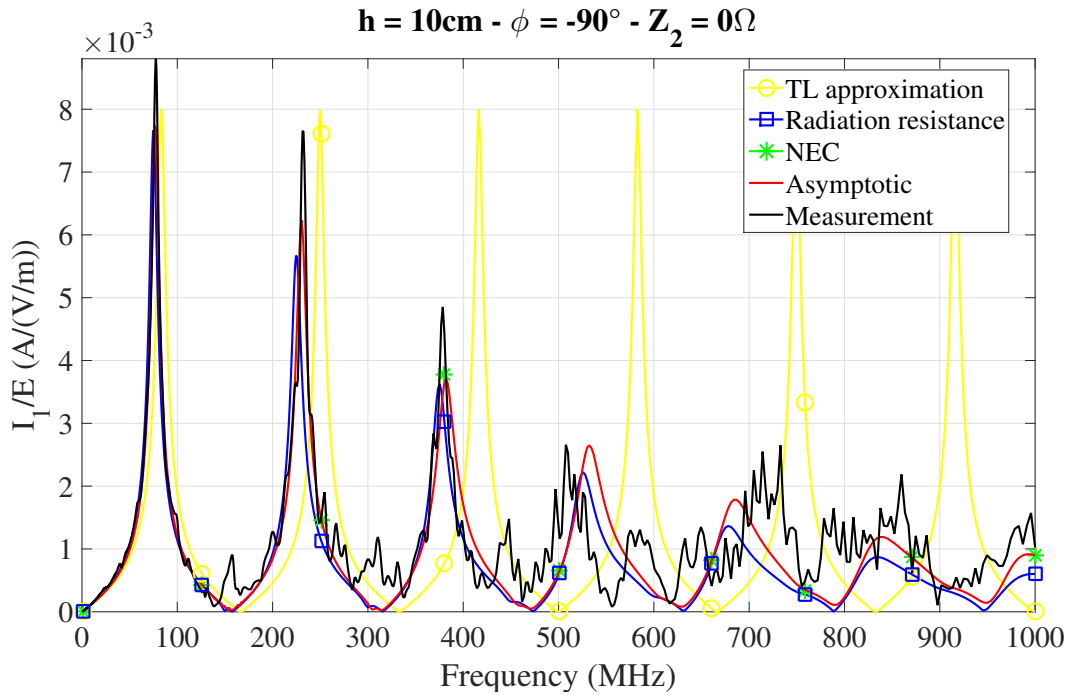


Figure A.1: Transfer function current/field. Comparison between measurements, TL theory, and full-wave simulation (CST).

Table A.1: Parameters associated to the figures displayed in Appendix A.

Figure #	h (cm)	ϕ	Z_2 (Ω)
A.1	10	-90°	low impedance
A.2	10	-90°	50
A.3	20	-90°	low impedance
A.4	20	-90°	50
A.5	30	-90°	low impedance
A.6	30	-90°	50
A.7	40	-90°	low impedance
A.8	40	-90°	50
A.9	10	-45°	low impedance
A.10	10	-45°	50
A.11	20	-45°	low impedance
A.12	20	-45°	50
A.13	30	-45°	low impedance
A.14	30	-45°	50
A.15	40	-45°	low impedance
A.16	40	-45°	50
A.17	10	0°	low impedance
A.18	10	0°	50
A.19	20	0°	low impedance
A.20	20	0°	50
A.21	30	0°	low impedance
A.22	30	0°	50
A.23	40	0°	low impedance
A.24	40	0°	50

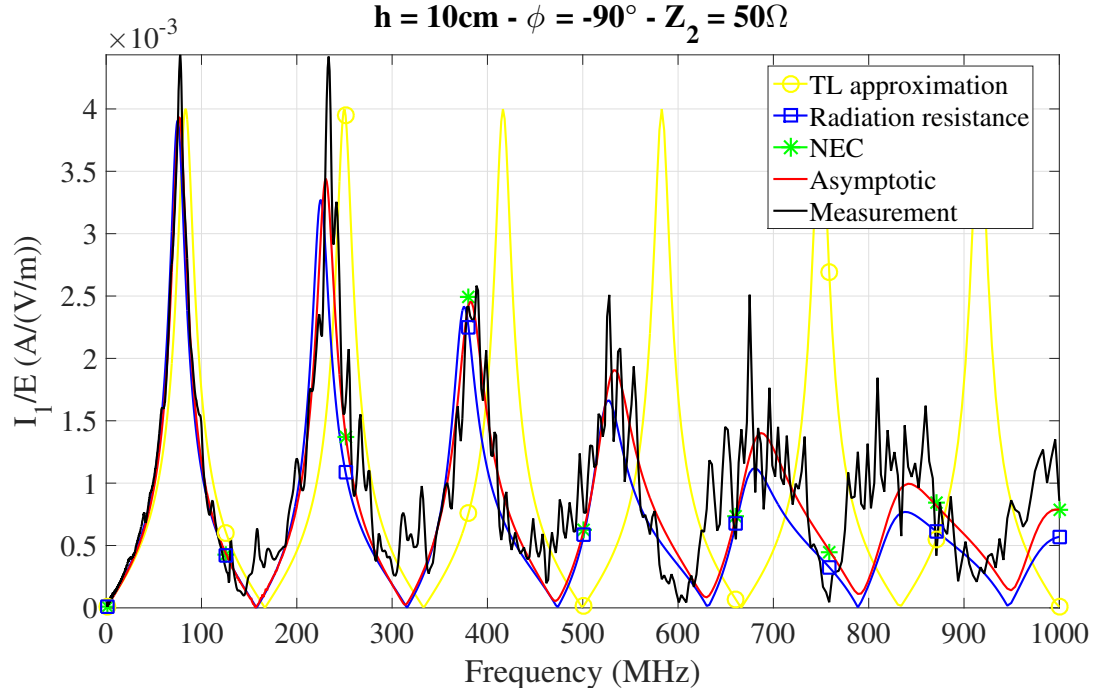


Figure A.2: Transfer function current/field.

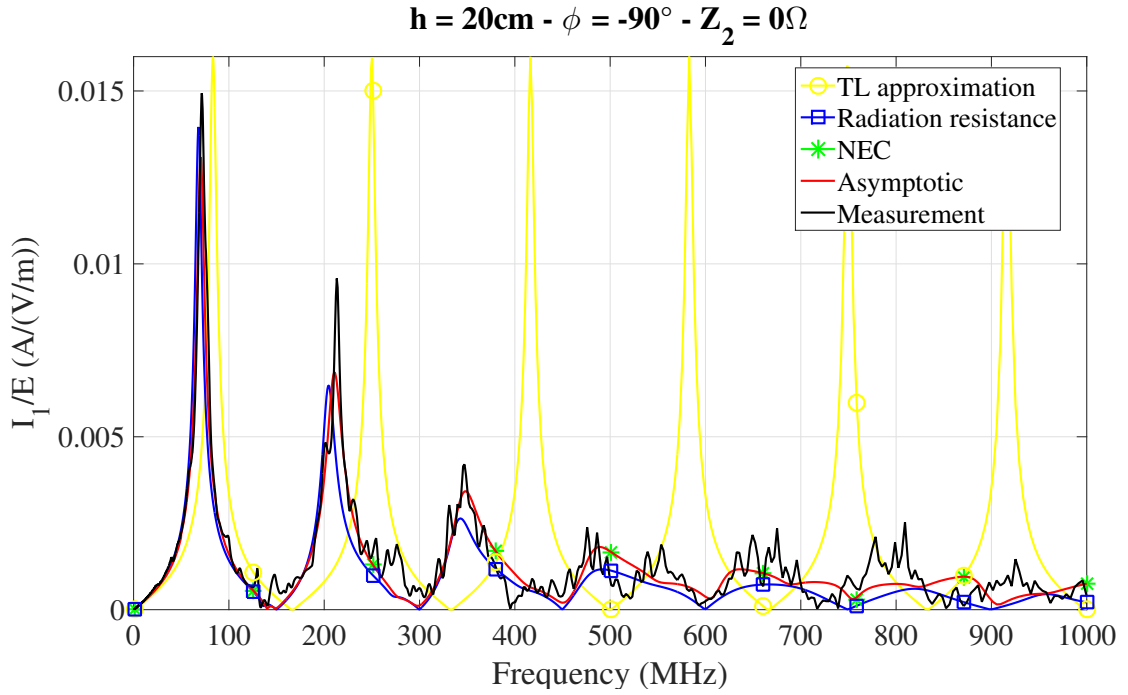


Figure A.3: Transfer function current/field.

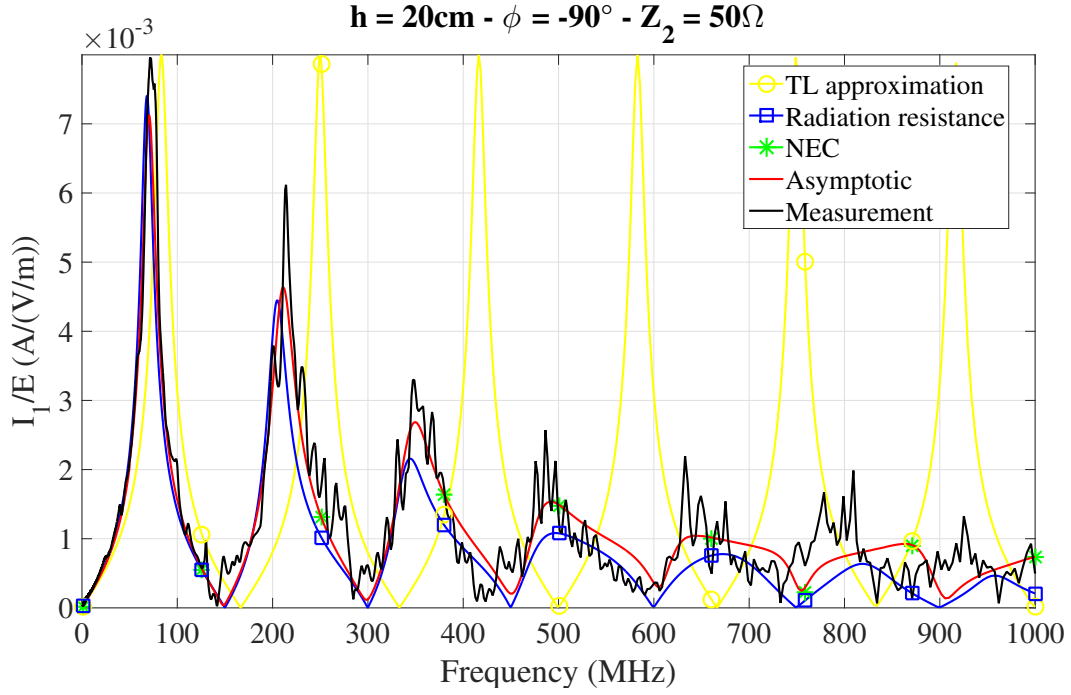


Figure A.4: Transfer function current/field.

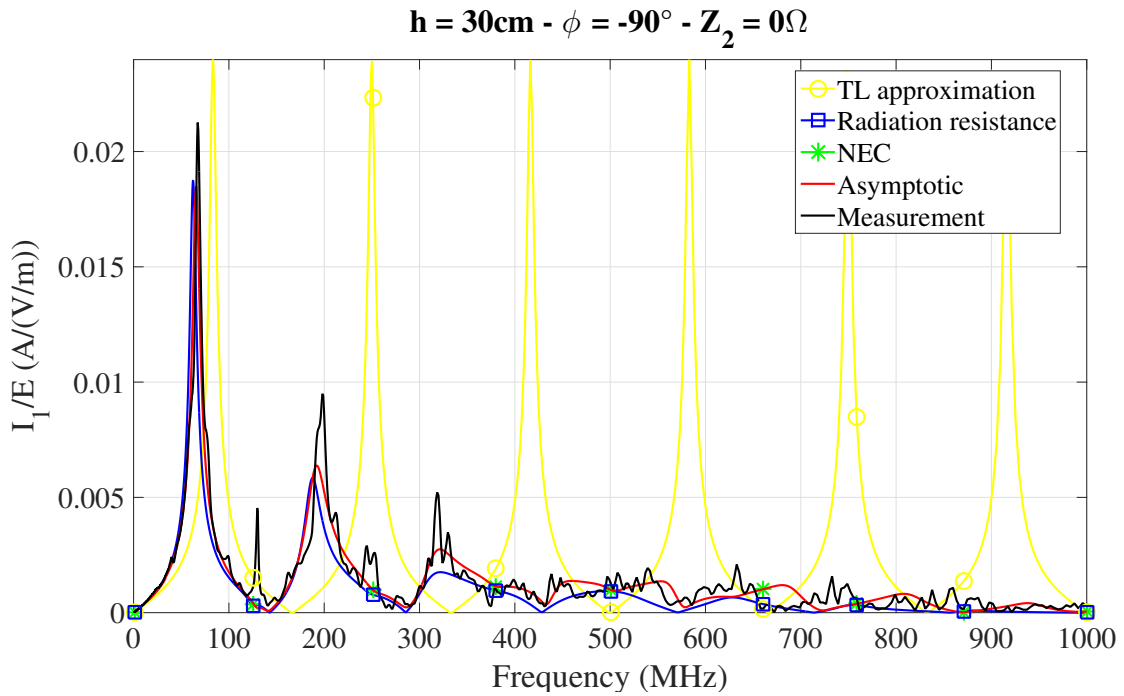
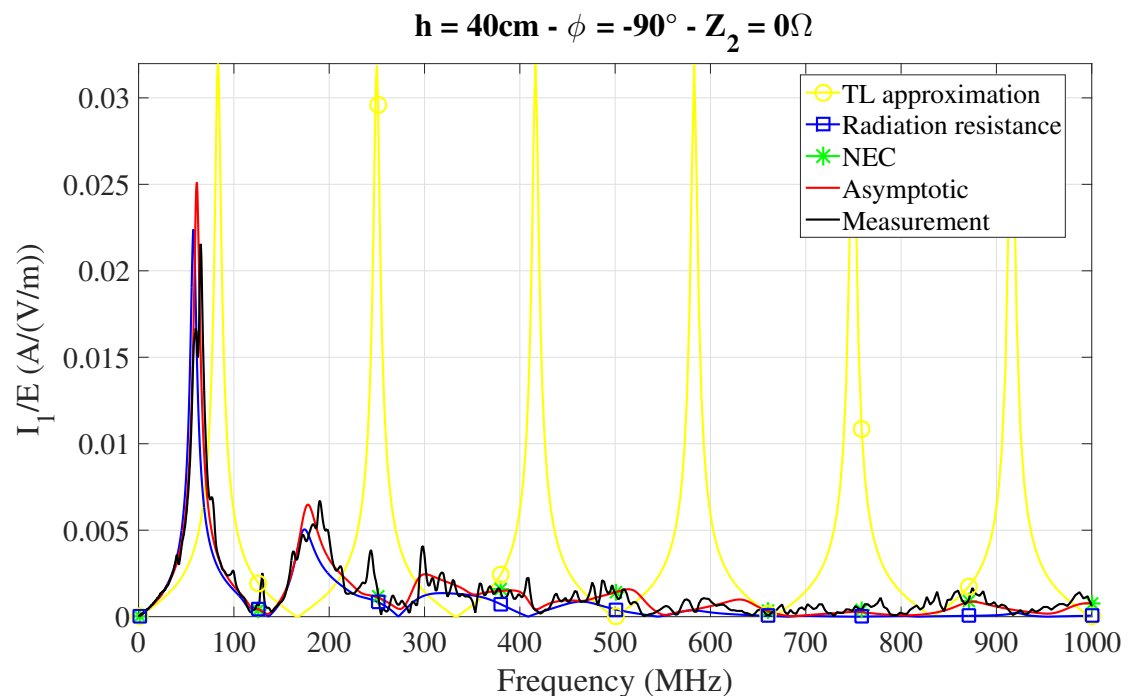
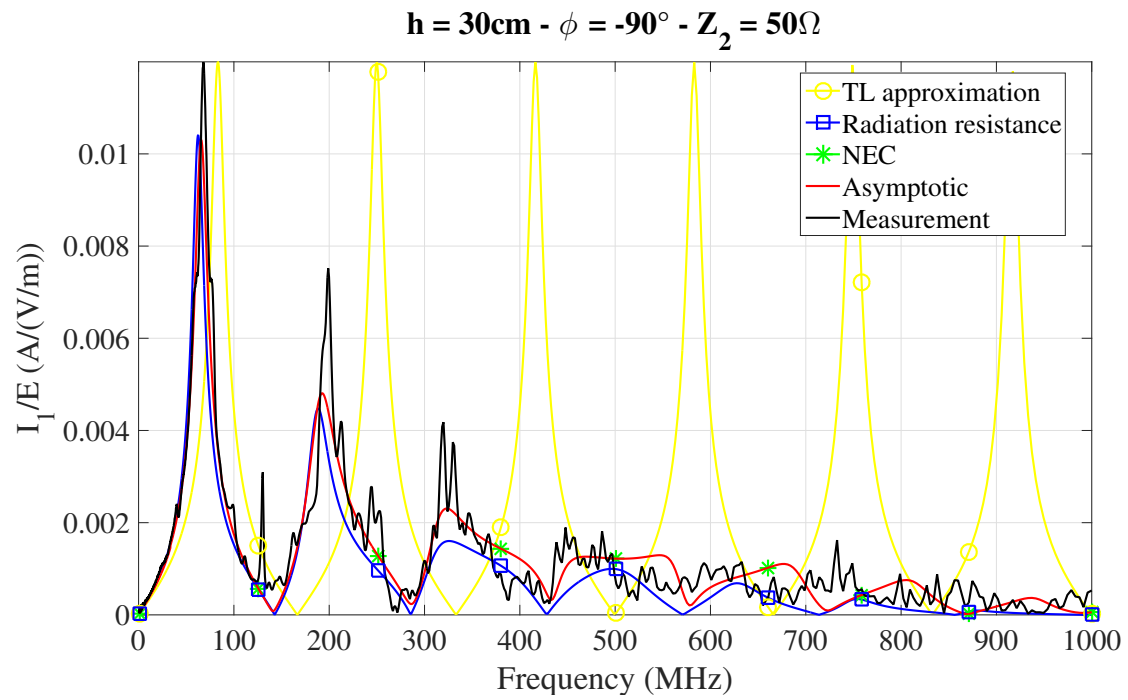


Figure A.5: Transfer function current/field.



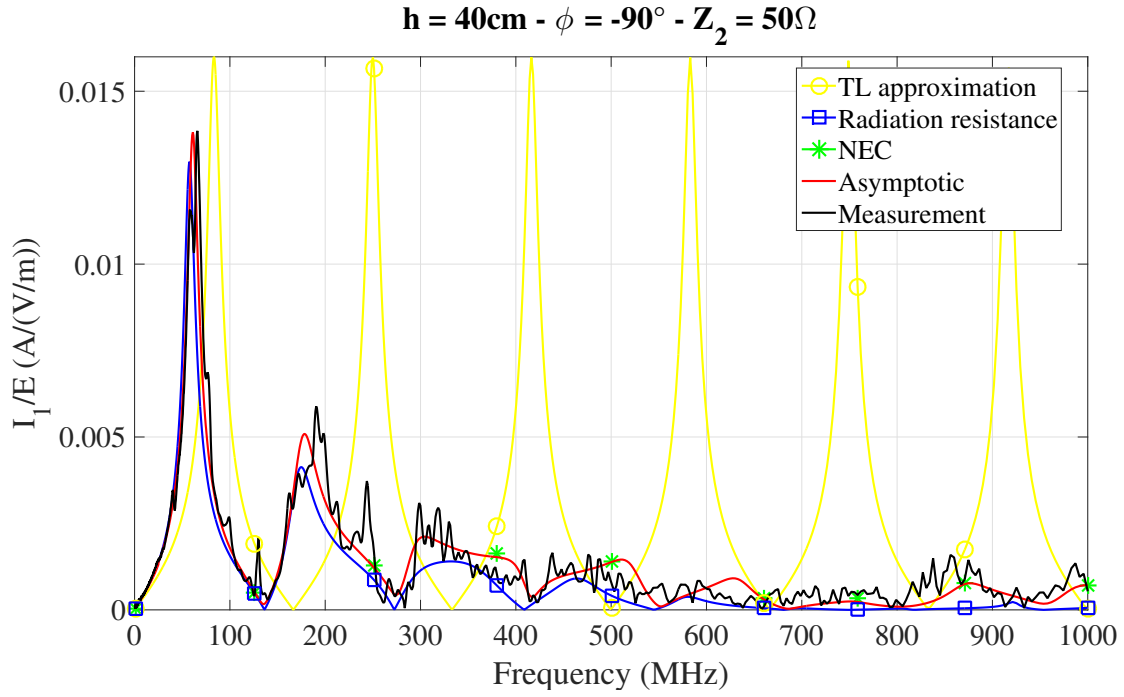


Figure A.8: Transfer function current/field.

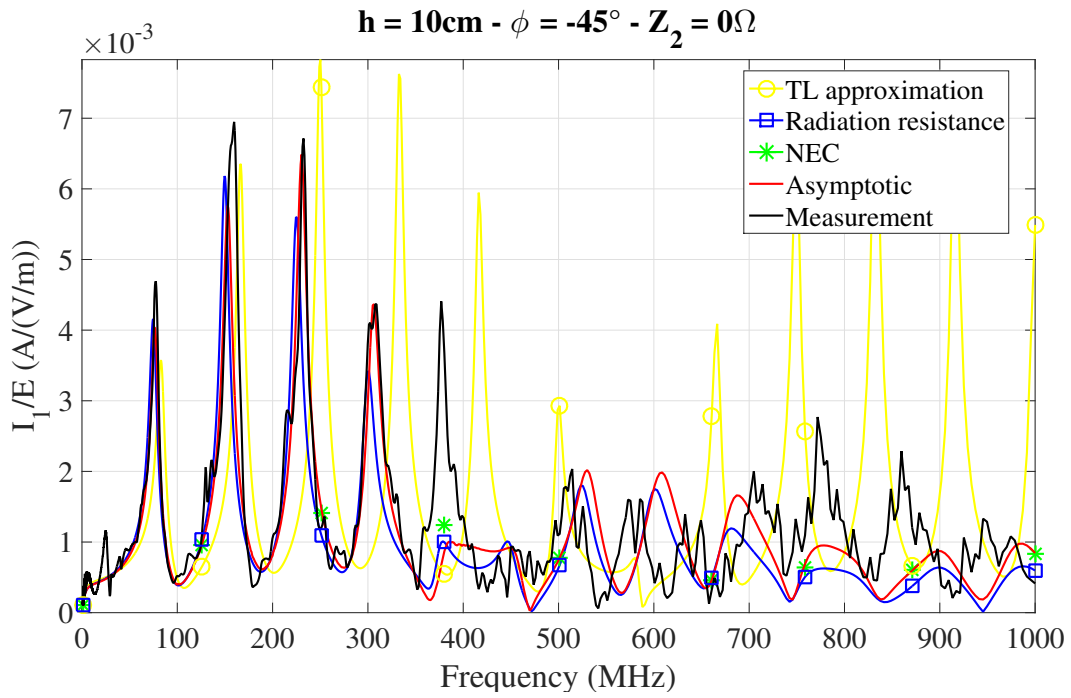


Figure A.9: Transfer function current/field.

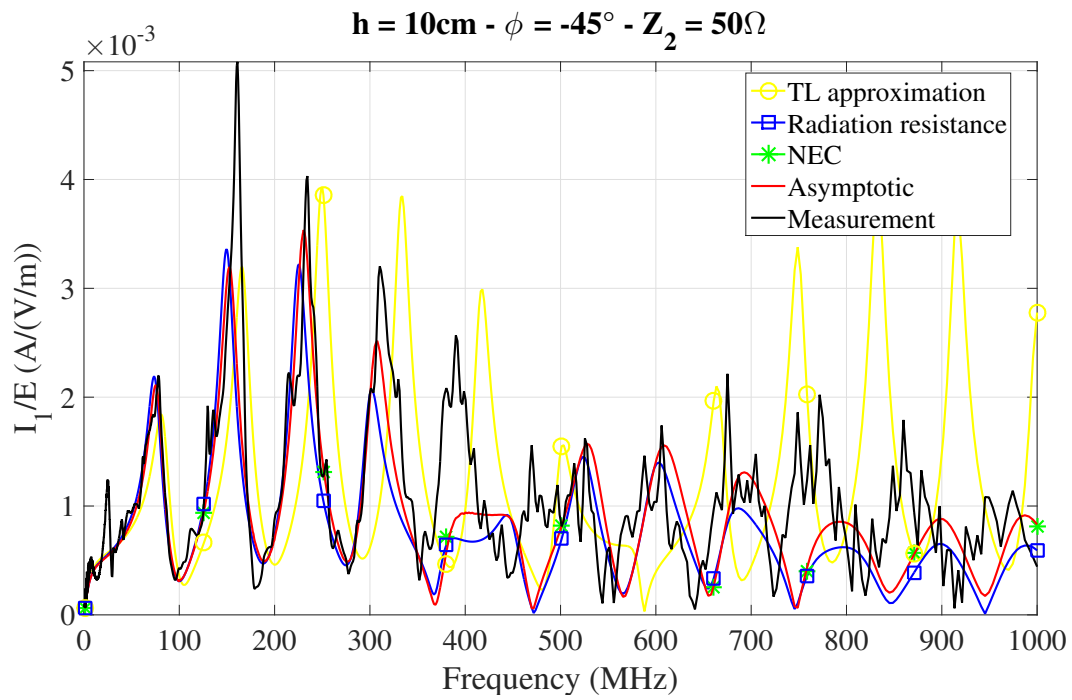


Figure A.10: Transfer function current/field.

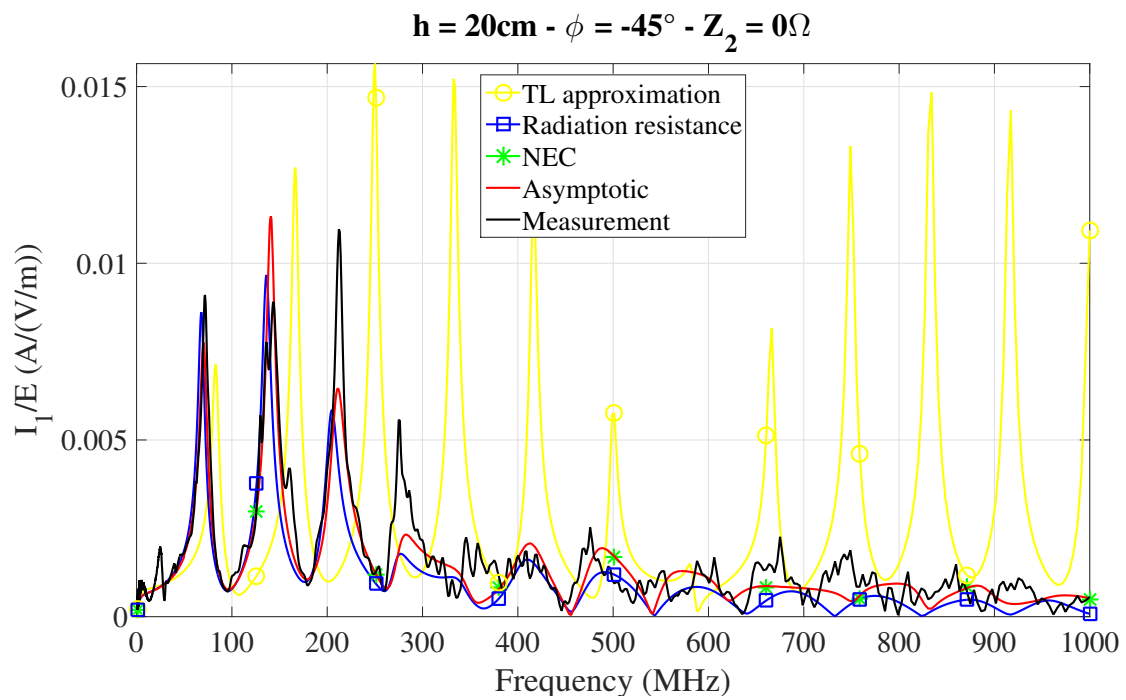


Figure A.11: Transfer function current/field.

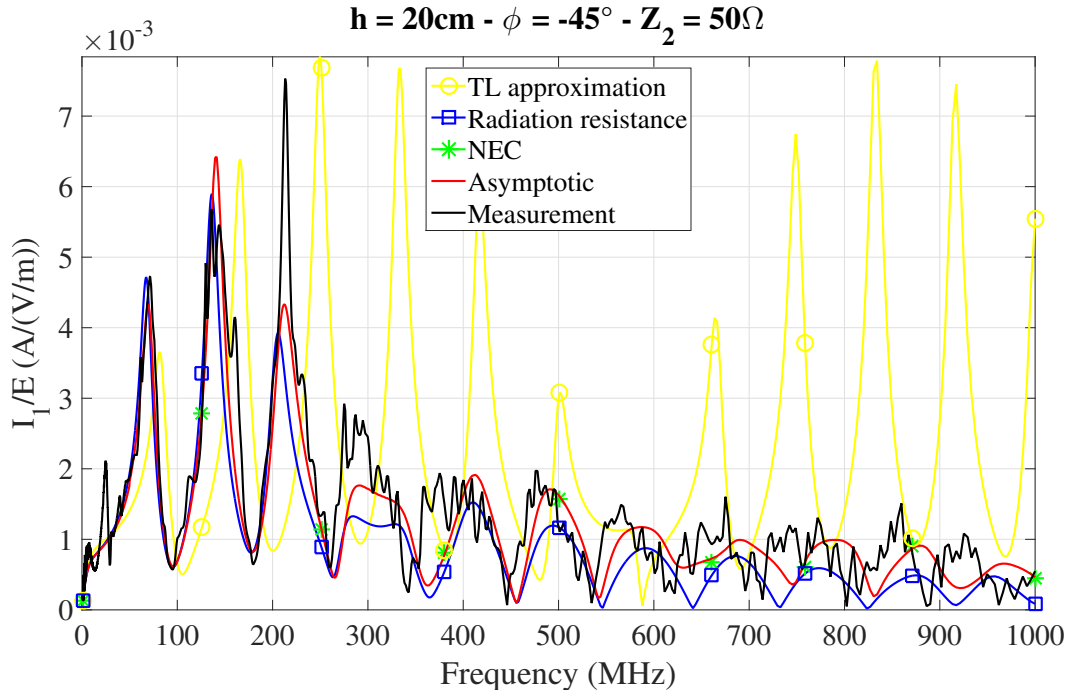


Figure A.12: Transfer function current/field.

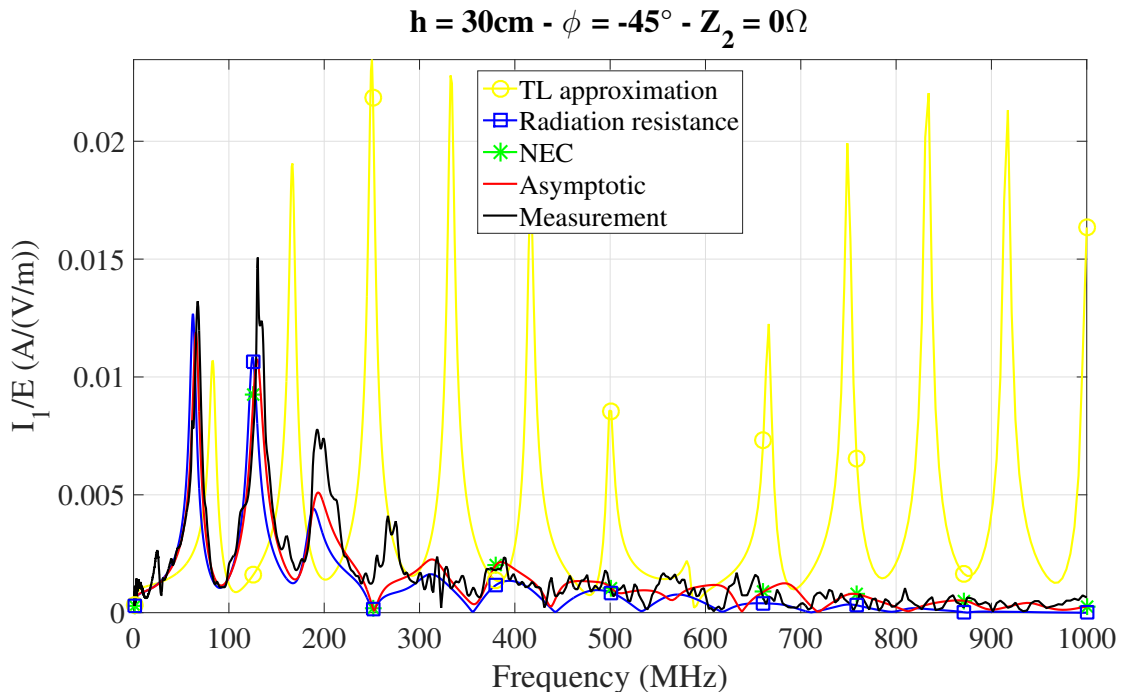


Figure A.13: Transfer function current/field.

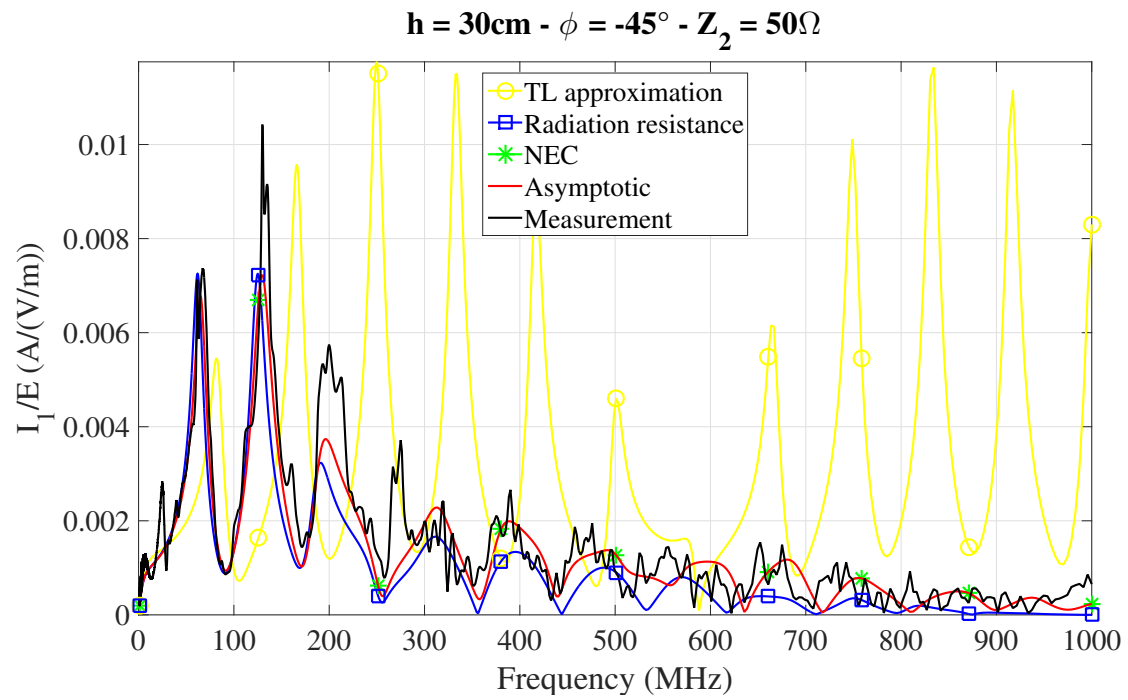


Figure A.14: Transfer function current/field.

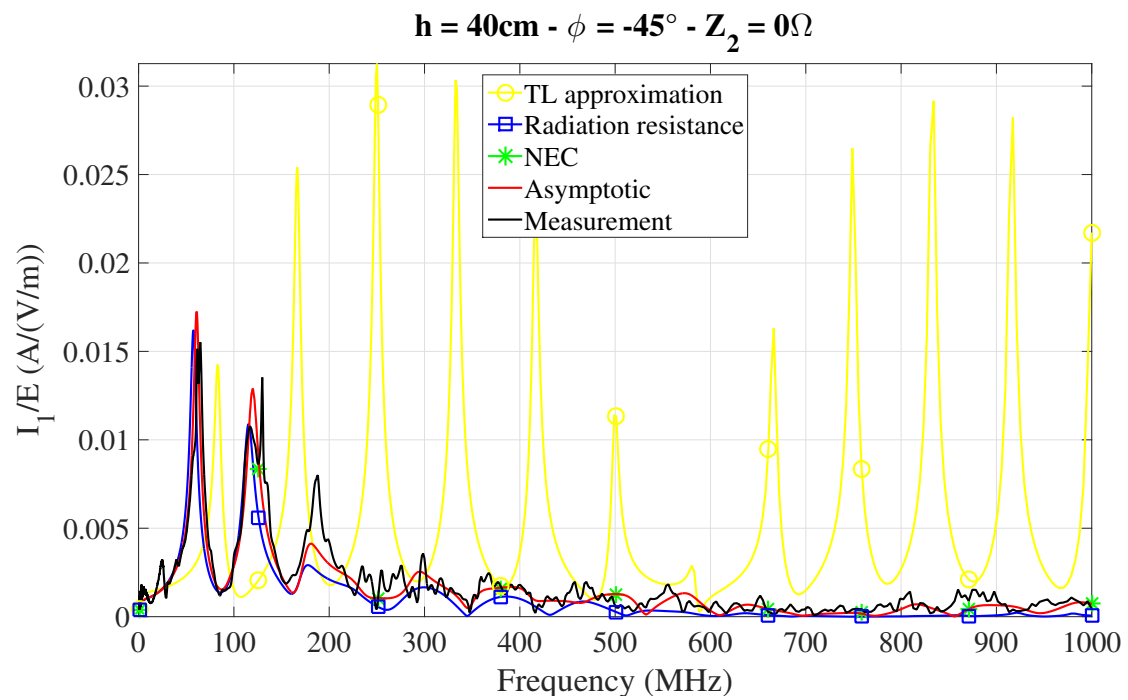


Figure A.15: Transfer function current/field.

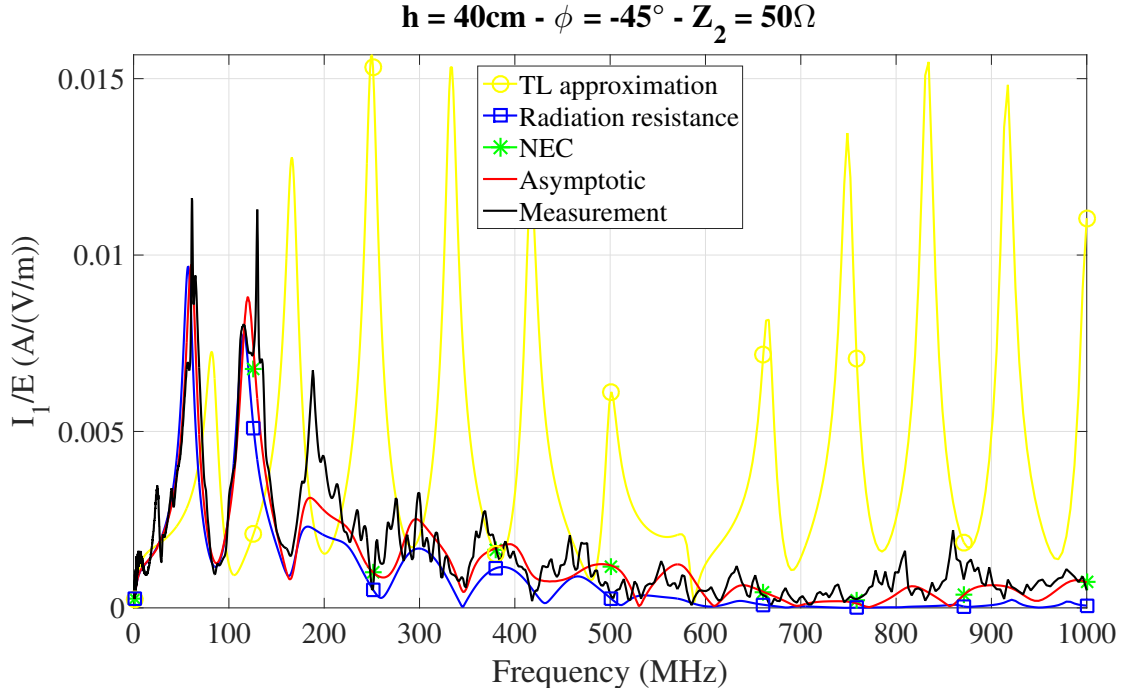


Figure A.16: Transfer function current/field.

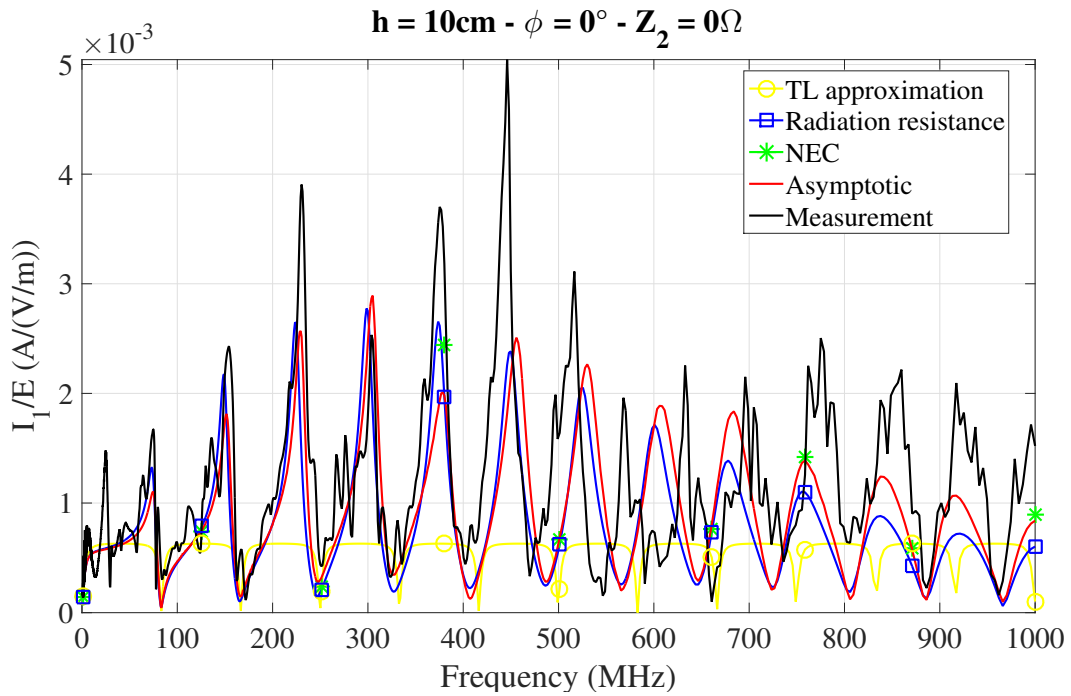


Figure A.17: Transfer function current/field.

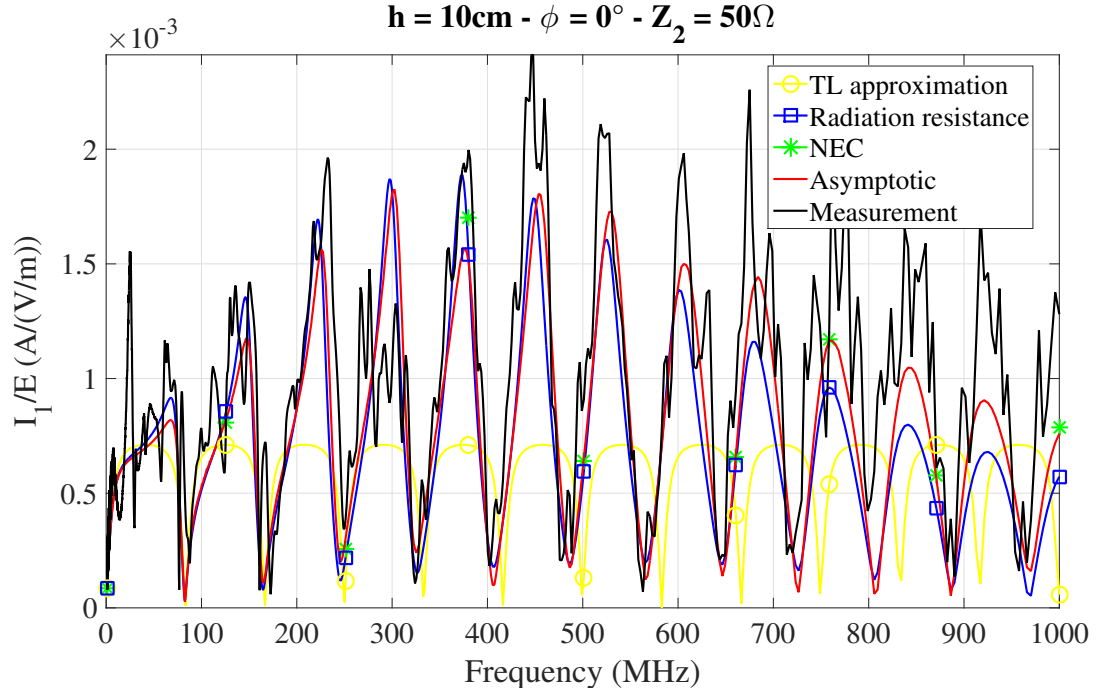


Figure A.18: Transfer function current/field.

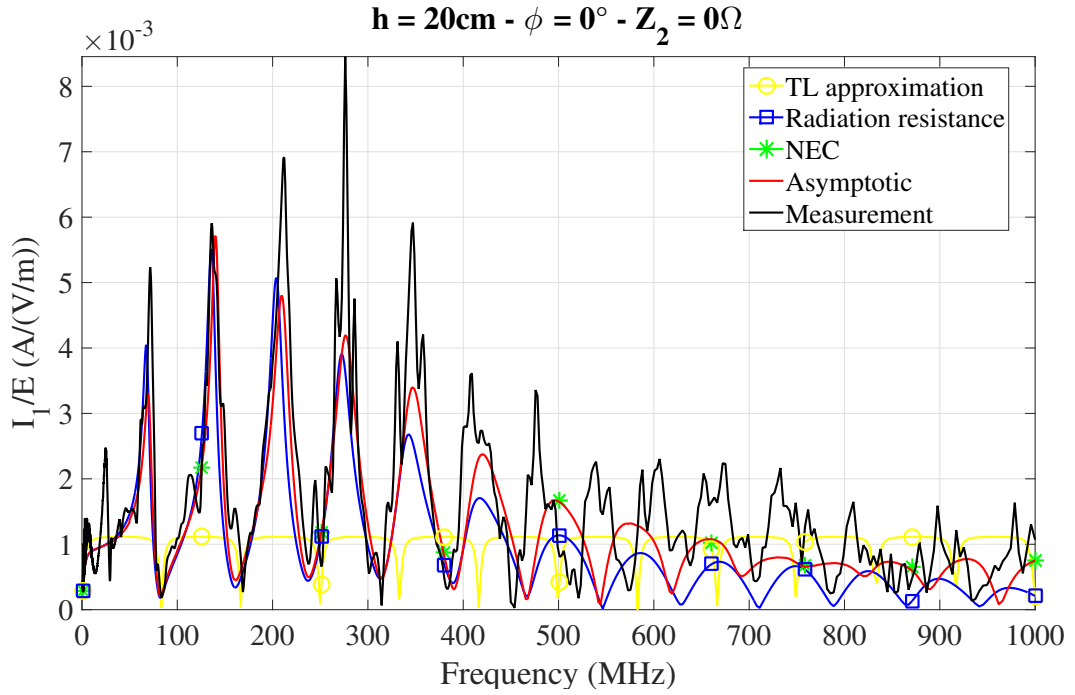


Figure A.19: Transfer function current/field.

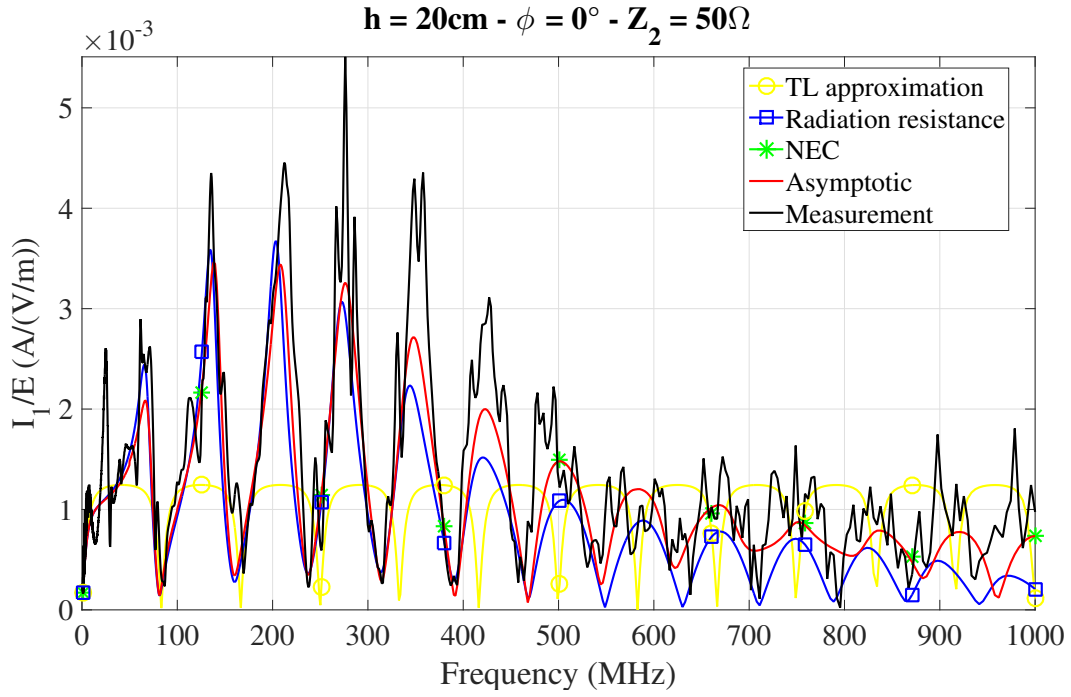


Figure A.20: Transfer function current/field.

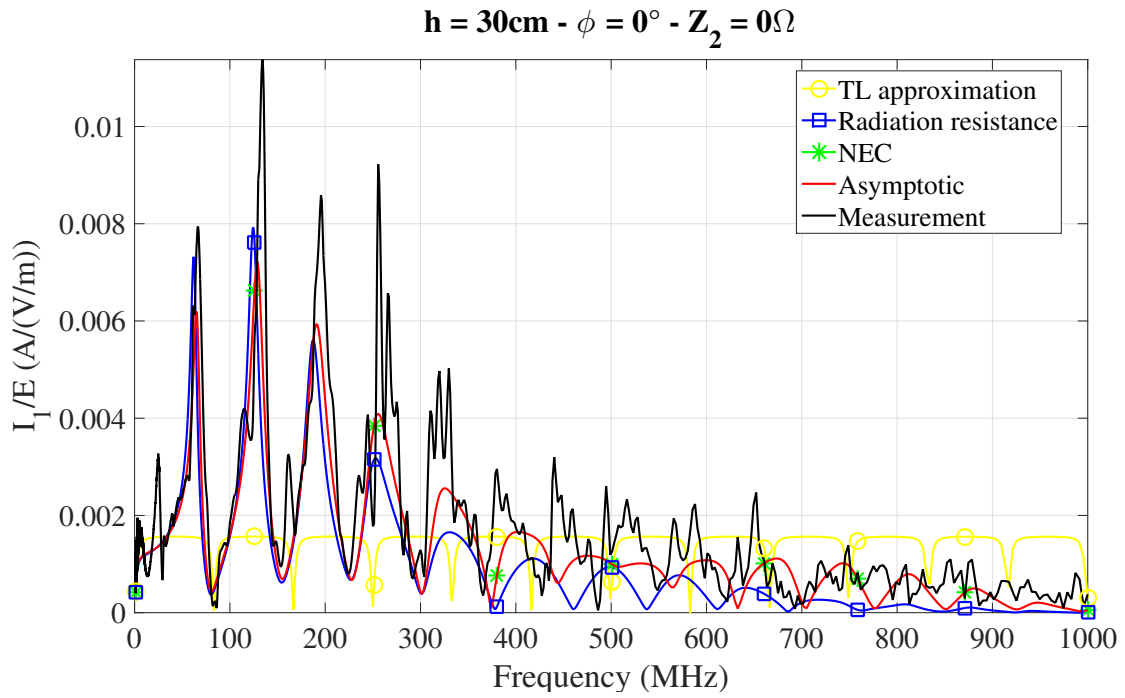


Figure A.21: Transfer function current/field.

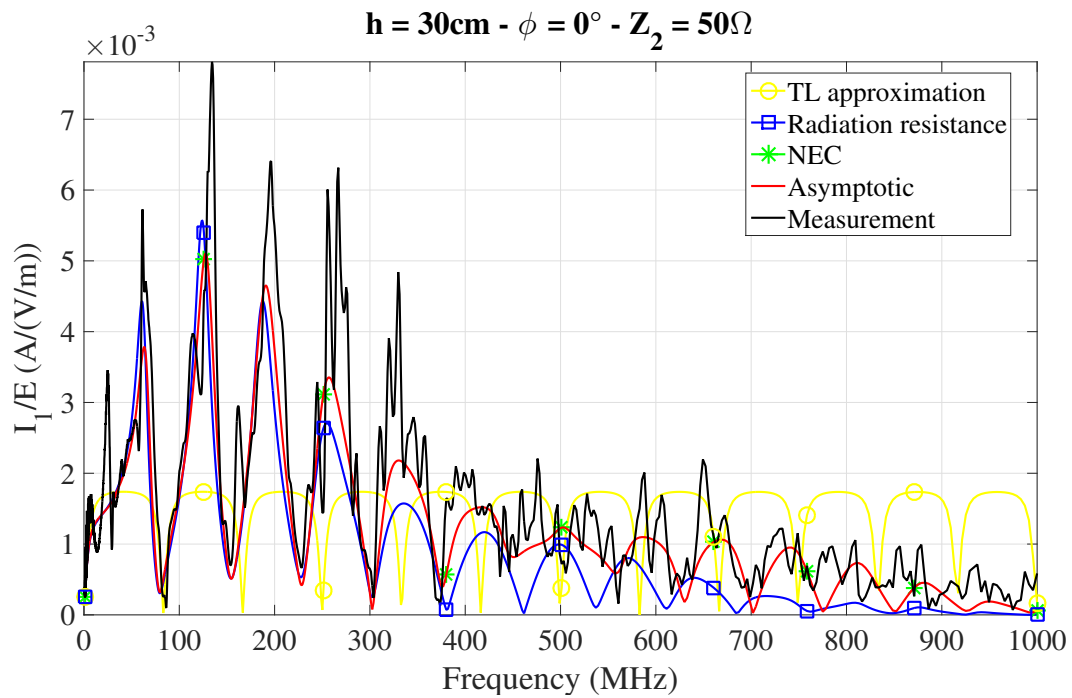


Figure A.22: Transfer function current/field.

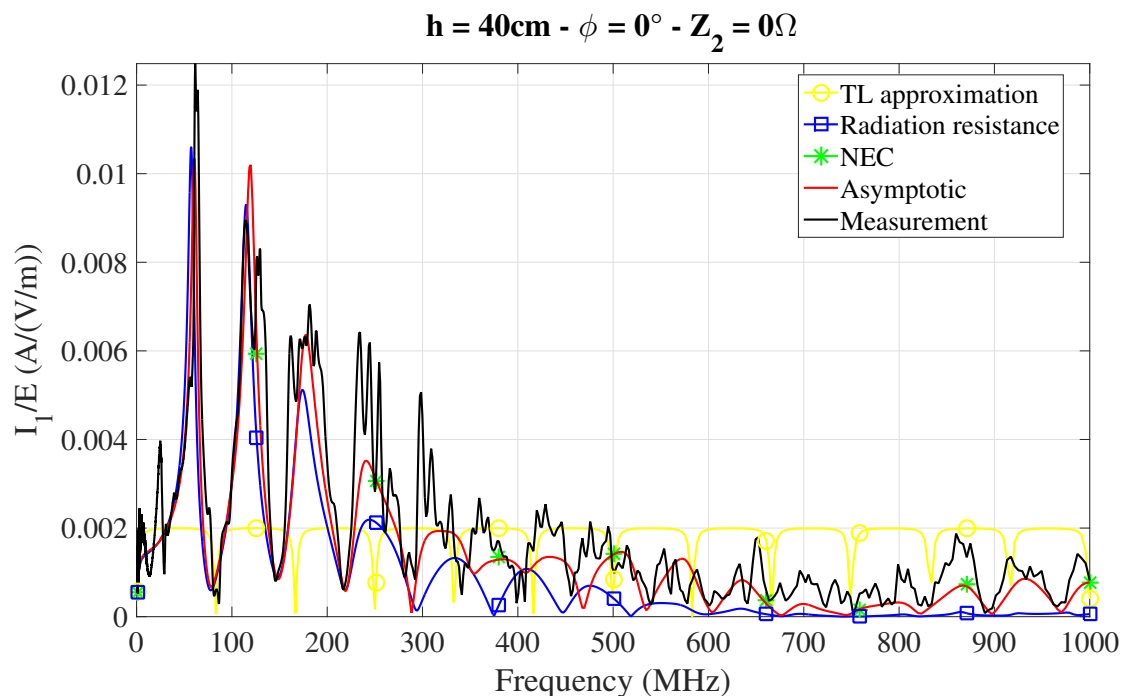


Figure A.23: Transfer function current/field.

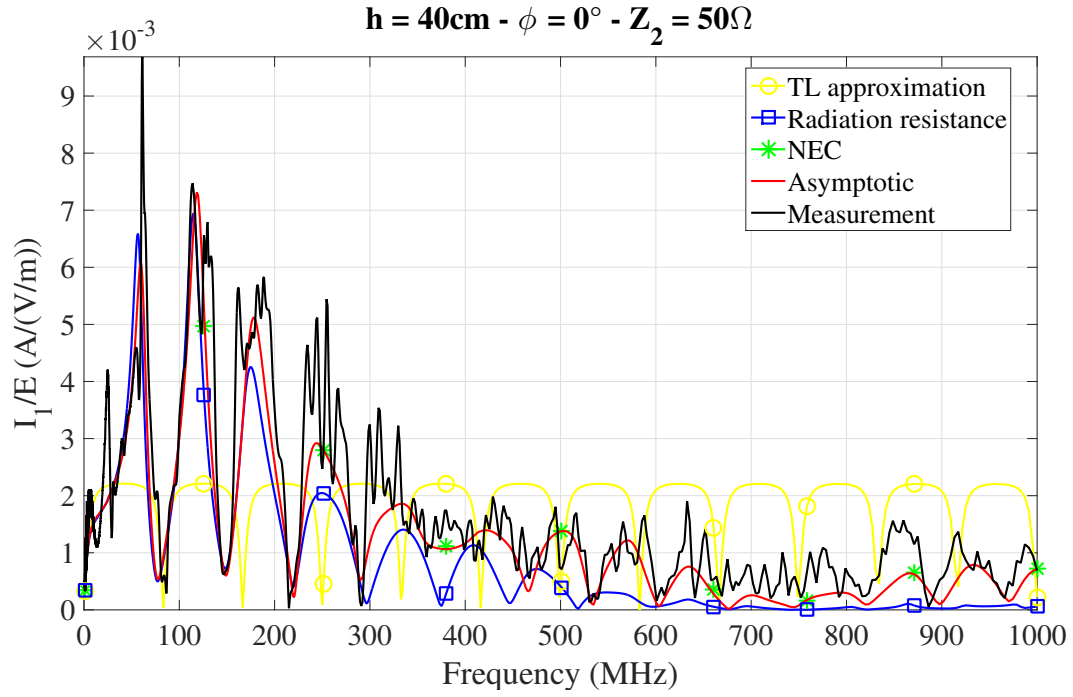


Figure A.24: Transfer function current/field.

Bibliography

- [1] F. Rachidi and S. Tkachenko, Eds., *Electromagnetic Field Interaction with Transmission Lines. From Classical Theory to HF Radiation Effects*. Southampton, Boston: WITpress, 2008.
- [2] M. Fink, “Time reversal of ultrasonic fields. i. basic principles,” *IEEE Transactions on Ultrasonics, Ferroelectrics, and Frequency Control*, vol. 39, no. 5, pp. 555–566, Sept 1992. <http://doi.org/10.1109/58.156174>
- [3] K. Cummins and M. Murphy, “An overview of lightning locating systems: History, techniques, and data uses, with an in-depth look at the u.s. nldn,” *IEEE Transactions on EMC*, vol. 51, no. 3, pp. 499–518, Aug 2009. <http://doi.org/10.1109/TEM.2009.2023450>
- [4] N. Mora, F. Rachidi, and M. Rubinstein, “Locating lightning using time reversal of electromagnetic fields,” in *30th International Conference on Lightning Protection (ICLP)*, 2010.
- [5] D. Giri and F. Tesche, “Classification of Intentional Electromagnetic Environments (IEME),” *IEEE Transactions on EMC*, vol. 46, pp. 322–328, August 2004.
- [6] W. Radasky, “The Threat of Intentional Electromagnetic Interference (IEMI) to Wired and Wireless Systems,” *17th International Zurich Symposium on Electromagnetic Compatibility*, 2006.
- [7] D. Månsson, R. Thottappillil, M. Bäckström, and O. Lunden, “Vulnerability of European Rail Traffic Management System to Radiated Intentional EMI,” *IEEE Transactions on Electromagnetic Compatibility*, vol. 50, pp. 101–109, February 2008.
- [8] F. Sabath, “What can be learned from documented Intentional Electromagnetic Interference (IEMI) Attacks?” *IEEE*, 2011.
- [9] C.R. Paul, *Analysis of multiconductor transmission lines*. Hoboken, N.J.: Wiley-Interscience : IEEE Press, 2008.
- [10] F. Tesche, M. Ianoz, and T. Karlsson, *EMC analysis methods and computational models*. New York: John Wiley & Sons, 1997.
- [11] V. A. Rakov and M. A. Uman, *Lightning, Physics and Effects*. Cambridge University Press, 2003.
- [12] T. R. Shepherd, W. D. Rust, and T. C. Marshall, “Electric fields and charges near 0°C in stratiform clouds,” *Monthly Weather Review*, vol. 124, no. 5, pp. 919–938, 1996. [http://dx.doi.org/10.1175/1520-0493\(1996\)124<0919:EFACNI>2.0.CO;2](http://dx.doi.org/10.1175/1520-0493(1996)124<0919:EFACNI>2.0.CO;2)

- [13] C. A. Romero, “Instrumentation of the Säntis tower for lightning current measurement,” Ph.D. dissertation, EPFL, 2012.
- [14] R. F. Griffiths and J. Latham, “Electrical corona from ice hydrometeors,” *Quarterly Journal of the Royal Meteorological Society*, vol. 101, no. 428, pp. 395–395, 1975. <http://dx.doi.org/10.1002/qj.49710142826>
- [15] A. J. Illingworth, “Charge separation in thunderstorms: Small scale processes,” *Journal of Geophysical Research: Atmospheres*, vol. 90, no. D4, pp. 6026–6032, 1985. <http://dx.doi.org/10.1029/JD090iD04p06026>
- [16] L. I. Dorman, *Cosmic Rays in Magnetospheres of the Earth and Other Planets*. Springer Science+Business Media B.V., 2009.
- [17] W. D. Rust and T. C. Marshall, “On abandoning the thunderstorm tripole-charge paradigm,” *Journal of Geophysical Research: Atmospheres*, vol. 101, no. D18, pp. 23 499–23 504, 1996. <http://dx.doi.org/10.1029/96JD01802>
- [18] M. Stolzenburg, W. D. Rust, and T. C. Marshall, “Electrical structure in thunderstorm convective regions: 3. synthesis,” *Journal of Geophysical Research: Atmospheres*, vol. 103, no. D12, pp. 14 097–14 108, 1998. <http://dx.doi.org/10.1029/97JD03545>
- [19] C. J. Rodger, “Red sprites, upward lightning, and vlf perturbations,” *Reviews of Geophysics*, vol. 37, no. 3, pp. 317–336, 1999. <http://dx.doi.org/10.1029/1999RG900006>
- [20] V. Cooray, *The Lightning Flash*, ser. Power and energy. Institution of Engineering & Technology (IET), 2008.
- [21] K. Berger, R. B. Anderson, and H. Kroninger, “Parameters of lightning flashes,” *Electra*, no. 41, 1975.
- [22] D. Pavanello, “Electromagnetic radiation from lightning return strokes to tall structures,” Ph.D. dissertation, EPFL, 2007.
- [23] M. A. Uman, *The lightning discharge*. Academic Press, 1987.
- [24] R. Solomon, V. Schroeder, and M. B. Baker, “Lightning initiation—conventional and runaway-breakdown hypotheses,” *Quarterly Journal of the Royal Meteorological Society*, vol. 127, no. 578, pp. 2683–2704, 2001. <http://dx.doi.org/10.1002/qj.49712757809>
- [25] D. Petersen, M. Bailey, J. Hallett, and W. H. Beasley, “Laboratory investigation of positive streamer discharges from simulated ice hydrometeors,” *Quarterly Journal of the Royal Meteorological Society*, vol. 132, no. 615, pp. 263–273, 2006. <http://dx.doi.org/10.1256/qj.05.32>
- [26] A. V. Gurevich, G. A. Mesyats, K. P. Zybin, A. G. Reutova, V. G. Shpak, S. A. Shunailov, and M. I. Yalandin, “Real-time observation of runaway-electron breakdown of air in the laboratory conditions,” in *2011 Abstracts IEEE International Conference on Plasma Science (ICOPS)*, June 2011, pp. 1–1. <http://doi.org/10.1109/PLASMA.2011.5993023>
- [27] G. Milikh and R. Roussel-Dupré, “Runaway breakdown and electrical discharges in thunderstorms,” *Journal of Geophysical Research: Space Physics*, vol. 115, no. A12, pp. n/a–n/a, 2010, a00E60. <http://dx.doi.org/10.1029/2009JA014818>

- [28] M. N. Plooster, “Shock waves from line sources. numerical solutions and experimental measurements,” *Physics of Fluids*, 1970.
- [29] —, “Numerical model of the return stroke of the lightning discharge,” *Physics of Fluids*, 1971.
- [30] —, “Numerical simulation of spark discharges in air,” *Physics of Fluids*, 1971.
- [31] Y. Baba and M. Ishii, “Numerical electromagnetic field analysis of lightning current in tall structures,” *IEEE Transactions on Power Delivery*, vol. 16, no. 2, pp. 324–328, Apr 2001. <http://doi.org/10.1109/61.915502>
- [32] R. Moini, B. Kordi, G. Z. Rafi, and V. A. Rakov, “A new lightning return stroke model based on antenna theory,” *Journal of Geophysical Research: Atmospheres*, vol. 105, no. D24, pp. 29 693–29 702, 2000. <http://dx.doi.org/10.1029/2000JD900541>
- [33] E. Petrache, F. Rachidi, D. Pavanello, W. Janischewskyj, A. M. Hussein, M. Rubinstein, V. Shostak, W. A. Chisholm, and J. S. Chang, “Lightning strikes to elevated structures: influence grounding conditions on currents and electromagnetic fields,” in *2005 International Symposium on Electromagnetic Compatibility, 2005. EMC 2005.*, vol. 2, Aug 2005, pp. 377–381 Vol. 2. <http://doi.org/10.1109/ISEMC.2005.1513543>
- [34] P. F. Little, “Transmission line representation of a lightning return stroke,” *Journal of Physics*, pp. 1893–1910, 1978.
- [35] G. H. Price and E. T. Pierce, “The modeling of channel current in the lightning return stroke,” *Radio Science*, vol. 12, no. 3, pp. 381–388, 1977. <http://dx.doi.org/10.1029/RS012i003p00381>
- [36] V. A. Rakov and M. A. Uman, “Review and evaluation of lightning return stroke models including some aspects of their application,” *IEEE Transactions on Electromagnetic Compatibility*, vol. 40, no. 4, pp. 403–426, Nov 1998. <http://doi.org/10.1109/15.736202>
- [37] F. Rachidi and R. Thottappillil, “Determination of lightning currents from far electromagnetic fields,” *Journal of Geophysical Research*, pp. 18 315–18 321, 1993.
- [38] F. Rachidi, “Formulation of the Field-to-Transmission Line Coupling Equations in Terms of Magnetic Excitation Field,” *IEEE Transactions on EMC*, vol. 35, pp. 404–407, August 1993.
- [39] N. Mora, F. Rachidi, and M. Rubinstein, “Application of the time reversal of electromagnetic fields to locate lightning discharges,” *Journal on Atmospheric Research*, 2011.
- [40] V. Cooray, “Propagation effects due to finitely conducting ground on lightning-generated magnetic fields evaluated using sommerfeld’s integrals,” *IEEE Transactions on Electromagnetic Compatibility*, vol. 51, no. 3, pp. 526–531, Aug 2009. <http://doi.org/10.1109/TEMPC.2009.2019759>
- [41] —, “On the accuracy of several approximate theories used in quantifying the propagation effects on lightning generated electromagnetic fields,” *IEEE Transactions on Antennas and Propagation*, vol. 56, no. 7, pp. 1960–1967, July 2008. <http://doi.org/10.1109/TAP.2008.924680>
- [42] G. Lugrin, “Localisation de la foudre par retournement temporel,” Master’s thesis, EPFL, 2011.

- [43] J. A. Cramer, K. L. Cummins, A. Morris, R. Smith, and T. Turner, "Recent Upgrades to the U.S. National Lightning Detection Network," in *18th International Lightning Detection Conference*, 2004.
- [44] K. L. Cummins, M. J. Murphy, E. A. Bardo, W. L. Hiscox, R. Pyle, and A. Pifer, "A combined toa/mdf technology upgrade of the u.s. national lightning detection network," *Journal of Geophysical Research*, vol. 103, no. D8, pp. 9035–9044, April 1998.
- [45] Meteorage, meteorage.fr.
- [46] J. Lojou, N. Honma, K. L. Cummins, R. K. Said, and N. Hembury, "Latest developments in global and total lightning detection," in *7th Asia-Pacific International Conference on Lightning (APL)*, Nov. 2011, pp. 924–932.
- [47] G. Diendorfer, W. Schulz, and V. Rakov, "Lightning characteristics based on data from the austrian lightning locating system," *IEEE Transactions on EMC*, vol. 40, no. 4, pp. 452–464, Nov 1998. <http://doi.org/10.1109/15.736206>
- [48] C. Romero, M. Paolone, F. Rachidi, M. Rubinstein, A. Rubinstein, G. Diendorfer, W. Schulz, M. Bernardi, and C. A. Nucci, "Preliminary comparison of data from the Saentis tower and the EUCLID lightning location system," in *2011 International Symposium on Lightning Protection (XI SIPDA)*, Oct 2011, pp. 140–145. <http://doi.org/10.1109/SIPDA.2011.6088468>
- [49] M. Azadifar, F. Rachidi, M. Rubinstein, M. Paolone, G. Diendorfer, H. Pichler, W. Schulz, D. Pavanello, and C. Romero, "Evaluation of the performance characteristics of the european lightning detection network euclid in the alps region for upward negative flashes using direct measurements at the instrumented saentis tower," *Journal of Geophysical Research: Atmospheres*, vol. 121, no. 2, pp. 595–606, 2016, 2015JD024259. <http://dx.doi.org/10.1002/2015JD024259>
- [50] G. Lugrin, N. Mora, F. Rachidi, M. Rubinstein, and G. Diendorfer, "Localisation de la Foudre par Retournement Temporel," in *16e Colloque International sur la Compatibilité Electromagnétique, Rouen*, April 2012.
- [51] —, "On the Location of Lightning Discharges Using Time Reversal of Electromagnetic Fields," *IEEE Transactions on EMC*, vol. 56, no. 1, pp. 149–158, Feb 2014. <http://doi.org/10.1109/TEMC.2013.2266932>
- [52] H. Jemaïel, "Application du retournement temporel pour la localisation de la foudre," Master's thesis, EPFL, June 2014.
- [53] H. Karami, F. Rachidi, and M. Rubinstein, "On practical implementation of electromagnetic time reversal to locate lightning," in *23rd International Lightning Detection Conference, Tucson, Arizona, USA*, March 2014.
- [54] B. Bogert, "Demonstration of delay distortion correction by time-reversal techniques," *IRE Transactions on Communications Systems*, vol. 5, no. 3, pp. 2–7, December 1957. <http://doi.org/10.1109/TCOM.1957.1097511>
- [55] A. Parvulescu and C. Clay, "Reproducibility of signal transmissions in the ocean," *The Radio and Electronic Engineer*, April 1965.

- [56] F. Wu, J.-L. Thomas, and M. Fink, "Time reversal of ultrasonic fields. il. experimental results," *IEEE Transactions on Ultrasonics, Ferroelectrics, and Frequency Control*, vol. 39, no. 5, pp. 567–578, Sept 1992. <http://doi.org/10.1109/58.156175>
- [57] D. Cassereau and M. Fink, "Time-reversal of ultrasonic fields. iii. theory of the closed time-reversal cavity," *IEEE Transactions on Ultrasonics, Ferroelectrics, and Frequency Control*, vol. 39, no. 5, pp. 579–592, Sept 1992. <http://doi.org/10.1109/58.156176>
- [58] M. Fink, "Time-reversed acoustics," *Scientific American*, 1999.
- [59] W. A. Kuperman, W. S. Hodgkiss, H. C. Song, T. Akal, C. Ferla, and D. R. Jackson, "Phase conjugation in the ocean: Experimental demonstration of an acoustic time-reversal mirror," *The Journal of the Acoustical Society of America*, vol. 103, no. 1, pp. 25–40, 1998. <http://dx.doi.org/10.1121/1.423233>
- [60] G. F. Edelmann, H. C. Song, S. Kim, W. S. Hodgkiss, W. A. Kuperman, and T. Akal, "Underwater acoustic communications using time reversal," *IEEE Journal of Oceanic Engineering*, vol. 30, no. 4, pp. 852–864, Oct 2005. <http://doi.org/10.1109/JOE.2005.862137>
- [61] M. Fink, "Time reversal and phase conjugation with acoustic waves: industrial and medical applications," in *Conference on Lasers and Electro-Optics, 2005 (CLEO).*, vol. 3, May 2005, pp. 2334–2335 Vol. 3. <http://doi.org/10.1109/CLEO.2005.202462>
- [62] *Time-reverse imaging for detection of landmines*, vol. 5415, 2004. <http://dx.doi.org/10.1117/12.542686>
- [63] *Time reversal acousto-seismic method for land mine detection*, vol. 5794, 2005. <http://dx.doi.org/10.1117/12.609838>
- [64] D. F. Gingras, P. Gerstoft, N. L. Gerr, and C. F. Mecklenbrauker, "Electromagnetic matched field processing for source localization," in *1997 IEEE International Conference on Acoustics, Speech, and Signal Processing (ICASSP-97)*, vol. 1, Apr 1997, pp. 479–482 vol.1. <http://doi.org/10.1109/ICASSP.1997.599679>
- [65] G. Lerosey, J. de Rosny, A. Tourin, A. Derode, G. Montaldo, and M. Fink, "Time Reversal of Electromagnetic Waves," *Physical Review Letters*, vol. 92, no. 19, p. 193904, May 2004.
- [66] J. Chaiken, R. Chevray, M. Tabor, and Q. M. Tan, "Experimental study of lagrangian turbulence in a stokes flow," *Proceedings of the Royal Society of London. Series A, Mathematical and Physical Sciences*, vol. 408, no. 1834, pp. 165–174, 1986. <http://www.jstor.org/stable/2398145>
- [67] R. Snieder, *Imaging of Complex Media with Acoustic and Seismic Waves*. Berlin, Heidelberg: Springer Berlin Heidelberg, 2002, ch. Time-Reversal Invariance and the Relation between Wave Chaos and Classical Chaos, pp. 1–16. http://dx.doi.org/10.1007/3-540-44680-X_1
- [68] C. Draeger and M. Fink, "One-Channel Time Reversal of Elastic Waves in a Chaotic 2D-Silicon Cavity," *Physical Review Letters*, vol. 79, pp. 407–410, Jul. 1997.
- [69] C. Draeger, J.-C. Aime, and M. Fink, "One-channel time-reversal in chaotic cavities: Experimental results," *The Journal of the Acoustical Society of America*, vol. 105, no. 2, pp. 618–625, 1999. <http://dx.doi.org/10.1121/1.426252>

- [70] G. Bal and R. Verástegui, "Time reversal in changing environments," *Multiscale Modeling & Simulation*, vol. 2, no. 4, pp. 639–661, 2004. <http://dx.doi.org/10.1137/030600837>
- [71] P. Blomgren, G. Papanicolaou, and H. Zhao, "Super-resolution in time-reversal acoustics," *The Journal of the Acoustical Society of America*, vol. 111, no. 1, pp. 230–248, 2002. <http://dx.doi.org/10.1121/1.1421342>
- [72] M. Fink, "Time-reversal acoustics in complex environments," *GEOPHYSICS*, vol. 71, no. 4, pp. SI151–SI164, 2006. <http://dx.doi.org/10.1190/1.2215356>
- [73] A. Dezfouliyan and A. M. Weiner, "Experimental investigation of uwb impulse response and time reversal technique up to 12 ghz: Omnidirectional and directional antennas," *IEEE Transactions on Antennas and Propagation*, vol. 60, no. 7, pp. 3407–3415, July 2012. <http://doi.org/10.1109/TAP.2012.2196927>
- [74] H. T. Nguyen, J. B. Andersen, G. F. Pedersen, P. Kyritsi, and P. C. F. Eggers, "Time reversal in wireless communications: a measurement-based investigation," *IEEE Transactions on Wireless Communications*, vol. 5, no. 8, pp. 2242–2252, Aug 2006. <http://doi.org/10.1109/TWC.2006.1687740>
- [75] R. J. Barton, J. Chen, K. Huang, S. Perotta, and D. Wu, "Optimality properties and performance analysis of co-operative time-reversal communication in wireless sensor networks," *IET Communications*, vol. 1, no. 1, pp. 64–70, February 2007. <http://doi.org/10.1049/iet-com:20050496>
- [76] H. El-Sallabi, P. Kyritsi, A. Paulraj, and G. Papanicolaou, "Experimental investigation on time reversal precoding for space-time focusing in wireless communications," *IEEE Transactions on Instrumentation and Measurement*, vol. 59, no. 6, pp. 1537–1543, June 2010. <http://doi.org/10.1109/TIM.2009.2024339>
- [77] B. Wang, Y. Wu, F. Han, Y. H. Yang, and K. J. R. Liu, "Green wireless communications: A time-reversal paradigm," *IEEE Journal on Selected Areas in Communications*, vol. 29, no. 8, pp. 1698–1710, September 2011. <http://doi.org/10.1109/JSAC.2011.110918>
- [78] M. Lienard, P. Degauque, V. Degardin, and I. Vin, "Focusing gain model of time-reversed signals in dense multipath channels," *IEEE Antennas and Wireless Propagation Letters*, vol. 11, pp. 1064–1067, 2012. <http://doi.org/10.1109/LAWP.2012.2215002>
- [79] R. Hashmat, P. Pagani, A. Zeddami, and T. Chonavel, "Time-Reversal for EMC improvement in Powerline Communications," in *CEM 2010, April 7-9, Limoges France*, 2010.
- [80] A. Mescoco, P. Pagani, M. Ney, and A. Zeddami, "Radiation mitigation for power line communications using time reversal," *Journal of Electrical and Computer Engineering*, 2013. <http://dx.doi.org/10.1155/2013/402514>
- [81] G. Montaldo, M. Tanter, and M. Fink, "Revisiting iterative time reversal processing: Application to detection of multiple targets," *The Journal of the Acoustical Society of America*, vol. 115, no. 2, pp. 776–784, 2004. <http://scitation.aip.org/content/asa/journal/jasa/115/2/10.1121/1.1636463>

- [82] D. Liu, G. Kang, L. Li, Y. Chen, S. Vasudevan, W. Joines, Q. H. Liu, J. Krolik, and L. Carin, "Electromagnetic time-reversal imaging of a target in a cluttered environment," *IEEE Transactions on Antennas and Propagation*, vol. 53, no. 9, pp. 3058–3066, Sept 2005. <http://doi.org/10.1109/TAP.2005.854563>
- [83] D. A. Bibb, Z. Yun, and M. F. Iskander, "Source localization using time reversal in urban environments: A ray tracing approach," in *Antennas and Propagation Society International Symposium (APSURSI), 2014 IEEE*, July 2014, pp. 945–946. <http://doi.org/10.1109/APS.2014.6904801>
- [84] J. Benoit, C. Chauvière, and P. Bonnet, "Source identification in time domain electromagnetics," *Journal of Computational Physics*, vol. 231, no. 8, pp. 3446 – 3456, 2012. <http://www.sciencedirect.com/science/article/pii/S0021999112000411>
- [85] L. Abboud, A. Cozza, and L. Pichon, "A noniterative method for locating soft faults in complex wire networks," *IEEE Transactions on Vehicular Technology*, vol. 62, no. 3, pp. 1010–1019, March 2013. <http://doi.org/10.1109/TVT.2013.2237796>
- [86] M. Kafal, A. Cozza, and L. Pichon, "Locating multiple soft faults in wire networks using an alternative dort implementation," *IEEE Transactions on Instrumentation and Measurement*, vol. 65, no. 2, pp. 399–406, Feb 2016. <http://doi.org/10.1109/TIM.2015.2498559>
- [87] H. M. Manesh, G. Lugrin, R. Razzaghi, C. Romero, M. Paolone, and F. Rachidi, "A New Method to Locate Fault in Power Networks Based on Electromagnetic Time Reversal," in *13th IEEE International Workshop on Signal Processing Advances in Wireless Communications, Cesme, Turkey*, June 2012.
- [88] R. Razzaghi, G. Lugrin, H. Manesh, C. Romero, M. Paolone, and F. Rachidi, "An Efficient Method Based on the Electromagnetic Time Reversal to Locate Faults in Power Networks," *IEEE Transactions on Power Delivery*, vol. 28, no. 3, pp. 1663–1673, July 2013.
- [89] R. Razzaghi, G. Lugrin, M. Paolone, and F. Rachidi, "On the use of electromagnetic time reversal to locate faults in series-compensated transmission lines," in *PowerTech (POWERTECH), 2013 IEEE Grenoble*, June 2013, pp. 1–5.
- [90] R. Razzaghi, G. Lugrin, H. Mahmoudimanesh, C. Romero, M. Paolone, and F. Rachidi, "An efficient method based on the electromagnetic time reversal to locate faults in power networks," in *PES General Meeting / Conference Exposition, 2014 IEEE*, July 2014, pp. 1–1. <http://doi.org/10.1109/PESGM.2014.6939067>
- [91] R. Razzaghi, M. Paolone, F. Rachidi, J. Descloux, B. Raison, and N. Retière, "Fault location in multi-terminal HVDC networks based on Electromagnetic Time Reversal with limited time reversal window," in *Power Systems Computation Conference (PSCC), 2014*, Aug 2014, pp. 1–7. <http://doi.org/10.1109/PSCC.2014.7038411>
- [92] G. Lugrin, R. Razzaghi, F. Rachidi, and M. Paolone, "Electromagnetic time reversal applied to fault detection: The issue of losses," in *2015 IEEE International Symposium on Electromagnetic Compatibility (EMC)*, Aug 2015, pp. 209–212. <http://doi.org/10.1109/ISEMC.2015.7256160>

- [93] I. E. Baba, S. Lalléchère, and P. Bonnet, *Time Reversal for Electromagnetism: Applications in Electromagnetic Compatibility, Trends in Electromagnetism - From Fundamentals to Applications*. Wiley, 2012. <http://www.intechopen.com/books/trends-in-electromagnetism-from-fundamentals-to-applications/timereversal-for-electromagnetism-applications-in-electromagnetic-compatibility>
- [94] M. Davy, J. de Rosny, J.-C. Joly, and M. Fink, “Focusing and amplification of electromagnetic waves by time reversal in an leaky reverberation chamber,” *Comptes Rendus Physique*, vol. 11, no. 1, pp. 37 – 43, 2010, propagation and remote sensing Propagation et télédétection. <http://www.sciencedirect.com/science/article/pii/S1631070509002205>
- [95] A. Cozza, “Emulating an anechoic environment in a wave-diffusive medium through an extended time-reversal approach,” *IEEE Transactions on Antennas and Propagation*, vol. 60, no. 8, pp. 3838–3852, Aug 2012. <http://doi.org/10.1109/TAP.2012.2201097>
- [96] M. Frazier, B. Taddese, T. Antonsen, and S. M. Anlage, “Nonlinear time reversal in a wave chaotic system,” *Phys. Rev. Lett.*, vol. 110, p. 063902, Feb 2013. <http://link.aps.org/doi/10.1103/PhysRevLett.110.063902>
- [97] S. K. Hong, V. M. Mendez, T. Koch, W. S. Wall, and S. M. Anlage, “Nonlinear electromagnetic time reversal in an open semireverberant system,” *Phys. Rev. Applied*, vol. 2, p. 044013, Oct 2014. <http://link.aps.org/doi/10.1103/PhysRevApplied.2.044013>
- [98] W. M. Dyab, T. K. Sarkar, and M. Salazar-Palma, “Antenna reciprocity and the theory of electromagnetic time reversal,” in *Antennas and Propagation Society International Symposium (APSURSI), 2012 IEEE*, July 2012, pp. 1–2. <http://doi.org/10.1109/APS.2012.6347959>
- [99] W. M. G. Dyab, T. K. Sarkar, A. Garcia-Lamperez, M. Salazar-Palma, and M. A. Lagunas, “A critical look at the principles of electromagnetic time reversal and its consequences,” *IEEE Antennas and Propagation Magazine*, vol. 55, no. 5, pp. 28–62, 2014. <http://doi.org/10.1109/MAP.2013.6735472>
- [100] W. G. Dyab, T. K. Sarkar, and M. Salazar-Palma, “What is time reversal and what it cannot do?” in *2014 IEEE Conference on Antenna Measurements Applications (CAMA)*, Nov 2014, pp. 1–3. <http://doi.org/10.1109/CAMA.2014.7003396>
- [101] C. Altman and K. Suchy, *Reciprocity, Spatial Mapping and Time Reversal in Electromagnetics*. Springer Netherlands, 2011.
- [102] P. Roux, W. A. Kuperman, W. S. Hodgkiss, H. C. Song, T. Akal, and M. Stevenson, “A nonreciprocal implementation of time reversal in the ocean,” *The Journal of the Acoustical Society of America*, vol. 116, no. 2, pp. 1009–1015, 2004. <http://scitation.aip.org/content/asa/journal/jasa/116/2/10.1121/1.1707089>
- [103] J. D. Jackson, *Classical Electrodynamics*. Wiley, 3rd ed., New York, 1999.
- [104] D. Z. Albert, *Time and Chance*. Cambridge, MA: Harvard UP, 2000.
- [105] J. Earman, “What time reversal invariance is and why it matters,” *International Studies in the Philosophy of Science*, vol. 16, no. 3, pp. 245–264, 2002. <http://dx.doi.org/10.1080/0269859022000013328>

- [106] D. B. Malament, "On the time reversal invariance of classical electromagnetic theory," in *Studies in the History and Philosophy of Modern Physics 35B*, 2004, pp. 295–315.
- [107] F. Arntzenius and H. Greaves, "Time reversal in classical electromagnetism," November 2007.
- [108] S. J. Orfanidis, *Introduction to signal processing*. Prentice Hall International, 1996.
- [109] G. Lugrin, N. Mora, F. Rachidi, M. Rubinstein, and G. Diendorfer, "On the use of the time reversal of electromagnetic fields to locate lightning discharges," in *2012 International Conference on Lightning Protection (ICLP)*, Sept 2012, pp. 1–4. <http://doi.org/10.1109/ICLP.2012.6344263>
- [110] F. Rachidi, W. Janischewskyj, A. Hussein, C. Nucci, S. Guerrieri, B. Kordi, and J. Chang, "Current and electromagnetic field associated with lightning-return strokes to tall towers," *IEEE Transactions on EMC*, vol. 43, no. 3, pp. 356–367, Aug 2001. <http://doi.org/10.1109/15.942607>
- [111] T. K. Sarkar and O. Pereira, "Using the matrix pencil method to estimate the parameters of a sum of complex exponentials," *IEEE Antennas and Propagation Magazine*, vol. 37, no. 1, pp. 48–55, Feb 1995. <http://doi.org/10.1109/74.370583>
- [112] K. Schmidt, H.-D. Betz, W. P. Oettinger, M. Wirz, O. P. Jr., K. Naccarato, and H. H. an Th. Fehr an G. Held, "A comparative analysis of lightning data during the EU-Brazil TROCCINOX/TroCCiBras campaign," in *VIII International Symposium on Lightning Protection (SIPDA)*, São Paulo, Brazil, 2005.
- [113] F. Heidler, J. Cvetic, and B. Stanic, "Calculation of lightning current parameters," *IEEE Transactions on Power Delivery*, vol. 14, no. 2, pp. 399–404, Apr 1999. <http://doi.org/10.1109/61.754080>
- [114] G. D. et al., "Cloud-to-ground lightning parameters derived from lightning location systems – the effects of system performance," *CIGRE report*, 2009.
- [115] C. Paul, *Analysis of Multiconductor Transmission Lines*. John Wiley & Sons, 1994.
- [116] F. Rachidi, "A review of field-to-transmission line coupling models with special emphasis to lightning-induced voltages on overhead lines," *IEEE Transactions on EMC*, vol. 54, no. 4, pp. 898–911, Aug 2012. <http://doi.org/10.1109/TEMC.2011.2181519>
- [117] P. Lorrain and D. R. Corson, *Electromagnetism: principles and applications*. San Fransisco: W. H. Freeman, 1979.
- [118] A. Vukicevic, F. Rachidi, M. Rubinstein, and S. Tkachenko, "On the Evaluation of Antenna-Mode Currents Along Transmission Lines," *IEEE Transactions on EMC*, vol. 48, no. 4, pp. 693–700, Nov 2006. <http://doi.org/10.1109/TEMC.2006.884511>
- [119] G. Bridges and L. Shafai, "Plane wave coupling to multiple conductor transmission lines above a lossy earth," *IEEE Transactions on EMC*, vol. 31, no. 1, pp. 21–33, Feb. 1989. <http://doi.org/10.1109/15.19904>
- [120] J. Nitsch and S. Tkachenko, "High-Frequency Multiconductor Transmission-Line Theory," *Found Phys*, March 2010.

- [121] J. Nitsch and S. Tkachenko, "Source dependent transmission line parameters - plane wave vs TEM excitation," in *2003 IEEE International Symposium on Electromagnetic Compatibility. EMC '03*, vol. 2, may 2003, pp. 1140 – 1143 Vol.2. <http://doi.org/10.1109/ICSMC2.2003.1429118>
- [122] A. Agrawal, H. Price, and S. Gurbaxani, "Transient Response of Multiconductor Transmission Lines Excited by a Nonuniform Electromagnetic Field," *IEEE Transactions on EMC*, vol. 22, pp. 119–129, May 1980.
- [123] C. Taylor and J. Harrison, C., "The response of a terminated two-wire transmission line excited by a nonuniform electromagnetic field," *IEEE Transactions on Antennas and Propagation*, vol. 13, no. 6, pp. 987–989, Nov 1965. <http://doi.org/10.1109/TAP.1965.1138574>
- [124] E. Vance, *Coupling to Shielded Cables*. New-York: John Wiley & Sons, 1978.
- [125] S. A. Schelkunoff and H. T. Friis, *Antennas: theory and practice*. New-York: John Wiley & Sons, 1952.
- [126] S. A. Schelkunoff, *Electromagnetic waves*. New-York: Van Nostrand, 1956.
- [127] P. Degauque and A. Zeddam, "Remarks on the transmission-line approach to determining the current induced on above-ground cables," *IEEE Transactions on EMC*, vol. 30, no. 1, pp. 77–80, Feb 1988. <http://doi.org/10.1109/15.19893>
- [128] P. Degauque and J. Hamelin, *Compatibilité électromagnétique : bruits et perturbations radioélectriques*. Paris: Dunod, 1990.
- [129] A. A. Smith, *Coupling of external electromagnetic fields to transmission lines*. New-York: John Wiley & Sons, 1977.
- [130] W. Liu and Y. Kami, "Vertical riser effects of a finite-length transmission line," in *1999 International Symposium on EMC*, 1999, pp. 642–645. <http://doi.org/10.1109/ELMAGC.1999.801410>
- [131] S. Pignari and D. Bellan, "Incorporating vertical risers in the transmission line equations with external sources," in *International Symposium on Electromagnetic Compatibility (EMC 2004)*, vol. 3, Aug 2004, pp. 974–979. <http://doi.org/10.1109/ISEMC.2004.1349958>
- [132] Y. Leviatan and A. Adams, "The response of a two-wire transmission line to incident field and voltage excitation, including the effects of higher order modes," *IEEE Transactions on Antennas and Propagation*, vol. 30, no. 5, pp. 998 – 1003, Sep. 1982. <http://doi.org/10.1109/TAP.1982.1142893>
- [133] H. Haase, J. Nitsch, and T. Steinmetz, "Transmission-line super theory: A new approach to an effective calculation of electromagnetic interactions," *Radio Sci. Bulletin*, vol. 307, pp. 33–60, 2003.
- [134] S. Tkachenko, F. Rachidi, and M. Ianoz, "Electromagnetic field coupling to a line of finite length: theory and fast iterative solutions in frequency and time domains," *IEEE Transactions on EMC*, vol. 37, no. 4, pp. 509–518, Nov. 1995. <http://doi.org/10.1109/15.477335>

- [135] S. Tkatchenko, F. Rachidi, and M. Ianoz, “High-frequency electromagnetic field coupling to long terminated lines,” *IEEE Transactions on EMC*, vol. 43, no. 2, pp. 117–129, May 2001. <http://doi.org/10.1109/15.925531>
- [136] S. Tkachenko, J. Nitsch, R. Vick, F. Rachidi, and D. Poljak, “Singularity expansion method (SEM) for long terminated transmission lines,” in *2013 International Conference on Electromagnetics in Advanced Applications (ICEAA)*, Sept 2013, pp. 1091–1094. <http://doi.org/10.1109/ICEAA.2013.6632411>
- [137] S. Tkachenko, F. Middelstaedt, J. Nitsch, R. Vick, G. Lugrin, and F. Rachidi, “Application of singularity expansion method (SEM) to long transmission lines,” in *AMEREM*, 2014.
- [138] D. M. Pozar, *Microwave engineering*. Hoboken, NJ: Wiley, 2012.
- [139] S. Ramo, J. R. Whinnery, and T. Van Duzer, *Fields and Waves in Communication Electronics*, 3rd ed. Wiley, 1994.
- [140] J. Nitsch and F. Gronwald, “Analytical Solutions in Nonuniform Multiconductor Transmission Line Theory,” *IEEE Trans. on EMC*, vol. 41, pp. 469–479, November 1999.
- [141] H. Haase and J. Nitsch, “Full-wave transmission line theory for the analysis of three-dimensional wire-like structures,” in *EMC Zurich 01*, February 2001, pp. 235–240.
- [142] H. Haase, T. Steinmetz, and J. Nitsch, “New propagation models for electromagnetic waves along uniform and nonuniform cables,” *IEEE Transactions on EMC*, vol. 46, no. 3, pp. 345–352, Aug 2004. <http://doi.org/10.1109/TEM.2004.831829>
- [143] H. Haase, “Full-wave field interactions of nonuniform transmission lines,” Ph.D. dissertation, Otto-von-Guericke-Universität Magdeburg, 2005.
- [144] J. Nitsch and S. Tkachenko, “Complex-Valued Transmission-Line Parameters and Their Relation to the Radiation Resistance,” *IEEE Transactions on EMC*, vol. 46, pp. 477–487, Aug. 2004.
- [145] —, “Newest Developments in Transmission-Line Theory and Applications,” *Interaction Notes*, vol. IN 592, Sept. 2004.
- [146] —, “Telegrapher equations for arbitrary frequencies and modes: Radiation of an infinite, lossless transmission line,” *Radio Science*, vol. 39, no. 2, 2004, rS2026. <http://dx.doi.org/10.1029/2002RS002817>
- [147] —, “Global and modal parameters in the generalized transmission line theory and their physical meaning,” *URSI Radio Science Bulletin*, 2005.
- [148] F. Gronwald, “On the applicability of conventional transmission line theory within cavities,” *Advances in Radio Science*, vol. 4, pp. 117–123, 2006. <http://www.adv-radio-sci.net/4/117/2006/>
- [149] J. Nitsch and S. Tkachenko, “Newest developments in transmission-line theory and applications,” in *Ultra-Wideband, Short-Pulse Electromagnetics 7*, F. Sabath, E. Mokole, U. Schenk, and D. Nitsch, Eds. Springer New York, 2007, pp. 21–32. http://doi.org/10.1007/978-0-387-37731-5_3

- [150] —, “High-Frequency Multiconductor Transmission-Line Theory,” *Interaction Notes, Note 611*, Sept. 2009.
- [151] —, “Physical Interpretation of the Parameters in the Full-Wave Transmission Line Theory,” in *2009 XV International Symposium on Theoretical Engineering (ISTET)*, June 2009, pp. 1–5.
- [152] F. Gronwald, J. Nitsch, and S. Tkachenko, “Generalized transmission line theory as an antenna theory for emc analysis,” *Electrical Engineering*, vol. 93, no. 3, pp. 147–155, 2011. <http://doi.org/10.1007/s00202-011-0200-z>
- [153] S. Tkachenko, F. Middelstaedt, J. Nitsch, R. Vick, G. Lugrin, and F. Rachidi, “High-frequency electromagnetic field coupling to a long finite line with vertical risers,” in *General Assembly and Scientific Symposium (URSI GASS), 2014 XXXIth URSI*, Aug 2014, pp. 1–4. <http://doi.org/10.1109/URSIGASS.2014.6929526>
- [154] J. Nitsch and S. Tkachenko, “A lumped excitation of a vertical half-circular loop above conducting ground,” in *International Conference on Electromagnetics in Advanced Applications (ICEAA 2007)*, Sept 2007, pp. 752–755. <http://doi.org/10.1109/ICEAA.2007.4387412>
- [155] F. Gronwald, J. Nitsch, and S. Tkachenko, “On equivalent circuit representations for radiating systems by means of complex-valued network elements,” in *2012 International Conference on Electromagnetics in Advanced Applications (ICEAA)*, Sept 2012, pp. 710–713. <http://doi.org/10.1109/ICEAA.2012.6328720>
- [156] T.-J. Cui and W. C. Chew, “A full-wave model of wire structures with arbitrary cross sections,” *IEEE Transactions on EMC*, vol. 45, no. 4, pp. 626–635, Nov 2003.
- [157] D. Poljak, F. Rachidi, and S. Tkachenko, “Generalized Form of Telegrapher’s Equations for the Electromagnetic Field Coupling to Finite-Length Lines Above a Lossy Ground,” *IEEE Transactions on EMC*, vol. 49, no. 3, pp. 689–697, Aug. 2007. <http://doi.org/http://doi.org/10.1109/TEMC.2007.902179>
- [158] D. Poljak, A. Shoory, F. Rachidi, S. Antonijevic, and S. Tkachenko, “Time-Domain Generalized Telegrapher’s Equations for the Electromagnetic Field Coupling to Finite Length Wires Above a Lossy Ground,” *IEEE Transactions on Electromagnetic Compatibility*, vol. 54, no. 1, pp. 218–224, Feb 2012. <http://doi.org/10.1109/TEMC.2011.2181518>
- [159] S. Falco, G. Miano, L. Verolino, A. Maffucci, and F. Villone, “A full-wave model for the analysis of the high-frequency behavior of open interconnect structures,” in *2003 IEEE International Symposium on Electromagnetic Compatibility, 2003. EMC ’03*, vol. 1, May 2003, pp. 292–295. <http://doi.org/10.1109/ICSMC2.2003.1428248>
- [160] A. Maffucci, G. Miano, and F. Villone, “Full-wave transmission-line theory,” *IEEE Transactions on Magnetism*, vol. 39, no. 3, pp. 1594–1597, May 2003. <http://doi.org/10.1109/TMAG.2003.810525>
- [161] —, “An Enhanced Transmission Line Model for Conducting Wires,” *IEEE Transactions on EMC*, vol. 46, pp. 512–528, Nov. 2004.

- [162] A. Chiariello, A. Maffucci, G. Miano, F. Villone, and W. Zamboni, "A transmission-line model for full-wave analysis of mixed-mode propagation," *IEEE Transactions on Advanced Packaging*, vol. 31, no. 2, pp. 275–284, May 2008. <http://doi.org/10.1109/TADVP.2008.920373>
- [163] M. Brignone, F. Delfino, R. Procopio, M. Rossi, F. Rachidi, and S. Tkachenko, "An effective approach for high-frequency electromagnetic field-to-line coupling analysis based on regularization techniques," *IEEE Transactions on EMC*, vol. 54, no. 6, pp. 1289–1297, Dec 2012.
- [164] J. Nitsch and S. Tkachenko, "Propagation of Current Waves along Quasi-Periodical Thin-Wire Structures: Accounting of Radiation Losses," *Interaction Notes*, vol. Note 601, May 2006. <http://ece-research.unm.edu/summa/notes/In/0601.pdf>
- [165] S. Chabane, P. Besnier, and M. Klingler, "Restrictions potentielles de l'application de la théorie des lignes de transmission: quantification des erreurs d'approximation et intérêt des approches correctives," in *16ème édition du Colloque International sur la Compatibilité ElectroMagnétique (CEM 2012)*, 2012.
- [166] —, "Enhanced transmission line theory: Frequency-dependent line parameters and their insertion in a classical transmission line equation solver," in *2013 International Symposium on Electromagnetic Compatibility (EMC EUROPE)*, Sept 2013, pp. 326–331.
- [167] P. Besnier, S. Chabane, and M. Klingler, "Some limiting aspects of transmission line theory and possible improvements," *Electromagnetic Compatibility Magazine, IEEE*, vol. 3, no. 2, pp. 66–75, nd 2014. <http://doi.org/10.1109/MEMC.2014.6849549>
- [168] N. Theethayi, Y. Baba, F. Rachidi, and R. Thottappillil, "On the Choice Between Transmission Line Equations and Full-Wave Maxwell's Equations for Transient Analysis of Buried Wires," *IEEE Transactions on Electromagnetic Compatibility*, vol. 50, pp. 347–357, May 2008.
- [169] G. Lugrin, S. Tkachenko, F. Rachidi, M. Rubinstein, and R. Cherkaoui, "High-frequency electromagnetic coupling to multiconductor transmission lines of finite length," *IEEE Transactions on EMC*, vol. PP, no. 99, pp. 1–10, 2015. <http://doi.org/10.1109/TEMC.2015.2475156>
- [170] A. Prudnikov, Y. Brychkov, and O. Marichev, *Integral and series, Volume 1: elementary functions*. Taylor and Francis, 1998.
- [171] M. Abramovitz and I. Stegun, *Handbook of mathematical functions*. National bureau of standards, 1972.
- [172] F. Gardiol, *Électromagnétisme*. Presses polytechniques et universitaires romandes, 2004.
- [173] T. Liu and F. Tesche, "Analysis of antennas and scatterers with nonlinear loads," *IEEE Transactions on Antennas and Propagation*, vol. 24, no. 2, pp. 131–139, Mar 1976. <http://doi.org/10.1109/TAP.1976.1141328>
- [174] C. A. Balanis, *Antenna Theory: Analysis and Design*. Wiley, 2005.
- [175] G. Burke, *Numerical Electromagnetic Code - NEC-4. Method of Moments. Part II: Program Description - Theory.*, Jan. 1992.

- [176] R. Rambousky, J. Nitsch, and S. Tkachenko, “Application of transmission-line super theory to classical transmission lines with risers,” *Advances in Radio Science*, vol. 13, pp. 161–168, 2015. <http://www.adv-radio-sci.net/13/161/2015/>

Curriculum Vitae

Education

2011 M.Sc. degree in Electrical and Electronic Engineering from EPFL, minor in Energy.

Publications

Peer-review journal papers

2016 G. Lugrin, R. Razzaghi, F. Rachidi and M. Paolone, “Assessment of the Losses Influence on the Performance of the Electromagnetic Time Reversal Fault Location Method,” submitted to the IEEE Transactions on Power Delivery.

2015 G. Lugrin, S. Tkachenko, F. Rachidi, M. Rubinstein, and R. Cherkaoui, “High frequency electromagnetic coupling to multiconductor transmission lines of finite length,” *IEEE Transactions on EMC*, vol. PP, no. 99, pp.1–10, 2015. <http://doi.org/10.1109/TEMC.2015.2475156>

2014 G. Lugrin, N. Mora, F. Rachidi, M. Rubinstein, and G. Diendorfer, “On the Location of Lightning Discharges Using Time Reversal of Electromagnetic Fields,” *IEEE Transactions on EMC*, vol. 56, no. 1, pp. 149–158, Feb 2014. <http://doi.org/10.1109/TEMC.2013.2266932>

2013 R. Razzaghi, G. Lugrin, H. Manesh, C. Romero, M. Paolone, and F. Rachidi, “An Efficient Method Based on the Electromagnetic Time Reversal to Locate Faults in Power Networks,” *IEEE Transactions on Power Delivery*, vol. 28, no. 3, pp. 1663–1673, July 2013. <http://doi.org/10.1109/TPWRD.2013.2251911>

Conference proceedings and other papers

2016 G. Lugrin, F. Rachidi and S. Tkachenko, “Coupling to Transmission Line: Enhanced Modelling of the Risers”, APEMC symposium.

2015 N. Mora, G. Lugrin and F. Rachidi, “Study of the Propagation of IEMI Signals Along Power and Communication Lines”, in Interaction Notes, IN 627. <http://ece-research.unm.edu/summa/notes/In/IN627.pdf>

G. Lugrin, R. Razzaghi, F. Rachidi, and M. Paolone, “Electromagnetic time reversal applied to fault detection: The issue of losses,” in *2015 IEEE International Symposium on Electromagnetic Compatibility (EMC)*, Aug 2015, pp. 209–212. <http://doi.org/10.1109/ISEMC.2015.7256160>

2014

N. Mora, G. Lugrin, F. Rachidi, M. Nyffeler and P. Bertholet et al., "Effect of the Penetration through a Concrete Wall on the Propagation of Common Mode IEMI Signals," Asia Electromagnetics International Symposium (ASIAEM).

G. Lugrin, N. Mora, F. Rachidi, P. Bertholet and M. Nyffeler et al., "On the Applicability of the Transmission Line Theory for the Analysis of Common-Mode IEMI-Induced Signals," in *Asia Electromagnetics International Symposium (ASIAEM)*.

G. Lugrin, N. Mora, F. Rachidi, P. Bertholet and M. Nyffeler et al., "Test of Surge Protective Devices to Mitigate Intentional Electromagnetic Interferences (IEMI)," in *Asia Electromagnetics International Symposium (ASIAEM)*.

G. Lugrin, N. Mora, F. Rachidi, M. Righero, and M. Rubinstein, "Protection contre les interférences électromagnétiques intentionnelles: Peut-on utiliser les techniques classiques de la CEM ?" *Bulletin SEV/AES*, 6/2015. http://www.bulletin-online.ch/uploads/media/38-41_1506_lugrin.pdf

R. Razzaghi, G. Lugrin, H. Mahmoudimanesh, C. Romero, M. Paolone, and F. Rachidi, "An efficient method based on the electromagnetic time reversal to locate faults in power networks," in *PES General Meeting / Conference Exposition*, 2014 IEEE, July 2014, pp. 1–1. <http://doi.org/10.1109/PESGM.2014.6939067>

P. Bertholet, A. Kaelin, G. Lugrin, N. Mora, M. Nyffeler, F. Rachidi, and M. Rubinstein, "Design and realization of a high-voltage adapter for the testing of surge protective devices against intentional electromagnetic interferences," in *American Electromagnetics International Symposium (AMEREM)*, Albuquerque, New Mexico, USA, 2014.

N. Mora, F. Vega, G. Lugrin, F. Rachidi, and M. Rubinstein, "Study and classification of potential IEMI sources," *System Design and Assessment Notes*, Note 41, 2014. <http://ece-research.unm.edu/summa/notes/SDAN/0041.pdf>

S. Tkachenko, F. Middelstaedt, J. Nitsch, R. Vick, G. Lugrin, and F. Rachidi, "Application of singularity expansion method (SEM) to long transmission lines," in *AMEREM*, 2014.

S. Tkachenko, F. Middelstaedt, J. Nitsch, R. Vick, G. Lugrin, and F. Rachidi, "High-frequency electromagnetic field coupling to a long finite line with vertical risers," in *General Assembly and Scientific Symposium (URSI GASS)*, 2014 XXXIth URSI, Aug 2014, pp. 1–4. <http://doi.org/10.1109/URSIGASS.2014.6929526>

D. Recordon, M. Rubinstein, M. Stojilovic, N. Mora, G. Lugrin, F. Rachidi, L. Rouiller, W. Hirschi, and S. Sliman, "A comparator-based technique for identification of intentional electromagnetic interference attacks," in *2014 International Symposium on Electromagnetic Compatibility (EMC Europe)*, Sept 2014, pp. 1257–1262.

- 2013 G. Lugrin, N. Mora, S. Sliman, F. Rachidi, M. Rubinstein, and R. Cherkaoui, "Overview of IEMI Conducted and Radiated Sources: Characteristics and Trends," in *2013 EMC Europe International Symposium*, Brugge, Belgium, 2013.
- G. Lugrin, N. Mora, S. Sliman, F. Rachidi, M. Rubinstein, and R. Cherkaoui, "La vulnérabilité des réseaux électriques en cas d'attaques électromagnétiques. Caractéristiques des sources d'interférences intentionnelles," *Bulletin SEV/AES*, 5/2013. http://www.bulletin-online.ch/uploads/media/1305_Seite_039-043.pdf
- R. Razzaghi, G. Lugrin, M. Paolone, and F. Rachidi, "On the use of electromagnetic time reversal to locate faults in series-compensated transmission lines," in *PowerTech (POWERTECH)*, 2013 IEEE Grenoble, June 2013, pp. 1–5. <http://doi.org/10.1109/PTC.2013.6652101>
- 2012 N. Mora, G. Lugrin, R. Cherkaoui, F. Rachidi, and M. Rubinstein, "On the vulnerability analysis against IEMI," in *European Electromagnetics International Symposium EUROEM 2012*, Toulouse, France, 2012.
- G. Lugrin, N. Mora, F. Rachidi, M. Rubinstein, and G. Diendorfer, "Localisation de la Foudre par Retournement Temporel," in *16e Colloque International sur la Compatibilité Electromagnétique*, Rouen, April 2012.
- G. Lugrin, N. Mora, F. Rachidi, S. Tkachenko, M. Rubinstein, and R. Cherkaoui, "Highfrequency Electromagnetic Coupling to Long Loaded Multi-conductor Transmission Line," in *European Electromagnetics International Symposium EUROEM*, Toulouse, July 2012.
- G. Lugrin, N. Mora, F. Rachidi, M. Rubinstein, and G. Diendorfer, "On the use of the time reversal of electromagnetic fields to locate lightning discharges," in *2012 International Conference on Lightning Protection (ICLP)*, Sept 2012, pp. 1–4. <http://doi.org/10.1109/ICLP.2012.6344263>
- H. M.Manesh, G. Lugrin, R. Razzaghi, C. Romero, M. Paolone, and F. Rachidi, "A New Method to Locate Fault in Power Networks Based on Electromagnetic Time Reversal," in *13th IEEE International Workshop on Signal Processing Advances in Wireless Communications*, Cesme, Turkey, June 2012. <http://doi.org/10.1109/SPAWC.2012.6292952>

Supervised student projects**Master's projects**

- 2014 H. Jemaïel, "Application du retournement temporel pour la localisation de la foudre," Master's thesis, EPFL, June 2014.
- 2012 H. Mahmoudimanesh, "Localisation de défauts dans les lignes de transmission d'énergie électrique par la méthode du retournement temporel," Master's thesis, EPFL, 2012.

Semester's projects

- 2015 F. B. Harrington, "Localisation de défauts dans les réseaux électriques en utilisant le retournement temporel: effet des pertes dans les lignes multiconducteur," Semester project, EPFL, June 2015.
- H. Khounat, "Illumination de câbles par des impulsions électromagnétiques rapides," Semester project, EPFL, February 2015.
- 2012 X. Zhou, "Electromagnetic coupling of a plane wave to an overhead transmission line," Semester project, EPFL, June 2012.